



**HAL**  
open science

# Dynamique de la combustion dans un foyer annulaire multi-injecteurs diphasique

Kevin Prieur

► **To cite this version:**

Kevin Prieur. Dynamique de la combustion dans un foyer annulaire multi-injecteurs diphasique. Autre. Université Paris Saclay (COmUE), 2017. Français. NNT : 2017SACLC070 . tel-01688256

**HAL Id: tel-01688256**

**<https://theses.hal.science/tel-01688256>**

Submitted on 19 Jan 2018

**HAL** is a multi-disciplinary open access archive for the deposit and dissemination of scientific research documents, whether they are published or not. The documents may come from teaching and research institutions in France or abroad, or from public or private research centers.

L'archive ouverte pluridisciplinaire **HAL**, est destinée au dépôt et à la diffusion de documents scientifiques de niveau recherche, publiés ou non, émanant des établissements d'enseignement et de recherche français ou étrangers, des laboratoires publics ou privés.

# Dynamique de la combustion dans un foyer annulaire multi-injecteurs diphase

Thèse de doctorat de l'Université Paris-Saclay  
préparée à CentraleSupélec

École doctorale n°579 sciences mécaniques et énergétiques,  
matériaux et géosciences (SMEMAG)  
Spécialité de doctorat: Combustion

Thèse présentée et soutenue à Gif-sur-Yvette, le 14/12/2017, par

**Kevin Prieur**

Composition du Jury :

Françoise Baillot Professeur, Université de Rouen (CORIA - UMR 6614)	Président
Nicolas Noiray Professeur, ETH Zürich (D-MAVT)	Rapporteur
Thierry Poinsot Professeur, Institut de Mécanique des Fluides de Toulouse	Rapporteur
Michel Cazalens Professeur, Safran Tech	Examineur
Christian Tenaud Directeur de Recherche, Université d'Orsay (LIMSI - UPR 3251)	Examineur
Thierry Schuller Professeur, Institut de Mécanique des Fluides de Toulouse	Directeur de thèse
Sébastien Candel Professeur, CentraleSupélec (EM2C - UPR 288)	Co-Directeur de thèse
Daniel Durox Ingénieur de Recherche, CentraleSupélec (EM2C - UPR 288)	Co-Directeur de thèse



*« Ne craignez pas d'être lent, craignez seulement d'être à l'arrêt »*

Proverbe Chinois



# Remerciements

J'aimerais ici commencer par remercier un certain nombre de personnes. C'est un exercice difficile car on oublie toujours des gens à qui on voudrait dire merci et qui se sentiront blessés. A ceux qui ne se retrouveront pas dans cette liste, merci quand même (...). Mes remerciements au laboratoire ont été longs, ce n'est pas une coutume dans ce lieu, mais j'ai voulu profiter de l'attention de tout le monde pour souligner l'apport de chacun à ce travail d'équipe.

Tout d'abord, un grand merci à tout le jury (Françoise, Nicolas, Thierry, Michel, Christian et mes trois encadrants) d'avoir accepté de relire et d'évaluer ce travail de 3 ans. Je connais vos emplois du temps et je sais à quel point la relecture d'un manuscrit peut être long : merci pour votre temps et votre attention. J'ai beaucoup apprécié cet après-midi de soutenance, j'en garderais un excellent souvenir par la suite. L'équipe dans laquelle j'ai eu la possibilité de m'inscrire mérite un tonnerre d'applaudissement. J'ai pu apprécier la disponibilité de tout le monde et le travail effectué pendant ces trois années est purement le fruit d'une collaboration efficace à quatre. Daniel, comme je l'ai déjà dit à l'oral, merci pour ce travail de tous les jours, ton investissement quotidien, diurne et nocturne (!). Je pense, au bout de trois ans, commencer à mesurer l'étendue de ton savoir technique, et il continue toujours à m'impressionner. Sébastien, un grand merci pour ta disponibilité. J'ai été impressionné de ton investissement malgré tes engagements, grandissant, en dehors du laboratoire. Ta force de travail m'a beaucoup impressionné au cours de ces trois années. Thierry, bien que tu aies changé de laboratoire au cours de ma thèse, tu as su rester investi et dynamique tout au long de ces quelques années. Merci pour tous tes conseils et tes avis toujours éclairés sur les chemins à prendre au cours de ce doctorat.

Merci à tout le laboratoire, où il règne, et pour longtemps j'espère, une très bonne ambiance. J'ai pu côtoyer un grand nombre de co-bureau au fur et à mesure des changements de locaux. Ils se reconnaîtront et je les remercie chaudement pour tous les moments de rire, de fou rire, de parties de nerf, d'histoires bizarres, de musiques insolites et autres. Ces quelques activités extra-professionnelles sont souvent celles qui font tenir !

Un merci appuyé aux différentes personnes que j'ai pu croiser en conférence, en travaillant dans d'autres laboratoires et en industrie. Encore plus à celles qui se sont déplacées pour ma thèse. Comme je l'ai dit, je ne vais pas faire de liste exhaustive des personnes que je remercie, car j'en oublierai. Je vais plutôt citer les groupes d'amis que je remercie, qui ont été tous présents ces dernières années. Une attention particulière à tous ceux qui ont pu faire le déplacement pour ma thèse. Cela m'a par-

ticulièrement touché quand je sais à quel point vous pouvez être occupés (comme un Ministre oui).

Un grand merci à mon groupe d'ami du lycée avec qui j'ai pu garder contact. C'est toujours marrant de voir comment on évolue, surtout quand on regarde les photos d'il y a quelques années (...) ! Mes amis de l'université ont été un grand appui avec qui j'ai pu bien profiter de restaurants, bars et autres activités afin de décompresser. Merci à tous les gens de l'ESPCI, en particuliers ceux de la promotion 129, qui sont maintenant majoritairement docteurs aussi et que je peux maintenant rejoindre. J'ai toujours plaisir à vous voir à l'occasion d'afterwork, de restaurants, de VnA, de week-ends organisés (ou non). Un merci spécial aux Bronzés avec qui j'ai partagé tant de choses au cours de ces cinq années ! Et avec qui je vais continuer à partager des choses bien évidemment.

Je n'oublie pas ceux avec qui j'ai partagé mon année de master à Centrale et avec qui j'ai toujours beaucoup d'affinités. J'y ai trouvé des camarades et je les garde comme amis proches. Merci pour les séances de rigolades à nos repas mensuels !

Mes amis, plus récents mais non moins éminents, tous sortis de l'ANAJ-IHEDN que j'ai découvert ces deux dernières années. Les nombreux événements auxquels nous avons pu participer ont tissé de forts liens. J'ai découvert à cette occasion des gens formidables, inhabituels pour certains, avec des valeurs qu'on ne rencontre pas partout.

Je remercie mes parents, sans qui tout cela ne serait évidemment pas possible. Merci de m'avoir donné la possibilité d'arriver jusque-là, ce n'est pas donné à tout le monde et je suis conscient du privilège que cela est. De manière plus générale, merci à ma famille, à Philippe en particulier d'avoir fait le déplacement. Merci à la famille d'Elodie qui s'est avérée très efficace pour la préparation du pot, pour son exécution et pour tout le reste.

Enfin, un grand merci à Elodie avec qui j'ai pu mutuellement faire ce chemin de 3 années en thèse, avec les voyages aux quatre coins du monde, les moments de joie et de moins grande joie et surtout une vie quotidienne riche et toujours pleine de surprises !

A bientôt à tous, on se recroisera bien quelque part.





# Résumé

Les chambres de combustion de moteurs aéronautiques et de turbines à gaz pour la production électrique adoptent une forme annulaire pour des raisons pratiques. Ces dernières décennies ont vu apparaître de nombreuses innovations dans le domaine de la combustion afin de réduire la consommation et les émissions polluantes. De nouveaux types d'injecteur, de type LPP - Lean Premixed Prevaporized, ont été mis au point. Ils permettent notamment de diminuer le rapport combustible/air et visent à pré-vaporiser le carburant en amont de la combustion afin de mieux le mélanger à l'air issu du compresseur. Cette architecture permet une amélioration de la consommation et des émissions polluantes, mais rend les foyers annulaires plus sensibles à des phénomènes instationnaires qui perturbent le fonctionnement du système, accroissent les flux de chaleur vers les parois de la chambre, induisent des vibrations de structures, entraînent une fatigue cyclique des pièces mécaniques et dans des cas extrêmes conduisent à des dommages irréversibles. Pour éviter les régimes instables, il est souvent nécessaire d'interdire certains domaines de fonctionnement, avec une réduction potentielle des performances. La majeure partie des expériences disponibles dans la littérature traitent de systèmes mono-injecteurs dans des géométries simplifiées. Il existe peu de données expérimentales de référence dans le domaine des chambres annulaires, pourtant nécessaires à la validation des modèles et des simulations numériques. Dans ce cadre général, l'objectif de cette thèse est de poursuivre l'effort engagé au laboratoire EM2C sur ce thème et plus particulièrement sur celui de la dynamique de la combustion dans les chambres annulaires comportant un ensemble d'injecteurs. La thèse concerne plus spécialement le cas où l'injection du combustible s'effectue sous forme liquide. Le banc d'essai MICCA, développé au laboratoire, a été adapté pour recevoir des injecteurs dotés d'atomiseurs et alimentés en combustible liquide. Cette configuration reproduit sous forme idéalisée celle que l'on trouve en pratique dans les moteurs aéronautiques et elle correspond au besoin industriel exprimé par Safran. La chambre, désignée sous le nom de MICCA-Spray, est équipée de 16 injecteurs swirlés pouvant être alimentés par un combustible liquide ou gazeux, permettant ainsi une combustion diphasique ou prémélangée. Le système possède des parois en quartz donnant un accès optique à la zone de flamme. Il est aussi équipé d'un ensemble de diagnostics tels des microphones, des photomultiplicateurs ainsi que des systèmes d'imagerie à haute cadence. Les résultats présentés dans ce document traitent à la fois de situations dans lesquelles le système est alimenté en prémélange air-propane et d'études dans le cas où les injecteurs forment un spray de gouttelettes de n-heptane/air. Les travaux sont découpés en deux grandes parties. Une première partie traite de la

dynamique de la combustion dans le cas d'une injection diphasique. L'allumage de la chambre annulaire dans le cas diphasique est étudié. La structure de la flamme ainsi que sa propagation sont analysées de manière systématique et une comparaison détaillée est réalisée entre plusieurs combustibles, liquides ou non. Il a ainsi été possible d'établir une base de données de référence pour l'allumage des chambres annulaires. Les paramètres principaux contrôlant l'allumage sont alors déterminés. Une attention particulière est portée sur l'influence du passage de la flamme au-dessus de plusieurs injecteurs. On montre alors que la forme de flamme est fortement affectée avec, dans un premier temps, une flamme accrochée aux lèvres du brûleur qui finit par se décrocher pour adopter sa forme définitive en M. La dynamique de l'injecteur doit alors être évaluée pour bien prendre en compte ce phénomène. Les phénomènes instationnaires pouvant être rencontrés dans ce type de système sont étudiés dans une deuxième partie du travail. On s'intéresse notamment aux instabilités de combustion couplées par des modes acoustiques azimutaux de la géométrie annulaire. Les études sont menées dans le cas de la combustion diphasique. Les modes d'instabilités déjà observés dans le cadre de la thèse de Jean-Francois Bourgouin sont retrouvés avec des amplitudes de fluctuation de pression acoustique plus importantes allant jusqu'à 6% de la pression moyenne dans le foyer. Ces oscillations peuvent alors engendrer un soufflage des flammes dans la chambre annulaire, diminuant de près de 50% son rendement. Une étude approfondie des phénomènes d'instabilité sur un brûleur comportant un seul injecteur, SICCA-Spray, correspondant à un secteur de la chambre annulaire, est effectuée afin de mieux comprendre la dynamique d'une seule flamme. Des conclusions sur la dynamique de la chambre annulaire sont alors proposées à partir de ces expériences. Ces expériences sur un mono-injecteur sont complétées par des simulations aux grandes échelles de l'écoulement. Dans un premier temps, une flamme stationnaire est établie et comparée avec celle étudiée expérimentalement. Deux cas sont ensuite étudiés, un cas où les instabilités de combustion se développent naturellement dans le foyer et un cas où l'injection d'air est modulée afin de reproduire la dynamique de la flamme lorsqu'elle est instable. Cette seconde étude permet l'évaluation numérique de la fonction de transfert de la flamme qui est alors comparée aux mesures expérimentales. L'ensemble de ces travaux permet de mieux cerner les conditions dans lesquelles un couplage azimutal peut apparaître et conduire à des oscillations auto-entretenues. La dernière partie de la thèse est consacrée à deux études expérimentales menées cette fois dans le cas d'une injection prémélangée d'air et de propane. La première étude concerne l'influence de la forme de la sortie de l'injecteur sur la forme prise par la flamme. On s'intéresse ici à l'effet de l'angle du bol et on montre notamment qu'à partir d'un certain angle critique, des flammes voisines peuvent adopter des formes différentes conduisant à une alternance. La seconde étude menée dans le cas prémélangé est réalisée pour mieux comprendre ce qui conduit à la sélection de mode. On traite de l'apparition de modes azimutaux stationnaires ou tournants et on montre qu'un phénomène d'hystérésis peut être observé et qu'il joue un rôle dans l'établissement du type de mode qui est finalement observé.





# Abstract

Combustion chambers of aircraft engines and gas turbines for electrical production adopt a ring shape for practical reasons. These last decades have seen many innovations in the field of combustion to reduce fuel consumption and pollutant emissions. The increase in air traffic and the establishment of new ACARE 2050 standards are leading aeronautical manufacturers to continue in this direction for the future. For this purpose, new types of injector, for example LPP - Lean Premixed Prevaporized, have been developed. They make it possible, in particular, to reduce the fuel / air ratio and aim to pre-vaporize the fuel upstream of the combustion in order to mix it better with the air coming from the compressor. This architecture allows an improvement of the fuel consumption and the pollutant emissions, but makes annular chambers more sensitive to unsteady phenomena which disturb the functioning of the system, increase the heat flows towards the walls of the chamber, induce vibrations of structures, cause cyclic fatigue of mechanical parts and in extreme cases lead to irreversible damage. To avoid unstable regimes, it is often necessary to prohibit certain areas of operation, with a potential reduction in performance. Many studies on combustion instabilities are available in the scientific literature. Most experiments deal with single-injector systems in simplified geometries. There are few experimental data of reference in the field of annular chambers, even if these data are necessary for the validation of models and numerical simulations. The objective of this thesis is to continue the effort undertaken at the EM2C laboratory on this topic and more particularly on the dynamics of combustion in annular chambers comprising a set of injectors. The thesis concerns more particularly the case where the injection of the fuel takes place in liquid form. The MICCA test bench, developed in the laboratory, has been adapted to receive injectors equipped with atomizers and supplied with liquid fuel. This configuration reproduces, in idealized form, what can be found in practice in aeronautical engines and it corresponds to the industrial need expressed by Safran. It is also a configuration studied at the fundamental level. The chamber, known as MICCA-Spray, is equipped with 16 swirled injectors that can be powered by liquid or gaseous fuel, thus enabling two-phase or fully premixed combustion. The system has quartz walls giving optical access to the flame zone. It is also equipped with a set of diagnostics such as microphones, photomultipliers and high-speed imaging systems. The results presented in this document deal with both situations in which the system is fed with an air-propane premixture and studies where the injectors form a spray of n-heptane / air droplets. The works are divided into two parts. A first part deals with the dynamics of combustion with liquid fuel injection. The ignition of the annular chamber is studied in

this case. The structure of the flame and its propagation are analyzed in a systematic way and a detailed comparison is made between several fuels, liquid or gaseous. It has thus been possible to establish a reference database for ignition in annular chambers. The main parameters controlling the ignition are then determined. Particular attention is paid to the influence of the passage of the flame over several injectors. It is shown that the flame shape is strongly affected with, at first, a flame attached to the burner's lips which finally breaks off to adopt its final form, with an "M" shape. The dynamics of the injector must then be evaluated to take this phenomenon into account. The unsteady phenomena that can be encountered in this type of system are then studied in the second part of the thesis. We are particularly interested in combustion instabilities coupled by azimuthal acoustic modes of the annular geometry. The studies are conducted in the case of two-phase flow combustion. The modes of instability already observed in the context of Jean-Francois Bourgouin's thesis are found with larger amplitudes of acoustic pressure fluctuation of up to 6% of the atmospheric pressure. These oscillations can then cause a blow-off of the flames in the annular chamber, decreasing by nearly 50% its combustion efficiency. A detailed study of the instability phenomena on a single-burner, SICCA-Spray, corresponding to a sector of the annular chamber, is carried out in order to better understand the dynamics of a single flame. Conclusions on the dynamics of the annular chamber are then proposed from these experiments. These experiments on a single-injector are supplemented by Large Eddy Simulations. At first, a stationary flame is established and compared with that studied experimentally. Two studies are then conducted. A first case where the combustion instabilities develop naturally in the combustion chamber and a second case where the air injection is modulated in order to reproduce the dynamics of the flame when it is unstable. This second study allows numerical evaluation of the flame transfer function which is then compared to measurements. All of this work makes it possible to better define the conditions in which an azimuthal coupling can appear and lead to self-sustaining oscillations. The last part of the thesis is devoted to two experimental studies conducted this time in the case of a premixed injection of air and propane. The first study concerns the influence of the geometric shape of the outlet of the injector on the shape taken by the flames. It is interesting here to note the effect of the angle of the cup. It is shown, in particular, that from a certain critical angle, neighboring flames can adopt different forms of flame leading to an alternation of flames of various types. The second study is carried out to better understand what leads to the selection of mode. The appearance of stationary or rotating azimuthal modes is discussed and it is shown that a hysteresis phenomenon can be observed and that it plays a role in establishing the type of mode which is finally observed. It is shown that the chamber can have either a spinning mode or a stationary mode depending on the path followed to reach the operating conditions.





# Contents

<b>Introduction</b>	<b>1</b>
<b>Publications</b>	<b>11</b>
<b>I A two phase flow annular combustor called MICCA-Spray</b>	<b>15</b>
<b>1 Experimental set-ups</b>	<b>17</b>
1.1 Introduction . . . . .	17
1.2 MICCA-Spray annular set-up . . . . .	18
1.3 Single burner SICCA-Spray set-up . . . . .	25
1.4 Conclusion . . . . .	27
<b>2 Light-round in an annular combustor</b>	<b>31</b>
2.1 Introduction . . . . .	33
2.2 Experimental configuration . . . . .	34
2.3 Light-round experimental data and interpretation . . . . .	40
2.4 Intermediate discussion . . . . .	44
2.5 Flame front passage $90^\circ$ from the ignition point . . . . .	46
2.6 Flame structure evolution during the light-round . . . . .	51
2.7 Dynamics of ignition in a single injector system . . . . .	57
2.8 A model of the injector response to light round . . . . .	59
2.9 Conclusions . . . . .	62
<b>3 Flame dynamics in a spray swirl annular combustor</b>	<b>65</b>
3.1 Introduction . . . . .	65
3.2 Experimental set up . . . . .	68
3.3 Single burner characterization . . . . .	70
3.4 Analysis of the self-sustained instabilities . . . . .	74
3.5 Flame blow-off under high pressure oscillations . . . . .	83
3.6 Theoretical analysis . . . . .	85
3.7 Conclusion . . . . .	87
<b>4 SICCA-Spray burner experiments</b>	<b>91</b>
4.1 Introduction . . . . .	91

4.2	Experimental configuration . . . . .	93
4.3	Frequency response of the system . . . . .	96
4.4	Self-excited instabilities . . . . .	97
4.5	Forced flame response . . . . .	100
4.6	Flame Describing Function measurements . . . . .	102
4.7	Conclusion . . . . .	107
<b>5</b>	<b>LES calculations of SICCA-Spray burner</b>	<b>111</b>
5.1	Introduction . . . . .	111
5.2	Numerical set-up . . . . .	114
5.3	Steady-state flame . . . . .	122
5.4	Self-excited flame . . . . .	138
5.5	Externally modulated flame . . . . .	148
5.6	Conclusion . . . . .	157
<b>II</b>	<b>A premixed annular combustor called MICCA</b>	<b>161</b>
<b>6</b>	<b>Flame pattern alternation</b>	<b>163</b>
6.1	Introduction . . . . .	163
6.2	Experimental Setup . . . . .	166
6.3	Analysis of flame patterns . . . . .	170
6.4	Alternating pattern switching . . . . .	173
6.5	Influence of the flame shape on the light intensity distribution . . . . .	175
6.6	Influence of the flame shapes on heat load on the inner wall . . . . .	176
6.7	Influence of the jet confinement on flame shape . . . . .	177
6.8	Conclusion . . . . .	179
<b>7</b>	<b>Flame dynamics during an hysteresis in an annular combustor</b>	<b>183</b>
7.1	Introduction . . . . .	185
7.2	Combustion instabilities coupled by azimuthal acoustic modes . . . . .	185
7.3	Experimental setup . . . . .	190
7.4	Instability regimes . . . . .	193
7.5	Hysteresis phenomenon . . . . .	201
7.6	Conclusions . . . . .	208
	<b>Conclusion</b>	<b>211</b>
	<b>A Flame shape during the MICCA ignition sequence</b>	<b>221</b>
	<b>B Decomposition of spinning and standing modes</b>	<b>225</b>
	<b>References</b>	<b>240</b>





# Introduction

Due to recent regulations on emissions and the corresponding need for new architectures, combustion dynamics has become a major issue in the design of aeronautical and gas turbine combustors. In most current aero-engines and land based gas turbines the combustor features an annular geometry due to technical requirements and is equipped with multiple injectors placed around the circumference of the annulus. The air is injected in a swirled fashion through “swirler” units. The swirling streams of air establish a Central Recirculation Zone (CRZ) downstream each injector in the near vicinity of the chamber backplane and Outer Recirculation Zones (ORZ) on the lateral sides of the air stream. When the system is ignited these regions are filled with hot combustion products that recirculate and serve as a continuous source of ignition to the incoming fresh reactants. In the aeronautical domain, the fuel is injected in a liquid form because it is easier to store a dense combustible featuring a large energy density. For kerosene the energy content is  $42 \text{ MJ kg}^{-1}$ . The latest technological developments focus on the injection system to be able to match required regulations on emissions and fuel consumption. The objective is to operate under lean conditions in a partially premixed mode with Lean Premixed Prevaporized (LPP) injectors to limit the formation of pollutants. These new injectors consist in burning the fuel that has been mixed to the air upstream of the combustion region with an increased ratio of air to fuel than with previous technologies.

Two constraints must then be fulfilled to validate this new technology. First, the engines must not suffer pressure oscillations and mechanical vibrations during their use with potential destructive consequences like enhanced heat fluxes to the chamber walls, cyclic fatigue and reduction of life duration. In the most difficult cases, unstable oscillations may also induce flashbacks or flame blow-off with serious consequences to the system. Unfortunately, the lean premixed combustion mode tends to increase the flame receptivity to external perturbations, promoting combustion instabilities. These take the form of thermo-acoustic instabilities that arise due to the resonant coupling of flame, flow, and acoustics. In these cases, the heat release of the flame couples to one of the acoustic resonant modes of the system and this may lead to large amplitude pressure excursions of up to a few % of the operating pressure in the chamber. Finally, due to the complex coupling between the different engine components, they can be a serious issue to tackle at a later stage in the design process.

Secondly, the jet engine has to be correctly and safely ignited when the aircraft is on

the ground and during relight if an extinction takes place during the flight. Ignition in harsh conditions and re-ignition in flight has to be ensured for many operating conditions with cold air at  $-50\text{ }^{\circ}\text{C}$  and in low pressure environments down to 0.35 bar. Currently, minimum fuel flow rate as well as igniters specifications are usually selected on the basis of OD models in combination with engineering know-how to fulfil these needs. The extension of these models to cutting edge technologies and new flight domains is not straightforward. A better understanding of the basic processes that control ignition is therefore needed. One major issue that needs to be considered is the optimization of the various choices made to diminish pollutant emissions and those made to ensure a secure ignition under relight conditions.

Before describing the objectives of the present work, it is worth briefly reviewing the scientific literature on annular combustors. One may note that there is a growing number of articles dealing with such configurations and that these articles are mainly theoretical and numerical. Ignition and combustion instabilities issues are the focal points of these investigations.

Numerical calculations relying on Large Eddy Simulations have brought considerable insight on these two items (see [Boileau et al. \(2008\)](#), [Staffelbach et al. \(2009\)](#), [Wolf et al. \(2012\)](#) and [Wolf et al. \(2012\)](#)). Theoretical studies have mainly dealt with the coupling between azimuthal modes and combustion dynamics ([Ghirardo and Juniper \(2013\)](#), [Bauerheim et al. \(2014\)](#), [Bauerheim et al. \(2015\)](#), [Bourgouin et al. \(2015\)](#), [Laera et al. \(2017\)](#)) but there are very few experimental validations. Experiments on annular combustors are limited due to the difficulties encountered in designing and operating such configurations. There are however a few exceptions. Industrial companies provide interesting but limited results on annular combustors, usually due to lack of diagnostic (see [Krebs et al. \(2002\)](#), [Noiray and Schuermans \(2013\)](#) and [Bothien et al. \(2015\)](#)). In the academia, one annular facility is that developed at the Technical University of Munich (TUM, [Kopitz et al. \(2005\)](#)) but with a reduced optical access to the flame region. A second model scale annular combustor is that designed at Cambridge by [Worth and Dawson \(2013b\)](#) and now duplicated at the Norwegian University of Science and Technology (NTNU) in Trondheim by [Worth et al. \(2017\)](#). This provides an improved access to the flame region but has a relatively small diameter and is fed by injection units with a fairly small swirl number. This facility has also been used at Cambridge to investigate ignition and light-round issues (see for example [Bach et al. \(2013\)](#)).

The third facility designed independently is the result of an ANR project (ANR-08-BLAN-0027-01) carried out at EM2C, CNRS and designated as MICCA (“Méthodes pour les Instabilités de Combustion Couplées par l’Acoustique”). This configuration comprises an annular combustor equipped with sixteen premixed swirled injectors. It was initially exploited in the doctoral thesis of Jean-François Bourgouin ([Bourgouin et al. \(2013a\)](#)). The originality of this model scale facility is the large optical access to the combustion region, the availability of numerous imaging diagnostics in

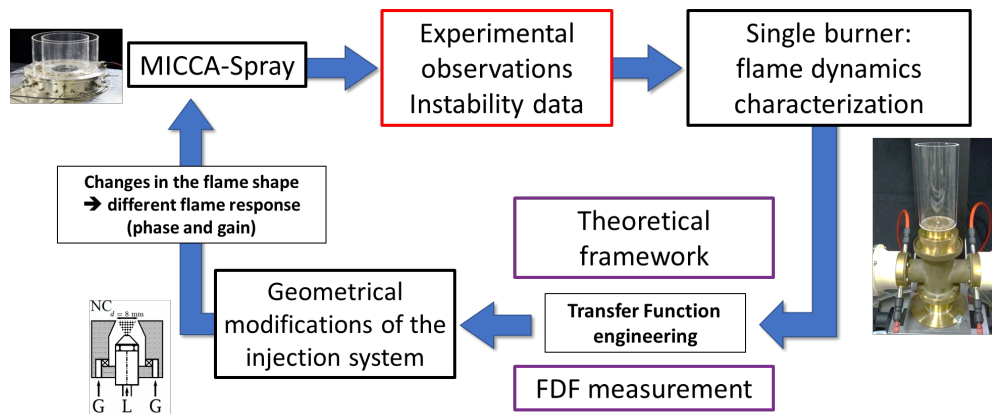


**Figure 1.** Engineering process loop in order to find a suitable injector geometry to excite natural azimuthal instabilities in the MICCA-Spray combustor.

combination with multiple pressure sensors recording signals in the plenum and at the chamber backplane. MICCA is an idealized version of industrial combustors with a reasonable power level of up to 120 kW and representative levels of swirl. Much data have been acquired during the thesis of Bourgouin on the MICCA facility under premixed conditions. Ignition (Bourgouin et al. (2013)) and flame dynamics (Bourgouin et al. (2015)) have been experimentally investigated and the effort has been accompanied by numerical simulations of the light-round carried out during the thesis of Maxime Philip (Philip et al. (2015)). The importance of combustion instabilities in this kind of geometry has been demonstrated for turbulent and laminar flames with the occurrence of a great variety of coupling modes.

A considerable number of papers deal with single injector configurations of various types including swirling injection systems and many types of laminar and turbulent flames. Fundamental investigations of combustion dynamics have led to significant progress in the understanding of the process (see for example the works made at EM2C Schuller et al. (2003), Noiray et al. (2008b), Palies et al. (2011) and Boudy et al. (2011)). Important progresses have been recently made in the understanding of the combustion dynamics of complex flames such as swirled flames. It was decided to continue the effort initiated more recently on multiple flame configurations and take advantage of the annular combustor MICCA. The originality of the present work lies in the adaptation of the MICCA system to a liquid fuel injection in the form of sprays. This is more representative of aeronautical configurations and closer to applications of interest to Safran. This project won the scientific and financial support of Safran allowing the development of MICCA-Spray, the liquid fuel injection version of MICCA. This facility is used in the present investigation to examine challenges in combustion dynamics of swirled spray flames formed by multiple injectors placed in the MICCA-Spray configuration. The manuscript deals with three major topics. The first two items use the spray configuration while the third item is examined in the ini-

tial MICCA configuration with premixed gaseous reactants.

1. The light-round process in MICCA-Spray is characterized with a detailed description of the propagation of the flame in the annular geometry. A particular attention is given to the impact of the fuel type on the process. Details on the process which leads to an established flame are also examined.
2. Combustion dynamics of the annular combustor MICCA-Spray and its detailed characterization in a single tubular burner called SICCA-Spray is investigated. A large dataset of instabilities and of their effect is established. The engineering method to find a correct injector geometry to trigger instabilities in MICCA-Spray is explained later on and in the sketch shown in Figure 1. This figure will be commented later on.
3. A focus on additional results obtained in the premixed combustor MICCA is finally made. First, it is observed that flame shapes in the annulus can switch from one to another pattern and are evenly distributed in the combustor. This phenomenon is quite important for industrial applications as it has large implications on the thermal load applied to the combustor walls and backplane. Secondly, laminar premixed flames are stabilized in the annular combustor. The study is concerned with an hysteresis phenomenon that occurs when a self-sustained excited azimuthal mode arises in the system. It is found that there is a memory effect and that the mode can be either standing or spinning and that this depends on the path followed to reach the operating conditions.

At this point it is interesting to give a brief account of the chronology of this investigation. Initial investigations were carried out on the MICCA configuration to examine the third item described previously. This allowed collection of further information on the possible regimes of combustion and in particular on the possibility to get an alternate pattern of flames *i.e.* a pattern where adjacent flames have different structures. The hysteresis phenomenon was also investigated because much of the current theoretical discussions focus on the selection process that define the spinning or standing nature of the azimuthal mode that assures the acoustic coupling. These studies were instructive but also necessary because of delays in the fabrication of the spray atomizers.

A first type of injector had been designed to accept liquid fuel injection and the atomizers which were difficult to machine were finally delivered by the manufacturer. The liquid fuel swirl spray injectors were then tested in the annular chamber MICCA-Spray. No natural combustion instability could be initiated whatever the effort made to obtain this kind of regime. It was then decided to examine the flame dynamics in a tubular burner comprising a single injector, named SICCA-Spray, equivalent to one sector of MICCA-Spray. A part of the work has consisted in the determination of the flame describing function in this geometry. The transfer function measurements may then be used in conduction with a simplified theoretical framework to examine changes that may give access to instabilities and that can be triggered in the annular

chamber. Depending on the predictions, geometrical modifications of the injection system were proposed and tested in the annular combustor. After a few iterations of the loop presented in Figure 1, the “correct” injector geometry was found. From an industrial point of view, the aim is of course just the opposite as one wishes to avoid naturally excited instabilities. The idea is then to work on the single tubular burner and, with the help of the theoretical framework, try to design an injector that will not be unstable when arranged in an annular combustor.

The reader should note that each chapter contains its own full literature review. This introduction only serves as a brief overview of the current state of the art when needed. Thus, one may find a much more precise analysis in each chapter. Several reviews have also been prepared recently and can be consulted by the reader to have a proper overview of the entire field: [Candel \(2002\)](#), [Culick and Kuentzmann \(2006\)](#), [Huang and Yang \(2009\)](#) and more recently [Poinsot \(2016\)](#) and ?.

## Thesis objectives and contents

The manuscript is divided into two parts arranged according to the following description.

### Part I: A two phase flow annular combustor called MICCA-Spray

This part presents results obtained on the annular combustor MICCA-Spray shown in Figure 2 and on the single tubular burner SICCA-Spray when both are fed with liquid n-heptane and air. A rapid description of the experimental configurations used through Chapter 2 to 5 is first proposed. The geometry is described with a particular focus on effects associated with the length of the side wall and with the spray injector design. Sensors and their location in the burners are also presented. More details on the devices are provided when needed throughout the different chapters.

Chapter 2 examines the characteristics of the ignition process in the annular combustor MICCA-Spray when it is fed with gaseous or liquid fuel. This study compares the impact of the type of combustion, premixed or spray, and the influence of the type of fuel injected, more or less volatile. The process, designated in the technical literature as the light-round, is extensively characterized with high-speed measurements with an intensified camera, a photomultiplier and a series of microphones placed in the plenum and in the chamber of the annular combustor. A large set of data is acquired and compared when the bulk velocity, the equivalence ratio or the power are varied. An example is given in Figure 3. A close-up view on the behavior of the flame propagation in an arch-like pattern is then presented in the second part of this chapter. Detailed imaging of the passing flame front gives indications on the flame wrinkling as well as the flame traveling velocity. By recording the Mie scattering of the n-heptane droplets, it is possible to observe the influence of the traveling flame front on the droplet distribution in the chamber. Once ignited, each injector develops

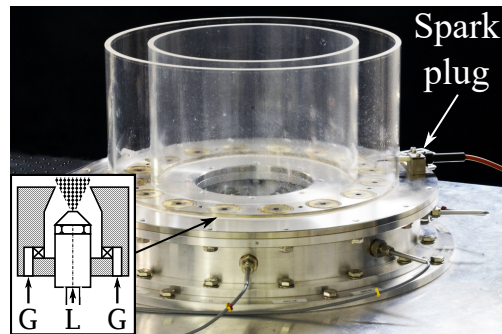


**Figure 2.** Photograph of the MICCA-Spray combustion chamber with sixteen liquid injectors and equipped with 200 mm quartz tubes and a single spark plug. An atomizer is sketched at the bottom left where “G” stands for gas and “L” for liquid injection channels.

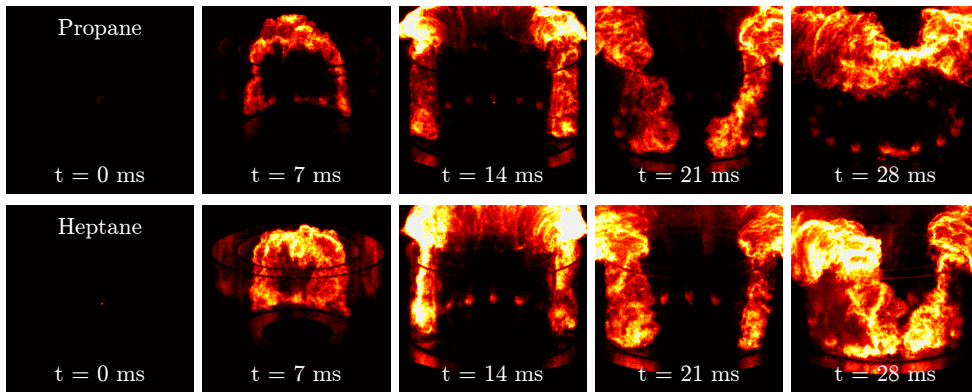


**Figure 3.** Light emission during the ignition sequence of propane (top) and n-heptane (bottom) fuels. Yellow corresponds to high light intensity while dark red represents low light emission. Each sequence features equivalent injection conditions :  $U_b = 31.5 \text{ m s}^{-1}$ ,  $\phi = 0.90$  and  $\mathcal{P} = 80 \text{ kW}$ .

a transient flame shape. It is shown that this shape evolves in time and can be linked to the perturbed incoming air flow rate. Rough models are then derived to estimate the time scales that control this process which finally leads to an established flame.

Chapter 3 focuses on the flame dynamics in an annular combustor when liquid fuel is used. Very large combustion instabilities coupled to the first azimuthal mode of the annular cavity are naturally triggered. Note that this mode appears in the form of long bursts at a repetition rate of approximately 2 Hz and that, during these bursts, the acoustic pressure in the chamber can reach up to 6% of the pressure in the chamber. The oscillation features a level of approximately 6000 Pa. The type of instability, that arises under these circumstances is then investigated. It is possible to see if the mode is spinning or standing by calculating the spin ratio. Specific attention is given to the

behavior of the flame at the nodal and anti-nodal positions during the standing mode. The flame motion is analyzed as well as the response of the heat release rate when the acoustic pressure oscillation amplitude increases. A particular focus is made on the flames at the nodal line, which exhibit a sweeping motion around their axis of symmetry. Above a certain acoustic pressure level, these flames can be destabilized and blown-off, decreasing dramatically the combustion efficiency of the annular combustor as shown in Figure 5. To explain this partial blow-off of the annular combustor, a model is developed that takes the aerodynamic dimensions of the flow into account. After studying the combustion instabilities in the annular combustor, Chapter 4 presents an analysis of the combustion dynamics in the SICCA-Spray burner. This single injector tubular chamber is representative of 1/16th of the annular combustor and is used to perform more detailed diagnostics on the combustion process. By changing the length of the chamber wall, this system features a steady flame when the size of the combustor is relatively small or exhibits longitudinal combustion instabilities at a limit cycle when the chamber is lengthened. This feature is used to first evaluate the flame dynamics when it is oscillating at the frequency of the thermo-acoustic instability. Several diagnostics are used to characterize the flame dynamics, in particular phase averaged  $\text{CH}^*$  chemiluminescence images as shown in Figure 6. The flame is then externally forced to reproduce its behavior when it is naturally unstable in order to evaluate the Flame Describing Function (FDF). The FDF describes the response of the flame when it is submitted to external forcing at a frequency  $f$  and for an amplitude  $A$  of the incoming perturbation. The acoustic pressure in the chamber  $p'$  or the incoming velocity fluctuation  $u'$  are both considered as an input of the FDF and are compared. One FDF is then used to predict the frequencies of the combustion instabilities that are naturally excited in SICCA-Spray and an extension to the MICCA-Spray instability observed in Chapter 3 is suggested.

The next Chapter 5 in this part reports Large Eddy Simulations of the SICCA-Spray flame using the AVBP solver. This code is jointly developed by CERFACS and IF-

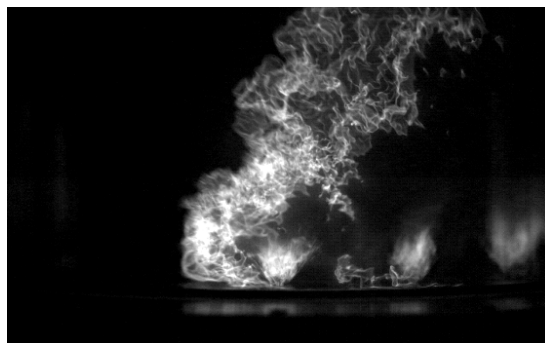


**Figure 4.** Top: instantaneous flame shape; Middle: flame cells extracted from the flame shape; Histogram of the flame cells sizes calculated over 300 images and 70,000 cells.

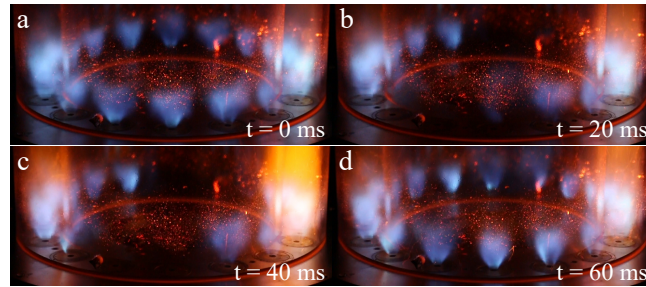


**Figure 5.** True-color photographs of the annular chamber when six flames are blown-off for  $\phi = 0.85$ ,  $\mathcal{P} = 111$  kW.

PEN. The manuscript first describes the numerical solver and the meshed geometry. For the un-confined geometry, cold flow is established and compared to experimental results acquired by Laser Doppler Velocimetry. Confined simulations under cold flow conditions and with injection of liquid n-heptane are then performed and validated. The flame is ignited by a hot sphere of burnt gas and then stabilizes in the combustion chamber. As for the experimental study of the SICCA-Spray burner, the wall length is increased and a longitudinal combustion instability is naturally predicted by the simulation. The phase average flame shape evolution during a cycle of instability is shown in Figure 7. Finally, well positioned probes in the numerical simulations are used to track the evolution of the axial velocity perturbation through the geometry.

The second part of the chapter is concerned with the external forcing of the flame as can be done experimentally. The inlet air flow is modulated at specific frequencies and amplitudes. The simulation is first validated at 530 Hz by examining the heat release rate and the acoustic pressure in the plenum. Several simulations are then run at different frequencies and amplitudes to numerically evaluate the Flame Describing Function (FDF) and compare results with those included in Chapter 4. The naturally excited flame and the forced one at the same amplitude and frequency are then compared numerically. In conclusion, difficulties induced by the forcing method are discussed in this manuscript.

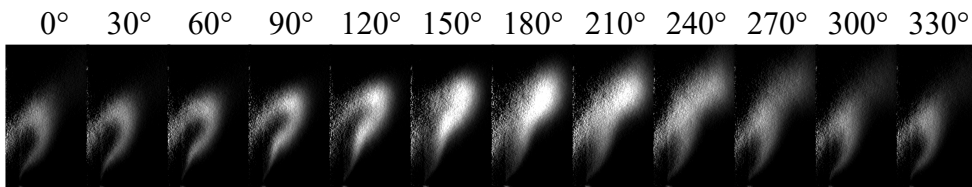


**Figure 6.** Phase average  $\text{CH}^*$  chemiluminescence of the flame during one cycle of oscillation for the naturally excited flame in the SICCA-spray setup. Images are averaged over 600 cycles.

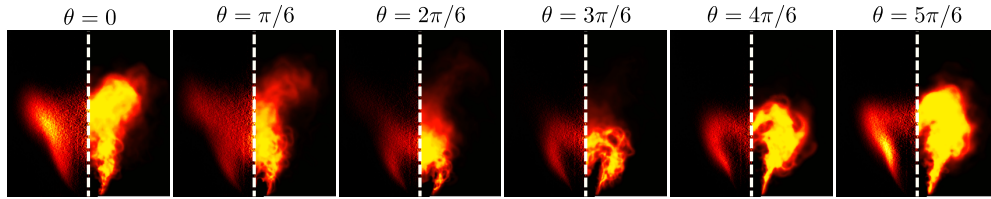


**Figure 7.** Comparison of the measured  $\text{CH}^*$  chemiluminescence intensity (left) and numerical heat release rate (right) during one cycle of oscillation. Experimental images are averaged over 600 cycles while numerical results are averaged over 20 cycles. Experimental images are displayed on a scale of false colors to ease comparison. The bottom of these images corresponds to the chamber backplane.

## Part II: a premixed annular combustor called MICCA

The second part of this manuscript focuses on the dynamics of the premixed combustion chamber MICCA, equipped with swirled injectors or laminar multiple flame perforated plate injectors. Each chapter comprises a detailed description of the experimental configurations as they differ from those investigated in Part I. A first study, presented in Chapter 6, is carried out with the MICCA annular chamber equipped with swirled premixed injectors. Several injector geometries are tested by changing the cup placed at their exit, linking the swirler to the combustion chamber. The study relies on parametric variations that correspond to changes in cup angles, from  $70^\circ$  to  $105^\circ$ , as well as changes in the axial offset, that is increased by up to 3 mm. The influence of these parameters on the flame shape is investigated with chemiluminescence images of the entire chamber. It is then shown that the chamber is capable of stabilizing “V” flames, “M” or amphora-like flames depending on the injection system used as shown in Figure 8. An Abel transform is applied to retrieve the different flame shapes and compare the corresponding structures. For some configurations, especially when the

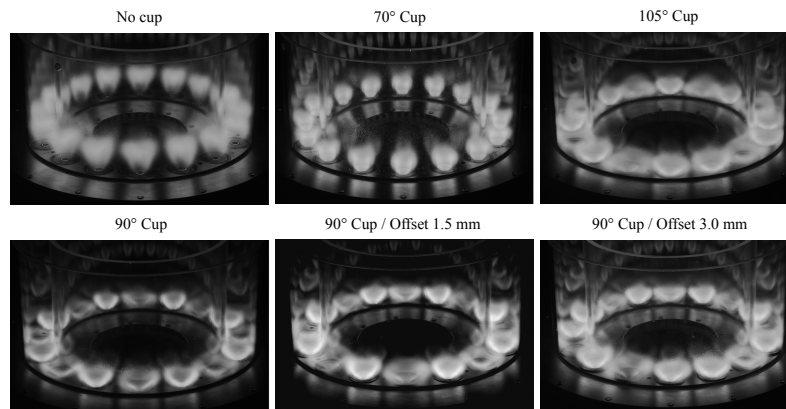


**Figure 8.** Typical flame shapes obtained for the different injector geometries.  $U_b = 17.1 \text{ m.s}^{-1}$ ,  $\phi = 0.74$ .

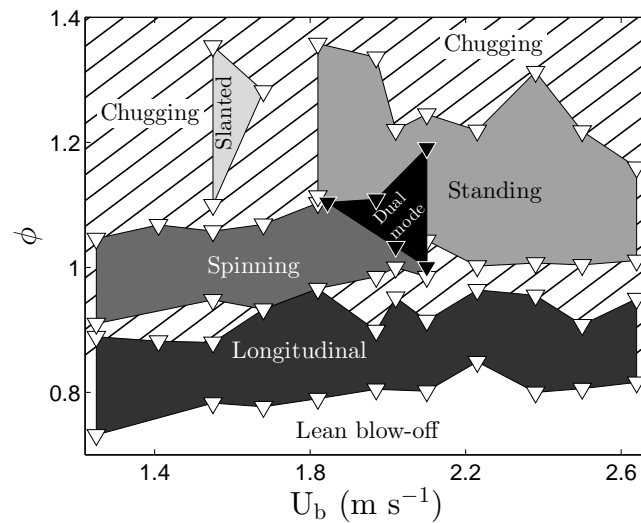


**Figure 9.** Stability map of the MICCA combustor delineating the different thermo-acoustic modes of the system. The “Dual mode” region is where the spinning and standing regions overlap. The hatched area is where the chugging mode is manifested. The blank area corresponds to the lean extinction limits of the chamber.

angle of the cup is increased, “V” shapes and “M” shapes can be alternated one flame in two. The influence of the operating conditions such as the equivalence ratio and the bulk velocity are also examined. For certain specific conditions, a pattern switching motion is observed. Neighboring flames alternately change their shape from a “V” flame to an “M” flame. This phenomenon is characterized using high speed imaging. Finally, the influence of the alternating pattern on the temperature distribution in the chamber is observed.

Chapter 7 describes experiments carried out using matrix injectors producing a multiplicity of small laminar flames stabilized in the MICCA combustion chamber. In this part, the system exhibits well controlled instabilities coupled to the first azimuthal acoustic mode of the chamber. These instabilities are characterized by high speed imaging and pressure sensors signals recorded in the plenum and in the combustion chamber. A large variety of already known unstable modes are analyzed, such as longitudinal, spinning, standing and slanted modes as illustrated in Figure 9. A novel mode, identified as the chugging mode, is described and observed whenever no pure combustion instability is triggered. A particular attention is given to a hysteresis phenomenon that is observed between the standing and the spinning modes. This novel phenomenon is analyzed by power spectral analysis of the pressure signals and by plotting state space maps.

# Publications

The work described in this thesis has been published in the following articles and conferences:

## Articles in rank A journals

- *Different Flame Patterns linked with Swirling Injector Interactions in an Annular Combustor*  
**D. Durox, K. Prieur, T. Schuller, S. Candel**  
Journal of Engineering for Gas Turbines and Power 138 (10), 101504, **2016**  
Presented at the ASME Turbo Expo 2015, Montreal, Canada
- *A hysteresis phenomenon leading to spinning or standing azimuthal instabilities in an annular combustor*  
**K. Prieur, D. Durox, T. Schuller, S. Candel**  
Combustion and Flame 175, 283-291, **2017**
- *Ignition dynamics in an annular combustor for liquid spray and premixed gaseous injection*  
**K. Prieur, D. Durox, J. Beaunier, T. Schuller, S. Candel**  
Proceedings of the Combustion Institute 36 (3), 3717-3724, **2017**  
Presented at the International Symposium on Combustion 2016, Seoul, South Korea
- *Impact of Heat Release Distribution on the Spinning Modes of an Annular Combustor with Multiple Matrix Burners*  
**D. Laera, K. Prieur, D. Durox, T. Schuller, SM. Camporeale, S. Candel**  
Journal of Engineering for Gas Turbines and Power 139 (5), 051505, **2017**
- *Flame describing function analysis of spinning and standing modes in an annular combustor and comparison with experiments*  
**D. Laera, T. Schuller, K. Prieur, D. Durox, SM. Camporeale, S. Candel**  
Combustion and Flame 184, 136-152, **2017**
- *Large-Eddy Simulation of Light-Round in an Annular Combustor With Liquid*

*Spray Injection and Comparison With Experiments*  
**T. Lancien, K. Prieur, D. Durox, S. Candel, R. Vicquelin**  
 J. Eng. Gas Turbines Power. 140, 021504, **2017**

- *Strong Azimuthal Combustion Instabilities in a Spray Annular Chamber With Intermittent Partial Blow-Off*  
**K. Prieur, D. Durox, T. Schuller, S. Candel**  
 J. Eng. Gas Turbines Power. 140, 031503, **2017**  
 Presented at the ASME Turbo Expo 2017, Charlotte, USA

### Conference papers (peer reviewed)

- *The describing function of swirled spray flames*  
**K. Prieur, D. Durox, T. Schuller, and S. Candel**  
 ICTAM, Montreal, August **2016**

### Conference papers (abstract reviewed)

- *Uncertainty quantification of injected droplet size in mono-dispersed Eulerian simulations*  
**T. Lancien, N. Dumont, K. Prieur, D. Durox, S. Candel, O. Gicquel, and R. Vicquelin**  
 ICMF, Firenze, Italy, May **2016**
- *Influence of cup angle on the Flame Describing Function of a swirled injector with liquid fuel*  
**K. Prieur, D. Durox, T. Schuller, S. Candel**  
 International Symposium on Thermoacoustic Instabilities in Gas Turbines and Rocket Engines: Industry meets Academia, TUM, Garching, Germany, May **2016**
- *Flame describing function analysis of standing modes in an annular combustor and comparison with experiments*  
**D. Larea, K. Prieur, D. Durox, T. Schuller, SM. Camporeale, S. Candel**  
 International Symposium on Thermoacoustic Instabilities in Gas Turbines and Rocket Engines: Industry meets Academia, TUM, Garching, Germany, May **2016**
- *Experimental determinations of Flame Describing Functions of swirling spray flames*  
**K. Prieur, D. Durox, G. Vignat, T. Schuller, S. Candel**

Colloque INCA, Safran Tech, Magny-Les-Hameaux, France, October **2017**

- *Etude détaillée de l'évolution du nombre de swirl dans un injecteur swirlé générique*

**G. Vignat, D. Durox, K. Prieur, T. Schuller, S. Candel**

Colloque INCA, Safran Tech, Magny-Les-Hameaux, France, France, October **2017**

- *Light-round in an annular combustor with liquid n-heptane injectors: study of flame propagation under several operating conditions*

**T. Lancien, K. Prieur, D. Durox, S. Candel, R. Vicquelin**

Colloque INCA, Safran Tech, Magny-Les-Hameaux, France, October **2017**



## **Part I**

# **A two phase flow annular combustor called MICCA-Spray**



# Chapter 1

## Experimental set-ups

### 1.1 Introduction

Devices developed by the aeronautical and the gas turbines industries usually feature annular combustors with a large number of injectors to provide high power in a relatively compact system. These combustors are characterized by an annular shape with a periodic arrangement of injectors around the axis of the gas turbine. Extensive dataset and precise diagnostics are scarce in the scientific literature on this kind of device. Data are usually gathered by industrial companies at the design stage by only recording pressure signals in their system because of the limited optical access of their devices. These results are, of course, generally not published in the scientific literature. Partial laboratory scale experiments exist with a limited number of injectors compared to industrial benches and with, usually, linear arrangements, making the analysis of azimuthal phenomena impossible. Due to this lack of datasets, the MICCA experiment has been developed at EM2C laboratory during the thesis of J-F. Bourgouin ((2013) and (2013a)). The MICCA bench is an annular combustor equipped with sixteen fully premixed swirled injectors and with a very good optical access. It is operating at atmospheric pressure and the air is injected at ambient temperature. Numerous studies have been made on this device, particularly on the ignition process in this kind of geometry, called light-round, and on the combustion dynamics of this system. The next step is to take into account the effect of the use of liquid fuel as observed in practical devices, which is the aim of this thesis. This new system, which is an adaptation of the MICCA burner, is called MICCA-Spray. The bench and its different arrangements are described in the next sections. Across this document, details will be given when needed. As combustion dynamics is a major topic of this thesis, a second bench in the form of a single tubular burner, is described in section 1.3. This burner, called SICCA-Spray, is representative of one sector of the annular combustor MICCA-Spray and is used to have a finer characterization of certain phenomena.

## 1.2 MICCA-Spray annular set-up

The MICCA-Spray bench is an annular combustor made of two cavities, linked together by multiple injectors. The particularity of this burner is that it can be fed with liquid fuels. A first general description of the combustor is given in section 1.2.1. Specificities are then explained in sections 1.2.2 and 1.2.3. These particularities induce several possible arrangements for the different studies of this document. Used diagnostics in those cases are exposed in section 1.2.4. A sum-up of the studied configurations is presented in section 1.2.5.

### 1.2.1 General description

The burner comprises an upstream plenum and a combustion chamber, linked by sixteen injectors mounted on the flange of the annular backplane, constituting the chamber backplane. This backplane, linking the two cavities, is cooled by a continuous flow of cold water to ensure a temperature lower than 323 K in the plenum. The injector design is universal and can be fed with liquid or gaseous. It is swirled and has firstly been designed to permit spray combustion but it can also be fed with a premixture of air and propane. In the case of premixed combustion, the fuel, which consists of gaseous propane, is premixed way upstream before the injection in the combustion chamber to provide perfectly premixed conditions. More details are given in the following sections. Eight channels feed the plenum with pure air, or premixture in the case of premixed combustion, injected at ambient temperature. The plenum is a circular piece with a cross section of the plenum which has a square dimension  $g_p = 70$  mm and a diameter equivalent to that of the chamber. The combustion chamber is symbolized by an inner and an outer cylindrical quartz tubes allowing a very good visualization of the flames in the ultraviolet and visible ranges. The inner and outer quartz respective diameters are  $d_i = 300$  mm and  $d_o = 400$  mm making a ring of 50 mm between the two elements. The length  $l_c$  of the tubes are varied depending on the application. The chamber is switch on by an igniter crossing the quartz tubes and inducing a spark near an injector. The spark plug is triggered repetitively at 100 Hz, making a 25 mJ energy deposit each time. If conditions for combustion are fulfilled, the chamber rapidly ignites. The spark plug remains in place during the operation of the chamber. It has been observed that it can induce a useful asymmetry in the system. The position of the igniter remains roughly the same during all the experiments, approximately 6-10 mm from the centre of the injector. Studying the influence of the position of the spark plug is not the purpose of this work.

### 1.2.2 Chamber walls length

As mentioned in section 1.2.1, the length  $l_c$  of the chamber can be adapted depending on the application. Several quartz tubes of length 200 and 400 mm have been manufactured, with a thickness of 5 to 8 mm. Steel tubes have also been ordered with an adaptation piece to be laid down on the top of the quartz tubes. This allows to easily extend the wall length  $l_c$ , keeping the same optical access to the combustion zone

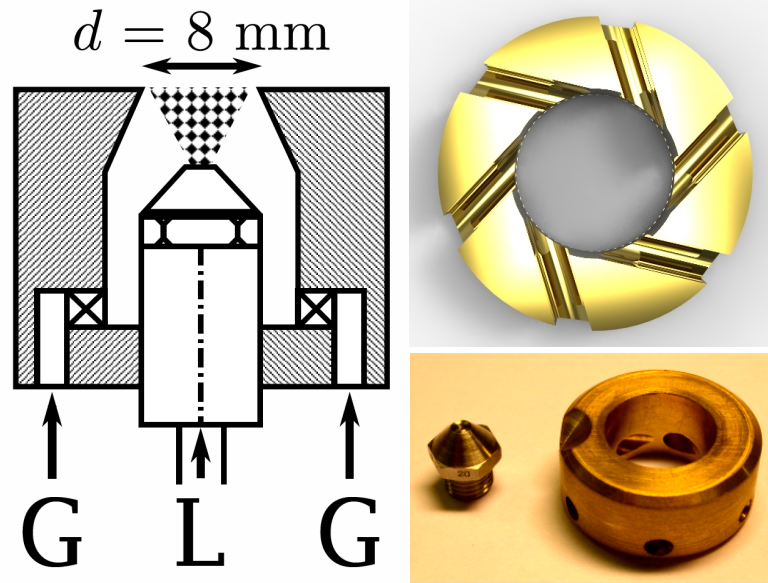


**Figure 1.1.** Left: Swirled turbulent injector design for the MICCA-Spray bench. Right, top: Cut of the radial viewed from above. Right, bottom: Photograph of the atomizer (left) and of a radial swirler (right)

provided by the quartz tubes. For the study of the ignition dynamics, inner and outer quartz walls share the same length  $l_c = 200$  mm providing clean and stable steady flames. For the study of combustion instabilities, the second configuration is with a longer outer quartz tube of 600 mm when swirled spray injectors are used. This later configuration promotes azimuthal modes in this case of swirled and highly turbulent injectors as already mentioned by [Worth and Dawson \(2013b\)](#) and [Bourgouin et al. \(2013a\)](#).

### 1.2.3 Swirled turbulent injectors

Swirled injectors are very common in practical systems because they produce high power, compact and stable flames. The annular bench can then be equipped with a new kind of injector that has been designed in order to permit swirled spray combustion which is more representative of industrial applications in aeronautical and gas turbines systems than premixed systems. These new type of injectors can be supplied with either gaseous or liquid fuels without changing the geometry and the injection system. In both cases the sixteen injectors are flushed mounted in the chamber back-plane. Their design is shown in Figure 1.1. The gaseous flow is conveyed by six ducts on the side, regularly spaced, leading to a radial swirler with six inclined circular vanes. This feature makes the air rotate in the clockwise direction, viewed from the downstream side, as it can be seen in Figure 1.1. Two swirlers have been studied during this thesis, one with tangential holes with a diameter of 3 mm and one with a diameter of 4.5 mm. Depending on the study, details on the swirler geometry will

be given in the different chapters. The swirled flow is injected into the combustion chamber through a convergent end piece with an exit diameter  $d = 8$  mm. The liquid fuel is conveyed through the plenum via a linear tube of outer diameter 4 mm. It is then injected in the swirled flow by a simplex atomizer sketched in Figure 1.1. It is placed after the swirler, 6 mm in recess with respect to the convergent exhaust establishing a hollow cone spray in the combustion chamber. The liquid is pressurized at 9 bar to ensure a good atomization process in the simplex atomizer. In the case of spray combustion, high and low volatility fuels are compared: n-heptane and dodecane. The vaporization rate of n-heptane is  $0.056 \text{ mm}^2/\text{s}$  in quiescent air at 300 K (see Wu et al. (2001)) and can be doubled when motionless droplets are injected in an airflow at  $1 \text{ m s}^{-1}$  (Wu et al. (2001) and Birouk and Gökalp (2006)). Dodecane can be considered as non-volatile at ambient temperature. It is less volatile as decane which has a low vaporization rate of  $0.0021 \text{ mm}^2/\text{s}$  in quiescent air (Wu et al. (2001)). Note that, in the case of spray combustion, whatever the effort made, it was not possible to obtain perfectly symmetric and uniformly balanced injectors due to the small atomizer sizes, inducing easily asymmetries in the liquid distribution through the sixteen injectors. Thanks to this injector design, two regimes of combustion are then possible:

- Premixed combustion: gaseous propane is premixed with the air upstream its injection in the plenum. No liquid fuel is injected. This results in a fully premixed combustion in the chamber
- Spray combustion: pure air is injected in the plenum and through the ducts of the injector. Liquid n-heptane or dodecane is injected through the atomizer. Fuel then vaporizes in the injector and until it reaches the combustion zone, carried by the air flow. This mode of combustion is then non-premixed.

In all the configurations, premixed or non premixed, the sixteen turbulent flames take a typical “M” shape with no mutual interaction. The generated flames are compact due to the highly turbulent flow generated by the swirler. This enhances the stability of the flame by creating recirculation zones which help the flame to keep its anchors. The Central Recirculation Zone (CRZ) and the Outer Recirculation Zone (ORZ) have stabilizing effects by bringing the hot burnt gases to the foot of the flame, mixing them with the unburnt gases. Flame shapes will be presented in details in the next chapters. The global equivalence ratio in these turbulent configuration usually ranges from  $\phi = 0.7$  to 1.1. Richer configurations have been avoided due to the risk induced by the very long flames generated. The power of the combustor can be varied from  $\mathcal{P} = 65$  to 120 kW and the bulk velocity can be increased from  $U_b = 25$  to  $50 \text{ m s}^{-1}$  with reference to the exit diameter of the injector  $d = 8$  mm. The corresponding Reynolds number based on the injector exit diameter varies from 15,400 to 25,600. Figure 1.2 shows a photograph of the MICCA-Spray chamber fully equipped.

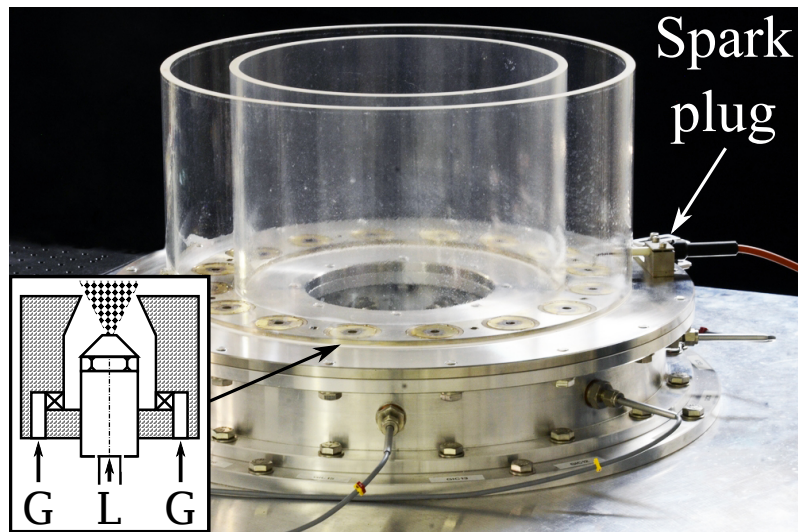


**Figure 1.2.** Photograph of the MICCA-Spray combustion chamber with sixteen liquid injectors and equipped with 200 mm quartz tubes and a single spark plug. An atomizer is sketched on the bottom left where G stands for gas and L for liquid injection channels.

### 1.2.4 Diagnostics

The device permit a very good access to the combustion zone which is not common in semi-industrial benches as the MICCA set-up. This allows precise optical diagnostics via heat release rate measurements or via  $\text{CH}^*$  or  $\text{OH}^*$  chemiluminescence images. The plenum and chamber cavities are also equipped with multiple pressure sensors giving access to the acoustic pressure field in both cavities. One or more photomultipliers (PM) with  $\text{OH}^*$  filters can also be placed to track the heat release rate fluctuations of one or more flames. Note that all diagnostics are acquired synchronously in order to compare different quantities such as the unsteady acoustic pressure  $p'$  and the heat release rate fluctuation  $\dot{Q}'$  during cycles. Figure 1.3 schematically depicts the different diagnostics used through the studies.

#### 1.2.4.1 Chemiluminescence

The transparent walls of the combustion chamber give access to the flames. Chemiluminescence of the entire system using low and high-speed cameras is then possible. The light intensity recorded by the cameras is assumed to be dominated by the emission of excited radicals in the visible domain, mainly originating from  $\text{CH}^*$  and  $\text{C}_2^*$  radicals. The color of the premixed flame is light blue and the soot production is negligible for equivalence ratio up to  $\phi = 1.2$ . Images recorded by this device can therefore be interpreted as representative of the instantaneous heat release rate (see [Hurle et al. \(1968\)](#), [Price et al. \(1969\)](#) and [Mirat et al. \(2015\)](#)). One low-speed CCD camera provides high quality images of the full annular combustor during its

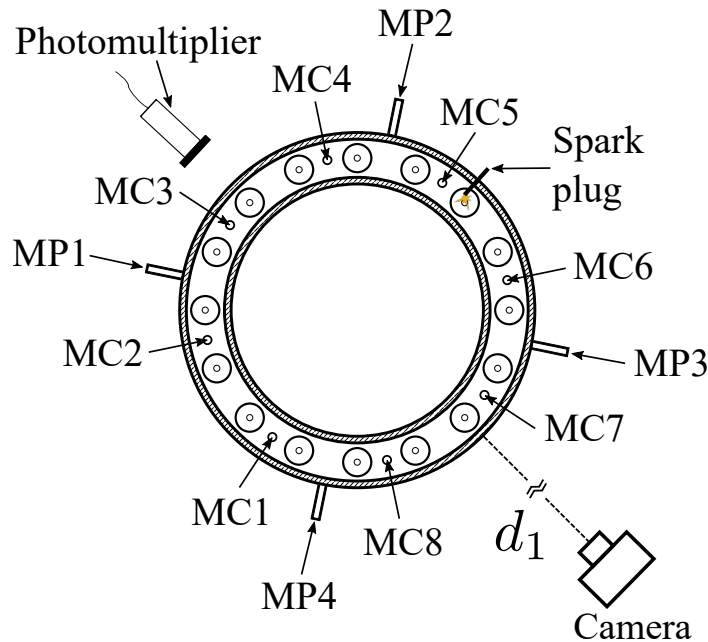


**Figure 1.3.** Diagnostics available on the annular benches MICCA and MICCA-Spray. Pressure sensors are designated as “MP” (for plenum) or “MC” (for chamber). A photomultiplier equipped with an OH\* filter can be placed on one chosen injector - only one PM is displayed here for the sake of clarity. A camera can also be placed at different position, close or away from the burner, depending on the aim.

operation. It is mainly used to observe mean flames. When needed, the flame motion can be characterized by an intensified high-speed CMOS camera APX-i2 comprising  $512 \times 512$  pixels with 8-bit resolution. The frame rate and shutter speed are respectively set at 6000 Hz and 166 ms. This camera is sensitive to radiation in the visible and UV ranges down to 200 nm. The amplifier gain of the camera remains constant in all experiments to ensure quantitative comparison. For certain applications needing a higher resolution, a high-speed, non intensified, camera Phantom V2512 monochrome or polychrome providing 16-bit images ( $1280 \times 800$  px) at a sampling rate of 6000 frames per second and with a shutter duration of  $166 \mu s$ , has been rent. Whereas the first camera is sensitive to the UV radiation, this one is sensitive to radiation from 350 to 105 nm. Note that, for several applications, image filtering will then be necessary or the infra-red radiation will contaminate the majority of the image. Lenses are adapted on the application, but two are commonly used. The first one is a 60 mm f/2.8 Nikkor and the second one is a 105 mm f/2.8 Nikkor macro.

#### 1.2.4.2 Heat release rate measurements

The set-up can be equipped with one or more photomultipliers each with a filter that is sensitive to the light emission of the OH\* chemical radical. These measurements are complementary to the chemiluminescence captured by the cameras. It is assumed that

the signal from the photomultiplier is roughly proportional to the combustion intensity therefore to the heat release rate of the flame. This is admittedly an approximation in a situation where reactants are only partially premixed, so when spray combustion is studied. A vertical steel plate can be placed in the inner quartz tube to prevent the photomultiplier from receiving the light from the flame at the opposite side. Additional protections are used to block the emissions from the other flames.

### 1.2.4.3 Acoustic pressure measurements

The annular chamber can be equipped with twelve Brüel & Kjær microphones in the plenum and in the chamber. Figure 1.3 specifies the positions. The phenomena that are studied in this manuscript are usually between 100 and 1000 Hz. The pressure sensors used respond linearly over a wide range of frequencies from 20 Hz to 100 kHz meaning that they are adapted to the phenomena. Note that each sensor is calibrated at a frequency of 1 kHz. For most of the experiments, the sampling rate is  $f_s = 32,768$  Hz and the data are recorded over a period of 2 to 8 s. Four microphones are located in the plenum (called MP“x”) and eight are located in the chamber (called MC“x”), each spaced by respectively  $90^\circ$  or  $45^\circ$ . Microphones are flush-mounted in the plenum. For the unsteady pressure measurements in the combustion chamber, waveguide microphones are used to avoid sensor exposure to excessive temperatures. These are made of a straight metallic tube flush mounted in the annular backplane of the combustion chamber centered between two injectors and terminated by a 25 m flexible closed tube. A microphone is then flush mounted perpendicular to the wave duct, at 170 mm from the chamber backplane. The microphone is located close to the injector compared to the length of the whole system, and the amplitude recorded by this sensor is a good approximation of the pressure in the chamber near the waveguide outlet, but with a delay that needs to be evaluated. If we consider that the medium between the chamber and the position of the sensor is only heated-up up to  $50^\circ\text{C}$  by the conduction due to the constant cooling of the plenum cavity, the corresponding time delay is equal to 0.5 ms. This time delay is then of the order of the period of 2 ms of one oscillation at 500 Hz. This is why it has to be taken into account in the signal processing when one compares pressure signals from the chamber to pressure signals from the plenum.

### 1.2.5 Studied configurations sum-up

Several configurations have been presented in the last sections which each allow two studies of different interesting phenomena: the ignition dynamics and the combustion dynamics of an annular combustor. Figure 1.4 presents the generic configuration of the MICCA-Spray bench used through these experiments. The main differences between those configurations are in the outer quartz length and in the injector design. For the sake of clarity, Table 1.1 synthesizes the configurations studied in the different chapters of this manuscript.

Domain	Flame shape analysis	Ignition dynamics	Combustion dynamics	Combustion dynamics
Injector type	Premixed swirled injectors	Spray swirled injectors	Laminar matrix injectors	Spray swirled injectors
Concerned chapters	6	2	7	3
Inner/outer chamber wall lengths (mm)	200/200	200/200	200/200	200/600

**Table 1.1.** Synthesis of the different configurations of the annular bench used through the manuscript.

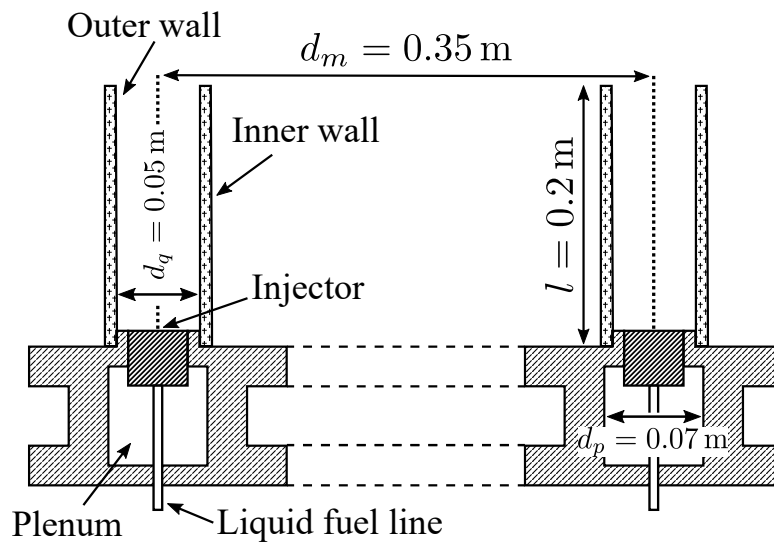


**Figure 1.4.** Generic configuration of the MICCA and MICCA-Spray chambers. In the MICCA configuration, the fuel lines are dismantled. Outer quartz length is variable.

### 1.3 Single burner SICCA-Spray set-up

As mentioned in the introduction, it is convenient to use a single injector to characterize precisely several phenomena observed in the annular combustor. This burner, called SICCA-Spray, has many advantages when compared to what can be done in the annular combustor MICCA-Spray. A large limitation for the diagnostics in the annular combustor is the curvature of the quartz and their thickness. This prevents one from doing fine optical measurements with lasers for example. The SICCA-Spray design is first described in section 1.3.1 and then section 1.3.2 describes the diagnostics used.

#### 1.3.1 Design

The experimental configuration represented schematically in Figure 1.5 comprises a plenum and a combustion chamber. The chamber is formed by a cylindrical quartz tube with a diameter  $d_c = 70$  mm, a thickness of 3 mm and of variable length  $l_c$ . To mimic as close as possible the flame dynamics observed in the MICCA-Spray bench, the surface of the confinement in SICCA-Spray  $S_{sicca}$  has been calculated equal to 1/16th (one sector) of the total surface of the annular bench  $S_{micca}$ :

$$S_{micca} = \frac{\pi}{4} (d_o^2 - d_i^2) \quad (1.1)$$

$$S_{sicca} = \frac{\pi}{4} d_c^2 \quad (1.2)$$

$$d_c = \sqrt{\frac{1}{16} (d_o^2 - d_i^2)} \quad (1.3)$$

Note that some discrepancy can still remain between the flame in the SICCA-Spray and in the MICCA-Spray burners, mainly due the differences in the aerodynamics [Fanaca et al. \(2009\)](#). A particular attention to the flame shape has been given. The swirled injection system is the exact same injector as described in section 1.2.3 for spray combustion. The injector is composed of an air circuit passing through a swirler and of a liquid atomizer to feed liquid fuel and form spray of droplets. Air is injected at ambient temperature at the bottom of the plenum. It then reaches the injector where it passes through a radial swirler with six 4.5 mm holes for this study. Fuel (n-heptane) is injected using a simplex atomizer under a pressure of 9 bar. The atomizer generates a hollow cone and is positioned in the middle of the swirler. The injector is terminated by a convergent section. Two driver units are plugged on the 300 mm cylindrical plenum to modulate the air flow if needed. This bench is capable of global equivalence ratios from  $\phi = 0.7$  up to 0.9. The global power is then around  $\mathcal{P} = 6$  kW. The bulk velocity of the air at the exit of the injector can reach  $U_b = 43$  m s<sup>-1</sup>.

### 1.3.2 Diagnostics

The tubular burner presented in this section allows a much easier access for finer diagnostics due its much more compact design and its finer combustor walls. Many diagnostics have been deployed on this bench for different purposes: experimental characterization of the injection system, characterization of the flame and dynamical flame behavior or even theoretical and numerical models validation. One may refer to Figure 1.5 where a lot of sensors are already presented. The different diagnostics to be used in the next chapters are briefly synthesised in the next list. More details may be given across the different chapters when needed. It is not the point of this manuscript to precisely describe the different measurement techniques as they are fairly standard and widely commented in the literature.

1. Acoustic pressure measurements are done with Brüel & Kjær microphones

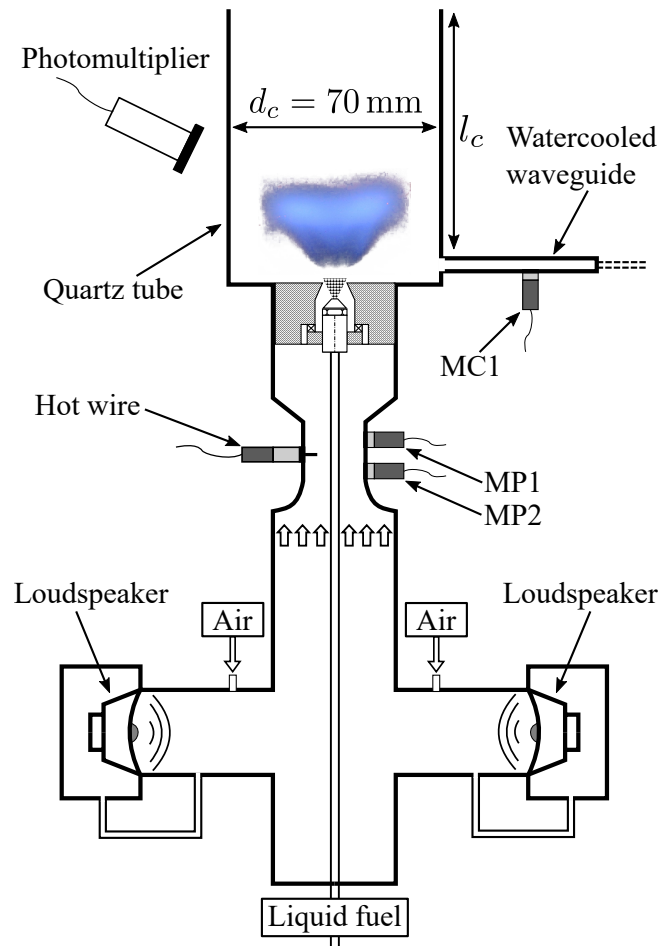


**Figure 1.5.** Schematic drawing of the SICCA-Spray bench equipped with all the diagnostics.

MP1, MP2 and MC1 in the plenum and in the chamber. As for the MICCA-Spray experiment, the microphone in the chamber is mounted on a cooled waveguide, flushed mounted 290 mm in recess of the combustion chamber, to avoid its exposure to high temperatures. The waveguide is terminated by a 25 m long closed tube.

2. Chemiluminescence is evaluated by low and high-speed camera through the transparent walls by the same techniques as in the MICCA-Spray chamber.
3. Heat release rate measurements are done with a photomultiplier equipped with an OH\* filter that collects all the luminosity from the combustion region.
4. A hot wire, placed in the plenum, 100 mm upstream the combustion chamber backplane, allows velocity measurements. This region is chosen in order to have a nearly laminar velocity profile, achieved by a convergent piece placed upstream the sensor position. Note that the hot wire is surrounded by two microphones that can be used to confirm the velocity measurements by a two-microphones technique ( $u = \Delta p / dx * \rho * \omega$  with  $dx$  the distance between the microphones) and to have access to the exact acoustic velocity when the hot wire reaches its limits at higher amplitude of perturbation.
5. A Laser Doppler Velocimetry (LDV) system is used to characterize the aerodynamic field in the combustion chamber in cold conditions with laser optical tools. The air flow can then be characterized by seeding it with small oil droplets ( $d < 2 \mu\text{m}$ ) that are assumed to have a negligible inertia.
6. Phase Doppler Anemometry (PDA) is used to obtain the spray structures formed by the simplex atomizer. This gives access to the spray shape, the mean droplet diameter  $d_{10}$  and the Sauter Mean Diameter  $d_{32}$ .
7. Particule Image Velocimetry under hot fire conditions is recorded with a continuous 20 W laser and a high-speed camera running at 100 kHz. With velocities around  $40 \text{ m s}^{-1}$ , this systems ensures data with a good quality factor. These data complete the LDV measurements under cold conditions and are of importance for numerical validation.
8. Wall temperature is measured on the quartz tubes on their inner and outer parts. The inner measurements are done with a thermochromic paint which is exposed for 5 min to the flame. The outer measurements are done with a contact thermocouple.

## 1.4 Conclusion

This chapter rapidly described the experimental set-ups and their associated diagnostics that will be studied in this document. The combustor called MICCA-Spray has been adapted from the previously studied MICCA combustor. It has an annular shape and is equipped with sixteen injectors with an accessible combustion zone thanks to the transparent quartz tubes of the combustion chamber. The main achievement is the possibility to do spray combustion by injecting the fuel in its liquid form through an atomizer. This allows a better representation of industrial applications on a laboratory scale experiment compared to the previous system MICCA only running in premixed

conditions. The main focus of this manuscript is to understand the influence of the spray on the ignition process of an annular combustor and on its combustion dynamics. As demonstrated in the last sections, this device is quite flexible with a lot of different injectors available, as much as many combustor wall lengths which allow the analysis of different phenomena quite easily. To complete investigations, a single tubular combustor, called SICCA-Spray, and representative of one sector of MICCA-Spray is presented with the possibility to do finer diagnostics.







## Chapter 2

# Light-round in an annular combustor

*The light-round process corresponding to the flame spreading phase in the ignition of annular combustors is examined in this chapter by performing experiments in the annular combustor MICCA-Spray. In the first part of the chapter, experiments are carried out with premixed gases as well as n-heptane and dodecane sprays. With n-heptane and dodecane fuel injection, it is found that the light-round process is similar to the one observed under fully premixed propane/air experiments but the duration of the process is augmented especially for the less volatile fuel. It is also confirmed that the delay is notably influenced by thermal conditions prevailing in the chamber at the moment of ignition, injection process and fuel composition. Making use of a flamelet like model of the combustion process, the relative changes in light-round time delay are found to be, to the first order, proportional to the relative changes in laminar burning velocity induced by the fuel spray in the air flow. The second part of the chapter focuses on the important step where the two turbulent travelling flames, nearly perpendicular to the combustor backplane, that successively ignite the injection units and finally collide head-on and merge. The behavior of one injector ignited by the passing flame front is examined. One finds that the flame structure formed by each injection unit evolves in time and that the anchoring location changes just a few milliseconds after the flame passage. This behavior can eventually lead to a flashback of the flame in the injector with possible severe damages. The propagation of the arch-like flame branch is then investigated. One may distinguish two regions for the flame propagation. One is near the backplane, moving in a purely azimuthal direction, while the other corresponds to the remaining flame motion in the azimuthal and axial directions due to the volumetric expansion of the burnt gases. Filtered images give indications on the typical length scales characterizing the moving front. Information is also obtained on the dynamics of the spray by shining a continuous laser sheet passing through one injector and recording the light scattered by the n-heptane spray of droplets. A major result is that the flame modifies the spray much before it reaches the injector unit and that its passage through the spray drastically changes the local droplet concentration and thus the local mixture composition.*

## 2.1 Introduction

In aircraft engine combustors ignition is critical and deserves considerable attention. Combustion is generally initiated by means of a pair of spark plug igniters, usually diametrically mounted in the chamber. Three stages can be identified in the process: (1) In the first, a spark produced by an electric discharge forms a hot gas core, (2) In the second stage, this kernel increases in volume and reaches an injector unit in its vicinity igniting the material exhausted in this region and establishing an initial flame and (3) In the last stage a flame progresses inside the annular chamber and ignites successive injectors, taking the form of two vertical arches that propagate, ultimately leading to combustion stabilization inside the system. This last phase designated as the “light-round” process is considered in this analysis.

At this point it is worth reviewing some of the related references. A variety of topics are covered in previous ignition research. Investigations deal with spark characteristics like the minimum spark energy, initial flame kernel size, radical creation for a successful ignition (studies by [Ballal and Lefebvre \(1974\)](#), [Lefebvre \(1983\)](#), [Champion et al. \(1986\)](#), [Lewis and Elbe \(1987\)](#) and [Bradley and Lung \(1987\)](#)), gas velocity effects, equivalence ratio, heterogeneity of the flow near the spark gap (studies by [Lefebvre \(1983\)](#), [Ballal and Lefebvre \(1977\)](#), [Ballal and Lefebvre \(1978\)](#) and [Ahmed et al. \(2007\)](#)), ignition probability and turbulence influence (studies by [Ahmed et al. \(2007\)](#), [Marchione et al. \(2009\)](#), [Mastorakos \(2009\)](#) and [Cordier et al. \(2013\)](#)). Many articles concern the influence of fuel spray parameters such as [Lefebvre \(1983\)](#) and [Ballal and Lefebvre \(1981\)](#), but most experiments deal with single injector ignition. Ignition experiments in multi-burner systems are scarce, until recently. Effects of burner separation on gaseous premixed flame ignition and propagation to neighboring injectors in a linear arrangement of 5 swirling injectors were reported by [Cordier et al. \(2013\)](#) and [Barre et al. \(2014\)](#). Only a few studies have been carried out in annular combustors under fully premixed or non-premixed conditions (see [Bach et al. \(2013\)](#), [Bourgouin et al. \(2013\)](#) and [Machover and Mastorakos \(2015\)](#)). [Bourgouin et al. \(2013\)](#) found that the light-round can be decomposed into five stages and that the delay before flames propagating in clockwise and counter-clockwise directions merge is reduced when the injection velocity increases. It is observed that the delay is notably influenced by thermal conditions prevailing in the chamber at the moment of ignition and that it is reduced if the chamber walls are at high temperature. Progress has also been accomplished with the development of simulation tools which have been mainly used to examine ignition processes in single injector configurations. There is however a notable exception with [Boileau et al. \(2008\)](#) reporting a simulation of a full ignition sequence in an annular multiple injector combustor. More recent LES calculations (see [Philip et al. \(2014a\)](#), [Philip et al. \(2015\)](#) and [Philip et al. \(2014b\)](#)) have been carried out in parallel with experiments done by [Bourgouin et al. \(2013\)](#) on a fully premixed swirling injector combustor (MICCA). This has led to high fidelity calculations of the light-round sequence observed experimentally.

At present one finds no experiment concerning the light-round in an annular configuration with liquid spray injection. The objective of this chapter is to provide such data from systematic experiments and to quantify the differences between a premixed ignition and a spray injection ignition in an annular system. Such experiments provide useful information on the process and the data could be effectively used to guide numerical modeling efforts. Moreover one important issue is to see how each flame is initiated at one of the injector units. This takes place when one of the travelling flames sweeps one of these units. The dynamical process that produces the flame and leads to its final anchoring is of considerable importance but does not seem to be well documented in the previous literature. The study relies on a laboratory scale apparatus designated as MICCA-Spray having multiple spray injectors and an annular geometry in a configuration which reflects in a simplified geometry the situation prevailing in practical combustors.

Details on the set-ups are given in section 2.2. Flow and spray are first characterized in the single injector tubular system SICCA-Spray under cold and hot fire conditions in section 2.2.1. Some results of systematic light-round in MICCA-Spray are reported in section 2.3 using high-speed imaging. These data are used to examine effects of operating conditions and in particular consider the influence of fuel state -gaseous or liquid- and nature on the light-round delay. A brief intermediate interpretation is proposed in section 2.4. Sections 2.6 and 2.5 focuses on the velocity fields in the vicinity of the flame as it moves around the circumference. It is concerned with observations of the flame structure as it evolves after the flame has swept an injector. It is shown that the flame initially penetrates in the injector body and is later expelled from this position to find its final configuration after a relatively long period of time. A mechanism of this type is also observed in the case of ignition of a single swirling injector of the same type as those used in the MICCA-Spray experiment. Results on this single injector are analysed in 2.7. An attempt is then made in section 2.8 to model the injector dynamical response when it is swept by the flame and describe the resulting consequences in terms of mass flow rate and subsequent flame motion.

## 2.2 Experimental configuration

The annular system (Fig. 4.1, left) is the MICCA-Spray combustor comprises a plenum connected to a combustion chamber by 16 swirling injectors. In this Chapter, they can be supplied with either gaseous or liquid fuels without changing the geometry and the injection system. More details on the injector geometry can be find in section 1.2.3 of Chapter 1. In the case of premixed combustion, air and propane are perfectly premixed upstream and injected in the chamber. In case of liquid injection, the simplex atomizer establishing a hollow cone spray in the chamber.

The inner and outer quartz tubes are 200 mm long and their diameters are respectively 300 and 400 mm. The ignition process is initiated by a spark plug positioned in front of the camera, located on the opposite side of the chamber. Unlike aeronau-

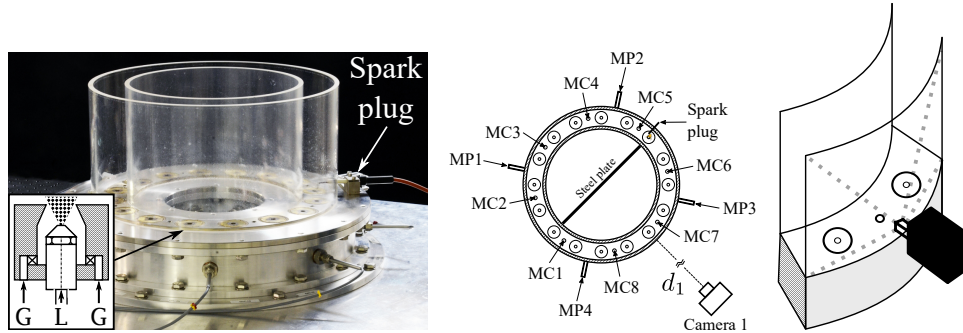


**Figure 2.1.** Left: Photograph of the MICCA-Spray annular combustor with sixteen liquid spray injectors. The chamber comprises 200 mm quartz tubes. A detailed schematic of the injector is available on the bottom left of the image. Middle: Schematic view of the chamber backplane showing the locations of the camera and of the different microphones “MCx” in the chamber and “MPx” in the plenum. The spark plug location is indicated and defines Flame 1. A steel plate is added in the centre to block the luminosity of the opposite flame branch. The aim of the camera is either one injector or between two injectors, depending on the experiment. Right: View of the position of the camera in black with a cut of two sectors of the annular combustor. The grey dashed lines symbolizes the field of view of the camera.

tical combustors, a single igniter is used so the camera can catch the entire dynamics of the light-round process. It should be recalled that the igniter is placed 10 mm from the center of the injector and fixed at the same location in all experiments as depicted in Fig. 4.1. A spark is formed every 10 ms and releases a mean energy of 25 mJ. The system is equipped with twelve 1/4 inch Brüel & Kjær microphones to measure the acoustic pressure in the plenum and in the chamber at a sampling rate  $f_s = 32.768$  Hz. No filtering is applied to the data except when this is mentioned. Eight of the microphones designated as “MC” are used to measure the pressure at the chamber backplane. A microphone is flush mounted on each waveguide at 170 mm from the chamber backplane. This distance defines a time lag  $\tau_{m-b} = 0.46$  ms when the combustion chamber has been running for 15 minutes, and the temperature in the plenum reaches 55 °C. This delay between the chamber and microphone is taken into account to synchronize the acoustic pressure measurements. Four additional microphones designated as “MP” are plugged on the plenum.

The ignition sequence can be recorded with different imaging systems. In section 2.3, an intensified high-speed CMOS camera APX-i2 comprising 512×512 pixels with 8-bit resolution is used. The frame rate and shutter speed are respectively set at 6000 Hz and 166 ms. The camera amplifier gain remains constant in all experiments. In sections 2.6 and 2.5, images of the combustion region are recorded by the high-speed camera Phantom V2512 providing 16-bit images covering 1280 × 800 pixels at a sampling rate of 6000 frames per second, with a shutter duration of 166 μs. Images are filtered to subtract the large infra-red and red components of the emission of the

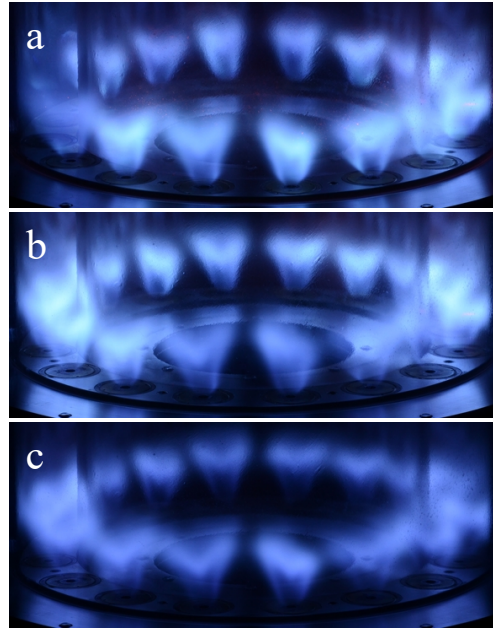


**Figure 2.2.** Direct true-color photograph of the annular chamber with different types of injection : (A) premixed propane and air, (B) n-heptane spray and air, (C) dodecane spray and air. The chamber is under steady operation at a bulk velocity  $U_b = 31.5 \text{ m s}^{-1}$ , an equivalence ratio  $\phi = 0.90$  and a total power of  $\mathcal{P} = 80 \text{ kW}$ .

quartz tubes heated up at 900 K. Depending on the experiment, a broadband  $\text{CH}^*$  filter (400 - 470 nm) with a high transmission factor (0.8) is applied to capture the luminosity from the flame in this band. When a laser is used, a broader filter (300 - 680 nm) is also needed. For some experiments, a thin metallic plate is placed in the centre of the annular chamber perpendicular to the camera to block the luminosity from one of the flame arches when looking at the other (see Fig. 4.1, middle). The pressure signals and flame images can be synchronized by making use of the external triggering signal of the camera.

The MICCA-Spray chamber features stable flames with gaseous and liquid fuels for a wide range of operating conditions. Flame shapes with the different fuels tested are shown in Fig. 2.2. In the three configurations, the sixteen turbulent flames take a typical “M” shape with no mutual interaction. Whatever the effort made, it was not possible to obtain perfectly symmetric and uniformly balanced injectors due to the small atomizer sizes and the differences in the swirler execution. Experiments are carried out for a broad range of conditions to compare premixed gaseous propane air injection with liquid spray injection. In the latter case, high and low volatility fuels are compared: n-heptane and dodecane. The vaporization rate of n-heptane is  $0.056 \text{ mm}^2/\text{s}$  in quiescent air at 300 K (Wu et al. (2001)) and can be doubled when motionless droplets are injected in an airflow at  $1 \text{ m s}^{-1}$  (see Wu et al. (2001) and Birouk and

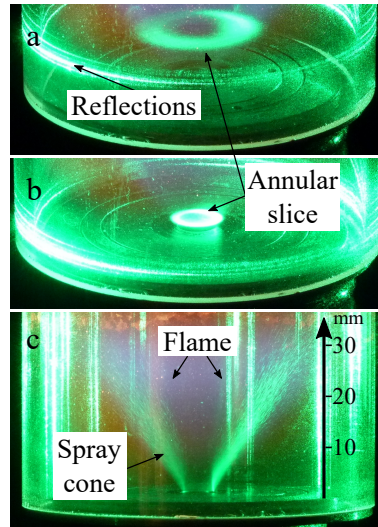


**Figure 2.3.** Horizontal (a,b) and vertical (c) tomographies of the n-heptane droplet spray with flame ( $\phi = 0.86$ ,  $U_b = 32 \text{ m s}^{-1}$ ,  $\mathcal{P} = 4.95 \text{ kW}$ ). Tomographies a and b correspond to  $z = 10 \text{ mm}$  and  $z = 2.5 \text{ mm}$  respectively. An indicative scale is placed in the second image.

Gökalp (2006)). Dodecane can be considered as non-volatile at ambient temperature. It is less volatile as decane which has a low vaporization rate of  $0.0021 \text{ mm}^2/\text{s}$  in quiescent air (Wu et al. (2001)). The global equivalence ratio ranges from  $\phi = 0.7$  to 1.1. The power of the chamber varies from  $\mathcal{P} = 65$  to  $100 \text{ kW}$  and the bulk velocity is increased from  $U_b = 25$  to  $41 \text{ m s}^{-1}$ . The corresponding Reynolds number based on the injector exit diameter varies from 15,400 to 20,500.

Throughout this chapter, the single tubular burner called SICCA-Spray, is also used to compare the behavior of the ignition of one isolated injector to the behavior of one flame during the light-round in the annular MICCA-Spray combustor. This second setup represents 1/16th of the MICCA-Spray annular chamber with a resulting flame similar in shape to that found in the annular chamber. When needed, air velocity measurements in the plenum are recorded with a hot wire located at 100 mm from the injector exhaust section. The fluctuating component of this signal can also be compared to the acoustic velocity deduced by a two-microphone method at the same position. Pressure loss and heat release rate measurements are also available. The burner is equipped with a 70 mm diameter and 150 mm long quartz tube. The length of the quartz tube does not affect the aerodynamic and spray structures. The total power of the single burner is close to  $\mathcal{P} = 5 \text{ kW}$ . A 9-bar pressurized fuel tank supplies the atomizer with n-heptane. An argon-ion laser at 514.5 nm is used to record horizontal and vertical tomographic slices of the droplet spray under hot fire conditions.

### 2.2.1 Single injector aerodynamic and spray structures

It is convenient to first use the single injector to characterize the aerodynamic and spray structures with laser optical tools. In Fig. 2.3a and b, the horizontal slices respectively correspond to a level  $z = 10$  mm and  $z = 2.5$  mm above the backplane (the  $z$ -axis is along the main air flow direction). The laser slice in Fig. 2.3A, at the foot of the flame, shows that droplets are still present in the combustion zone. One can see in Fig. 2.3B that the hollow cone seems congruent to the exit of the convergent plate. This indicates that the periphery of the hollow cone generated by the simplex atomizer partially interacts with the injector walls prior to entering the combustion chamber. This airblast effect is present but only affects a small part of the liquid stream. The vertical slice in Fig. 2.3c is observed at  $\theta = 45^\circ$  in the forward direction to maximize the Mie scattering signal. In this image, some blue luminosity indicates that the flame develops from 8 to 30 mm from the chamber backplane. This slice also reveals the persistence of droplets in the burning area confirming the non-premixed character of the flame. The hollow shape of the liquid cone is also visible in all these images.

A Phase Doppler Anemometer (PDA) yields the velocity profiles of the air flow and the n-heptane droplet diameters in the single burner, under cold conditions. Measurements are carried out without confinement to avoid laser beam deflections due to wall wetting. Measurements with confinement under hot fire conditions confirm that this procedure is adequate. Figure 2.4 displays the three components  $\{U_r, U_\theta, U_z\}$  mea-

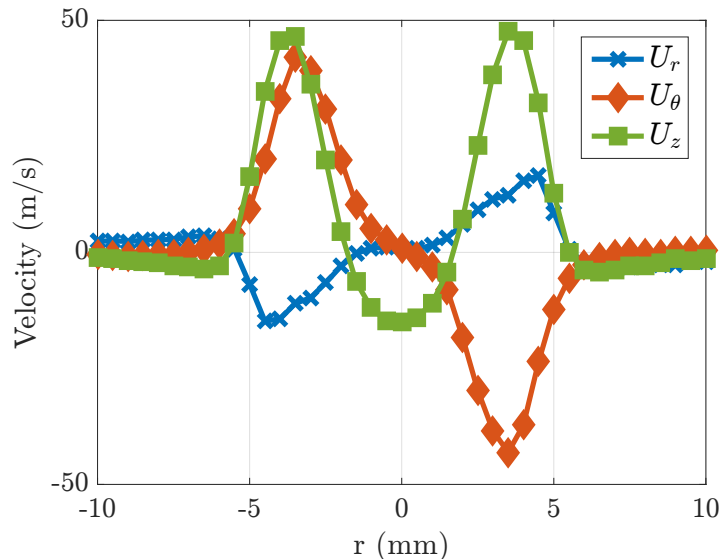


**Figure 2.4.** Mean air velocity profiles  $\{U_r, U_\theta, U_z\}$  measured at  $z = 2.5$  mm for a nominal flow rate  $\dot{m}_{air} = 1.94 \text{ g s}^{-1}$ .

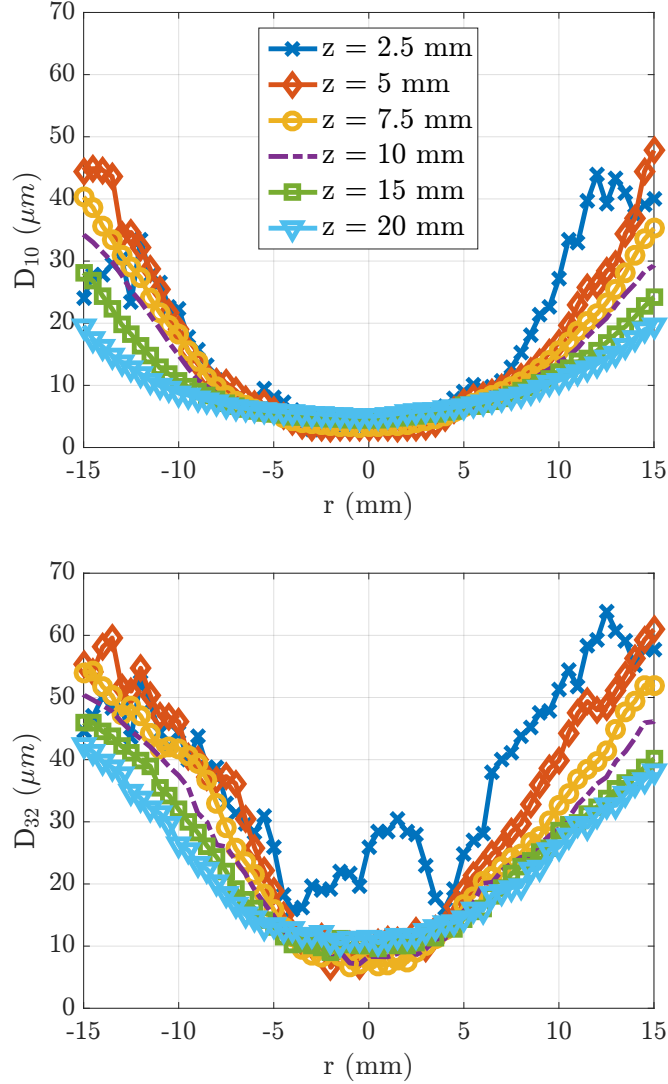


**Figure 2.5.** n-Heptane droplet diameter profiles  $\{d_{10}, d_{32}\}$  in non-reactive case at different altitudes  $z$  for a nominal flow rate  $\dot{m}_{fuel} = 0.11 \text{ g s}^{-1}$  and  $\dot{m}_{air} = 1.94 \text{ g s}^{-1}$ .

sured velocity profiles of the air flow obtained at  $z = 2.5 \text{ mm}$  for nominal injection conditions. No fuel is injected at this stage and LDA measurements are based on seeding oil droplets (diameter  $d_{10} < 2 \mu\text{m}$ ) giving access to the entire air dynamics. As the liquid loading is low, the spray only weakly interacts with the air flow. Mean data are shown for 50,000 droplets to ensure good data convergence. High axial velocities are observed with, at peak,  $U_z \simeq 50 \text{ m s}^{-1}$ . A strong recirculation zone is present in the center of the chamber. The air flow also features a sizable azimuthal component. The measured velocity profiles used to determine the swirl number provide an experimental value  $S = 0.68$ . Figure 3.4 shows the diameter profiles at several levels

of the n-heptane droplets injected by the liquid atomizer within the swirling air flow field shown in Fig. 2.4. At  $z = 2.5$  mm and  $r = 5$  mm, the mean diameter  $d_{10}$  is  $\sim 8$   $\mu\text{m}$ . At the same location, the Sauter Mean Diameter (SMD)  $d_{32}$  is  $\sim 27$   $\mu\text{m}$ . These relatively small diameters confirm the good atomization provided by the liquid fuel injector. One can deduce from measurements at different levels a mean value of the SMD averaged along the radial axis, representing the general droplet population at the top of the swirling jet,  $d_{32} = 30$   $\mu\text{m}$ . Note that the particular behavior of the SMD in the center of the chamber at  $z = 2.5$  mm is not found downstream. These measurements might have been altered as they were done just at the exit of the injector, in the recirculation zone, where the droplet number is low.

### 2.3 Light-round experimental data and interpretation

The light-round processes in the annular chamber are now compared for three fuels : propane (gaseous), n-heptane (liquid) and dodecane (liquid). The sequence is characterized by the time delay  $\tau_l$  corresponding to the duration between the initial growth of the flame kernel around the igniter and the merging point of the two flame branches propagating in the annulus. A strict experimental protocol is used in order to keep a hot constant temperature of the walls between the different experiments:

- The chamber is preheated until stable thermal conditions are reached (thermocouple measurements indicate a stable wall value of 900 K after 500 s at  $\mathcal{P} = 80$  kW);
- Fuel (gaseous or liquid) is turned off and kept off for 5 seconds to avoid autoignition;
- Fuel injection is turned on for a few seconds until the fuel flow rate is stabilized (this time depends on the flow meter dynamics);
- The high speed camera is triggered and the chamber is ignited using the spark plug;
- When the process is terminated, another can be initiated until the memory of the camera is filled up.

The residence time in the 200 mm-long chamber calculated for the different injection velocities varies from  $\tau_r = 0.3$  to 0.5 s and one may safely assume that the volume is homogeneously filled with the mixture during the ignition procedure. Several sparks are needed to ignite a small flame kernel near the plug. This time delay defines the spark delay  $\tau_s$ . Depending on the equivalence ratio and on the velocity,  $\tau_s$  can take from 5 to almost 1000 ms. Spark delays are longer with liquid fuels due to the need to evaporate some fuel before it can burn and probably due to heterogeneous mixtures close to the injector outlet. Also, the number of sparks required increases under lean conditions. This is because the probability of formation of the initial flame kernel is reduced. Several attempts are then needed to ignite. Energy deposited at each spark is small and the heated volume is convected away if no flame kernel is formed and does not alter the light-round process.

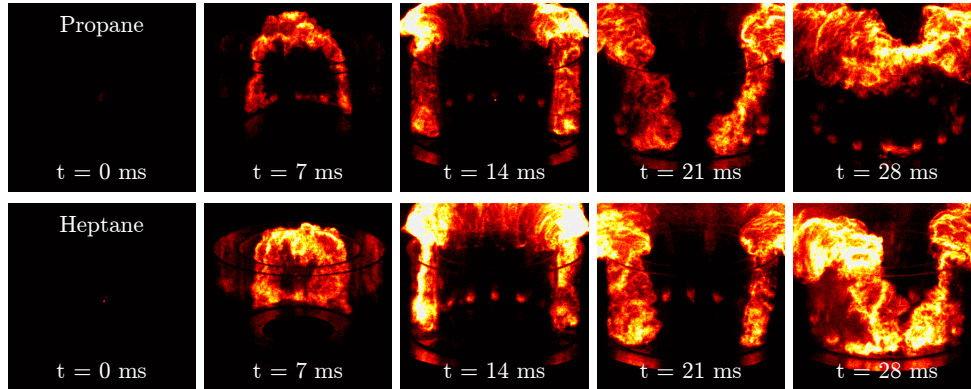


**Figure 2.6.** Light emission during the ignition sequence of propane (top) and n-heptane (bottom) fuels. Yellow corresponds to high light intensity while dark red represents low light emission. Each sequence features equivalent injection conditions :  $U_b = 31.5 \text{ m s}^{-1}$ ,  $\phi = 0.90$  and  $\mathcal{P} = 80 \text{ kW}$ .

Figure 2.6 shows the full ignition sequences of propane gaseous fuel (top) and n-heptane spray injection (bottom) for identical operating conditions. The same time scales are used for the two sequences in order to compare the evolution of the process. To improve the visualization, each image is plotted on a scale of false colors where yellow corresponds to the highest intensity value, while dark red represents the lowest value in terms of flame radiation intensity. In the first milliseconds, the spark ignites a small flame kernel which determines the initial instant of the light-round time delay  $\tau_l$ . Looking at the n-heptane sequence (bottom of Fig. 2.6), the flame kernel is first quickly convected between two injectors after the first image ( $\sim 0 \text{ ms}$ ). In the second image, at  $t \sim 7 \text{ ms}$ , once this pocket is ignited, it expands in a spherical way. In the third image, at  $t \sim 14 \text{ ms}$ , the flame features two vertical symmetric arches igniting the burners one after the other. In the fourth image, at  $t \sim 21 \text{ ms}$ , when approaching the merging point, the flame velocity decreases due to the compression of unburnt gases upstream the two branches, causing the arches to take back a spherical shape. The branches meet in the fifth image, at  $t \sim 28 \text{ ms}$ , defining the light-round time delay  $\tau_l$ . For gaseous fuel, this sequence is quite similar and nearly symmetric. For most runs with propane, the merging point is diametrically opposed to the spark plug. Some asymmetry can however be induced by the general swirl direction of rotation. In the case of liquid fuel, the asymmetry can be stronger and partially strengthened by the convected kernel in the first milliseconds. After collapse of the left and right arches, the front is convected upward by the hot gases originating from the burners and steady state is reached as can be seen in the last image of the propane sequence (top of Fig. 2.6).

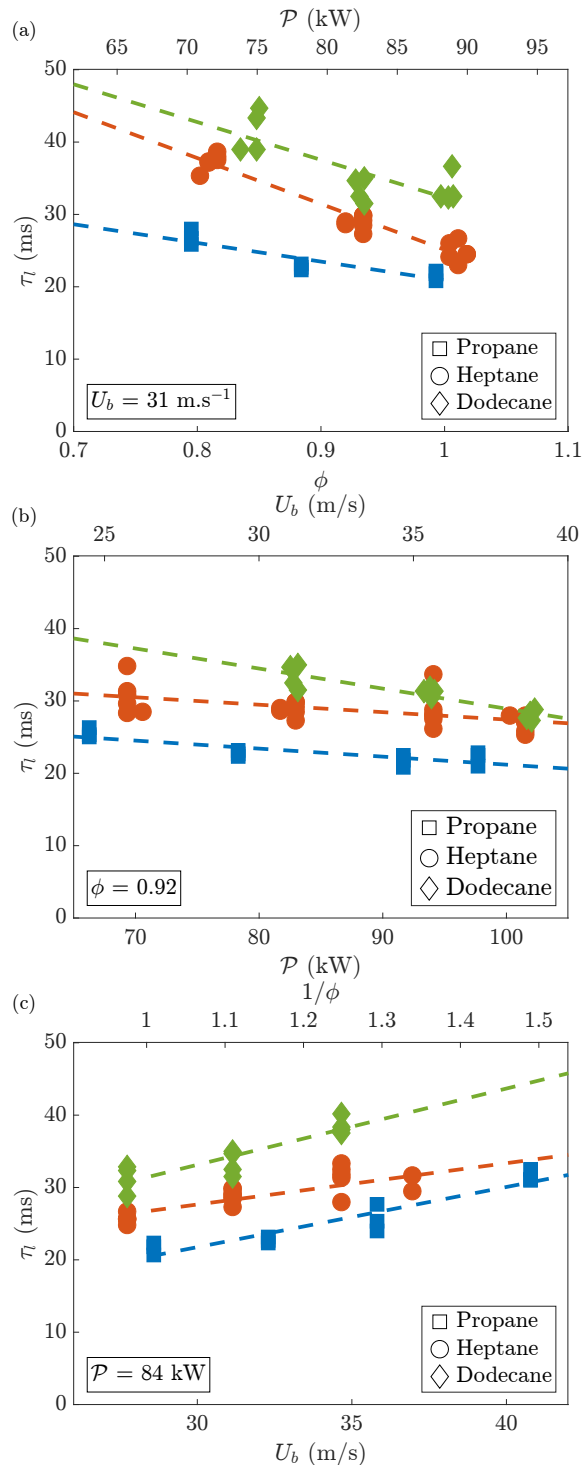


**Figure 2.7.** Light-round delay  $\tau_l$  when: **(a)** the bulk velocity  $U_b$ , **(b)** the equivalence ratio  $\phi$  or **(c)** the power  $\mathcal{P}$  is kept constant for multiple fuels : propane (gaseous), n-heptane (liquid spray) and dodecane (liquid spray). Linear fits in dashed lines give the general trend for the different fuels.

A wide range of experimental conditions has been explored to examine the influence of the fuel type on the delay  $\tau_l$ . Three sets of experiments are described below. Note that for premixed propane, the fuel flow rate only slightly increases the bulk velocity  $U_b$  ( $< 1.5\%$ ) and this effect may be neglected.

1. Bulk velocity  $U_b = 31 \text{ m s}^{-1}$  is kept constant, equivalence ratio varies from  $\phi = 0.80$  to  $1.05$  and power  $\mathcal{P}$  varies simultaneously from  $70$  to  $90 \text{ kW}$ ;
2. Equivalence ratio  $\phi = 0.92$  is kept constant, bulk velocity varies from  $U_b = 25$  to  $39 \text{ m s}^{-1}$  and power  $\mathcal{P}$  varies simultaneously from  $65$  to  $100 \text{ kW}$ ;
3. Power  $\mathcal{P} = 84 \text{ kW}$  is kept constant, bulk velocity varies from  $U_b = 27$  to  $41 \text{ m s}^{-1}$  and equivalence ratio varies simultaneously from  $\phi = 0.70$  to  $1.05$ ;

Each point in Fig. 2.7 corresponds to an ignition sequence with specific injection conditions. Experiments are repeated three to six times to allow accurate delay determinations. The number of experiments is smaller under lean condition due to difficulties in synchronizing the high-speed imaging acquisition and the light-round because the ignition probability is reduced in these conditions. The maximum data scatter is of the order of  $10\%$  in Fig. 2.7a and stays relatively small for the other operating points so that three readings are meaningful.

In Fig. 2.7a, one can see that the general trend is a decrease of  $\tau_l$  when  $\mathcal{P}$  or  $\phi$  are increased. For propane fuel, for example,  $\tau_l$  decreases from  $28 \text{ ms}$  at low power to  $23 \text{ ms}$  at higher power. The same trend is found for n-heptane and dodecane. Experiments also indicate that when the equivalence ratio rises, the delay is reduced. This corresponds to an increase in the burnt gas temperature and in the laminar burning velocity. Both factors tend to reduce the delay  $\tau_l$  as discussed in section 2.4. In Fig. 2.7b, as  $\phi$  is fixed,  $\mathcal{P}$  and  $U_b$  are linearly linked. When the power is increased, more fuel is injected in the chamber so the air flow rate has to be increased to keep a constant equivalence ratio. As a consequence, the quantity of burnt gases increases. The temperature of these burnt gases is constant. Bourgoïn et al. (2013) has shown that the volumetric expansion of these gases is a key parameter for the propagation of the flame front in the ignition sequence. As a consequence, increasing the amount of burnt gases results in a slight decrease of the light-round delay  $\tau_l$ . In Fig. 2.7c, as the power is fixed, the equivalence ratio and the burnt gas temperature decreases when the bulk velocity increases. In this case  $\tau_l$  increases with  $U_b$  confirming that the burnt gas temperature plays a key role.

Table 2.1 compares the delay  $\tau_l$  at two injection conditions for the three fuels when the power is kept constant. The delay  $\tau_l$  varies from  $20$  to  $40 \text{ ms}$ . One finds that n-heptane fuel takes roughly  $20\%$  more time to ignite the chamber than propane fuel while dodecane fuel takes  $50\%$  more time with respect to the premixed propane air case. These relative changes are much greater than the maximum relative scatter indicating that the differences in the light-round delay between the three fuels are

meaningful.

**Table 2.1.** Mean light-round time delay  $\tau_l$  for propane (gaseous), n-heptane (liquid) and dodecane (liquid) fuels for increasing equivalence ratio and power when the bulk velocity  $U_b = 31 \text{ m s}^{-1}$  is kept constant. Relative changes  $\Delta\tau_l/\tau_l$  are given in parenthesis.

	$\phi = 0.92$ $\mathcal{P} = 82 \text{ kW}$	$\phi = 1.0$ $\mathcal{P} = 89 \text{ kW}$
Propane	23.5 ms	21 ms
n-Heptane	29 ms (+ 23 %)	25 ms (+ 19 %)
Dodecane	35.5 ms (+ 51 %)	32 ms (+ 52 %)

## 2.4 Intermediate discussion

Presented experiments indicate that the delay  $\tau_l$  is augmented when gaseous injection is replaced by liquid spray injection. This delay is increased further when a lesser amount of liquid fuel is vaporized at the start of the process, i.e. when n-heptane is replaced by dodecane. A rough interpretation of these data may be put forward by making use of the theoretical framework developed in [Bourgouin et al. \(2013\)](#) where it was shown that flame spreading could be represented by an absolute displacement velocity  $(\rho_u/\rho_b)S_d$  where  $\rho_u/\rho_b$  designates the volumetric expansion effect and  $S_d$  is a normal displacement velocity in a turbulent combustible mixture which depends on the turbulence level and spray characteristics. In a simplified flamelet-like description of this process one may assume that  $S_d = \Xi S_L^{sp}$  where  $\Xi$  is a mean wrinkling factor and  $S_L^{sp}$  is a laminar burning velocity in a spray/air mixture. These various factors are examined below.

Concerning the ratio  $\rho_u/\rho_b$  for the three fuels, one has to evaluate the adiabatic combustion temperature under the same conditions of overall equivalence ratio and injection temperature. In the present experiments, air and fuel are injected at  $T_u \simeq 300 \text{ K}$ . Estimates can be made at  $\phi = 1$  with chemical equilibrium calculations. For the three fuels, propane, n-heptane and dodecane, the adiabatic flame temperatures are respectively 2267, 2274 and 2279 K. In these calculations, the heat of vaporization is neglected for n-heptane and dodecane, but this contribution is small (less than 1%). Thus, the three fuels induce about the same volumetric expansion with a maximum deviation of 1.5%.

Considering now the laminar burning velocities at ambient temperature  $T_u \simeq 300 \text{ K}$  and  $\phi = 1$ , an experimental value  $S_L = 0.40 \text{ m s}^{-1}$  is found both for propane ([Vagelopoulos et al. \(1994\)](#)) and for pre-vaporized n-heptane ([Davis and Law \(1998\)](#)). The laminar flame calculations of [Neophytou and Mastorakos \(2009\)](#) give  $0.41 \text{ m s}^{-1}$  for

the n-heptane. For dodecane, an extrapolation of numerical results of [Neophytou and Mastorakos \(2009\)](#) and experimental results from [Wagner and Dugger \(1955\)](#) and [Kumar and Sung \(2007\)](#) gives  $\simeq 0.40 \text{ m s}^{-1}$  in pre-vaporized conditions. One may thus conclude that the three fuels have about the same laminar burning velocities with less than 2.5 % variations in perfectly premixed conditions.

The information on the wrinkling factor  $\Xi$  is at this point more qualitative. Turbulent eddies observed in Fig. 2.6 during the light-round sequences of the propane/air mixture and the n-heptane spray flame are visually similar. Flame wrinkling is due to fluctuations in the gas flow on the upstream side of the flame front. This agitation is generated by the interaction of the swirling flows coming from the injectors. Given the small droplet size and the low concentration of fuel, the turbulent structures in fresh gases are weakly affected by the spray. Thus the value of  $\Xi$  is most probably of the same order of magnitude for the three fuels at the same operating point. Differences observed in flame propagation during light-round are therefore linked to the laminar flame burning velocity in the spray/air mixture.

One has now to consider the influence of the presence of the droplet spray on  $S_L^{sp}$ . Even if the spray is quite heterogeneous at the injectors exit, very quickly the droplet cloud becomes more homogeneous in the chamber, and to a first approximation, one can consider that the flame spreads in a uniform medium. It is known from experiments such as [Ballal and Lefebvre \(1981\)](#), [Myers and Lefebvre \(1986\)](#) or [Neophytou and Mastorakos \(2009\)](#) that  $S_L^{sp}$  depends on four key parameters,  $\phi$  the global equivalence ratio,  $\Omega = m_{GF}/(m_{GF} + m_{LF})$  the vaporized fuel mass fraction,  $m_{GF}$  and  $m_{LF}$  respectively correspond to the mass of fuel in gaseous and liquid forms in a volume,  $d_{32}$  the SMD and  $\lambda$  an effective evaporation constant. For a given global equivalence ratio,  $S_L^{sp}$  decreases when  $\Omega$  is reduced ([Ballal and Lefebvre \(1981\)](#)). The smallest value of  $S_L^{sp}$  is obtained when  $\Omega = 0$ , i.e. in a case without initial fuel evaporation in the mixture.  $S_L^{sp}$  also decreases when  $d_{32}$  increases.

Using the framework defined in the beginning of this section,  $S_L^{sp}$  can be estimated for the operating points presented in Tab. 2.1 and compared with numerical results given in [Neophytou and Mastorakos \(2009\)](#). As already indicated, the laminar burning velocity for the three fuels is about  $0.40 \text{ m s}^{-1}$  in pre-vaporized conditions. At  $\phi = 1$  an increase by 19% for the mean light-round time delay of the n-heptane flame corresponds to an opposite reduction for  $S_L^{sp}$ . In that case  $S_L^{sp} = 0.34 \text{ m s}^{-1}$ . From [Neophytou and Mastorakos \(2009\)](#), in a n-heptane-air mist with a mean diameter  $d_{32} = 30 \mu\text{m}$ , this velocity is obtained when  $\Omega = 0.75$ , i.e. when 75% of n-heptane is vaporized in front of the flame. For dodecane, the time delay is increased by 52% at  $\phi = 1$  in Tab. 2.1. Then  $S_L^{sp}$  must be of the order of  $0.26 \text{ m s}^{-1}$  in that case. In contrast to n-heptane, one may consider that there is no evaporation of dodecane at ambient temperature. From [Neophytou and Mastorakos \(2009\)](#), a calculation made with a decane-air mist (the decane is close to dodecane) gives a velocity of  $0.26 \text{ m s}^{-1}$  when the mean droplet size is equal to  $30 \mu\text{m}$ , which corresponds well to the estimated  $d_{32}$  in the mist, at the top of swirling jets in Fig. 3.4. One may then consider that the

relative changes in light-round delay correspond to the relative changes in burning velocities induced by the presence of a volatile or less volatile fuel in the spray.

## 2.5 Flame front passage 90° from the ignition point

An analysis of the images of the Travelling Flame Branch (TFB) viewed from the side of the MICCA-Spray system is now carried out. The evolution in flame structure and shape of individual flames formed after the passage of the TFB is then discussed in

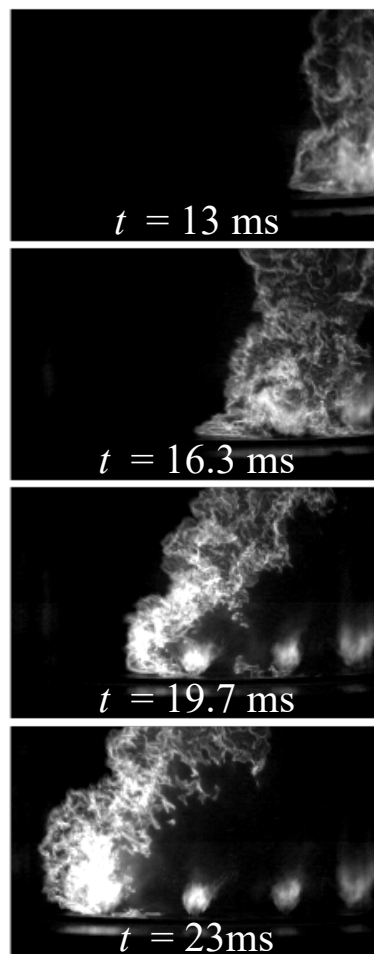


**Figure 2.8.** Passage of the travelling flame at four different instants during the light-round. The camera is placed on the side of the combustor and its optical axis is at the level of the chamber backplane. The luminosity of the other flame branch propagating in the other half of the annular combustor is blocked by a steel plate placed in the central plane of the system. The origin of time  $t = 0 \text{ ms}$  corresponds to the ignition of hot kernel by the spark plug.

this section. The high-speed camera (Phantom V2512) is placed on the side of the annular combustor facing the region between two injectors (see Fig. 4.1). The optical axis is at the level of the backplane of the chamber. This is used to observe one branch of the flame in the light-round as shown in Fig. 2.8. The time instants are counted with respect to an initial time  $t = 0$  ms when the spark plug initiates a flame kernel at the first injector. The flame then propagates from right to left in the sequences of images displayed in this figure. These images provide information on the flame propagation during the process as it will be investigated in the next paragraphs. The structures that are observed in Fig. 2.8 can be used to estimate the propagation speed of the flame front using Particle Image Velocimetry (PIV) algorithms. The camera runs at 6000 Hz which is, of course, not enough to sample the displacement of PIV particles, but the motion of the large structures characterizing the flame is well captured at this frame rate. Open source PIV software such as PIVlab, interfaced with Matlab, can then be used to determine the velocity of these structures. The velocity field  $(u_\theta, u_z)$  is superimposed to the flame front propagation in Fig. 2.9 with  $u_z$  the axial velocity and  $u_\theta$  the azimuthal component. This last component is in fact an estimation of the azimuthal velocity as the flame propagation is curved due to the annular shape of the chamber. This deviation is small as the radius of curvature is large. Velocity vectors are spatially filtered in order to be calculated when there are well defined flame structures.

One observes, in Fig. 2.9, that the velocity fields may be divided into regions I and II where the velocity orientations are distinct. In region I, the velocity of the flame front is purely azimuthal with essentially no axial component. The part of the travelling flame in this zone is stuck to the chamber backplane and moves forward from one injector to the next. This indicates that zone I is the part of the flame front responsible for the ignition of the 8 injectors on its path covering half of the annular chamber. Velocities in this region can be estimated from the different instantaneous images. One obtains a mean velocity of  $v_\theta$  comprised between 15 and 20  $\text{m s}^{-1}$  for zone I. Zone II corresponds to the region where the flame is propagating azimuthally and axially due to the burnt gas expansion pushing the reactive front towards the exit of the combustion chamber. In this region, the velocity magnitude is estimated to be in the range 10-15  $\text{m s}^{-1}$ , confirming the trend that the leading point of the flame propagation is close to the chamber backplane. This type of propagation consists of a burner-to-burner propagation and has already been discussed in some previous articles (see Bourgouin et al. (2013) and Bach et al. (2013)). This feature is also observed numerically in full annular light-round Large Eddy Simulations (LES) calculations done by Lancien et al. (2017).

The novelty of this study is the clear characterization of the phenomenon with high-resolution diagnostics, giving access to a large set of data on the light-round in annular combustor. Images available in Fig. 2.8 are processed to extract flame structure details such as the flame wrinkling cell sizes. These data may be used to guide the selection of the grid and filter sizes of importance for Large Eddy Simulations. This estimation is performed by using the following procedure:

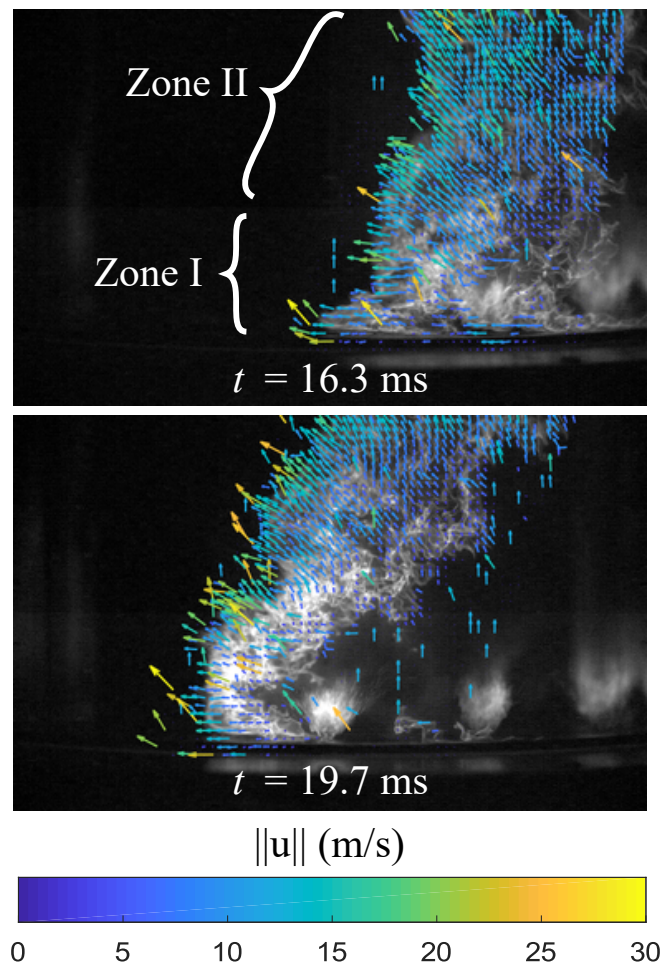


**Figure 2.9.** Result of a PIV processing of the flame passage at two different instants during the light-round. Regions I and II correspond to different flame propagation behaviors and are explained in the text. The origin of time  $t = 0 \text{ ms}$  corresponds to the ignition of a hot kernel by the spark plug. Velocity vectors are colored by their magnitude using the colormap inserted below the images.

- Images are scaled via a recorded known pattern
- Large structures are enhanced by filtering images in the frequency domain on the basis of spectral analysis
- A threshold is applied in order to retain the most energetic structures
- Edges are found and kept to obtain binary images
- A classical particle analysis by surface and circularity is run to estimate the cell sizes

An example of the original flame image and the result of this processing are displayed

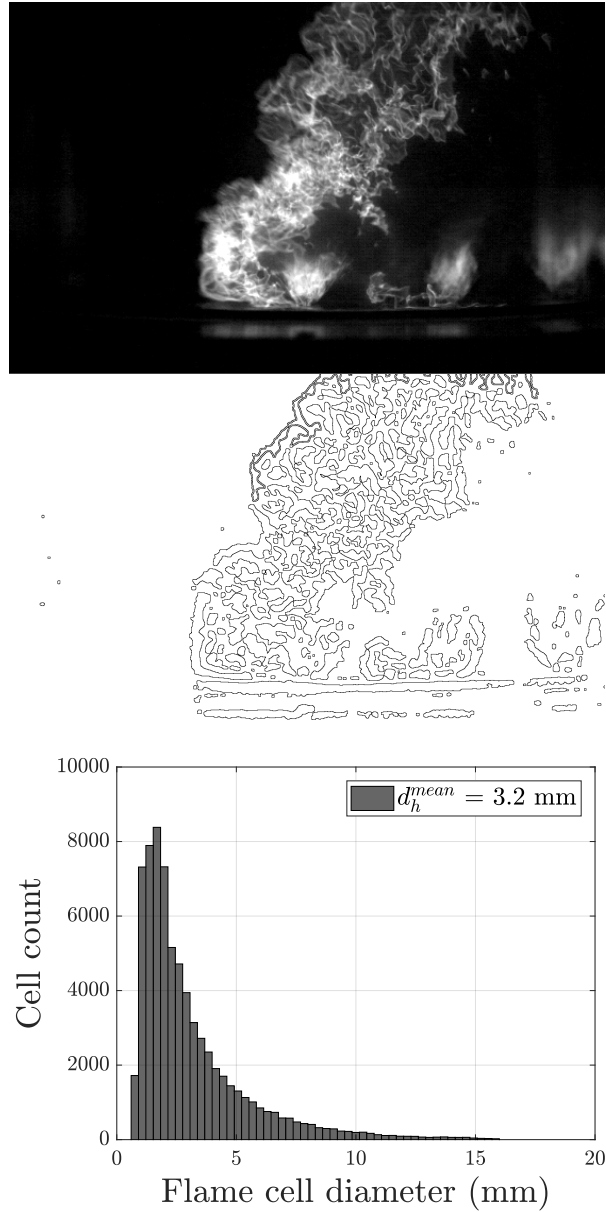


**Figure 2.10.** Top: instantaneous flame shape; Middle: flame cells extracted from the flame shape; Histogram of the flame cells sizes calculated over 300 images and 70,000 cells.

in Fig. 2.10, top and middle, for a single image. Data are averaged over 70,000 particles detected in 300 images corresponding to three different successful light-rounds. The histogram of the equivalent wrinkling size is shown in the bottom of Fig.2.10. The mean wrinkle size is  $\lambda_w^{mean} = 3.2 \text{ mm}$ . This is a rough estimate of the flame wrinkling due to the projection imposed by the camera shots. But this gives an es-

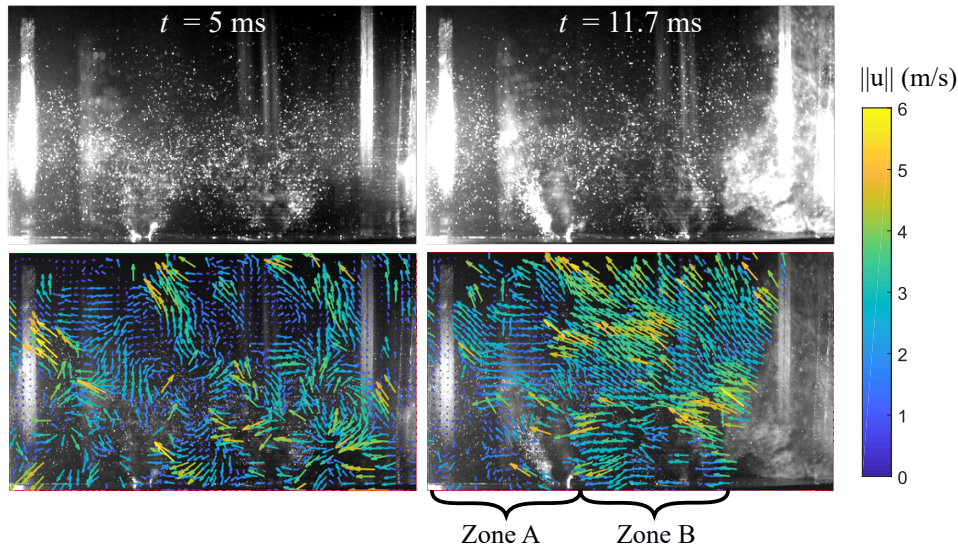


**Figure 2.11.** Top: Images of the flame propagation with a laser slice to visualize the motion of the droplet spray. Bottom: Velocity fields calculated using the n-heptane droplets. False vectors have been eliminated. The time origin  $t = 0 \text{ ms}$  corresponds to the ignition of a hot kernel by the spark plug. Velocity vectors are colored by their magnitude using the colormap inserted on the right of the images.

estimate of the size of flame wrinkles that can be used to adjust the element sizes that need to be adopted in high fidelity Large Eddy Simulations and require that the wrinkle size be greater than the element size in the simulation.

A 1.5 W continuous 532 nm laser is then used to generate a vertical slice of approximately 2 mm width. The laser light beam crosses the outer quartz tube and forms a vertical sheet that is perpendicular to the camera line of sight. The slice contains the axis of one injector. Figure 2.11 shows two non-consecutive images recorded at 6000 Hz. One can see that the laser slice features striations due to the crossing of the 6 mm-thick quartz tube. This cannot be easily corrected since the tube thickness is necessary to sustain the high temperature combustion conditions. In this experiment, the chamber walls had to be maintained cold in order to obtain a sufficient number of droplets to be visualized. If the walls were preheated as in the other experiments, the evaporation of the liquid n-heptane would have been too fast and no droplet would have remained a few centimeters downstream the injector exit. Top images in Fig. 2.11 show the behavior of the n-heptane droplets when the flame is sufficiently far from the injector and when it approaches this unit. At  $t = 5 \text{ ms}$ , the droplets appear as brilliant point sources, indicating that they are nearly still. At  $t = 11.7 \text{ ms}$ , the flame front approaches from the right side of the image. Note that the flame front is not clearly identified due to the high luminosity of the droplets. In contrast with the previous image, droplets are globally displaced to the left, spray zones are densified whereas other zones feature a lower fuel load when the two images are compared. PIV algo-

rithms are again applied to the n-heptane droplets to deduce the velocity field of the liquid fuel. Images showing the corresponding velocity vector fields are at the bottom of Fig.2.11. In the left image, all the vectors have either a global axial component or are trapped in the recirculation regions. This trend is then strongly perturbed when the flame front arrives from the right. Two regions can then be clearly identified. Zone A is where the droplets are not affected by the incoming flame front. Zone B is the region where the fuel is influenced by the incoming flame front. A part of the droplets are displaced to the left with an estimated velocity of 5 to 10 m s<sup>-1</sup>. Note that these values are lower than those found by determining the flame front motion in Fig. 2.9. This is so for two reasons. First, the droplets have their own inertia and the flame front is progressively advancing faster and consuming the n-heptane droplets. Second, velocities are lower because of the cold walls that increase the light-round time delay. This droplet motion is the result of the piston effect induced by the flame on the fresh gases flowing on its upstream side as discussed in [Bourgouin et al. \(2013\)](#). These measurements yield clues on the distance of influence of the travelling flame branch. Taking into account all the available images, the distance is approximately equal to the spacing between two injectors  $s = 68$  mm. This value of course depends on the configuration and ignition conditions. Note that this phenomenon can have a strong impact on the ignition sequence as it will change the concentration of liquid droplets, thus modifying the local equivalence ratio. Rich regions may appear inducing hot spots while lean regions may form in other parts of the system eventually leading to a local reduction in combustion intensity. These effects of the flame on the droplet distribution have to be taken into account in models of the light-round in combustors.

## 2.6 Flame structure evolution during the light-round

The fine definition of the recorded images gives access to details of the flame shape during the ignition process of the annular chamber. In order to get turbulence-free images, 50 consecutive instantaneous images, corresponding to approximately 8 ms, are recorded and averaged to get the mean flame shape. During this period the flame shape barely changes. Figure 2.12 presents the mean flame shape evolution of one injector for four different successful ignitions of the annular combustor. The initial time  $t = 0$  ms corresponds to the ignition of this injector by the passing flame branch. One can see that the flame seems to be quite compact at first and close to the chamber backplane. After 20 ms it expands in a clear “M” shape and reaches its final position after 50 ms. This defines the time delay  $\tau_s$  between the time of ignition and the flame shape switch. On average,  $\tau_s = 30$  ms. One other important observation is that, in the first few milliseconds, the flame is much brighter than after stabilization 50 ms later. This indicates that the flame is first rich before reaching the global equivalence ratio  $\phi = 0.89$ . This can be the result of an initial densification of the spray discussed previously.

The top Fig. 2.13 shows two images of the flame 5 and 21 ms after the injector ignition. Luminosity levels are saturated in order to enhance the differences. One can

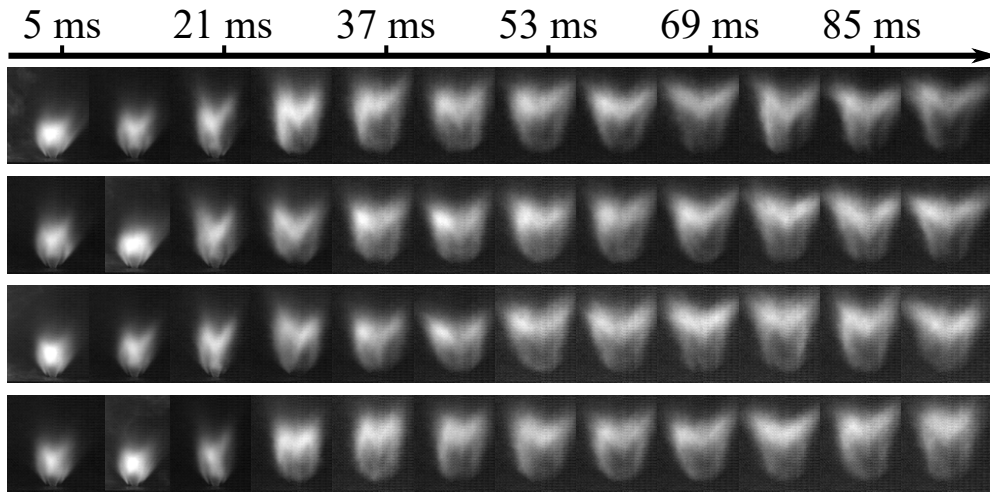


**Figure 2.12.** Evolution of the mean flame shape after the passage of the flame front for several successful sequences. The time origin  $t = 0$  ms corresponds to the instant when the injector is ignited by the incoming flame front.

see that the left flame is clearly attached to the lips of the burner and is even entering in the injector, drawn into by the central recirculation zone (CRZ) formed by the swirler. After several milliseconds, the inner flame stabilized in the recirculation zone vanishes and the flame lifts its anchoring points. A schematic representation of the flame fronts in both cases is proposed in the lower part of Fig. 2.13, featuring two flames shapes “A” and “B”. This phenomenon of upstream propagation of the flame front in the injector can be detrimental to industrial applications. As the flame travels in the injector, internal metallic parts are exposed to high temperatures. Although this takes place over a period of a few milliseconds, this thermal loading might degrade the injection components. It is worth noting that this process is repeatable and not specific to the configuration described in the present chapter. Appendix A reports the same phenomenon in a different configuration of the MICCA chamber [Bourgouin et al. \(2013\)](#) corresponding to a premixed injection system and to swirlers with a different geometry.

It has been seen in the previous paragraphs that it takes approximately  $\tau_s = 30$  ms to expel the flame from the injection unit and reach its final shape. Figure 2.14 shows mean images of three different neighboring flames in the MICCA-Spray chamber during the light-round. The averaging method over 8 ms is identical to the one used for images shown in Figs. 2.12 and 2.13. Flames are designated by letters “ $\alpha$ ”, “ $\beta$ ” and “ $\gamma$ ”, from right to left. The time step between each mean image is approximately 17 ms. In the first snapshot, one can see that flames “ $\alpha$ ” and “ $\beta$ ” are adopting an “A” shape as described before. Flame “ $\gamma$ ” is not yet perfectly ignited. After 16 ms, flame “ $\alpha$ ” switches to a “B” shape while “ $\beta$ ” and “ $\gamma$ ” adopt an “A” shape just after their ignition. 16 ms later, flame “ $\beta$ ” switches to the “B” shape while flame “ $\gamma$ ” stays

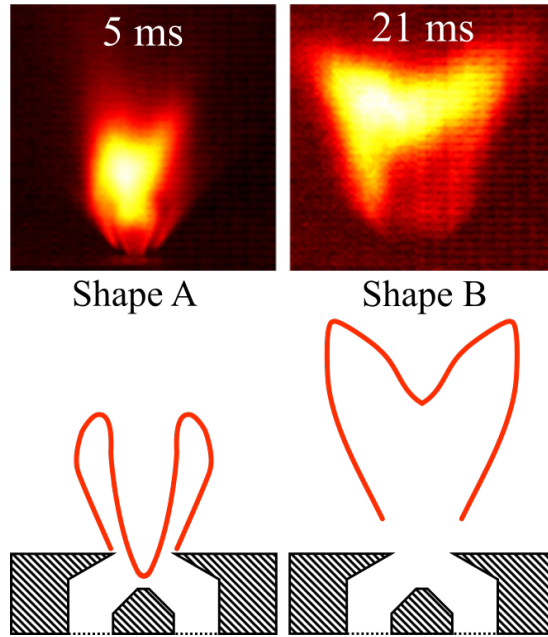


**Figure 2.13.** Left: Flame shape 5 ms after the flame front ignites this injector (top) and schematics of the flame front (bottom). Right: Flame shape 21 ms after the flame front ignites this injector (top) and schematics of the flame front (bottom). Both images are represented in false colors and saturated to underline the differences. Yellow corresponds to high light intensity while dark red represents low light emission levels.

in the “A” shape. After 54 ms, all the flames are lifted and have adopted the “B” shape.

In conclusion, one can see that all the flames do not switch simultaneously from “A” to “B” shapes. The time delay  $\tau_p$  between these changes is the delay for the flame front to travel from one injector to the next. The distance  $s$  between two injectors is  $s = 1/16\pi D = 68$  mm with  $D$  the mean diameter of the chamber. If one considers that the flame front absolute velocity  $v_f$  is a constant with  $v_f = 17$  m s<sup>-1</sup> (see Fig. 2.9), the time delay  $\tau_p$  is 4 ms. In the annular combustor, the first flame ignited will switch from “A” to “B” shapes after  $\tau = \tau_s = 30$  ms, whereas the second one will change after  $\tau = \tau_s + \tau_p = 34$  ms. The  $n$ -th flame will then change after  $\tau = \tau_s + (n - 1)\tau_p$ . Reasons for this flame shape switching are now investigated by considering several scenarios:

1. The aerodynamic disturbance due to the creation of the flame takes several milliseconds to dissipate,
2. Ignition of a given injector generates a pressure wave that pushes the flame in the axial direction, forcing it to stay in the backplane area and close to the nozzle exit,
3. Local thermal conditions take several milliseconds to stabilize and influence the

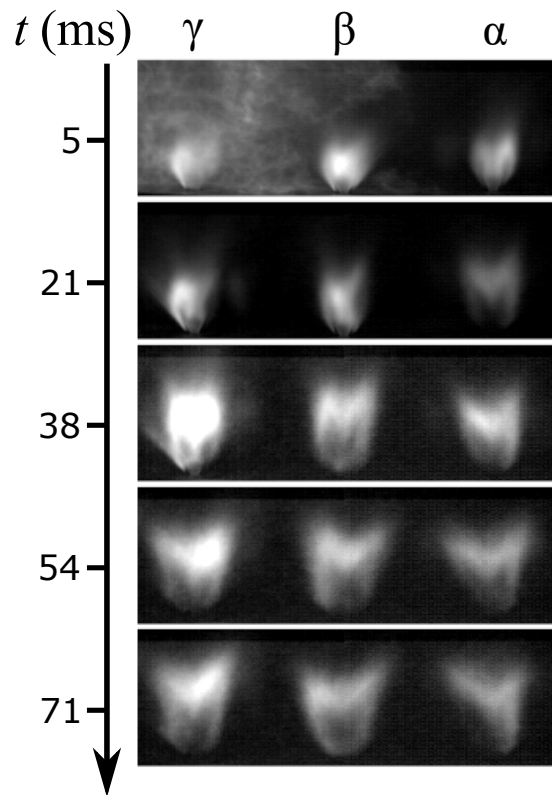


**Figure 2.14.** Mean images of three consecutive flames of the annular combustor progressively switching from shape “A” to shape “B”. In the first image, the flame front propagates from right to left. The first flame to be ignited is flame “ $\alpha$ ”.

central and outer recirculation zones,

4. The passage of the flame when it ignites a given injector induces a negative disturbance of the mass flow rate in the injection unit, reducing the incoming air velocity that favors the penetration of the flame in the injection unit.

The first scenario is not to be considered as the flames take at least 50 ms to completely stabilize. This delay is too large to correspond to a characteristic aerodynamic time. The second scenario has to be evaluated with experimental data. The pressure wave can be tracked by making use of pressure signals available in the chamber and plenum cavities. Figure 2.15 displays records of the different microphones before and after the light-round. One can see that the acoustic pressure is suddenly rising in the plenum around 4000 ms which corresponds to the ignition of the system. The key information is that the signals of the four different microphones, spaced by  $90^\circ$  from each other, appear to be in phase. This is more obvious in the chamber, where the pressure signals are plotted in the bottom of Fig. 2.15. For clarity, the signals are low-pass filtered with a cut off frequency of 500 Hz. All microphone signals recorded in the chamber are displayed in this figure and correspond to microphones separated

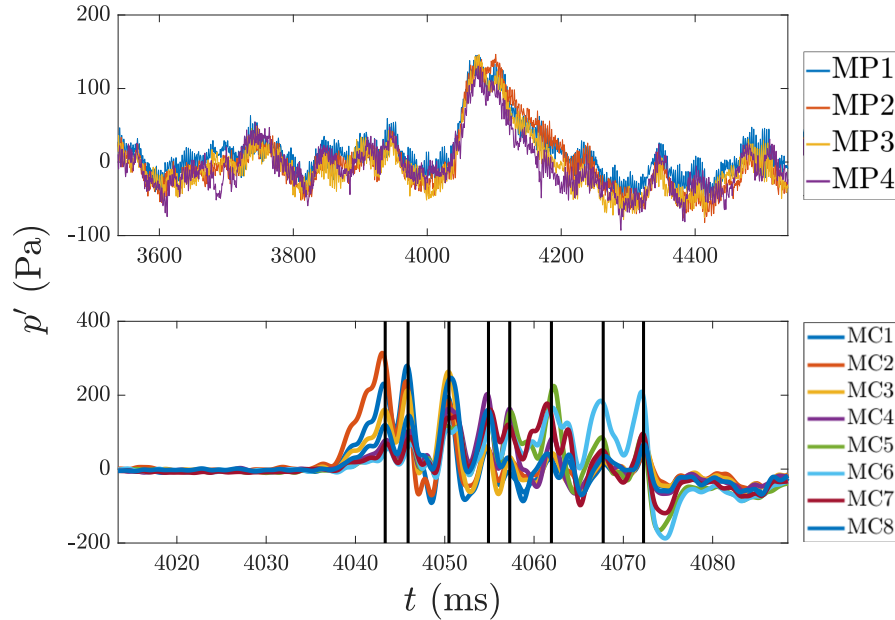


**Figure 2.15.** Acoustic pressure recorded by four pressure sensors in the plenum (top) and by 8 pressure sensors in the chamber (bottom) before and after the light-round. Note that the bottom figure is a zoom of the pressure in the chamber during the ignition. The black lines identify the different peaks that each correspond to the ignition of one injector.

by an angle of  $45^\circ$ . All the pressure peaks in the bottom figure, occur at the same time. One can see that the pressure arrives at nearly the same instant at every sensor position indicating that it propagates at the sound velocity  $c$  of the medium which is typically  $720 \text{ m s}^{-1}$  and which corresponds to a delay of  $0.1 \text{ ms}$ . This is incompatible with what has been observed in Fig. 2.14. This hypothesis must then be rejected. Note that more information can be extracted from Fig. 2.15. The peaks in the bottom plot correspond to the ignition of the eight successive injectors in the annular combustor. This feature is underlined by the different black vertical lines in the bottom figure. The peaks are all quasi-equally spaced in time and the delay is  $\Delta t = 4 \text{ ms}$  which corresponds to the time for the travelling flame branch to propagate from one injector to the next.

The third scenario concerns the influence of the thermal conditions on the flame. It is well known that flames are sensitive to thermal conditions prevailing near the injector exhaust and at the surrounding boundaries. The light-round time delay is modified if the chamber walls are cold as shown in Section 2.3. Temperature measurements with thermocouples and thermochromic paint have been done in annular and tubular experiments under the same injection condition. They indicate a maximum temperature of  $900 \text{ K}$  on the outer part of the wall and  $1200 \text{ K}$  on the inner part of the wall.

These temperatures are reached after 10 min of operation. Note that the present experiments are all run under pre-heated conditions, meaning that the chamber has been run for several minutes to keep the walls at the stabilized thermal conditions. This indicates that, if the temperature conditions had an influence, the characteristic time delay would be much larger than 30 ms. On the other hand, LES calculations have proved the influence of the boundary conditions of the chamber walls on the flame shape. If the walls are considered adiabatic or isothermal, the flame shape is radically different. This subject is then still to be discussed.

In the last scenario the travelling flame branch sweeps a new injector and perturbs the flow that is exhausted by this device. This may cause a negative disturbance of the local velocity, thus reducing the airflow rate for a certain period of time. The fuel flowrate cannot be affected as the pressure loss in the fuel line is around 10 bars. It was found in Fig. 2.13 that the luminosity of the flame increased during the first milliseconds of the study. This is consistent with the airflow disturbance hypothesis as this increased luminosity may indicate that less air arrives in the combustion zone while the fuel load is the same thus augmenting the equivalence ratio and resulting in brighter flames. The relaxation of the airflow rate from its perturbed state to its initial nominal value is a function of the injector geometry and flow conditions. This will in turn induce a first delay  $\tau_m$ . Important parameters are the pressure loss in the injector and the volume of air that is perturbed by the pressure wave. A second delay is also caused by the process that brings the flame out of the injector. This second delay  $\tau_d$  is essentially governed by the absolute velocity of the flame inside the injector and by the distance that separates the flame position inside this unit from the injector exhaust section. This absolute velocity changes as the flow velocity progressively retrieves its nominal value. The total time required for switching  $\tau_s$  may then be essentially formed by the sum  $\tau_m + \tau_d$ , but there may be some additional time lag corresponding to some further fluctuations of the flame position. This scenario, in which the incoming airflow is disturbed when the travelling flame branch ignites the injector unit, seems to be the most plausible and it is investigated in section 2.8 where the time lag  $\tau_m$  is estimated. Before doing this, it is interesting to examine a process where a single injector is ignited by a travelling flame colliding head on the injection unit.

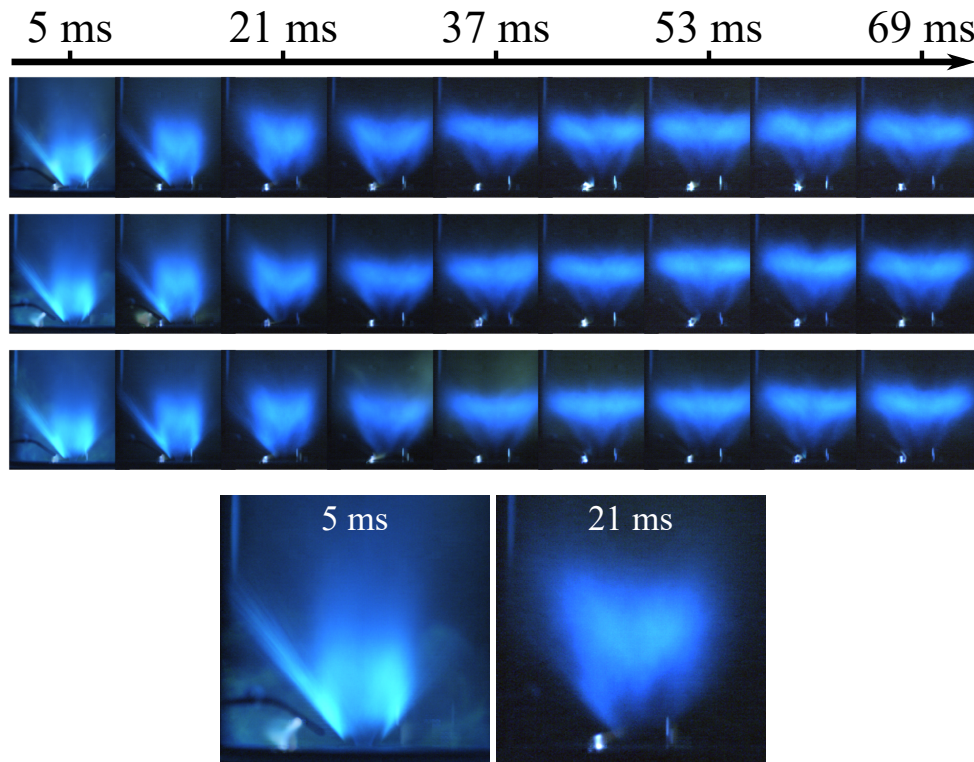


**Figure 2.16.** Top: True-color ignition sequences in SICCA-Spray. Bottom: Close-up images at  $t = 5$  and 21 ms. Extra white luminosity is due to the sparks to ignite the system.

## 2.7 Dynamics of ignition in a single injector system

The single tubular burner SICCA-Spray described in section 2.2, is equipped with the same injection system as the MICCA-Spray combustion chamber. The section is circular and designed to generate a flat velocity profile. The burner is equipped with a hot wire in the plenum, 100 mm upstream of the exit of the chamber backplane. The resulting average velocity at nominal operating conditions is  $2.06 \text{ m s}^{-1}$ .

In section 2.6 it was found that the flame from shape “A” switched to shape “B” during the ignition of the annular chamber MICCA-Spray. This feature was characterized by a time delay  $\tau_s = 30 \text{ ms}$ . The first step is to verify that the same feature is found in the single injector system. Figure 2.16 presents three successful ignition runs. The same averaging method is used as for the annular data. One can see that the flame is first attached to the burner lips and quite compact, which can be identified as an “A” shape. After roughly the same delay as in MICCA-Spray, the flame detaches and adopts a “B” shape. This is confirmed by larger chemiluminescence images displayed in the bottom of Fig. 2.16.

Next, it is interesting to examine air velocity and heat release rate measurements

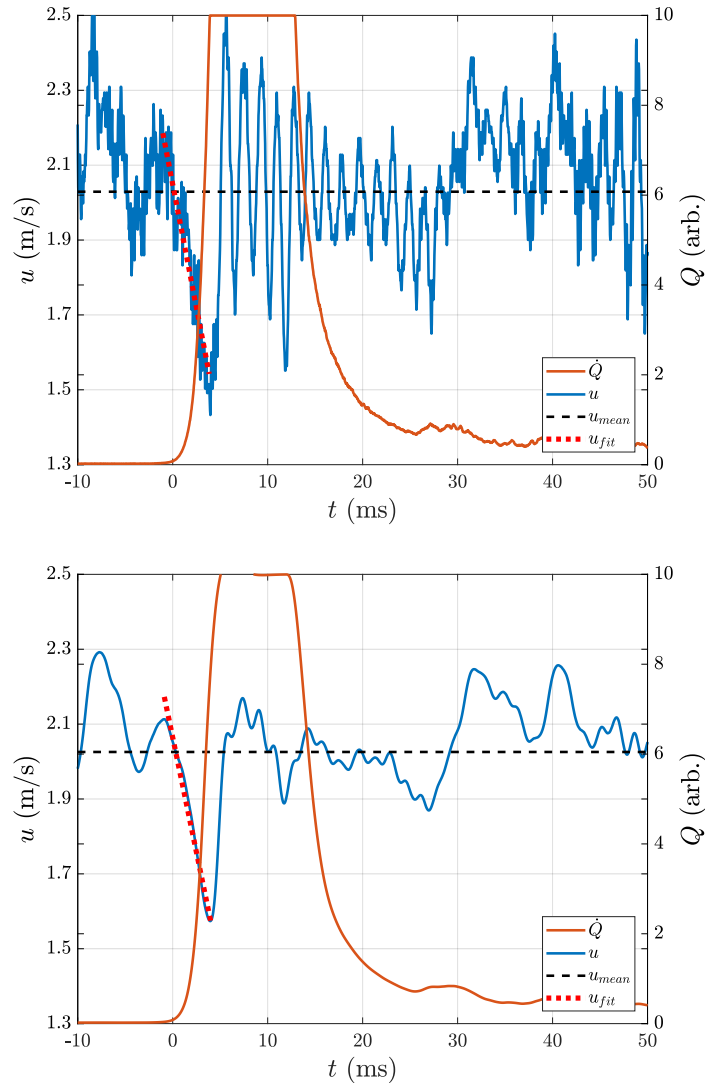


**Figure 2.17.** Top: Velocity and heat release signals during ignition of a single injector. The black dotted line corresponds to the mean velocity at nominal operating conditions. The red dotted line is a linear regression of the measured air velocity. Bottom: The signal are processed using a Butterworth low pass filter at 200 Hz, underlining the sudden decrease of the flow rate and its readjustment.

recorded simultaneously during several ignitions of the burner. Figure 2.17 presents results obtained during a period of 60 ms around the ignition time  $t = 0$  ms. It is worth noting that, even under these non-premixed conditions, one may assume that the PM signal intensity provides to some extent an indication on the combustion intensity. This is because most of the droplets are vaporized and vapor mixes with the air before burning takes place. The high luminosity during the ignition process is due

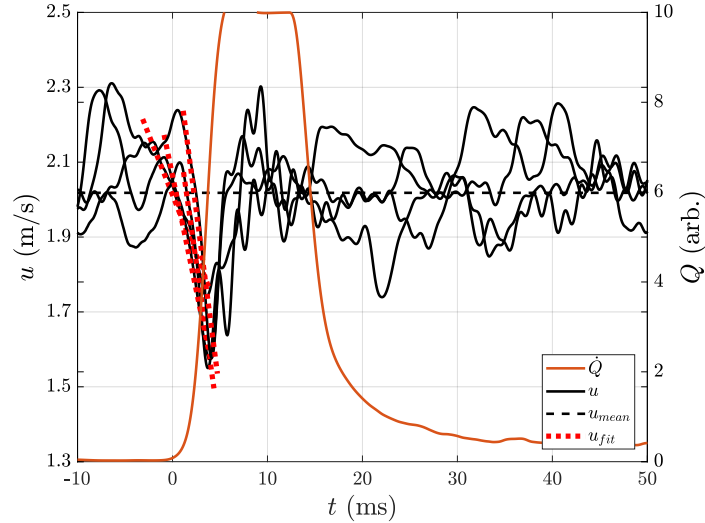


**Figure 2.18.** Velocity and heat release signals during four ignition experiments of SICCA-Spray. The signals are processed using a Butterworth low pass filter at 200 Hz, underlining the sudden decrease of the flow rate and its readjustment. The black dotted line corresponds to the mean velocity at nominal operating conditions. The red dotted lines are linear regressions of the measured air velocity.

to the burning of all the fresh mixture in the chamber resulting in a saturation of the photomultiplier signal. The relevant information is the position of the start of the ignition. One can see in the plot that, as soon as the heat release  $\dot{Q}$  begins to rise at  $t = 0$  ms, the velocity at the hot wire decreases with a constant slope. This is best seen in the bottom plot where the velocity signal has been low pass filtered to eliminate a high frequency periodic oscillation at 600 Hz already present before ignition and probably associated with one of the resonant modes of the combustor. The slope  $\alpha = -140.0 \text{ m/s}^2$  of the velocity drop is evaluated by averaging values corresponding to four ignition sequences. The minimum value of velocity roughly decreases down to  $1.5 - 1.3 \text{ m/s}^{-1}$ . The time of decay is constant and equal to 4 ms on average. The air velocity then rapidly increases and overshoots above its mean value before stabilizing once again around it. This takes approximately 20 to 40 ms, defining the time delay  $\tau_m$ , depending on the sequence. These time delays are of the same order of magnitude as that required for shape switching  $\tau_s$ . Figure 2.18 presents results of the same experience repeated four times to measure the discrepancy in the response of the hot wire. One can note that the four signals of the axial velocity have a really similar behavior.

## 2.8 A model of the injector response to light round

A framework for the injector dynamics is derived to represent changes in the air flow-rate  $\dot{m}$ . One may first consider the conservation of momentum in the injection system

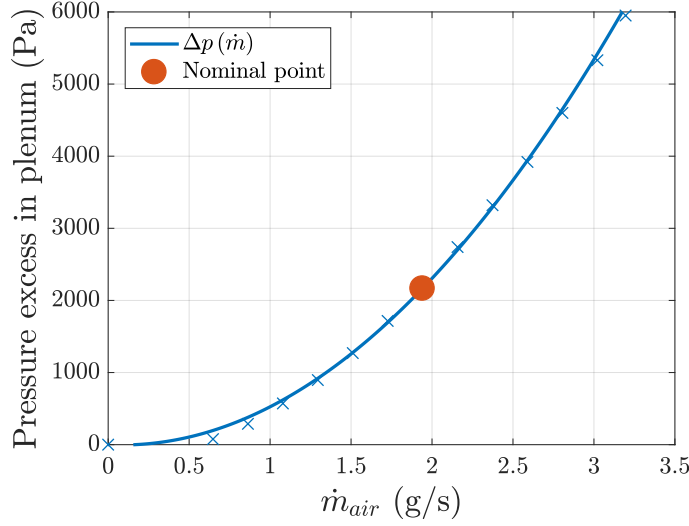


**Figure 2.19.** Pressure loss measurements in the SICCA-Spray burner. The values are fitted with a 2nd order polynomial curve. The value at the nominal operating conditions is indicated by a red dot.

and write

$$\frac{l}{A} \frac{d\dot{m}}{dt} + \frac{1}{2} \sigma \frac{\dot{m}^2}{\rho A^2} = \Delta p + \Delta p' \quad (2.1)$$

with  $l$  the length of the air column displaced by the perturbation,  $A$  the equivalent surface of the column,  $\dot{m}$  the air flow-rate,  $\sigma$  a head loss factor,  $\rho$  the air density and  $\Delta p$  the steady state pressure loss and  $\Delta p'$  represents a pressure perturbation acting on the system. This equation is considered as model M1.

Since the head loss is an important parameter of injection units, it is important to determine this quantity. As the combustion chamber is open to the atmosphere, one may consider that the pressure in the chamber is approximately equal to  $p_0 = 1013 \text{ hPa}$ . The pressure loss is then measured between the plenum and the atmosphere with a Kimo MP111 pressure-gauge. Measurements for a wide range of air flow-rates are plotted in Fig. 2.19. At nominal operating conditions, the pressure loss is  $\Delta p = 2100 \text{ Pa}$ . This value is relatively large but is quite close to typical values found in practice. Several parameters have also to be evaluated. One may take  $\rho = 1.2 \text{ kg/m}^3$  as temperature and mean pressure in the plenum are considered to be near atmospheric. The length  $l$  of the air column displaced can be estimated from the hot wire measurements. The probe is located 100 mm upstream the combustion chamber, indicating that  $l$  is at least 100 mm. By calculating the volume of air contained in the device from the hot wire to combustion chamber, one can deduced the equivalent surface  $A$  of the air column. The head loss coefficient  $\sigma$  can be evaluated from the steady

state case of Eq. (2.1).

$$\Delta p = \frac{1}{2} \sigma \frac{\dot{m}_0^2}{\rho A^2} \quad (2.2)$$

with  $\dot{m}_0 = 1.89 \text{ g s}^{-1}$  the nominal flow-rate. Knowing the other parameters, one finds  $\sigma = 8$ . Equation Eq. (2.1) can be integrated to determine the air flow-rate dynamics. The initial condition  $m_{ini} = 1.35 \text{ g s}^{-1}$  is estimated from the minimum velocity measured with the hot wire and integrated over the cross section with a flat profile. Results are shown in Fig. 2.20. The delay to reach the nominal flow-rate  $m_0$  is around 20 ms which is quite close to what is found experimentally but the oscillation of the flowrate is not recovered. To account for the oscillations of the mass-flow seen in Fig. 2.17, a second model, called model M2, may be employed that comprises a second order term in Eq. (2.3). By considering that  $\dot{m} = \rho A u$ , the model is expressed in a non-dimension fashion using the reduced velocity  $v_* = u/u_0$  with  $u_0 = 2.06 \text{ m s}^{-1}$  the steady-state velocity.

$$\frac{1}{\omega_0^2} \frac{d^2 v_*}{dt^2} + \frac{\tau}{\sigma} \frac{dv_*}{dt} + \frac{1}{2} v_*^2 = \frac{\Delta p}{\sigma \rho u_{inj}^2} \quad (2.3)$$

In this expression,  $\tau = l/u_0$  is a characteristic time,  $u_{inj} = 10 \text{ m s}^{-1}$  is an estimated mean velocity near the exit in the injector (based on LES calculations, performed by Lancien et al. (2017)) and  $\omega_0 = 2\pi f$  is the angular frequency at the frequency  $f$ . This frequency  $f$  can be estimated from the velocity measurements in Fig. 2.17. The oscillations to take into account are not those corresponding to 600 Hz, which are the effect of the acoustic resonance of the burner, but the low frequency responsible for the overshoot of the flow-rate. This frequency is around  $f = 60 \text{ Hz}$  in the different recorded ignition sequences. Equation (2.3) is integrated with the initial conditions  $\alpha/u_0 = -68$  the slope of the hot wire signal measured in the previous paragraphs and with  $u_0 = 2.06 \text{ m s}^{-1}$  the initial velocity. Results are plotted in Fig. 2.20. The system approaches the steady state operation after about  $\tau_m \simeq 30\text{-}40 \text{ ms}$ , a value that is of the order of magnitude of the delay observed in the flame structure evolution as a function of time.

These models constitute rough approaches to evaluate the important phenomena involved. Note that the delay  $\tau_m$  might not be the only delay to be responsible in the flame shape switching. As described in section 2.6, the flame first flashbacks in the injector, meaning that it reaches zones where the velocity is much lower than in the vicinity of the exit of the swirler. If we consider the absolute velocity of the flame  $v = v_0 - S_t$ , with  $v_0$  the local velocity of the flow and  $S_t$  the turbulent burning velocity,  $v$  can be less than a few meters per second. In case of a velocity decrease, the flame would likely move back upstream. After the delay  $\tau_m$ , the velocity reaches once again its nominal value but it will take another delay  $\tau_s$  for the flame to be destabilized from the low-velocity zone inside the injector to its new position, in the chamber, lifted at 10 mm.

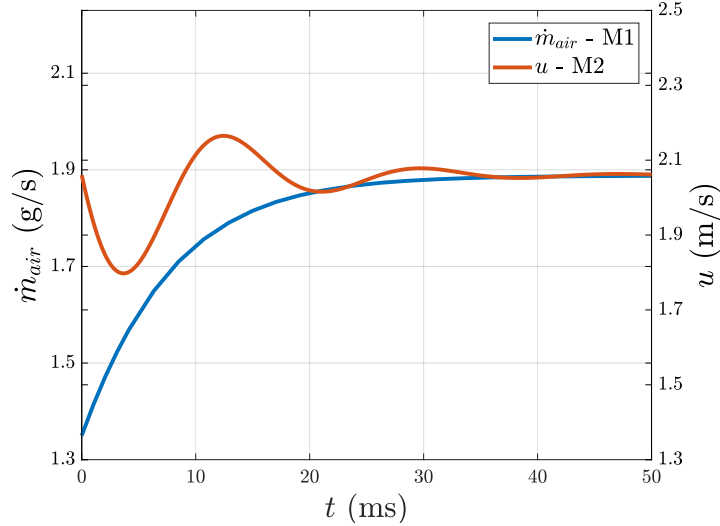


**Figure 2.20.** Models M1 results with  $m_{ini} = 1.35 \text{ g s}^{-1}$  and model M2 results with  $u_0 = 2.06 \text{ m s}^{-1}$  and  $f = 60 \text{ Hz}$ .

## 2.9 Conclusions

The dynamics of the light-round process in an annular chamber equipped with multiple swirling injectors is examined experimentally. The ignition process is specifically considered for premixed gaseous propane air and liquid n-heptane and dodecane injection. High-speed imaging carried out systematically provides a direct view of the flame as it spreads in the annular chamber enabling the characterization of the light-round delay  $\tau_l$  for a wide range of experimental conditions and indicating that the shape of the flame during light-round is similar for the three fuels. The data indicate how the time delay evolves as a function of equivalence ratio, power level and injection velocity. In general, premixed gaseous injection yields the shortest delay. For liquid fuel spray injection, the delay is shorter when the fuel is easy to vaporize (n-heptane) and it is the longest for dodecane spray injection. The data can be explained at least qualitatively by making use of correlations established for gaseous mixtures in combination with calculations and experiments on laminar flame propagation in sprays. The present experiments can be interpreted in terms of a propagation speed which mainly depends on the thermal expansion, turbulent flame wrinkling and on laminar burning velocity in the spray reactive mixture. This investigation also focuses on the dynamics of the flame during light-round process in annular combustors and specifically considers the evolution of the flame structure established by each injector after it is swept by the travelling flame branch. PIV measurements of the flame wrinkles give access to the behaviour of the travelling flame. It has been shown that it exists two major zones of propagation. The first has a pure horizontal component, moving stuck to the backplane. The second is expanding toward the exit of the com-

bustor. These fine images also provide information on the wrinkling of the flame with a mean cell size of 3.2 mm. It is then shown that the travelling flame has a strong effect on the flow well before it reaches the point of observation. This is due to the piston effect associated with the volumetric expansion induced by the flame. The flow in front of the flame is set into motion and the spray of droplets delivered by a given injector is blown sideways. A second observation indicates that the azimuthal sweeping of an injector by the travelling combustion wave initiates a flame at this injector that is initially penetrating the body of this unit. This flame is then expelled from this region and after a certain delay anchors at its final position. This dynamical effect is of practical importance because it indicates that prior to the final stabilization at a distance from the injection unit, the flame takes positions that can have detrimental effects on the injection units. Of course, this is only a model scale version of what is being used in real systems but it shows that some attention needs to be given to the injector dynamics as it is swept by the combustion wave travelling in the chamber. Similar features are observed when a single injector is ignited by the head on collision of a combustion wave. The dynamics of the injector response is then examined by considering a simplified model representing the mass flow rate evolution after an initial disturbance induced by the sweeping or head on colliding combustion wave. The mechanism that is inferred is that the combustion wave induces a large negative disturbance in the mass flow rate delivered by the injector reducing the velocity in the unit and allowing the penetration of the flame front. The injector then responds to this perturbation by progressively retrieving the steady state mass flow rate and the flame is expelled from this unit. Calculations based on a simplified model tend to retrieve this behavior. The model is admittedly highly idealized and needs further improvements if one wishes to get quantitative matching with data, but it supports the idea that the initial disturbance produced by the travelling or colliding combustion wave is responsible for the time evolution of the flame established by each injection unit.



## Chapter 3

# Flame dynamics in a spray swirl annular combustor

*This chapter reports experiments carried out in the MICCA-Spray combustor equipped with 16 swirl spray injectors. Liquid n-heptane is injected by simplex atomizers. The combustion chamber is formed by two cylindrical quartz tubes allowing full optical access to the flame region and it is equipped with twelve pressure sensors recording signals in the plenum and chamber. A high-speed camera provides images of the flames and photomultipliers record the light intensity from different flames. For certain operating conditions, the system exhibits well defined instabilities coupled by the first azimuthal mode of the chamber at a frequency of 750 mm. These instabilities occur in the form of bursts. Examination of the pressure and the light intensity signals gives access to the acoustic energy source term. Analysis of the phase fluctuations between the two signals is carried out using cross-spectral analysis. At limit cycle, large pressure fluctuations of 5000 Pa are reached, and these levels persist over a finite period of time. Analysis of the signals using the spin ratio indicates that the standing mode is predominant. Flame dynamics at the pressure anti-nodal line reveals a strong longitudinal pulsation with heat release rate oscillations in phase and increasing linearly with the acoustic pressure for every oscillation levels. At the pressure nodal line, the flames are subjected to large transverse velocity fluctuations leading to a transverse motion of the flames and partial blow-off. Scenarios and modelling elements are developed to interpret these features.*

### 3.1 Introduction

It has been demonstrated that a considerable research effort has concerned combustion dynamics issues with much of this work focused on problems raised by gas turbines and aeronautical engines. These machines operate in a lean premixed combustion mode to reduce NO<sub>x</sub> emissions, the flames are more compact, the power density is augmented and the damping rate is reduced, a combination of factors that promotes

instabilities. In addition, the combustor diameter is in most cases the largest combustor dimension so that instabilities are most often coupled by azimuthal acoustic modes. Under certain conditions this leads to unacceptable levels of pressure oscillations in the system and this has become an essential issue in the design of gas turbine combustion systems. To investigate this class of phenomena it is important to consider annular combustor geometries featuring azimuthal resonances. This has given rise to a variety of analytical investigations including time domain descriptions based on modal expansions and frequency domain representations relying on flame transfer functions or describing functions. Among the more recent works, one may refer to some of the many works of these teams: [Noiray et al. \(2011\)](#), [Camporeale et al. \(2011\)](#), [Campa and Camporeale \(2014\)](#), [Bauerheim et al. \(2014\)](#), [Bauerheim et al. \(2014\)](#), [Ghirardo et al. \(2015\)](#), [Ghirardo et al. \(2016\)](#), [Laera et al. \(2016b\)](#) and [Poinsot \(2016\)](#). Many models in these chapters consider a nonlinear relationship between heat release and pressure fluctuations in the chamber with a saturation at high amplitude (see [Schuermans et al. \(2006\)](#), [Noiray et al. \(2011\)](#) and [Ghirardo et al. \(2016\)](#)). [Noiray and Schuermans \(2013\)](#) found that limit cycles coupled to a spinning mode prevail in perfectly axisymmetric systems with intermittent transitions to standing modes due to turbulence. This behavior may be characterized by a spin ratio defined by [Evesque et al. \(2003\)](#) and [Bourgouin et al. \(2013a\)](#). [Ghirardo and Juniper \(2013\)](#) introduced additional effects of transverse acoustic disturbances in their model and found that standing modes may prevail for systems featuring large transverse flow oscillations. Note that standing mode may prevail for the nonlinear response depending on transverse velocity amplitude. The limit cycle nodal line will always depend on the initial condition and there is no reason that it stays the same throughout the experiment (see also [Saurabh and Paschereit \(2017\)](#) and [Saurabh et al. \(2017\)](#)).

Annular system combustion dynamics has also been examined with modern large eddy simulation techniques. [Staffelbach et al. \(2009\)](#) carried out an informative simulation of combustion instabilities in an annular chamber demonstrating that when coupling is induced by an azimuthal mode, the flames located near the pressure antinode strongly oscillate in the axial direction while flames located near the pressure nodal line are periodically displaced in the lateral (azimuthal) direction. Simulations reported by [Wolf et al. \(2012\)](#) and [Wolf et al. \(2012\)](#) showed that phenomena of flashback and lift-off could occur under the effect of large amplitude pressure modes and that fluctuations in the heat release rate increased linearly with the level of pressure fluctuations as shown by [Wolf et al. \(2012\)](#). To validate these theoretical and numerical investigations, it is important to have experimental data at hand and more specifically to examine the dynamics of flames in annular combustor configurations under azimuthal modal coupling. The present chapter reports such data in the case the MICCA-Spray annular combustion equipped with multiple swirling spray injectors. A basic description of the set-up can be found in Chapter 1 and details are given in Section 3.2.

It is worth examining at this point what has been found in simpler configurations.

One may for example simulate the effects of azimuthal waves in annular combustion chambers by considering a linear setup like those used by O'Connor and Lieuwen (2011) and O'Connor and Lieuwen (2012) or by Lespinasse et al. (2013). In both cases, a premixed "V" flame is placed in a transverse acoustic field. At the pressure antinode, the flame is essentially deformed in the axial direction, it exhibits nonlinear features and some lateral ejections of fluid are observed at the injector outlet by Baillet and Lespinasse (2014). At the pressure node, the flames oscillate in the transverse direction and if the flow is swirling, one observes helical perturbations of the reactive front as a result of interaction of the acoustic field with shear regions and with the vortex breakdown process as observed by O'Connor and Lieuwen (2011) and O'Connor and Lieuwen (2012). The influence of transverse waves acting on the upstream side of the injector unit is analysed by Hauser et al. (2011). An azimuthal wave established in the plenum of an annular combustor induces a rotational motion of the flames at the injector outlets, associated to asymmetric perturbations of the velocity field in the injector nozzles. The robustness of flames subjected to a transverse acoustic field is investigated by Lespinasse et al. (2013). They showed that gaseous "V" flames located at a pressure node were much more sensitive to blow-off than the same flames placed at a pressure antinode. There are however yet no detailed investigation of the response of spray flames subjected to a transverse acoustic field.

There is a small number of experiments on laboratory scale annular configurations allowing optical access to the combustion region and reproducing, in an idealized fashion, conditions encountered in gas turbines and jet engines (see Worth and Dawson (2013b), Worth and Dawson (2013a), Bourgouin et al. (2013a), Bourgouin et al. (2015), Bourgouin et al. (2015)). In these combustors, spinning or standing modes were observed, usually with transitions between the two types of modes. With premixed flames, anchored on a bluff-body, Dawson and Worth (2014) studied the dynamics of the reactive layers depending on their position relative to the azimuthal mode. Although the flames were close to each other, and therefore strongly interacting, flames located near a pressure antinode featured an axial motion, while flames located at a pressure node exhibited a strong lateral motion. To facilitate the observation of standing modes, Worth et al. (2016) installed an acoustic forcing system in the combustion chamber to fix the nodal line. In Worth and Dawson (2013b) Worth and Dawson (2013a), Bourgouin et al. (2013a) and Dawson and Worth (2014), azimuthal instabilities were induced by creating strong interactions between adjacent reactive layers. However other experiments indicate that a small relative spacing between the injectors is not necessarily required to trigger azimuthal instabilities, as shown in studies carried out with matrix burners by Bourgouin et al. (2015), Bourgouin et al. (2015) and as evidenced by the present investigations in this manuscript. Additional references dealing with combustion instabilities and interactions with transverse acoustic modes are included in O'Connor et al. (2015). It is interesting to note that experiments carried out with swirling injectors by Bourgouin et al. (2013a) and Worth and Dawson (2013a), featuring significant pressure losses in the injection unit generally lead to azimuthal instabilities localized in the combustion chamber, while investiga-

tions carried out with matrix injectors (Bourgouin et al. (2015) and Bourgouin et al. (2015) for example), characterized by lower pressure losses indicate that azimuthal instabilities are mainly driven by the plenum. In the annular chamber MICCA equipped with matrix injectors studied in Bourgouin et al. (2015) and Bourgouin et al. (2015) instabilities arise over a large domain of operation, whereas with swirling injectors, the system is stable over a broad range of operating points. Bourgouin et al. (2013a) showed that the unstable areas are narrow, probably because of the head losses in the injection elements.

This brief review indicates that there are many issues that need further investigation of combustion instabilities coupled by azimuthal modes in annular systems. As all laboratory scale experiments were carried out with premixed flames, it is important to examine cases where the fuel is injected as a spray. Many of the previous studies were conducted with closely packed injectors, and therefore with interacting flames but this does not correspond to the real situation found in industrial combustors. The quantitative evaluation of the flame dynamics with respect to the amplitude of the pressure oscillations is not available but the corresponding data would be of considerable value for theoretical model validation. The levels of oscillations that have been achieved so far in laboratory scale facilities remain modest and it would be important to gather data corresponding to higher pressure amplitudes. The present investigation is intended to deal with the previous issues. Experiments are carried out with liquid fuel spray injection. The annular combustor features combustion instabilities which are mainly of the standing type allowing detailed studies of the dynamics of flames depending on their azimuthal position relative to the nodal line.

This chapter begins with rapid details on the experimental configuration in section 3.2. The characterization of the flow on the single burner SICCA-Spray is reported in section 3.3. Typical instability signals recorded by microphones and a photomultiplier are analysed in section 3.4. The motion of flames located in the vicinity of the pressure antinode and near the pressure nodal line are also considered in this section. When the pressure amplitude reaches high levels it is found that the flames located near the pressure nodal lines may be blown out, a process that may have considerable technical consequences. This point is examined in section 3.5 and a model is proposed for this mechanism in section 3.6.

## 3.2 Experimental set up

The MICCA-Spray annular system, described in Chapter 1, is shown in Fig. 4.1, left. The combustor walls allow adapting the impedance of the system to obtain self-sustained instabilities as in Worth and Dawson (2013b), Worth and Dawson (2013a) and Bourgouin et al. (2013a). The inner wall is made of a quartz tube with a length of 200 mm and a diameter of 300 mm. The outer wall is made of two parts, a 200 mm long cylindrical quartz tube and a 400 mm metal piece. Both pieces share the same inner diameter of 400 mm. The air flow, injected in the plenum at ambient pressure and

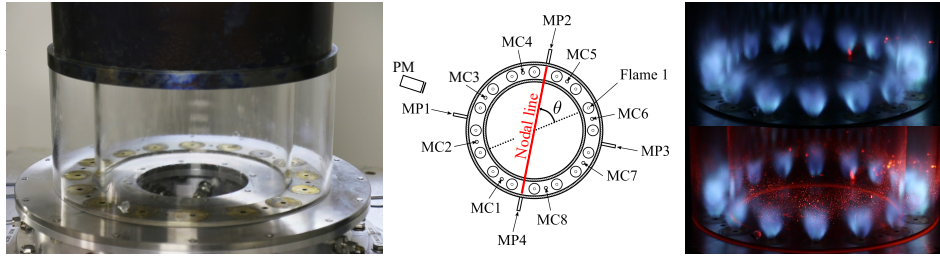


**Figure 3.1.** Left: photograph of the MICCA-Spray annular combustor with sixteen liquid spray injectors. The chamber comprises 200 mm quartz tubes and a 400 mm metal cylindrical tube on the outer part of the annulus. The quartz tubes allow full visualization of the flames in the annulus. Middle: Schematic view of the chamber backplane showing the locations of the photomultiplier (PM) and of the different microphones “MCx” in the chamber and “MPx” in the plenum. Flames are numbered from Flame 1 in the clockwise direction. The fixed nodal line position is indicated in red. Right: Direct true-color photograph of the annular chamber showing the influence of the wall temperature. The chamber is under steady operation at a bulk velocity  $U_b = 46 \text{ m s}^{-1}$ , a global equivalence ratio  $\phi = 0.86$  and a total power of  $\mathcal{P} = 113 \text{ kW}$ . Top: flame configuration after a few seconds of operation. Bottom: flame configuration after 10 minutes of operation.

temperature, is set in a rotating motion in the injector by a tangential swirler with six 4.5 mm diameter holes (notably larger than the study on ignition described in Chapter 2). The injector is terminated by the same convergent end piece with an exit diameter  $d = 8 \text{ mm}$ . Liquid n-heptane is injected in the chamber by the same simplex atomizer to establish a hollow cone spray in the chamber. In the present experiments n-heptane fuel is chosen for its high volatility. Heavier fuel like dodecane or even kerosene could be used in future studies. Ignition is initiated by the spark plug positioned approximately at 10 mm from the center of one injector and remaining roughly at the same position during the experiment and for all the different tests.

The system is equipped with twelve microphones and a photomultiplier (PM) as shown in Fig. 4.1, middle. This optical sensor called PM in the following and equipped with an OH\* filter can be placed around the annulus to follow the dynamics of one flame using a spatial filter. It provides a measure of the light intensity radiated by excited hydroxyl radicals. In the case of premixed flames, this signal can be interpreted as a measure of the heat release rate. The case at hand is not premixed but we will nevertheless assume that the PM signal intensity provides to some extent an indication on the combustion intensity. In this set of experiments, the PM is positioned close to the pressure anti-node. Optical and pressure signals are recorded simultaneously. Images of the combustion region are also recorded by two cameras. One CCD camera provides images of the full annular combustor while the second, a high speed intensified camera, yields closer views of the flames for a detailed analysis of the flame motion. The fast motion of the flame during combustion instabilities is observed with a high

speed intensified CMOS camera APX-i2 ( $512 \times 256$  px) providing an 8-bit grey level resolution. This unit was set to record images at a sampling rate of 6000 frames per second, with a shutter duration of  $166 \mu\text{s}$ . In each test, 49,152 images are recorded. The camera amplifier gain remains constant in all experiments. Acoustic pressure is measured by 1/4 inch Brüel & Kjær microphones at a sampling rate  $f_s = 32,768$  Hz and the corresponding data are recorded over a period of 8 s. The signals shown in this chapter are never filtered. Eight of the microphones (designated as “MC”) are used to measure the pressure at the chamber backplane. The pressure taps drilled in the annular chamber base (Fig. 4.1, middle) are located at equal distance from two injectors and connected to straight metallic waveguides. The distance where the microphone is placed defines a time lag  $\tau_{m-b} = 0.46$  ms when the combustion chamber has been running for 15 minutes, and the temperature in the plenum reaches  $55^\circ\text{C}$ . This delay between the chamber and microphone is taken into account to synchronize the acoustic pressure and heat release rate signals with the camera images. Four additional microphones (designated as “MP”) are plugged on the plenum. Note that the pressure signals and the flame images can be synchronized using the external signal of the camera.

Flame shapes in the annulus are shown in Fig. 4.1, right, adopting an “M” shape, with no mutual interaction and slightly lifter 8 mm from the chamber backplane. Whatever the effort made, it was not possible to obtain perfectly symmetric and uniformly balanced injectors due to the small differences in pressure loss induced by the sixteen atomizers. Wall temperature effects can be seen in Fig. 4.1 with a photograph taken just after the ignition (top) and after 10 minutes of operation (bottom). The MICCA-Spray chamber can be operated over a broad range of conditions but instabilities are found for specific injection parameters. Experiments are then carried out for a global equivalence ratio which ranges from  $\phi = 0.8$  to  $0.9$ . The power of the chamber varies from  $\mathcal{P} = 105$  to  $120$  kW and the bulk velocity calculated with the injector diameter  $D = 8$  mm ranges from  $U_b = 45$  to  $50$   $\text{m s}^{-1}$ . The corresponding Reynolds number based on the injector exit diameter varies from 25,800 to 28,700. It is interesting to quickly estimate the resonant frequency of the annular combustor at which self-sustained instabilities could be triggered. The chamber has a perimeter  $P = 2\pi R \simeq 1.1$  m and a length  $l = 200$  mm. The backplane of the chamber is considered as a solid wall and the top of the chamber is an open end. We make the hypothesis of a mean temperature of 1300 K equivalent to a global speed of sound  $c = 720$   $\text{m s}^{-1}$  in the entire chamber. The first resonant frequency  $f$  can be estimated as follows  $f = \left[ (c/P)^2 + (c/4l)^2 \right]^{1/2} = 746$  Hz. This frequency is close to that observed experimentally as it will be shown in the following.

### 3.3 Single burner characterization

The SICCA-Spray burner is used to characterize the aerodynamic and spray structures with laser optical tools. The burner is equipped with a 70 mm diameter and 200 mm

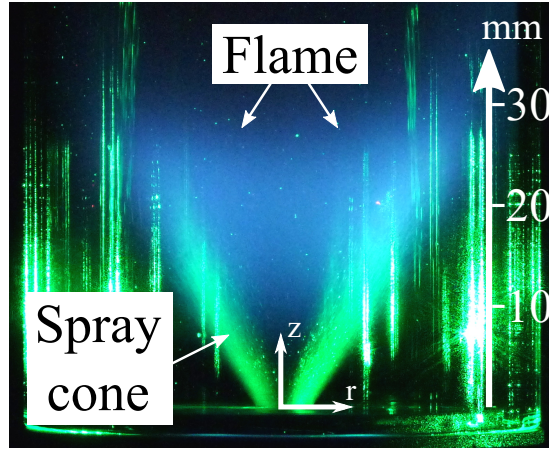


**Figure 3.2.** Vertical tomography of the n-heptane droplet spray with flame for  $\phi = 0.86$ ,  $U_b = 46 \text{ m s}^{-1}$ ,  $\mathcal{P} = 7.1 \text{ kW}$  in the single burner setup.

long quartz tube. The total power of the single burner is close to  $\mathcal{P} = 7 \text{ kW}$ . A 9-bar pressurized fuel tank supplies the atomizer with n-heptane. An argon-ion laser at 514.5 nm is used to create vertical tomographic slices of the droplet spray under hot fire conditions. The laser slice in Fig. 3.2 shows the hollow liquid spray cone established in the chamber. Note that droplets are still present all along the combustion zone. This confirms the non-premixed two-phase character of the flame. In this image, some blue luminosity indicates that the flame develops from 8 to 30 mm from the chamber backplane.

The velocity profiles of the air flow and the n-heptane droplet diameters in the single burner are determined with a Phase Doppler Anemometer (PDA) under cold flow conditions. Measurements are carried out without confinement to avoid laser beam deflections due to wall wetting and to the cylindrical shape of the quartz. Measurements with confinement under hot fire conditions confirm that this procedure is adequate. Figure 3.3 displays the three velocity profiles of the air flow  $\{U_r, U_\theta, U_z\}$  measured at  $z = 2.5 \text{ mm}$  above the injector outlet for nominal injection conditions, where the chamber is the most unstable. No fuel is injected at this stage and LDA measurements are based on seeding oil droplets (diameter  $d_{10} < 2 \mu\text{m}$ ) giving access to the entire air dynamics. Mean data are shown for 50,000 oil droplets to ensure statistical convergence. High axial velocities are observed with a peak  $U_z \simeq 55 \text{ m s}^{-1}$ . A well defined recirculation zone is present in the center of the chamber. The air flow also features a sizable azimuthal component. The measured velocity profiles used to determine the swirl number provide a value  $S = 0.55$ . Figure 3.4 shows the diameter profiles of the n-heptane droplets injected by the liquid atomizer within the swirling air flow field shown in Fig. 3.3. Measurements are carried out at  $z = 2.5 \text{ mm}$  from the injector outlet. At  $r = 5 \text{ mm}$ , i.e. in the dense zone of the spray (see Fig. 3.2), the mean diameter  $d_{10}$  is  $\simeq 8 \mu\text{m}$ . At the same location, the Sauter Mean Diameter (SMD)  $d_{32}$

is  $\simeq 30 \mu\text{m}$ . These relatively small diameters confirm the good atomization provided by the liquid fuel injector.

It is worth estimating the vaporization time  $\tau_v$  corresponding to these droplet diame-

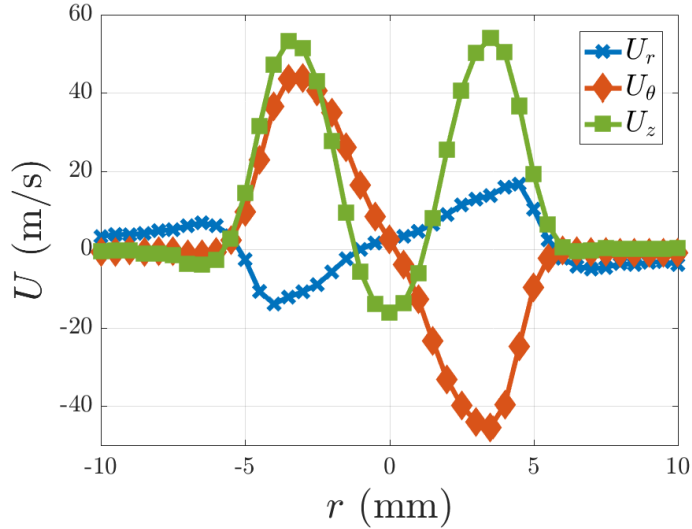


**Figure 3.3.** Mean air velocity profiles  $U_r$ ,  $U_\theta$  and  $U_z$  measured at  $z = 2.5 \text{ mm}$  for a nominal air flow rate  $\dot{m}_{air} = 2.79 \text{ g s}^{-1}$  (corresponding to  $U_b = 46 \text{ m s}^{-1}$ ).

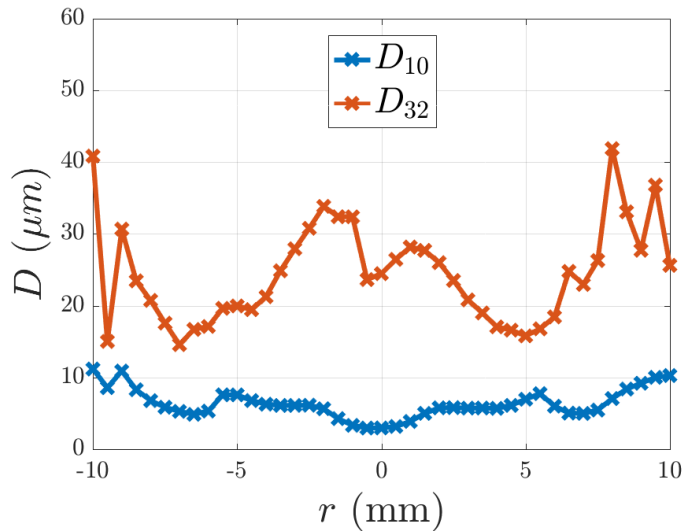


**Figure 3.4.** n-Heptane droplet diameter profiles  $d_{10}$  and  $d_{32}$  in cold flow conditions without confinement,  $2.5 \text{ mm}$  above the injector outlet for nominal flow rates  $\dot{m}_{fuel} = 0.16 \text{ g s}^{-1}$  and  $\dot{m}_{air} = 2.79 \text{ g s}^{-1}$  (corresponding to  $U_b = 46 \text{ m s}^{-1}$ ).

ters. This can be based on the  $d^2$  law proposed by [Ranz and Marshall \(1952\)](#):

$$\tau_v \simeq \frac{1}{8} \frac{c_p^g}{\lambda_g} \rho_l d^2 \frac{1}{\ln(1 + B_T)} \quad (3.1)$$

$$\lambda_g = \lambda_{g0} \left(1 + 0.276 \text{Re}^{1/2} \text{Sc}^{1/3}\right) \quad (3.2)$$

where  $c_p^g$ ,  $\lambda_{g0}$  are the specific heat capacity and heat conductivity of the gas and  $\rho_l$  and  $d$  the liquid density and droplet diameter, and Re and Sc are respectively the Reynolds and Schmidt numbers. The Spalding transfer number  $B_T = c_p^g(T_g - T_l)/L_v$  is here expressed in terms of the gas  $T_g$  and liquid  $T_l$  temperatures and latent heat  $L_v$ . These expressions account for convective effects by making use of an effective heat conductivity  $\lambda_g$  appearing in Eq. (3.2). It is standard to evaluate the gas properties by the 1/3-2/3 rule  $\bar{T} = (1/3)T_g + (2/3)T_l$ . Figure 3.5 shows vaporization time estimates  $\tau_v$  and distances of vaporization  $l_v$  for different gas temperatures  $T_g$ . The

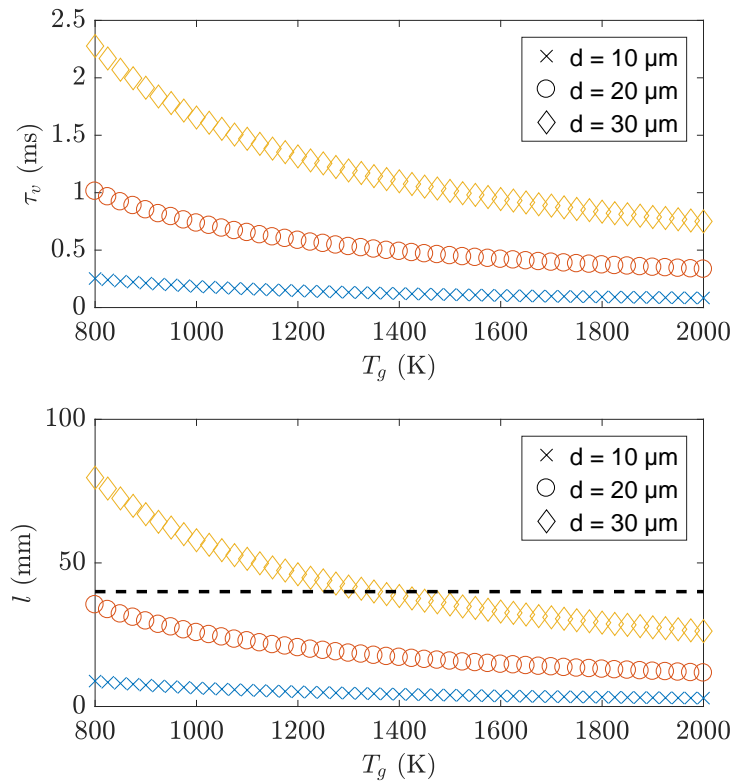


**Figure 3.5.** Estimated vaporization times  $\tau_v$  and vaporization distances  $l_v$  for different gas temperatures  $T_g$  and for three droplets diameters  $d$ . The black dotted line in the second plot corresponds to the distance from the injection point to the quartz wall where n-heptane droplets impact the confinement (approximately 40 mm).

reference temperature  $T_l = 300$  K is kept constant. Assuming that the gas and liquid temperatures are  $T_g = 1000$  K,  $T_l = 300$  K and that the velocity differential between the droplets and flow is small, one obtains  $\tau_v \simeq 0.18$  ms for droplets with a diameter of  $10 \mu\text{m}$  and a value four times larger for droplets with a diameter of  $20 \mu\text{m}$ . Considering the latter droplets, their vaporization delay combined with the chemical time yields a characteristic combustion delay  $\tau_{cd} = \tau_v + \tau_c$  which may be estimated to be about  $0.5$  ms. It will be seen that this delay is of the order of one half acoustic period  $\tau_{cd} \simeq T/2$ , a condition that often leads to an unstable behavior.

### 3.4 Analysis of the self-sustained instabilities

The MICCA-Spray combustor features self-sustained instabilities with acoustic peak pressure levels of up to  $3500$  Pa for a broad range of operating conditions. For specific injection conditions, the peak level may reach up to  $6000$  Pa and this then triggers partial blow-off of the annular combustor. This point is examined in section 3.5.

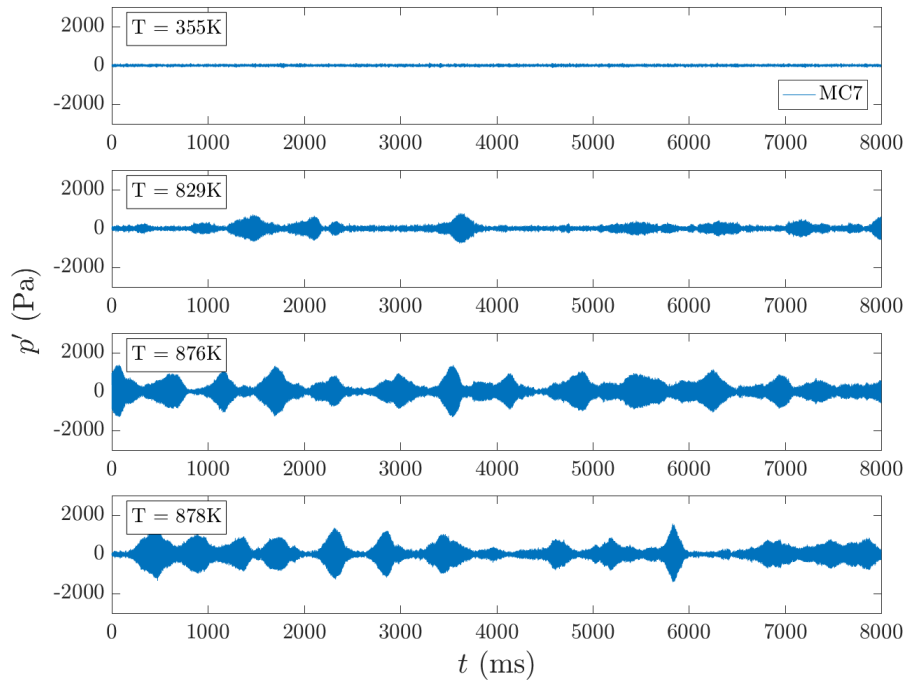


**Figure 3.6.** Influence of the wall temperature on the acoustic pressure in the chamber (only microphone “MC7” is plotted). The temperature of the wall is indicated on the top left of each plot. The operation conditions have been kept constant at  $\phi = 0.85$  and  $\mathcal{P} = 110$  kW.

### Influence of the wall temperature

The analysis of combustion instabilities is carried out on the annular combustor with hot walls, as typified at the bottom in Fig. 4.1, right. The self triggering of the instabilities depends on the wall temperature. Figure 3.6 shows the acoustic pressure in the chamber during 8 s records corresponding to different wall temperature conditions. The temperature is measured using a surface K-thermocouple placed on the external side of the outer quartz tube, between two injectors, 40 mm above the back of the chamber. While no pressure fluctuations can be seen when the chamber walls have a temperature under 800 K, one finds that, as soon as the temperature reaches 830 K, instabilities are self triggered. The maximum acoustic level in the chamber increases until the wall temperature is stabilized around 900 K after 10 minutes of operation. In the next experiments, wall temperature equilibrium is reached before the data acquisition.

The top plots in Fig. 3.7 show a typical record of the acoustic pressure in the chamber and in the plenum. In this test, the acoustic pressure reaches peak values of 3500 Pa

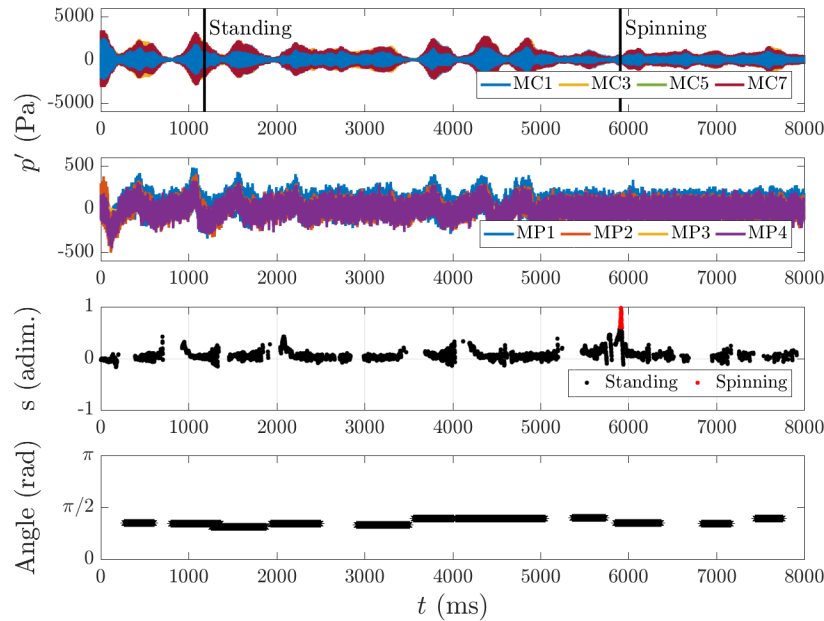


**Figure 3.7.** Analysis of a sequence with different instability modes in the MICCA-Spray combustor for  $\phi = 0.86$ ,  $\mathcal{P} = 113$  kW. Top: From top to bottom, acoustic pressure in the chamber and in the plenum (locations of the microphones “MPx” and “MCx” are indicated in Fig. 4.1, middle), associated spin ratio  $s$  and orientation of the nodal line. Bottom: zoom of the acoustic pressure in the chamber for two types of modes, standing (top) and spinning (bottom).

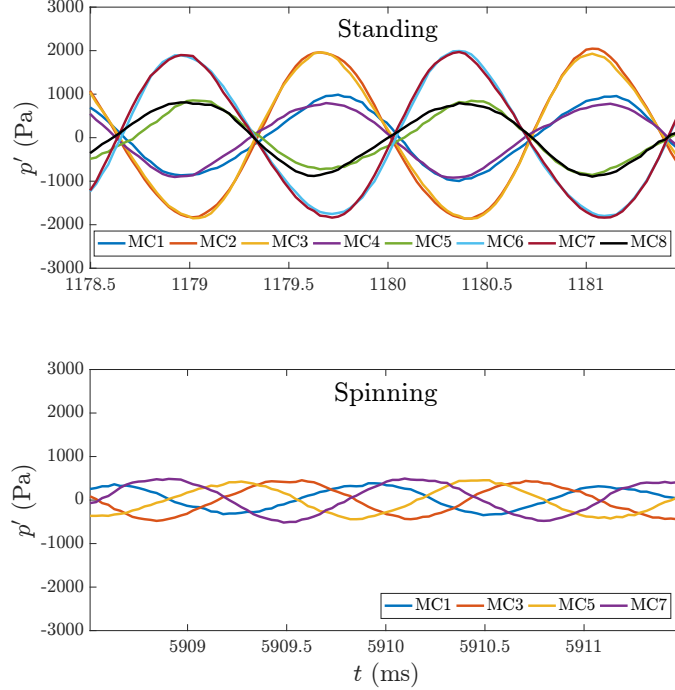


**Figure 3.7.** Analysis of a sequence with different instability modes in the MICCA-Spray combustor for  $\phi = 0.86$ ,  $\mathcal{P} = 113$  kW. Top: From top to bottom, acoustic pressure in the chamber and in the plenum (locations of the microphones “MPx” and “MCx” are indicated in Fig. 4.1, middle), associated spin ratio  $s$  and orientation of the nodal line. Bottom: zoom of the acoustic pressure in the chamber for two types of modes, standing (top) and spinning (bottom).

in the chamber and peak values of 500 Pa in the plenum. The modes triggered in this annular combustor with swirled spray injectors are mainly chamber modes as in previous experiments carried out with premixed propane and air showed by [Bourgouin et al. \(2013a\)](#). The frequency of oscillation when the mode is established is around 750 Hz (see Fig. 3.9).

The spin ratio  $s$ , defined in [Evesque et al. \(2003\)](#) and modified in [Bourgouin et al. \(2013a\)](#), is a dimensionless number that characterizes azimuthal modes. This ratio is obtained by decomposing the acoustic pressure in two waves spinning in the counter-clockwise and clockwise directions with complex amplitudes  $a$  and  $b$  (see Appendix B) and can then be expressed as:

$$s = \frac{|a| - |b|}{|a| + |b|} \quad (3.3)$$

It is used to determine if the mode is standing ( $s = 0$ ) or spinning in the counter-

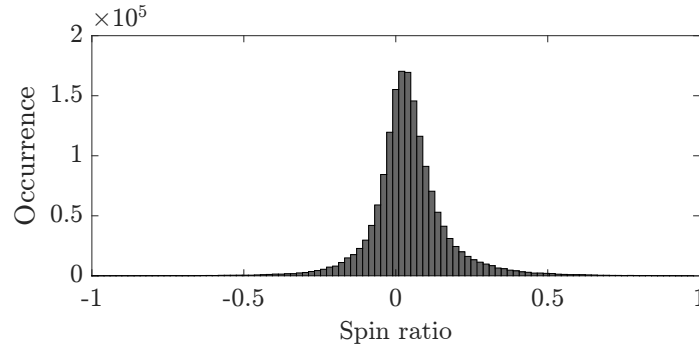


**Figure 3.8.** Spin ratio distribution calculated over 121 bursts.

clockwise direction ( $s = +1$ ) or in the clockwise direction ( $s = -1$ ). In the studied sequence, the standing mode prevails but a spinning mode is triggered for a short period of time near  $t = 6000$  ms. A zoom on the acoustic pressure in the chamber is provided when the mode is standing (top right of Fig. 3.7) and when the mode is spinning (bottom right of Fig. 3.7). For the standing mode, microphones MC3 and MC7 are in phase opposition. The amplitude slowly decreases for the other microphones meaning that they tend to be close to the pressure node. This mode adopts a nearly perfect first azimuthal (1A) transverse structure. For the spinning mode (Fig. 3.7, bottom right),  $90^\circ$  spaced microphones are in phase quadrature and every signal has the same amplitude. Note that the pressure level for the standing mode is at least 4 times greater than that recorded for the spinning mode. During the previous sequence, the chamber mode is mainly standing as can be deduced from the spin ratio plot in Fig. 3.7. The nodal line position is determined at several instants in time. The orientation of this line is determined by reconstructing the acoustic mode in the chamber for a large number of angular positions and determining the angle corresponding to the minimum amplitude. One can see in the plot that the nodal line is naturally fixed at  $70^\circ$  and does not spin during the entire experiment.

Figure 3.8 shows the distribution of the spin ratio for 121 different bursts confirming the predominance of the standing mode. One should note that, in a configuration with an even number of injectors like the MICCA-Spray chamber, the nodal line will always lie between two injectors. It is at this point not easy to say why the standing mode is much more probable than the spinning mode but one may propose a few explanations. One possibility could be that the standing mode features a larger growth rate than the spinning mode thus promoting the standing mode. This possibility is demonstrated by calculations done by Laera et al. (2016a) and carried out by combining the flame describing function with a Helmholtz solver in an analysis of the MICCA combustor dynamics equipped with gaseous laminar matrix injectors. Of course the present configuration differs from that investigated in Laera et al. (2016a) but the conclusion may hold. Another reason may be linked to large transverse velocity fluctuations as will be revealed later, a feature which has been shown to promote standing

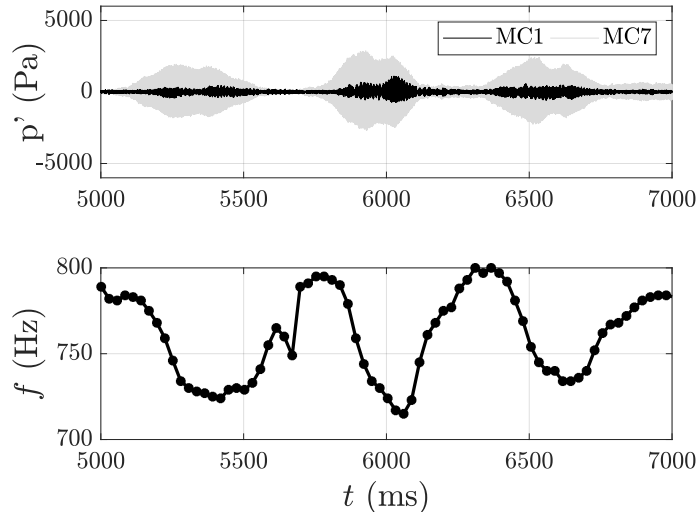


**Figure 3.9.** Top: acoustic pressure in the chamber over two different bursts recorded by MC1 (blue) and MC7 (red). Bottom: evolution of the instability frequency during the burst. Calculations are made for sections of 27 ms of oscillations corresponding to approximately 20 periods with a spectral resolution  $\Delta f = 1$  Hz.

patterns by [Ghirardo and Juniper \(2013\)](#). The last possibility is that the system is not fully symmetric because there are small differences between the flames due to small differences in the atomization process that can be responsible for this prevalence of the standing mode as mentioned in [Noiray et al. \(2011\)](#). To verify that this break in symmetry is influential, the azimuthal position of the eight injectors neighboring the nodal line were exchanged with the eight injectors neighboring the anti-nodal line. This resulted in a  $90^\circ$  rotation of the nodal line thus underlining the importance of the injector behavior on the mode shape in annular combustors. The tests confirm that the position of the nodal line is related to the inhomogeneity in the flame repartition.

### Frequency shift during mode growth and decay

Note that instabilities develop in the form of long bursts of 100 to 500 ms corresponding to  $\simeq 75$  to 325 cycles of oscillation in [Fig. 3.7](#). The occurrence frequency of these bursts is close to 1.5 Hz, no matter the operating conditions or the mean acoustic pressure in the chamber. Three bursts of a signal similar to that plotted in [Fig. 3.7](#) are analysed to track the evolution of the frequency during the growth and subsequent decay of the mode. The instability frequency in [Fig. 3.9](#) is first stable around 800 Hz when the mode begins to grow. As the mode grows to reach a limit cycle, the frequency drops progressively to 720 Hz. This underlines the nonlinear behavior of the flame dynamics as shown in [Noiray et al. \(2008b\)](#). The phase between the heat release rate and the acoustic pressure will be investigated in the next section. After this decrease, the frequency stabilizes as the mode is at limit cycle for a short period of time and rapidly starts to decay. At the end of the decay, the frequency increases to get back

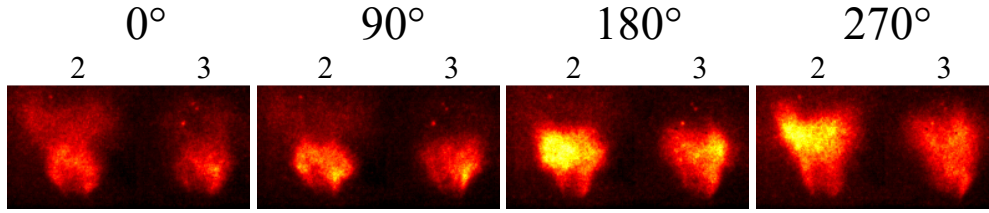


**Figure 3.10.** Light emission of two flames for  $\phi = 0.84$ ,  $\mathcal{P} = 112\text{ kW}$  around the anti-nodal line during a full cycle of oscillation. Images are averaged over four cycles. Yellow and dark red respectively correspond to high and low light emission levels.

to approximately 800 Hz. This behavior can then be observed for the next two bursts shown in this Figure. Since the combustion process is mainly coupled by a standing mode, it is natural to observe the flame dynamics at the nodal and anti-nodal lines. As described before, the nodal line is fixed by the injector inhomogeneities. This eases recording the flame behavior at different positions with respect to the nodal line.

#### Flame dynamics at the anti-nodal line

The anti-nodal line is where the pressure fluctuations reach their highest value and the azimuthal velocity oscillations are lowest. Flames fluctuate at the frequency of the acoustic mode. Figure 3.10 shows two flames around this line during a full cycle of oscillations. One can see that the flame motion is purely axial with large heat release rate excursions over a cycle: the brightness of the first ( $0^\circ$  and  $90^\circ$ ) and the last ( $180^\circ$  and  $270^\circ$ ) two images are radically different. The flames are highly perturbed but this does not seem to change their stability whatever the amplitude of the mode. The flame foot remains roughly the same even when the flame is slightly lifted and not anchored at the injector lips.

A photomultiplier, located as shown in Fig. 4.1, records the heat release rate fluctuations  $\dot{Q}'(t)$  of one flame close to the anti-nodal position. As indicated before, it is assumed that the signal from the photomultiplier is roughly proportional to the combustion intensity therefore to the heat release rate of the flame. This is admittedly an approximation in a situation where reactants are not premixed. Figure 3.11 shows this signal synchronized with the acoustic pressure  $p(t)$  recorded by the closest microphone (MC3). Data are processed to extract the relations between the amplitudes of  $\dot{Q}'(t)$  and  $p(t)$  and the relative phase  $\varphi$  between these two signals at the frequency  $f$  of oscillation. Three different bursts are displayed in this figure, corresponding to a small time interval in the sequence. For each burst, one can see that the phase between  $\dot{Q}'(t)$  and  $p(t)$  progressively increases from a negative value of  $-1$  rad to about zero, i.e. the two signals are then in phase, before the oscillation amplitude begins to decrease.

The relationship between root-mean-square values of relative heat release rate  $\dot{Q}'/\bar{Q}$

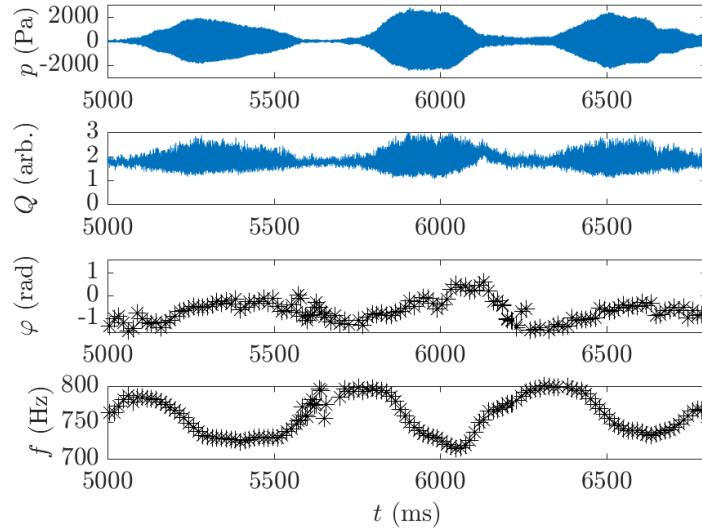


**Figure 3.11.** Acoustic pressure  $p'$  and heat release rate  $\dot{Q}$  (light intensity) fluctuations for a flame at the anti-nodal position for  $\phi = 0.85$ ,  $\mathcal{P} = 109$  kW. The evolution of the phase between  $p'$  and  $\dot{Q}$  is plotted in the last graph.

and pressure  $p'$  fluctuations is plotted in Fig. 3.12 during different bursts to see if there is any saturation of the flame response. For the five bursts of the sequence under investigation, one finds that the trend is quasi-linear and perfectly repeatable. This is in agreement with findings reported in Wolf et al. (2012) but at variance with the nonlinear amplitude saturation models proposed by Noiray et al. (2011) and modeled in the form of  $\dot{Q}' = \alpha p' - \beta p'^3$ . In the present study, the amplitude saturation cannot

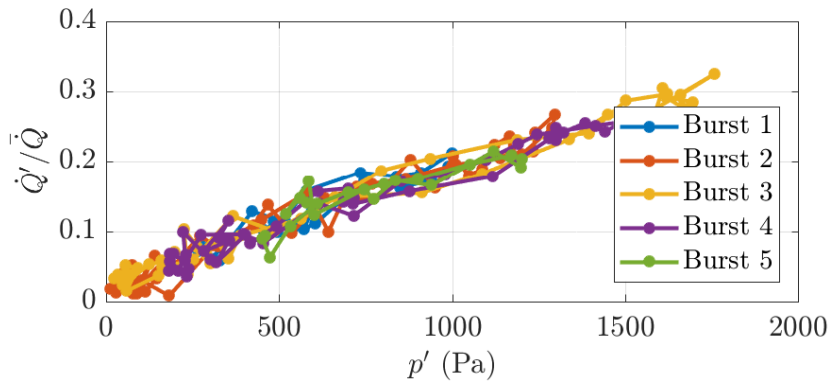


**Figure 3.12.** Relationship between  $p'$  and  $\dot{Q}'/\bar{Q}$  computed for the different bursts in the sequence.  $\dot{Q}'/\bar{Q}$  is the relative amplitude of the RMS heat release rate fluctuation and  $p'$  is the RMS value of the pressure fluctuation.

be invoked to explain the sudden decay of the modal oscillations. At the maximum of the amplitude of the bursts, the signals are almost in phase and the fluctuation of the heat release rate remains important. The Rayleigh source term in the acoustic energy balance equation is maximum when the oscillation is at its peak and when it suddenly begins to decrease.

Different scenarios may be invoked to explain this behavior:

1. The decay of the acoustic pressure during the second part of the burst might tentatively be attributed to a dissipation mechanism that has not yet been identified.
2. Another possibility is that the large frequency shift of the oscillations observed during the growth of the bursts leads to a sudden detuning of resonance, a feature observed in some nonlinear coupled oscillators.
3. An alternative is that saturation of the flame response is not due to their longitudinal motion, but rather due to their transverse response at the other injector locations.
4. Strong oscillations may also destroy the central recirculation zone (CRZ) of the swirling flow leading to important modifications of the flame dynamics and spray atomization, with, as a consequence, a suppression of the instability during some instants.

### Flame dynamics at the nodal line

The second remarkable position in the annulus during a standing mode is at the nodal line where the pressure fluctuations are the lowest and the transverse velocity oscillations are the highest. Figure 3.13 presents a full cycle of oscillation for three flames

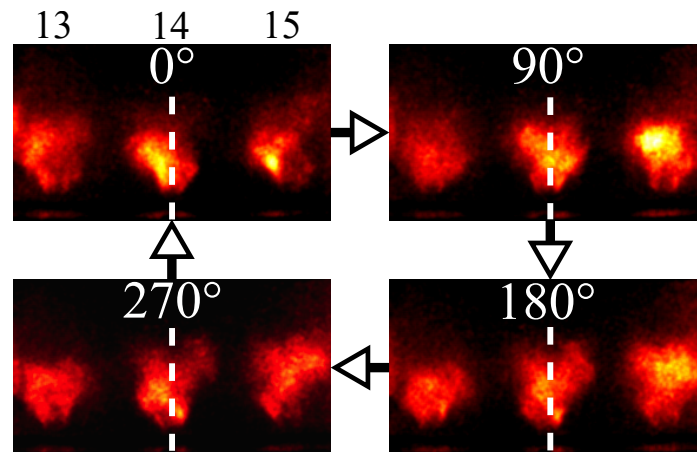


**Figure 3.13.** Light emission of three flames for  $\phi = 0.85$ ,  $\mathcal{P} = 113$  kW around the nodal line during a full cycle of oscillation. Images are averaged over four cycles. Yellow corresponds to high light intensity while dark red represents low light emission. The center of the flame is indicated by a white dashed line.

close to the nodal line. The nodal line is between flames 14 and 15. Contrary to the anti-nodal line position, the heat release rate does not seem to fluctuate much over a cycle. But these images underline the lateral displacement of flame 14 and 15 during the cycle of oscillation. Flame 14 is on the left of its center at  $0^\circ$  and then swings to the right at  $180^\circ$ . This is not easy to visualize in still photographs but there is a helical motion associated to the rotating motion of the air stream. Dynamic Mode Decomposition (DMD) described in Schmid (2010) of half of the annular chamber is presented in Fig. 3.14 to enhance the lateral motion of the flame close to the nodal line. This decomposition, at the frequency of the oscillation  $f = 732$  Hz, clearly shows the axial motion of the flame on the sides (as described in the last section) and the lateral sweeping motion of the flame close to the nodal line. This transverse displacement is particularly important for the flame destabilization as will be shown in section 3.5.

An analysis of the behavior of flame 14 is carried out to characterize the lateral sweeping motion when a standing mode is triggered. For that the flame is cropped into two half flames from its symmetry axis. The light emission of each half flame  $\dot{Q}'_h$  is determined at each instant of the video sequence (49,152 images at 6000 frames per second). The RMS of the fluctuating light emission  $\dot{Q}'_h$  is calculated by blocks of 4 periods of oscillation. It is again assumed that the light emission is roughly pro-

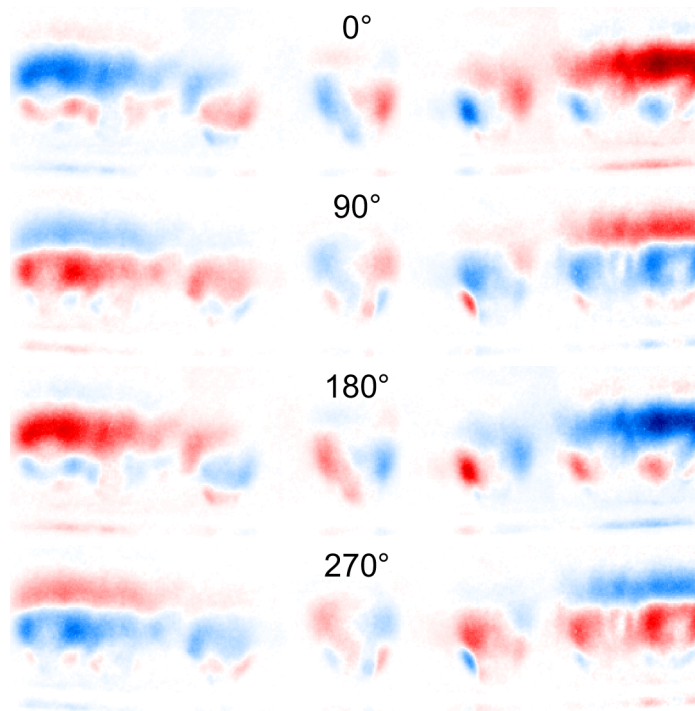


**Figure 3.14.** Lateral and axial flame oscillations enhanced using DMD (false colors) at the frequency of the instability  $f = 732$  Hz for one cycle. The camera is aligned on flame 14 close to the nodal line (see Fig. 4.1) and records the flame luminosity of half of the annulus during several periods of oscillation.

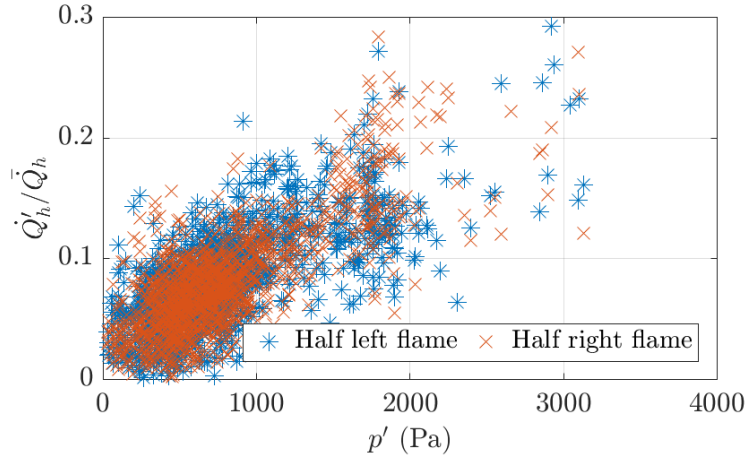


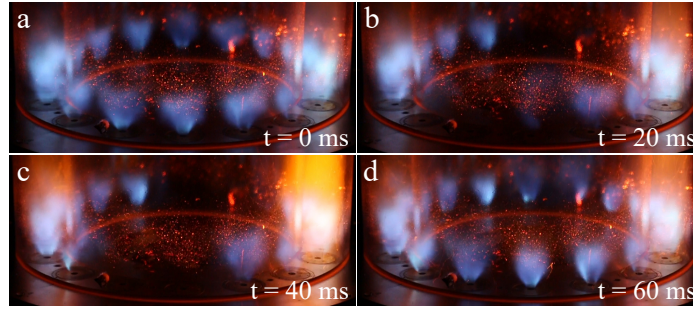
**Figure 3.15.** Relative light intensity fluctuations of half flames when the acoustic pressure increases during several instability bursts for  $\phi = 0.86$ ,  $\mathcal{P} = 113$  kW.  $\dot{Q}'_h / \overline{Q}_h$  is the relative amplitude of the RMS heat release rate fluctuation and  $p'$  is the RMS value of the pressure fluctuation.

portional to the heat release rate, which is only an approximation under conditions that are not premixed. The RMS values are then divided by the respective mean intensity of all half images of the sequence to give the relative light intensity variation  $\dot{Q}'_h / \overline{Q}_h$ . As there are many strong bursts in the processed sequence, the relative light intensity can be plotted versus the RMS level of the pressure signal measured close to the anti-nodal position (MC7). Data are plotted for the two half flames in Fig. 3.15. Given the small size of each block of images (28 images to have about 4 periods at 750 Hz), there is some data scatter, but one can see, on average, a linear evolution of the RMS intensity fluctuation related to the pressure fluctuation. This result indicates that the lateral fluctuations of the flames close the nodal line increase regularly with the instability amplitude.

### 3.5 Flame blow-off under high pressure oscillations

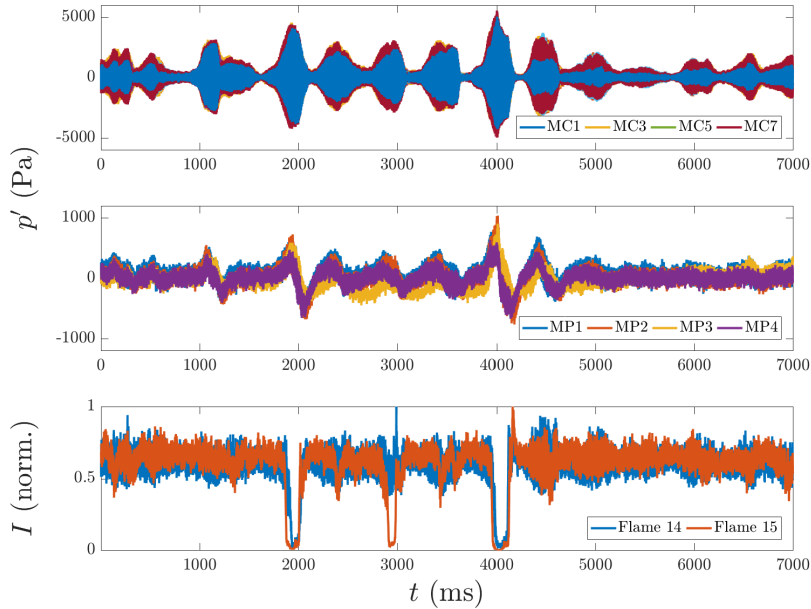
The phenomenon described in the last section can lead, in certain conditions, to a blow-off of several flames around the nodal line. At some point, the flame sweeping motion becomes so intense that the combustion is disrupted eventually leading to a complete extinction of flames close to the nodal line. Figure 3.16 shows four successive images of the entire annular combustor when this phenomenon is observed. This happens for a short period of time ( $t < 100$  ms) when the acoustic pressure in the chamber reaches a sufficiently large amplitude.

Figure 3.17 shows a typical sequence where several blow-off events occur. The acoustic pressure in the plenum exceeds three times a peak value 3000 Pa and one burst



**Figure 3.16.** True-color photographs of the annular chamber when six flames are blown-off for  $\phi = 0.85$ ,  $\mathcal{P} = 111$  kW.

reaches a peak value of up to 5500 Pa. In the plenum, a characteristic waveshape can be observed each time the pressure in the chamber exceeds these values. This phenomenon arises when a flame loses its stable position due to the high level of azimuthal velocity fluctuations. This corresponds to the wave generated when the flame re-ignites after being blown-off. Similar waveforms were observed in the large eddy simulations of the light-round in the MICCA annular combustor done by Philip et al. (2014a). At the bottom of Fig. 3.17, the light intensity recorded for flames 14 and 15



**Figure 3.17.** Acoustic pressure in the chamber (top), in the plenum (middle) and the light intensity signal from two flames around the nodal line (bottom) for  $\phi = 0.81$ ,  $\mathcal{P} = 111$  kW.

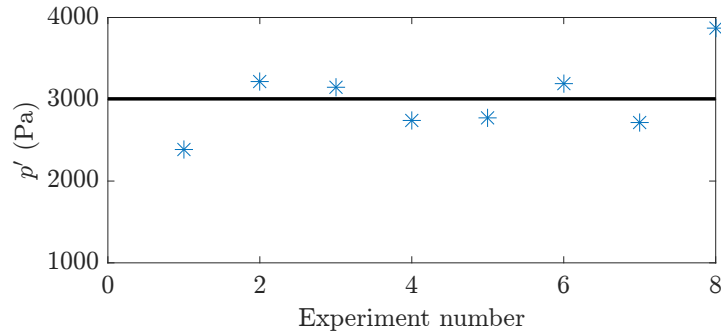


**Figure 3.18.** Pressure in the chamber when the blow-off appears for eight different experiments. The mean acoustic pressure is indicated with the black line.

around the nodal line is plotted. One can see that the two flames are entirely blown-off twice during this sequence.

Several experiments with partial blow-off events have been analysed and used to determine the limit pressure where this process is initiated. Results are plotted in Fig. 3.18. This estimated limit value is 3000 Pa peak and this value is repeatably obtained in several experiments corresponding to different operating conditions. This value is of course specific to the injector geometry and to the flame anchoring mechanism. A theoretical approach is proposed in the next section, in which a criterion is derived for the occurrence of this partial flame extinction. Observations concerning the blow-off close to the nodal line confirm results reported in [Lespinasse et al. \(2013\)](#) about the sensitivity of flames established near a pressure node compared to those located at a pressure anti-node.

### 3.6 Theoretical analysis

A framework is derived that can be used to interpret the blow-off phenomenon observed for flames located near the pressure nodal line. The data indicate that this phenomenon occurs under high amplitude oscillations. It is also found that the azimuthal velocity induced by the acoustic field displaces the flames in the transverse direction with a direct effect on the heat release rate in the flames located near the pressure nodal line where the transverse velocity reaches its maximum.

One may then consider that it is the displacement amplitude that governs the flame extinction process. When this amplitude is sufficiently large with respect to the size of the central recirculation zone which stabilizes the flame, then the flow is perturbed in a significant manner and the flame is destabilized. The flame displacement induced by the acoustic field can be estimated by  $\delta_\theta \simeq v'_\theta/\omega$  where  $v'_\theta$  designates the transverse velocity fluctuation associated with the acoustic mode and  $\omega$  denotes the angular frequency of this mode. When this displacement divided by a typical transverse

dimension of the Central Recirculation Zone (CRZ) is larger than a certain critical value one may expect a flame blow-off. It is convenient to use the injector diameter  $d$  to characterize the size of the CRZ and the previous condition may be cast in the form:

$$\frac{v'_\theta}{\omega d} > \psi_0 \quad (3.4)$$

with  $\psi_0$  a certain function representing the stability of the recirculation zone. This criterion probably catches much of the physics behind the extinction phenomenon observed in the experiments reported in this chapter. However, one may consider that this is perhaps not quite enough for the description of this mechanism. One may think for example that the stability margin of the flame is important. If the flame is stabilized but close to blow-off, the situation may be easily perturbed by the external acoustic field. If the stability is assured with a greater margin then it will be less easy to perturb the process. It is then natural to perform a dimensional analysis of this situation. This begins by listing parameters governing the process. In addition to  $v'_\theta$ ,  $\omega$  and  $d$  one may consider that the typical mean injection velocity  $U_b$  and a typical combustion delay time  $\tau_{cd}$  also intervene. It is also known that the swirl number  $S$  controls the aerodynamics of the flow. There are six parameters and two independent variables. One may then write the blow-off condition in a new form:

$$\frac{v'_\theta}{\omega d} > \psi_1 \left( \frac{v'_\theta}{U_b}, \frac{U_b \tau_{cd}}{d}, S \right) \quad (3.5)$$

In the previous expression  $b = U_b \tau_{cd} / d$  defines the stability of the flame and one may note that  $v'_\theta / U_b$  has to be sufficiently large if the acoustic field is to play a role and induce flame blow-off. This can be used to tentatively write the previous expression in the form :

$$\left( \frac{v'_\theta}{\omega d} \right) \left( \frac{v'_\theta}{U_b} \right) > \psi_2 \left( \frac{U_b \tau_{cd}}{d}, S \right) \quad (3.6)$$

Let us assume that in the absence of perturbation the flame is stable if  $b = U_b \tau_{cd} / d$  is less than a critical value  $b_*$ . Then, the stability margin may be estimated by the difference between this critical value and the actual value of the stability number :  $b_* - b$ . One may then tentatively propose a blow-off condition in the form :

$$\left( \frac{v'_\theta}{\omega d} \right) \left( \frac{v'_\theta}{U_b} \right) > \psi_3(S)(b_* - b), \quad \text{where } b = \frac{U_b \tau_{cd}}{d} \quad (3.7)$$

This criterion takes the form of set of hyperbolic lines shown in Fig. 3.19. This diagram indicates that flame blow-off will occur if the two parameters  $v'_\theta / \omega d$  and  $v'_\theta / U_b$  have sufficiently large values to exceed the product of some function  $\psi_3(S)$  times the stability margin estimated by  $b_* - b$ . The present experimental data cannot be used to confirm this criterion but they comply with the conclusion that  $v'_\theta / \omega d$  and  $v'_\theta / U_b$  should be sufficiently large.

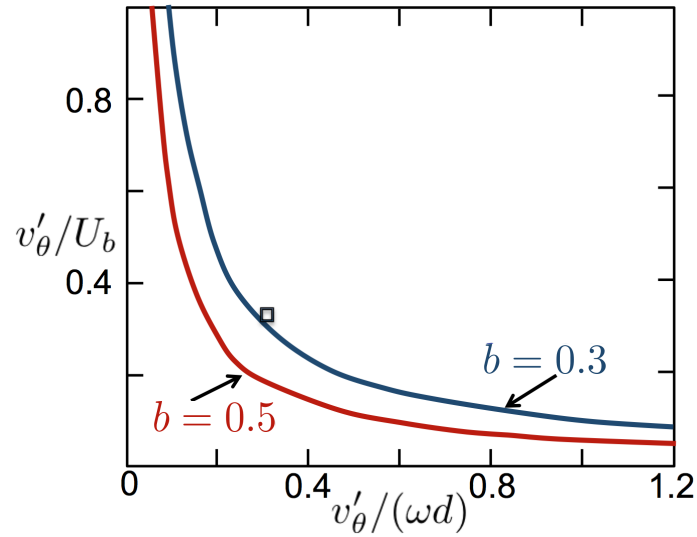


**Figure 3.19.** Blow-off limits calculated by assuming that  $b_* = 1$ ,  $\psi_3(S) = 0.19$ . The square symbol corresponds to an operating condition leading to blow-off (a peak value of the pressure equal to 3000 Pa).

### 3.7 Conclusion

Experiments have been carried out in a laboratory scale system comprising multiple swirling injectors fed with liquid n-heptane and air in an annular combustor operating at atmospheric conditions. This configuration exhibits strong instabilities coupled by a mode featuring a quasi perfect first azimuthal (1A) transverse structure. The instability arises in the form of a sequence of large excursions of pressure followed by rapid decays. The pressure oscillation reaches peak values of the order of 5000 Pa peak (about 5% of the chamber pressure). These experiments reveal that high acoustic pressure levels can be reached without any flame interaction. The microphone signals recorded in the chamber indicate that the instability is always coupled by a quasi standing mode. The nodal line is nearly fixed at the same position in the chamber. Despite the cautions taken to homogenize the liquid fuel distribution in the chamber, it is not possible to suppress some small differences in flow rate and atomization quality. A  $90^\circ$  interchange of the injectors located near the nodal and anti-nodal lines turned the nodal line by the same value, indicating that the asymmetries associated with the injection system essentially control the nodal line position. Observations indicate that the unsteady combustion process markedly changes with the position of the flame with respect to the azimuthal mode structure:

- Near the pressure anti-node, where the flames sense maximal axial velocity perturbations from the injector, the flame executes a movement in the axial direction with a strong positive heat release rate pulse when the flame extension reaches its maximum value. The relationship between the heat release rate and

the pressure oscillation in the chamber has been analysed in terms of amplitude and phase lag.

- The flames located near the pressure nodal line, submitted to large transverse velocity fluctuation levels are notably displaced in the azimuthal direction. This in turn is reflected in the unsteady heat release rate in opposite parts of these flames. Image processing allowed to determine the evolution of the lateral flame sweeping motion as a function of the amplitude of the pressure fluctuations.
- It is found that the Rayleigh source term always brings energy to the system during the instability bursts. The heat release rate at the anti-nodal line continues to grow linearly with the pressure oscillation and these two quantities are nearly in phase when the amplitude reaches its maximum.
- Saturation and decay that take place at this point might perhaps be due to an additional dissipation in the system, to a sudden detuning of resonance due to a frequency shift or to an alternate flame dynamics saturation mechanisms taking place at the other injector locations. This mechanism requires further investigation.
- When the pressure oscillation amplitude exceeds a certain threshold, the flames located near the pressure nodal line are extinguished, a mechanism that has the immediate effect of reducing the pressure amplitude and allowing re-ignition of the extinguished flames. These local extinctions are accompanied by a strong pressure wave in the combustor and a special signature in the plenum.

A mechanism is proposed for the flame extinction process that defines a critical value for the pressure amplitude. The data reported in this chapter provide unique indications on the instability process in annular combustors equipped with swirl spray injectors and they can serve to guide modelling and simulations of annular configurations.





## Chapter 4

# SICCA-Spray burner experiments

*Studies of the dynamics of spray swirling flames are of importance from a fundamental point of view and also because these flames are used in many practical systems like aero-engine combustors. Under certain conditions these flames give rise to various types of undesirable combustion instabilities. This chapter focuses on the measurement of the combustion dynamics of a system comprising a single injector designated as SICCA-Spray and reports novel Flame Describing Function (FDF) data on spray swirling flames. The test configuration comprises a tubular plenum fed with air by a swirling injector, a simplex atomizer that injects the liquid fuel (n-heptane) within a hollow cone spray and a cylindrical combustion chamber where the air and the fuel spray mix and burn. The air flow can be excited with two driver units plugged on the plenum, creating a flow perturbation which acts on the flame. The amplitude of fluctuation  $u'$  is controlled with a hot wire in the plenum. The flame response to incoming perturbations is then examined by recording the  $OH^*$  signal with a photomultiplier equipped with an interferometric filter. It is assumed that fluctuations of the light emission from this excited radical is proportional to heat release rate perturbations  $\dot{Q}'$ . The acoustic pressure  $p'$  at the backplane of the chamber is also recorded with a cooled waveguide microphone. Two different FDFs are defined and compared:  $\dot{Q}'/\bar{Q} = f(p'/\bar{p})$  and  $\dot{Q}'/\bar{Q} = g(u'/\bar{u})$ . The data are then used to analyse self-excited instabilities observed in the SICCA-Spray burner and to interpret some recent observations of strong self-sustained azimuthal instabilities in the MICCA-Spray annular combustor, equipped with sixteen injectors identical to that used in the SICCA-Spray set-up.*

### 4.1 Introduction

Chapter 3 reported recent experiments in the MICCA-Spray annular combustion chamber equipped with sixteen swirling injectors and powered by fuel spray which revealed regimes with strong self-sustained combustion oscillations. These instabilities were found to appear in the form of periodic bursts coupled to the first azimuthal 1A1L

mode of the combustion chamber with acoustic pressure levels up to 5% of the chamber static pressure. The frequency of these instabilities was also shown to feature an intriguing pattern with large variations between 700 and 800 Hz during their growth and decay. One motivation of the present study is to gather data on the Flame Describing Function (FDF) of a single spray injector of the MICCA-Spray chamber to help unravel this complex dynamics.

In many theoretical analysis of combustion instabilities coupled to azimuthal modes (see [Schuermans et al. \(2006\)](#), [Noiray and Schuermans \(2013\)](#) and [Ghirardo et al. \(2016\)](#)), the flame response is modelled by a relationship linking the heat release rate oscillations  $\dot{Q}'$  directly to pressure oscillations  $p'$  in the chamber. The modelling effort carried out in parallel has emphasized the fundamental role of the flame response to mass flow rate perturbations and a large number of studies have focused on the determination of Flame Transfer Functions (FTF) linking heat release rate fluctuations in the flame to incoming flow-rate disturbances (see [Dowling \(1999\)](#), [Ducruix et al. \(2000\)](#), [Candel \(2002\)](#) and [Schuller et al. \(2003\)](#)). The case of swirling flames of considerable technical interest was considered more recently by [Borghesi et al. \(2009\)](#), [Palies et al. \(2011\)](#). An extension of the transfer function concept in the form of the Flame Describing Function (FDF) framework was developed by [Dowling \(1997\)](#) and [Noiray et al. \(2008a\)](#) to account for nonlinearities by representing the flame response in terms of frequency and amplitude of the impinging perturbation.

$$\mathcal{F}(\omega, u') = \frac{\dot{Q}' / \overline{\dot{Q}'}}{u' / \overline{u}} = G(\omega, u') e^{i\varphi(\omega, u')} \quad (4.1)$$

This nonlinear framework was successfully applied to determine the oscillation frequencies and oscillation levels of unstable modes in a premixed swirling combustor equipped with a single injector by [Palies et al. \(2011\)](#). Analysis of the flame response to forced flow disturbances indicates that the flame shape defines to a large extent its linear ([Kim, K.T. and Lee, J.G. and Quay, B.D. and Santavicca, D.A. \(2010\)](#)) and nonlinear ([Durox et al. \(2009\)](#)) dynamical response.

Many of the available investigations concern premixed flames while practical systems are often fed with liquid fuel. The later injection systems are also prone to thermoacoustic instabilities ([Giuliani et al. \(2002\)](#), [Gajan et al. \(2007\)](#), [Yi and Santavicca \(2009\)](#), [Yi and Santavicca \(2012\)](#), [Providakis et al. \(2012\)](#) and [Mirat et al. \(2015\)](#)). A few studies report characterizations of the limit-cycle oscillations with OH\* or CH\* chemiluminescence measurements correlated with the spray dynamics (see [Eckstein et al. \(2006\)](#), [Yi and Santavicca \(2012\)](#) and [Providakis et al. \(2012\)](#)). In most cases there is a sizable pressure drop in the liquid fuel feed line providing a large impedance to impinging pressure perturbations so that one only needs to consider fluctuations in the air feeding manifold and injection unit. Laboratory scale experiments reported in the literature explore the sensitivity of the flame to these air flow rate modulations but are limited to just a few forcing frequencies at fixed amplitudes ([Haile et al. \(1996\)](#)),

Giuliani et al. (2002) and Gajan et al. (2007)).

The acoustic response and FDF of swirling spray flames to a broad frequency range of air modulation was recently considered in Mirat et al. (2015) where the spray flames investigated feature a distinct response compared to those obtained for premixed swirling flames. In particular, the low frequency limit of the FDF gain differs from that found in the premixed case and tends to zero in that limit. The FDF phase lag was also found to depend on the perturbation level, a feature already observed in partially premixed systems by Kim and Hochgreb (2011). Measurements in Mirat et al. (2015) were carried out in the case of steam assisted liquid fuel injectors. This short review of the literature indicates that the dynamical response of spray flames and more specifically swirling spray flames is not well documented. The present study tries to reduce this lack of knowledge.

In this Chapter, the first section quickly gives details on the SICCA-Srapy experimental set-up (section 4.2). The acoustic response to external modulations is discussed in section 4.3. The system features natural, self-excited instabilities that are characterized in section 4.4. The forcing of the flame is compared to the self-excited case (section 4.5) to validate the methodology. The response of swirling spray flames is then examined using the FDF framework for nonlinear combustion instability analysis (section 4.6). The frequency response of the flame to acoustic perturbations is characterized by comparing the chemiluminescence signal generated by combustion and assumed to represent the heat release rate in the flame to the velocity signal measured upstream the injector. The present investigation aims at identifying parameters that control the sensitivity of spray flames to incident velocity perturbations. It is also indicated that the knowledge obtained and theoretical results can be used to predict the behavior of such injection systems when they are placed in an annular configuration.

## 4.2 Experimental configuration

To complement Section 1.3 of Chapter 1, one can find a quick description in the following. The burner, sketched in Figure 4.1, comprises a plenum and a combustion chamber. The chamber is formed by a cylindrical quartz tube with a diameter  $d_c = 70$  mm and of variable length  $l_c$ . Two driver units are plugged on the 300 mm cylindrical plenum to modulate the air flow. A swirled injection unit links the plenum to the combustion chamber. The injector is exactly the same as the one used on MICCA-Spray, composed of an air circuit passing through a swirler and of a liquid atomizer to feed liquid fuel and form spray of droplets.

Air is injected at ambient temperature at the bottom of the plenum. It then reaches the injector where it passes through a radial swirler with six 4.5 mm holes and exits the injector with a measured swirl number of 0.55. The head loss through the injector is of the order of 4% of the atmospheric pressure at the nominal operating conditions investigated. Fuel (n-heptane) is injected using a simplex atomizer supplied pressur-

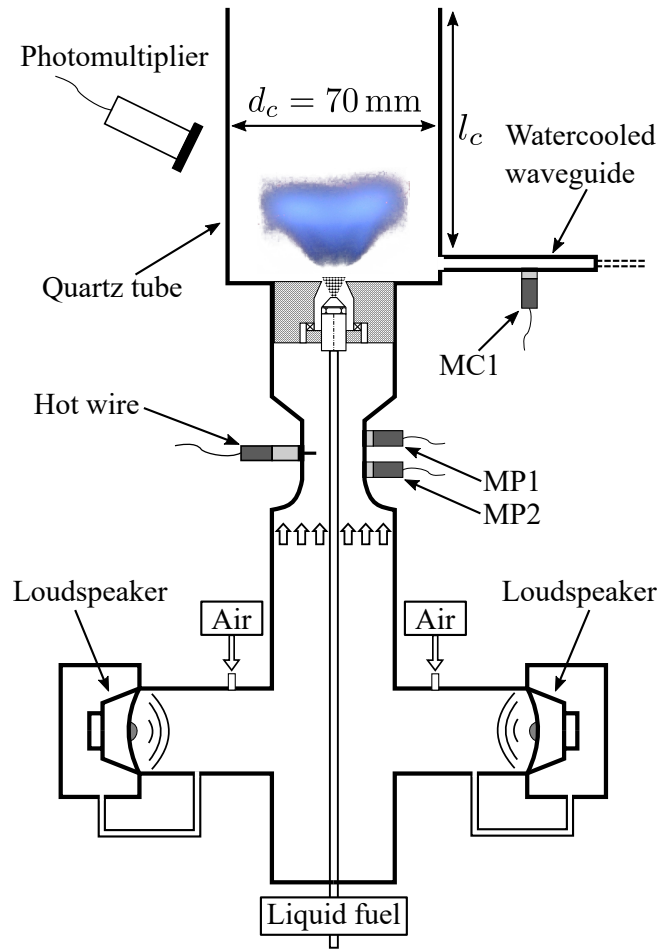


**Figure 4.1.** Schematic of the SICCA-Spray burner to characterize flame dynamics with FDF measurements.

ized at 9 bar. The atomizer generates a hollow cone and is positioned in the middle of the swirler. The droplet spray formed by this system has a mean diameter  $d_{10} = 8 \mu\text{m}$  and a SMD  $d_{32} = 25 \mu\text{m}$ . The injector is terminated by a convergent section. Nominal injection conditions, used throughout this chapter, are as follows. Air flow rate is fixed at  $\dot{m}_{air} = 2.59 \text{ g s}^{-1}$  and fuel flow rate is  $\dot{m}_{fuel} = 0.144 \text{ g s}^{-1}$ . The global equivalence ratio is  $\phi = 0.85$  and the global power  $\mathcal{P} = 6.5 \text{ kW}$ . The bulk velocity of the air at the exit of the injector is  $U_b = 43 \text{ m s}^{-1}$ . Figure 4.2 presents the Abel transform of the  $\text{CH}^*$  chemiluminescence of the flame using a Princeton Instrument PiMax 4 intensified camera. The flame takes a well defined M-shape, slightly lifted 10 mm above the chamber backplane. Detailed characterizations of the spray and of the airflow with laser optical diagnostics can be found in Section 3.3 of Chapter 3.

The Flame Describing Functions (FDF) based on the velocity perturbation  $u'$  and on the acoustic pressure fluctuation  $p'$  in the chamber are respectively defined by:

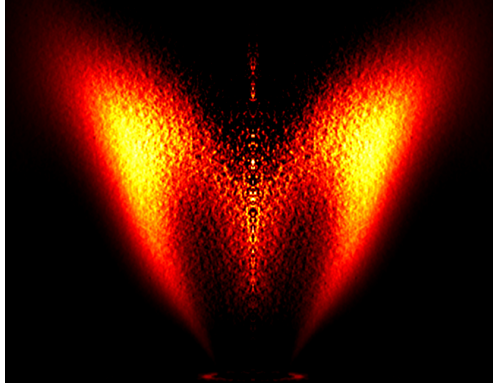


**Figure 4.2.** Image in false colors of the Abel transform of the  $\text{CH}^*$  chemiluminescence of the flame with  $\phi = 0.85$ ,  $\mathcal{P} = 6.5 \text{ kW}$ ,  $U_b = 43 \text{ m s}^{-1}$ . For symmetry, the Abel transform of one branch of the M-shape flame is deconvoluted using the Abel transform and replicated to generate the entire flame. The image is cropped in order to exhibit the exit of the burner on the bottom of the image.

$$\mathcal{F}(\omega, |u'|) = \frac{\dot{Q}'/\bar{Q}}{u'/\bar{u}} \quad (4.2)$$

$$\mathcal{F}(\omega, |p'|) = \frac{\dot{Q}'/\bar{Q}}{p'/\bar{p}} \quad (4.3)$$

These two complex functions are measured with the diagnostics indicated in Figure 4.1 of Chapter. The gaseous flow is modulated by the two driver units of 150 W and 8  $\Omega$  each plugged in the plenum. Due to the relatively high head loss induced by the swirlers, these two units are enclosed in cavities linked to the plenum to balance the pressure on both sides of the driver unit membrane. The frequency of the oscillations ranges from 250 to 900 Hz. A sine-wave generator and an amplifier actuates the loudspeakers over this range. The amplitude  $u'$  of the perturbation generated in the upstream flow is determined using a hot wire placed 100 mm upstream the combustion chamber backplane. This region is chosen in order to have a nearly laminar velocity profile. Measured  $u'/\bar{u}$  range from 0.1 to 1.3. Two microphones (MP1 and MP2) are placed around the same position to evaluate  $u'$  using a second method and check the hot wire measurements. A third microphone (MC1) measures the acoustic pressure  $p'$  in the chamber, pressure which appears in Eq. (4.3). It is flush mounted on a cooled waveguide directly plugged on the chamber backplane. A photomultiplier (PM) with an  $\text{OH}^*$  filter is placed on the side of the combustion chamber to record the flame emission. The PM sensor is tilted towards the injector position in order to capture the entire flame luminosity whatever its shape. It is known that the  $\text{OH}^*$  emission signal is proportional to the heat release rate in premixed flames. It is assumed in what follows and this is admittedly an approximation that there is a link between the

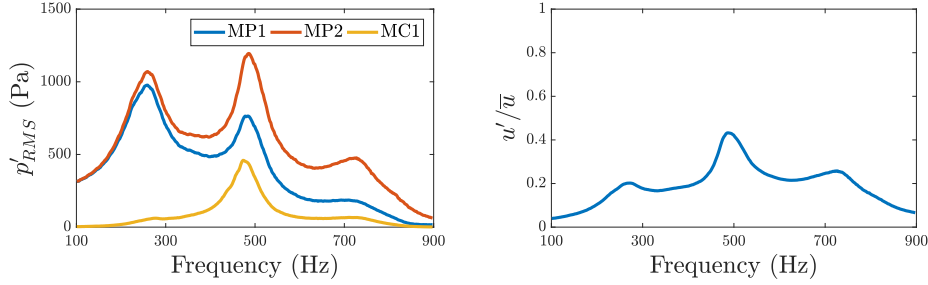


**Figure 4.3.** Left: Acoustic response of the system for a range of frequencies up to 900 Hz under cold conditions with flowing air at  $\dot{m}_{air} = 2.59 \text{ g s}^{-1}$ . The voltage of the excitation system is kept constant. Right: Measured velocity fluctuation ratio  $u'/\bar{u}$  obtained with the hot wire.

two quantities in the present case where the flame is fed by a spray of droplets and it is considered that  $I'/\bar{I} \simeq \dot{Q}'/\bar{Q}$ . It was shown in [Mirat et al. \(2015\)](#) that this approximation yielded reasonable results for instability predictions for globally lean injection conditions ( $\phi < 1$ ).

### 4.3 Frequency response of the system

In these first experiments there is no combustion and the system operates under cold flow conditions. The driver units are used to modulate the flow with increasing frequency from 100 to 900 Hz at a fixed voltage  $V_0$  and the air flow is maintained constant at  $\dot{m} = 2.59 \text{ g s}^{-1}$ . The resulting acoustic signals recorded using MP1, MP2 and MC1 are plotted in Figure 4.3, left. Two resonance peaks are found, one at 260 Hz and the other at 490 Hz. The first resonance corresponds to a pure plenum mode whereas the second is a coupled chamber-plenum mode. The right plot in Figure 4.3 shows the computed velocity fluctuation ratio  $u'/\bar{u}$  with  $\bar{u}$  the mean velocity, when the frequency  $f$  is increased at fixed voltage  $V_0$ . It is easy to see that  $u'/\bar{u}$  is not constant over the frequency range. This is due to an acoustic resonance near 490 Hz increasing the velocity ratio and the nonlinear response of the loudspeaker. It is important to underline this feature as it will be the method used to evaluate the FDF in section 4.6. A Helmholtz solver is used to calculate the mode shape in the system at the frequency of  $f_h = 543 \text{ Hz}$  corresponding to one of the self-sustained combustion oscillation observed in the setup and analysed in section 4.4 when the chamber length is varied. In this simulation, the temperature in the plenum is considered to be constant  $T_1 = 300 \text{ K}$  while the temperature in the combustion chamber is  $T_2 = 1200 \text{ K}$ . The length of the chamber is augmented to  $l_{tot} = l_c + l_{end} = 320 \text{ mm}$  in the simulation with  $l_c = 280 \text{ mm}$  the combustion chamber length and  $l_{end} = 40 \text{ mm}$  the end-correction which has been measured. For simplicity, the complex injector system has been replaced by an single hole of equivalent surface with the same length. Note that the convergent end-piece of the injector is taken into account in this simulation. The mode shape is

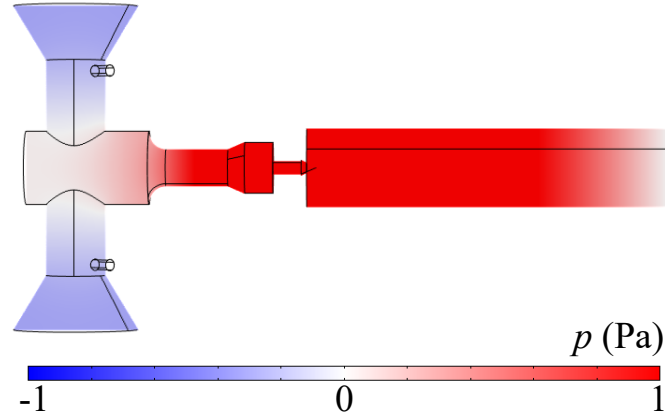


**Figure 4.4.** Acoustic pressure  $p$  at 543 Hz calculated using a Helmholtz solver and assuming a constant temperature of 1200 K in the combustion chamber.

shown in Figure 4.4 through a cut of the system. One can see that the mode is longitudinal, with a maximum pressure near the backplane. The cylindrical pipe where the hot wire is located (see Figure 4.1), has only a slightly lower amplitude level, but with the same sign.

#### 4.4 Self-excited instabilities

For certain geometrical lengths  $l_c$  of the combustion chamber, the system exhibits well defined self-excited longitudinal instabilities. Frequency  $f$ , velocity fluctuation rate  $u'/\bar{u}$ , heat release rate  $\dot{Q}'/\bar{\dot{Q}}$  ratios and acoustic level in the chamber  $p'$  are given in Table 4.1 for different lengths  $l_c$ . One finds that a critical chamber length is necessary to observe thermo-acoustic modes and, in the case of the SICCA-Spray burner,  $l_c$  needs to be greater than 245 mm to observe combustion instabilities. All self-excited

$l_c$ (mm)	$f$ (Hz)	$u'/\bar{u}$	$\dot{Q}'/\bar{\dot{Q}}$	$p'$ (Pa)
215	595	0.06	0.01	19
230	605	0.08	0.07	175
245	565	0.36	0.34	1370
265	535	0.49	0.21	1170
280	530	0.38	0.16	890
295	455	0.63	0.28	1550
315	415	0.76	0.48	3020

**Table 4.1.** Characterization of the self-excited instabilities as a function of the combustion chamber length  $l_c$  in the SICCA-Spray bench.

instabilities are longitudinal modes developing in the chamber.

An example with  $l_c = 280$  mm is now examined. Combustion instabilities appear in this case at 530 Hz. This frequency can be retrieved by considering a quarter-wave mode of the combustion chamber cavity. The mean temperature in the system is of the order of  $T = 1200$  K giving a speed of sound  $c = \sqrt{\gamma r T} = 694$  m s<sup>-1</sup> in the medium. The natural resonant frequency is thus  $f = c/4L = 540$  Hz with  $L = l_c + l_{end}$  and  $l_{end} = 40$  mm the measured end-correction. This calculation is confirmed by the Helmholtz analysis presented in Figure 4.4. Figure 4.5 presents the filtered velocity,

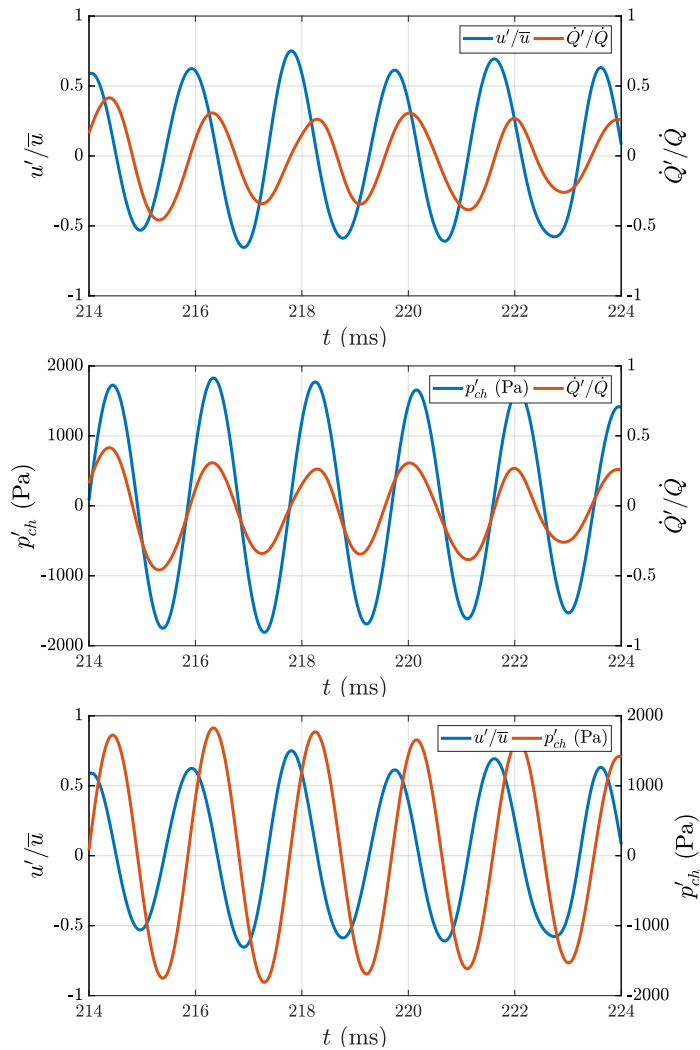


**Figure 4.5.** Time series of velocity, acoustic pressure in the chamber and heat release rate fluctuations for the self-triggered flame with  $l_c = 280$  mm. Data are normalized by their mean value except for the acoustic pressure. Signals are low pass filtered with a cut-off frequency  $f_c = 1000$  Hz.

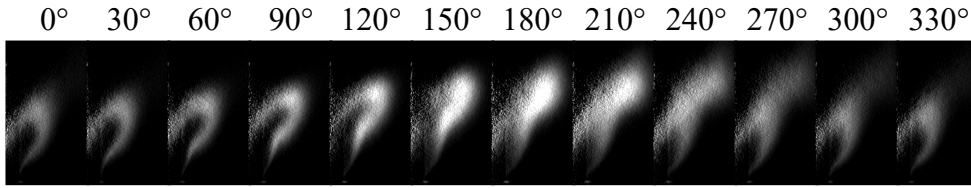


**Figure 4.6.** Phased CH\* chemiluminescence of the flame during one cycle of oscillation. Images are averaged over 600 cycles.

acoustic pressure and heat release rate signals during the instability. The velocity fluctuations at the hot wire, in the top figure, are plotted along with the heat release rate fluctuations. One can see a clear sinusoidal response of the velocity with a fluctuation of  $u'/\bar{u} = 0.5$  stable over the 2 s of recording. The heat release rate oscillates at the same frequency and with a phase  $\varphi_{uQ}$  of  $\pi/2$  between the velocity and the heat release signals. The heat release ratio  $\dot{Q}'/\bar{Q}$  fluctuates around 0.25 while the acoustic pressure in the chamber  $p'_{ch}$  reaches a peak value of 1700 Pa. Acoustic pressure and heat release rate are oscillating perfectly in phase, at the same frequency, indicating that the Rayleigh criterion is satisfied. This implies that  $p'_{ch}$  and  $u'$  at the injector outlet are in phase quadrature because  $i\rho\omega = \nabla p$ . Note that the velocity  $u'$  which is plotted in Figure 4.5 is measured by the hot wire 100 mm upstream the combustion zone, where  $\dot{Q}$  is measured by the photomultiplier. Between these two points, the information may not always travel at the acoustic velocity  $c \sim 340 \text{ m s}^{-1}$  all the way. It is known for example from Palies et al. (2011) that the swirler induces a vorticity mode that propagates at the flow velocity in the injector unit. One may have to consider the energy transfer from the acoustic to the convective propagation mode which would indicate a major shift in the propagation velocity. LES calculations, presented later, have demonstrated that the velocity perturbation  $u'$  is transported at the acoustic speed for approximately 80 mm, corresponding to the beginning of the injector unit in the system. The velocity then evolves in a complex manner in the injector.

Phased chemiluminescence images are recorded using a PiMax 4 camera equipped with a CH\* filter. Images are then Abel transformed to retrieve the contribution of a slice to the flame emission. As the flame is axisymmetric, only half images of the right part of the flame are shown in Figure 4.6 corresponding to phases from 0 to 330°. One may note the strong flame displacement in the axial direction and a flame brush curving during the peak of the cycle around 180°. The flame length is also notably affected. The luminosity of the flame varies along its length. Note that the algorithm used to extract the flame slice allows a quantitative comparison of luminosity between the different images. The anchoring point of the flame is essentially fixed in space at a distance of 10 mm from the injector exhaust.

## 4.5 Forced flame response

In this section, the combustion chamber is equipped with a shorter flame tube  $l_c = 165$  mm to avoid self-excitation of instabilities. As in section 4.4, the dynamics of the flame is recorded using a photomultiplier and three microphones. Loudspeakers depicted in Figure 4.1 are actuated by a function generator and an amplifier to force the flame motion at a chosen frequency. The amplitude is modulated in order to get the desired velocity fluctuation rate  $u'/\bar{u}$  at the hot wire location.

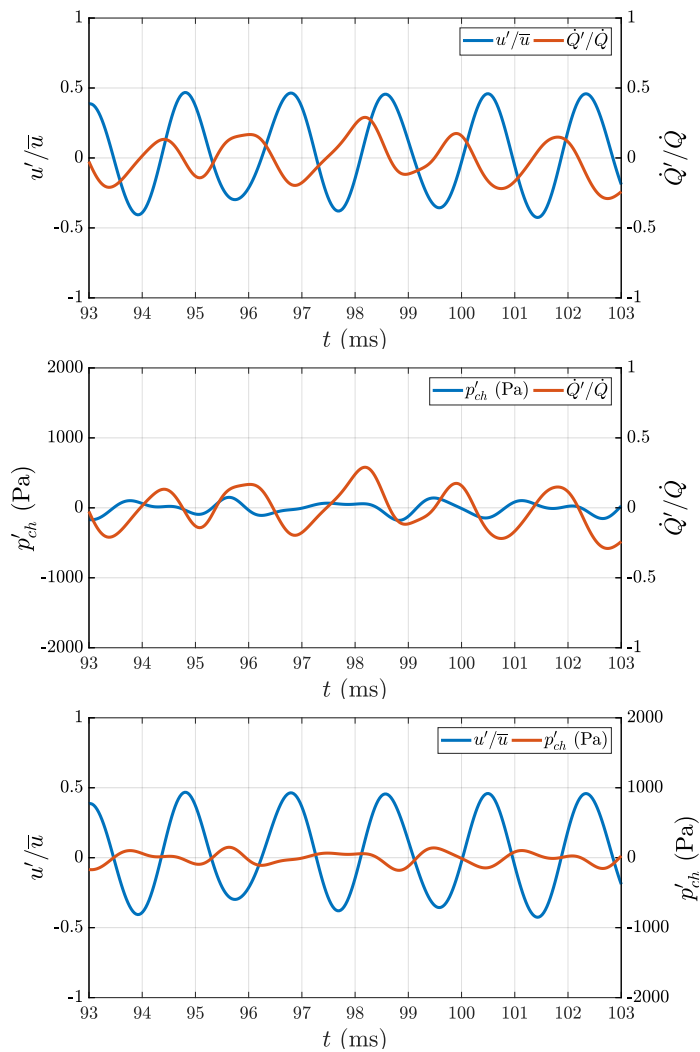


**Figure 4.7.** Time series of velocity, acoustic pressure in the chamber and heat release rate fluctuations for the forced flame at 530 Hz. Data are normalized by their mean quantity except for the acoustic pressure. Signals are filtered with a low-pass filter at 1000 Hz.

In Figure 4.7, the flame is forced at  $f = 530$  Hz and at an amplitude  $u'/\bar{u} = 0.45$  to match the conditions corresponding to the self-excited instability with the  $l_c=280$  mm flame tube. Velocity fluctuations are sinusoidal and at the same frequency and with a difference in amplitude of 10% in order to match with the self-excited case. The heat release rate fluctuations  $\dot{Q}'/\bar{Q}$  in the modulated case are nearly the same as those recorded in the naturally excited case. The main difference is found in the phase  $\varphi_{uQ} = -\pi/2$  between velocity fluctuations and heat release rate fluctuations which is the opposite of that found in the self-excited case. The second difference is in the acoustic pressure in the combustion chamber  $p'_{ch}$  which is much lower in the forced case. The pressure is around 200 Pa peak whereas the pressure in the self-excited flame is around 2000 Pa. This is the consequence of the length of the combustion chamber cavity (165 mm) that is not scaled to resonate at this frequency. Considering, as in the last section, the quarter-wave mode of the 165 mm tube, the resonant frequency is 850 Hz which is much higher than the excitation at 530 Hz. Thus the acoustic level is not amplified by the system resonance. This is an important result as many theoretical models take  $p'$  as an input to deduce  $\dot{Q}'$ . The present experiment shows that, in the case of a forced flame,  $p'$  is not an input but a result of  $\dot{Q}'$ . An alternative is to consider that  $p' \sim d\dot{Q}/dt$  as for flames radiating noise in the free field, implying in this case a phase quadrature between the signals. These models might help to shed light on certain phenomena but they will always face the problem of their experimental validation. It is then more natural to take  $u'$  as the input of  $\dot{Q}'$  but problems still rise as seen here. Where  $\varphi_{uQ} = \pi/2$  when the flame naturally oscillates,  $\varphi_{uQ} = -\pi/2$  when the flame is forced. This is the consequence of the velocity measurement method, as mentioned before. These observations will be examined in section 4.6 when looking at different Flame Describing Functions. It is worth noting that numerical results using LES exhibits the same behavior concerning the phase difference  $\varphi_{uQ}$  in the case of the self-excited flame or in the forced case.

CH\* chemiluminescence images for the forced case are now compared with the images corresponding to the self-excited case. In Figure 4.8, the forced case is on the left hand side of each image while the self-excited case is on the right hand side. One can identify similar shapes in the flame motion as described before. The luminosity, the flame brush and the anchoring point vary in the same fashion.

In conclusion, the previous data indicate that the flame dynamics under external forcing and under self-excited oscillations at one particular frequency have similar characteristics. The flame shapes at different phases during the cycle are the same and the relative velocity and heat release rate levels have the same amplitude levels but the phase difference  $\varphi_{uQ}$  between velocity and heat release rate in the forced and in the self-excited case do not match. It is  $+\pi/2$  in the first case and  $-\pi/2$  in the second and this difference needs to be interpreted.

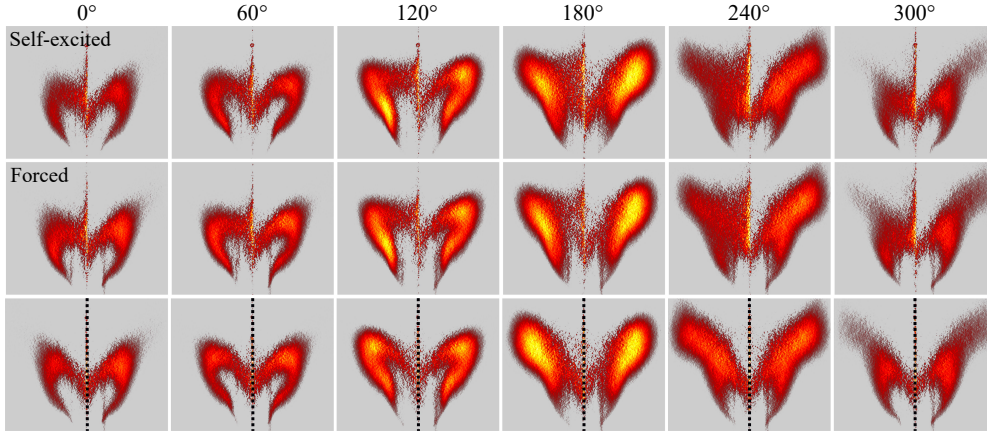


**Figure 4.8.** Phased average CH\* chemiluminescence of the flame during one cycle of oscillation for the forced flames (left branch of the flame) and for the self-triggered flames (right branch of the flame). Images are averaged over 600 cycles.

#### 4.6 Flame Describing Function measurements

In this section, the Flame Describing Function (FDF) of the spray flame is evaluated using the SICCA-Spray burner shown in Figure 4.1. As described in section 4.3, if the frequency is increased with the voltage of the driver units kept constant, the resulting  $u'/\bar{u}$  is not constant. A two-microphone method is also used to avoid signal aliasing when the velocity fluctuations become large enough to induce a bias in the hot wire measurements. Microphones MP1 and MP2 in the plenum are used to reconstruct the acoustic field. They are spaced by a distance  $\Delta x = 50$  mm and placed on the sides of the hot wire (see Figure 4.1). The velocity fluctuation  $u'$  at the hot wire point can be deduced from the following equation:

$$u' = \frac{1}{i\rho_0\omega} \frac{p'_2 - p'_1}{\Delta x} \quad (4.4)$$

where  $p'_2$  and  $p'_1$  are measured by microphones MP2 and MP1 respectively. The air density is taken  $\rho_0 = 1.2 \text{ kg/m}^3$  and  $\omega = 2\pi f$  denotes the angular frequency. This method has been validated on the bench for several conditions. Calculated  $u'$  values with Eq. (4.4) will then be used in the rest of this chapter for consistency. To obtain an FDF, one has then to sweep the excitation frequency from  $f_1 = 100$  Hz to  $f_2 = 900$  Hz for several output voltages  $V_0$  of the function generator. Frequencies lower than 100 Hz are not explored for several reasons. First, the excitation system using loudspeakers has a low efficiency at frequencies under 200 Hz, making so that high amplitudes perturbations are difficult to reach. Secondly, the frequencies of interest are in the higher spectral range, around 500 Hz for both the single burner SICCA-Spray and the annular combustor MICCA-Spray.

A frequency ramp from  $f_1$  to  $f_2$  at a constant rate of  $1 \text{ Hz s}^{-1}$  is then used to modulate the system. Signals are recorded at a sampling frequency  $f_s = 32,768 \text{ Hz}$  during  $2 \text{ s}$ , ensuring that the forcing signal frequency only increases by  $2 \text{ Hz}$  and is essentially constant during the acquisition time. The transfer function is then estimated using the Welch's averaged periodogram method to calculate the Cross-Power Spectral Density (CPSD). The  $2 \text{ s}$  signals are divided into eight segments with Hamming windows and a  $50\%$  overlap. The gain  $G(f)$  and phase  $\varphi(f)$  of the transfer function are then deduced at the modulation frequency  $f$ . This processing is done to evaluate the transfer functions between  $u'/\bar{u}$  and  $\dot{Q}'/\bar{Q}$  and  $p'/\bar{p}$  and  $\dot{Q}'/\bar{Q}$ . This gives a large dataset of Flame Transfer Functions for different  $u'/\bar{u}$  between  $f_1$  and  $f_2$ . Data are finally processed to only keep specific values for  $u'/\bar{u}$  ranging from  $0.1$  to  $1.3$  with a spacing of  $0.1$ . For each  $u'/\bar{u}$  value, a  $5\%$  error in the estimation of the velocity fluctuation ratio is admitted. Data are then interpolated for  $u'/\bar{u} < 0.9$ .

The FDF based on the velocity  $u'/\bar{u}$  and the heat release rate  $\dot{Q}'/\bar{Q}$  ratios is displayed in Figure 4.9. The left figures represent 2D-plots of phase (top) and gain (bottom).

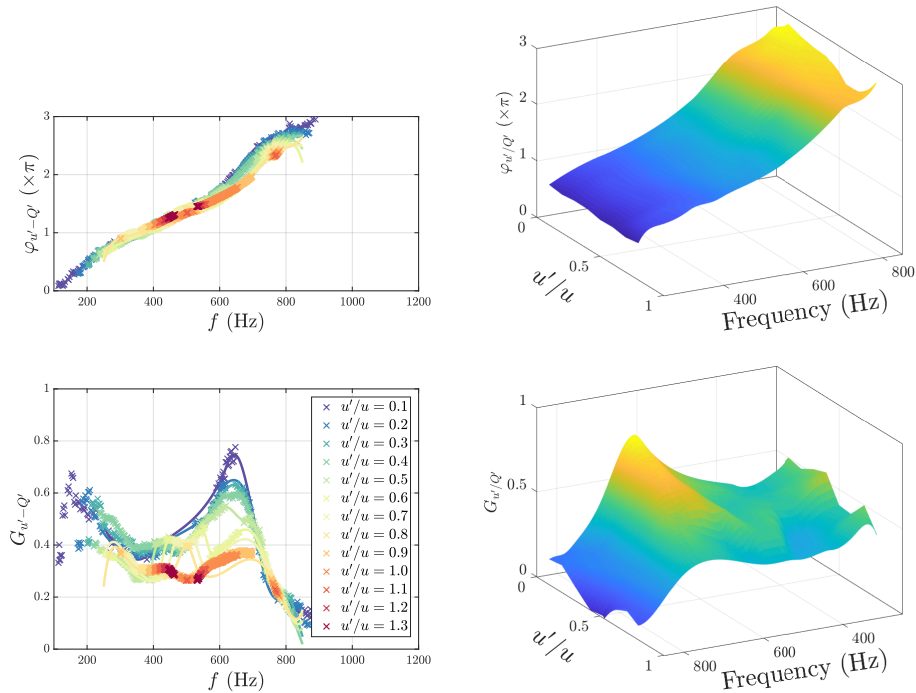


**Figure 4.9.** FDF based on the velocity  $u'$  and the heat release rate  $\dot{Q}'$ . Left: Phase  $\varphi$  and gain  $G$  of the FDF between the velocity and the heat release rate ratio and their fit. Right: Linear interpolation of the FDF between  $u'/\bar{u} = 0.1$  and  $0.9$  based on the results presented in the left hand side. Note that the frequency axis of the two figures are inverted.

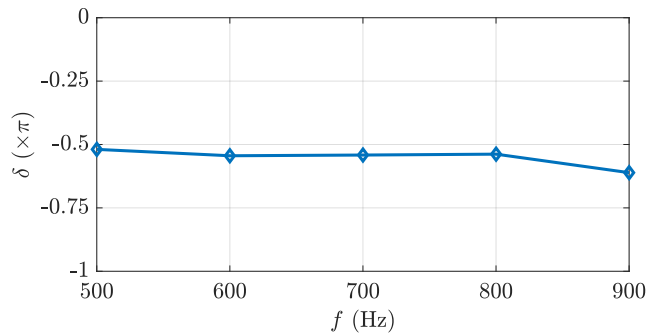


**Figure 4.10.** Evaluation of the phase of the injector admittance  $\delta$  for frequencies between 500 and 900 Hz.

Data are fitted for  $u'/\bar{u}$  up to 0.8. This value is limited on purpose because higher values cannot be applied in various frequency ranges due to the difficulty to excite high levels of fluctuations over a wide range of frequencies. On the right hand side, a linear interpolation is applied to  $u'/\bar{u}$  to give a better understanding of the flame response. One observes that the phase increases quasi linearly across the frequency range. The impact of the velocity ratio  $u'/\bar{u}$  ratio is small except in the band 600 700 Hz where one can find a difference of 1 rad between the FDF phase lags for  $u'/\bar{u} = 0.1$  and 0.8. Based on the phase  $\varphi$ , the time lag  $\tau = \varphi/(2\pi f)$  can be estimated. Considering that the phase slope is rather constant across the frequency range,  $\tau = 1.8$  ms.

In the gain plot (bottom left), the amplitudes at low frequencies are scattered. The trend in gain is clearer when the frequency reaches 300 Hz. One can then observe a peak at 640 Hz. Note that this value is far from the natural resonant frequency of the system, indicating that this is the result of the flame response. The gain strongly decreases when  $u'/\bar{u}$  is increased, demonstrating the nonlinearity of the phenomenon and the saturation of the flame response at high amplitudes of modulation.

Theory provides possible bands of instability. These bands plotted in gray in the following phase diagrams are approximately bounded by horizontal lines corresponding to  $\{\pi, 2\pi\}$ . When  $\pi < \varphi < 2\pi$  [mod.  $2\pi$ ], the configuration is potentially unstable, a result already reported by Schuller et al. (2003), Durox et al. (2009) and Durox et al. (2013). This first consideration does not take into account the possible role of the injector on the stability. The admittance of the injector has to be considered because the velocity measurement, made with the hot wire, is carried out on the upstream side of the injector. Thus the measured transfer function is not only linked to the flame contribution but also to the impact of the injector. To include this admittance, one has to shift the phase of the FDF by the value measured in Figure 4.10. It is now possible to estimate the bands of instability of the system by analysing the phase diagram with

the following expression:

$$\pi < \varphi + \delta < 2\pi \pmod{2\pi} \tag{4.5}$$

with the flame contribution to the instability between  $\{\pi, 2\pi\}$  and the injector admittance  $\delta$ , shifting the phase. To estimate  $\delta$ , a velocity perturbation at variable frequency is applied to the system using the excitation system under cold conditions. The velocity fluctuation is first measured with the hot wire and, during another experiment, with a Laser Doppler Anemometry (LDA) system at the exit of the burner, in the air jet. The phase between the velocity fluctuation  $u'$  and the reference signal from the function generator is calculated in both cases. One can then deduce the phase between the velocity fluctuation at the hot wire and at the exit of the burner. The measurement of  $\delta$  is presented in Figure 4.10 for several frequencies. One can see that it is quite constant with the frequency and may be considered to be close to  $-\pi/2$ . Figure 4.11, top, shows the position of the two instability bands in grey. It is then possible

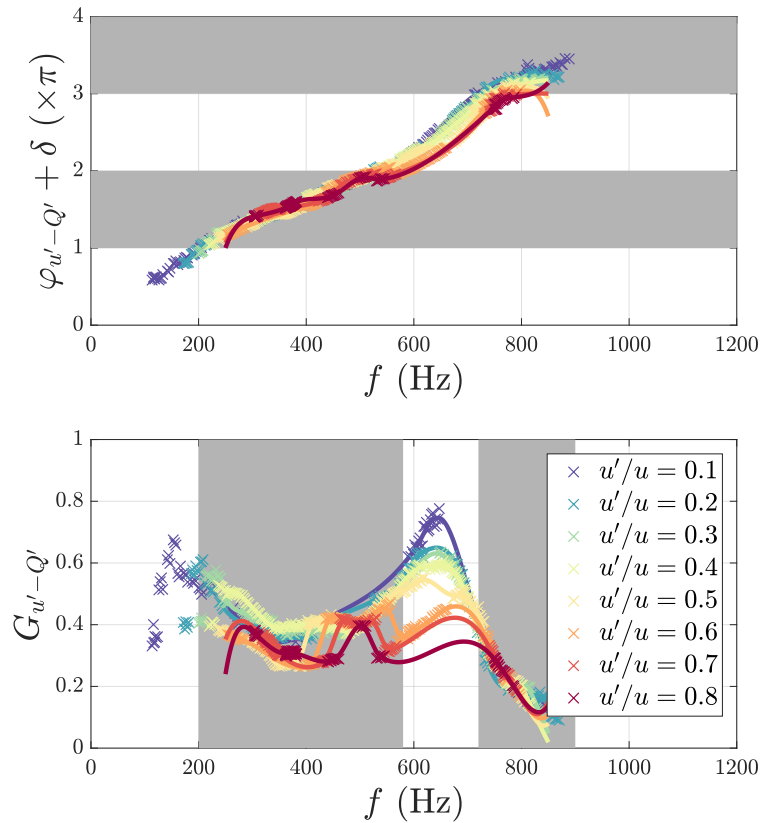


**Figure 4.11.** Top: Phase  $\varphi$  of the FDF and burner admittance coupled with the instability band in grey. Bottom: Gain  $G$  with the deduce position of the instability bands.

to calculate the frequency boundaries of the potential unstable modes. One can see that the phase enters the first instability band around 200 Hz and up to 580 Hz for the highest levels of  $u'/\bar{u}$ . It enters the second band at 720 Hz until the end of the FDF estimation at 900 Hz. This explains why the SICCA-Spray bench exhibits powerful naturally excited instabilities when the different length  $l_c$  of the walls is increased. When the resonant frequency of the system becomes lower than 550 Hz, the system is potentially unstable. The more the resonant frequency decreases, the more the system becomes unstable. This is confirmed by the increase in  $\dot{Q}'/\bar{Q}$  observed in Table 4.1 when  $l_c$  increases. Note that the forced flame with  $l_c = 165$  mm is not naturally unstable. As indicated before, the resonant frequency would be 850 Hz. This value is in a potential unstable band but the gain is very low in this region with  $G < 0.08$ , probably much lower than the damping of the system.

One may infer from the previous considerations the stability or instability of a com-

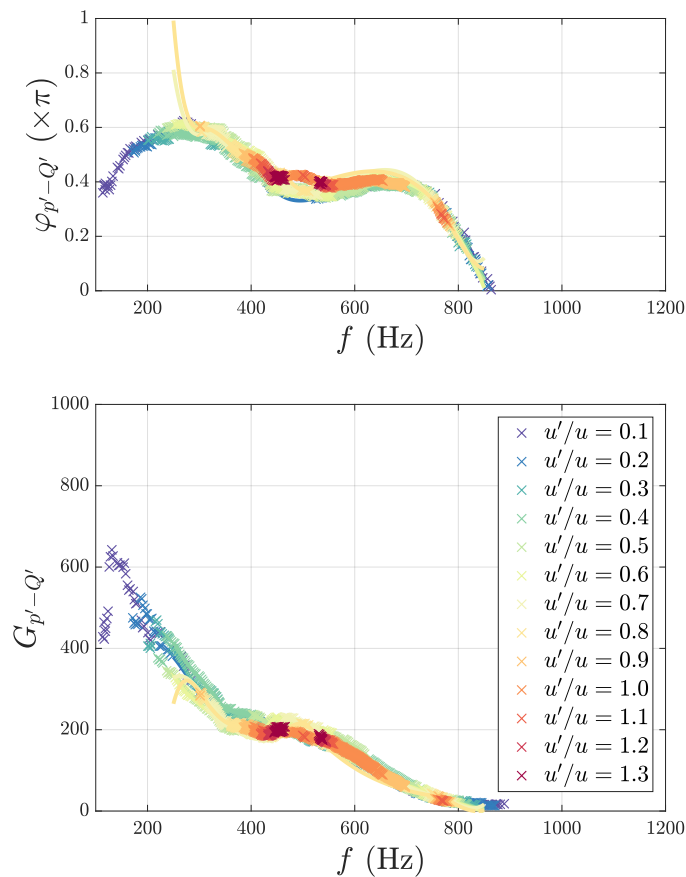


**Figure 4.12.** FDF based on the acoustic pressure in the chamber  $p'$  and the heat release rate  $\dot{Q}'$ . Top: Phase  $\varphi$  and gain  $G$  of the FDF for the velocity and the heat release rate ratio and their fit.

bustion chamber equipped with multiple swirl spray injectors. Considering an annular combustor like the MICCA-Spray system investigated at EM2C lab where the fundamental frequency of the first azimuthal mode (1A1L) is around 750 Hz (see Chapter 3 for details). The instability intervals in Figure 4.11 contains the eigenfrequency  $f = 750$  Hz of the 1A1L mode. One may note however that this criterion is not sufficient to ensure that the system will be linearly unstable. This will be the case if the growth rate at low amplitude is greater than the damping rate. For this to be the case, the gain of the FDF must be sufficiently large, but one also notices that this gain is relatively low at the frequency of the 1A1L mode ( $G < 0.4$ ). An issue that is not considered in the previous analysis is that of the possible influence of mutual interactions between adjacent flames and that of a suitable representation of the thermal conditions of the annular combustor. One then can expect that interactions between flames might modify the FDF determined on a single burner, but this is not yet quantified.

Note that the SICCA-Spray bench is equipped with a pressure sensor in the chamber (MC1), giving access to the acoustic pressure  $p'$  at the flame base during the forcing of the flame. This can be used to determine an FDF based on the pressure  $p'$  and on the heat release rate  $\dot{Q}'$  as shown in Figure 4.12. The behavior of this FDF is quite different from that of the standard FDF based on the velocity  $u'$ . The phase does not evolve in a linear fashion with increasing frequency, it is nearly equal to  $\pi/2$  over most of the frequency range. The measured  $p'_{ch}$  corresponds to the combustion noise induced by the flame in the combustion chamber. This radiated noise is in phase quadrature with the heat release rate fluctuation because  $p'_{ch} \propto d\dot{Q}'/dt$  (Hurle et al. (1968) and Schuller et al. (2002)). The gain has also a different shape as it decreases with frequency. No peak can be detected but there is a small bump around 450 Hz probably due to a coupling with a resonant mode of the system (see Figure 4.3). One may note that the gain and the phase barely change when the forcing amplitude is increased. These measurements confirm the observations made on the forced case in section 4.5 where it has been seen that the acoustic pressure in the chamber  $p'$  has a low amplitude that is not representative of the self-excited flame. The conclusion on the phase  $\varphi_{pQ}$  also holds as it is constant over most of the frequency range of the FDF.

## 4.7 Conclusion

This chapter is concerned with the determination of the Flame Describing Functions of swirling spray flames. These functions are obtained by making use of a single injector combustion system comprising a set of driver units. The system is used in two modes, the first of which corresponds to external modulation while the second pertains to self-excited oscillations. FDFs are determined in the first mode and the flame dynamics is observed using phase average imaging. In the second mode, the oscillation corresponds to a resonance of the system and is coupled by a longitudinal acoustic mode of the system. It is then possible to compare the flame response under external modulation to the response observed under self-excitation. Potential bands of instability are inferred from an examination of the measured FDF phase response

measured in the single injector configuration and the possibility of instability in the MICCA-Spray annular system is deduced from these data. The FDF measured considering the acoustic pressure recorded in the chamber is investigated. It is shown that the pressure is not a proper input to the FDF as it does not provide a suitable portrayal of the dynamics of the combustion region. In effect the measured pressure is more of an output of the unsteady flame and cannot be taken as an input. This illustrates the difficulty of experimental determinations of relations linking the heat release rate fluctuations to the pressure signal. It is finally shown that the classical FDF linking the heat release rate to the velocity fluctuation can be used effectively to predict instability trends of the single injector system and to predict possible unstable operation of the MICCA-Spray annular combustor but this can be done by accounting for the injector response if the velocity measurement point is not in the near vicinity of the flame zone.





## Chapter 5

# LES calculations of SICCA-Spray burner

*This chapter is concerned with the numerical simulation of a single injector configuration designated as “SICCA-Spray” under conditions similar to those used previously in the experimental investigation of the dynamics of this system (see Chapter 4). The objective is to see to what extent one can retrieve experimental features with Large Eddy Simulation (LES) of the tow phase reacting flow, but also to complement the data with numerical simulations. The simulation is also intended to provide further information on the mechanisms defining the flame response to external modulations and the coupling leading to self-sustained oscillations.*

### 5.1 Introduction

Many interesting phenomena linked to combustion instabilities that can be observed in the single tubular experiment SICCA-Spray are reported in Chapter 4. The literature review done in the previous chapters has shown the challenges for the Flame Describing Function (FDF) experimental determination. It is now interesting to consider the numerical evaluation of such a function to see if modern Large Eddy Simulations are capable of retrieving such phenomena. A quite comprehensive review of Large Eddy Simulations of gaseous flames is proposed by [Gicquel et al. \(2012\)](#). Simulations of several laboratory scales and real combustion chambers are summed up and compared to underline the potential of LES when dealing with mean and unsteady flows in complex geometries. Several attempts in the prediction of the flame dynamics that can be found in the literature are now reviewed. One major problem for the evaluation of this type of function is the number of required calculations. Despite recent progresses in massively parallel machines, researchers only have a limited number of possible simulations. As the FDF is based on the variation of the frequency and the amplitude of forced excitation, choices have to be made. A first step is to evaluate the Flame Transfer Function (FTF) which is the linear response of a flame when it is forced at one amplitude of excitation.

It is worth noting the study by [Armitage et al. \(2006\)](#) that was early done but with a Unsteady Reynolds-averaged Navier-Stokes (URANS) solver. The turbulent "V" shape ethylene-air premixed flame is first stabilized and compared with experimental OH PLIF images. The flame is then excited at two low frequencies and at two amplitudes to analyse the non-linearities of its response. The numerical results are compared to experimental OH PLIF and OH\* and CH\* chemiluminescence with a rather good agreement. The simulation seems to be able to catch qualitatively the flame motion. Please note that the swirl number of this device is pretty low.

[Tay-Wo-Chong et al. \(2010\)](#) used the LES solver AVBP to calculate a premixed flame externally excited with a broadband perturbation at one amplitude in order to retrieve the FTF and compare it to experiments. The simulation was run for more than 200 ms to have a satisfactory frequency resolution  $< 5$  Hz. The advantage of this technique is the relatively low computational cost as only one simulation is run. On the other hand, the gain and phase of the transfer function identification is quite complex and can be difficult when the flame is highly turbulent. The phase of the FTF is correctly predicted by the LES but the gain is largely underestimated by the simulation. More recent work by the same team ([Tay-Wo-Chong et al. \(2017\)](#)) and on the same burner focuses on the impact of the combustion model (heat loss and stretch) on the flame dynamics. After correctly predicting the flame shape, the same technique as described above is applied. A broadband perturbation is imposed at the inlet and the FTF is extracted by System Identification methods (auto and cross-correlation techniques) from only one calculation. This time, results prove to be much more in agreement with the experimental data for the phase as well as for the gain.

[Palies et al. \(2010\)](#) and [Palies et al. \(2011\)](#) experimented, modelled and simulated a premixed "V" shape flame with the AVBP code. The numerical simulation proved to be able to correctly predict the flame response to external forcing. It gave access to interesting phenomena such as the swirl number fluctuation and the flame roll-up impact on the flame dynamics. In particular, the role of the swirler as a mode converter is emphasized. In this work, two frequencies of interest are calculated but no FTF or FDF is extracted.

Once again with the AVBP solver, [Hermeth et al. \(2013\)](#) studied the dynamics of a real gas turbine combustion chamber at two amplitudes of excitation, one low and one high, in order to evaluate the non-linearity induced by the flame response. Once again, this study is done with gaseous fuel (methane) but only partially premixed. It was shown that the global level of heat release rate fluctuation is the same for both simulations, but significant differences were found in the equivalence ratio fluctuations with a strong impact on the mixture at the inlet.

It is also worth noting the study by [Han et al. \(2015\)](#) where the Flame Describing Function was calculated numerically and compared to experimental results. The

flame is premixed "V" shape flame stabilized by a bluff body. The results proved to be in agreement with experimental data but the flame do not exhibit a very complex dynamics and is operated under premixed conditions.

More recent work by [Mejia et al. \(2018\)](#) investigated on the influence of the temperature of a flame-holder on the combustion dynamics of a laminar premixed methane-air flame. They simulated the experimental bench using DNS as a very fine resolution of the flame holder is mandatory to correctly predict the flame position. One amplitude of fluctuation over a wide range of frequencies is applied to two types of flames: one stabilized on the flame holder and one slightly lifted. Results are compared to experiment and are proved to be qualitative but not quantitative as a major difference in the gain is found for one of the two flames.

This brief literature review demonstrates the research effort on flame dynamics prediction. It also shows that mainly FTF are predicted and only in the case of gaseous fuels injection. A significant step forward is possible by taking into account the effect of liquid fuels. One particular interest is the behavior of the fuel during the cycles of the flame oscillation.

The experimental test facility called SICCA-Spray and used in this document is presented in Figure 5.1. It is composed of a plenum, an injection system and a cylindrical combustion chamber. It has already been investigated numerically by [Lancien et al. \(2017\)](#) using LES but this was done to examine ignition dynamics and the system was equipped with the swirler that was used in the light-round experiments (this swirler features 3 mm channels). The LES were aimed at preparing full system calculation of the ignition process in the annular combustor MICCA-Spray. Thus SICCA-Spray was used to validate the methodology on a well instrumented system. The goal of the present investigation is to extend the previous numerical work to the case where the flame dynamics gives rise to self-sustained oscillations. Another aim is to see if it is possible to determine the Flame Describing Function and reproduce the experimental data using simulation. The work reported in this chapter comprises three main items:

1. An accurate description of the steady state flame and a comparison with experimental results,
2. The simulation of a self-excited flame to represent the naturally self-sustained combustion oscillation observed in the single injector configuration,
3. The evaluation of the Flame Describing Function at a few frequencies and levels of forcing and its comparison with experimental results.

This chapter is organized as follows. The numerical method is described in the next section 5.2. Detailed validations of the simulation are reported in Section 5.3 in the case of a steady flame, without any forcing or self-sustained thermo-acoustic instability. The self-excited case is then considered in section 5.4. This instability is obtained by changing the combustion chamber length. The oscillation then naturally appears

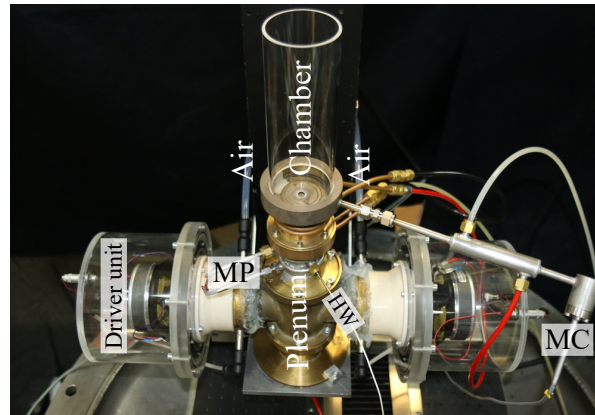


**Figure 5.1.** Experimental bench SICCA-Spray to be numerically calculated. Driver units are loudspeakers placed in the plenum. The hot wire (HW) is located in the plenum, 100 mm before the exit of the injector, in a laminar flow. Microphones (MP and MC) records the acoustic pressure in the plenum and in the chamber.

in the simulation and combustion is strongly coupled by a longitudinal acoustic mode of the chamber. Finally, section 5.5 is concerned with the estimation of the Flame Describing Function. It contains a comparison between results of calculations and experimental data.

## 5.2 Numerical set-up

This section describes the numerical set-up used to simulate the single injector combustion system. LES has been chosen for its ability to retrieve, at a reasonably affordable computational cost, the largest unsteady flow structures and the propagation of acoustic waves, that are prerequisite to the the study of flame dynamics. Moreover, access to large computational resources unlocks the possibility to mesh a representative domain of the experimental bench.

### 5.2.1 Numerical solver

Calculations are carried out with a three-dimensional compressible Navier-Stokes flow solver allowing acoustic and reactive flow calculations. Simulations are carried out on unstructured meshes using the AVBP software developed by Cerfacs in partnership with IFP Energies Nouvelles (Schönfeld and Rudgyard (1999)). The integration relies on a two-step Taylor-Galerkin weighted residual central distribution scheme with a third order precision in space and time (Colin and Rudgyard (2000)), for both liquid and gaseous phases. The Wall Adapting Local Eddy model developed by Nicoud and Ducros (1999) is used as a subgrid scale model.

The air and liquid phases are described by an Eulerian-Eulerian representation as-

suming that the droplet spray is mono-disperse. Six equations describing the liquid mass concentration, the volumetric droplet number, the three components of the liquid momentum and the liquid enthalpy are integrated with the gaseous phase equations (Boileau et al. (2008)). Droplet evaporation is described by the Abramzon-Sirignano model (Abramzon and Sirignano (1989)) by assuming a uniform droplet temperature. The combustion of the n-heptane spray is represented with a two-step mechanism (2S\_C<sub>7</sub>H<sub>16</sub>\_DP). This descriptions was derived in Shum-Kivan et al. (2016) and Paulhiac (2015) by making use of the methodology proposed in Franzelli et al. (2010). It is adjusted to reproduce the laminar burning velocity and the adiabatic flame temperature over a wide range of operating conditions. The Thickened Flame scheme (TFLES, Colin et al. (2000)) is employed to represent the unresolved small scale flame structures and the propagation of the flame and its interaction with turbulence. In this model, an artificial thickening of the flame front is used to resolve the flame on the mesh. This is coupled with an efficiency function  $\mathcal{E}$  that accounts for the subgrid scale flame wrinkling that is diminished by making use of the thickening procedure. The thickening factor is defined dynamically according to Legier et al. (2000) so that it only operates in the flame region. This procedure is used in combination with the efficiency function described in Charlette et al. (2002).

Navier-Stokes characteristic boundary conditions (NSCBC) derived in Poinso and Lele (1992) are employed at the inlet, outlet and lateral boundaries. In the experiment, the air injection is made with two tubes plugged in the plenum. It has been chosen to cut part of the plenum in the numerical model and impose a mass flow rate at the inlet as well as temperature and gaseous species mass fractions. At the outlet, the pressure is set to atmospheric pressure 101,325 Pa. Adiabatic conditions are imposed at the walls except in the combustion chamber where isothermal walls are considered. Slip conditions are applied to the liquid velocity and a wall law is defined for the gaseous velocity on certain surfaces.

The fuel injection patch needs a more detailed treatment since the internal geometry producing the hollow cone of the fuel spray is not known and therefore not simulated. Under these circumstances it is natural to impose experimentally determined profiles for the droplet velocities and for the particle number density. These are measured 2 mm downstream the injector. Since the liquid phase is represented by a mono-disperse spray, the choice of the injected droplet diameter requires special care. Under such conditions, one often uses the experimental Sauter Mean Diameter (SMD)  $D_{32} = (\sum_N d^3) / (\sum_N d^2)$  to represent the polydisperse spray (Lefebvre (1989)). The  $D_{32}$  measured inside the spray ( $D_{32} = 20 \mu\text{m}$ ) has firstly been used for the first simulations carried out. A detailed study has been done by Lancien et al. (2017) to derive an optimal value to better represent the spray, depending on the physical parameters that are identified as important to retrieve.

The overall equivalence ratio considered for both simulation and experiment for this study is  $\phi = 0.84$  with a fuel liquid mass flow rate  $\dot{m} = 0.144 \text{ g s}^{-1}$ .

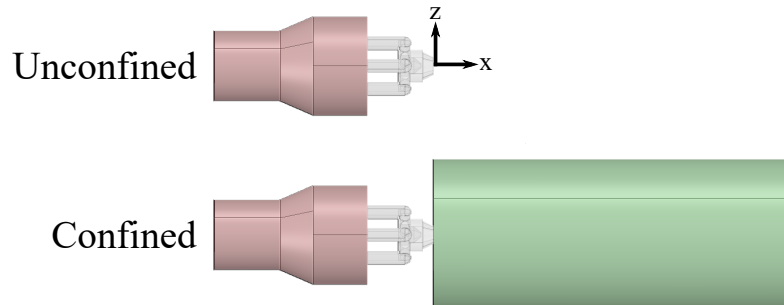


**Figure 5.2.** Simulated geometries with, in red, the plenum, in grey, the injector and, if this applies, in green, the combustion chamber. Top: Unconfined numerical domain for simulation validations. Bottom: Confined numerical domain with a 165 mm long chamber wall, representing the SICCA-Spray chamber.

### 5.2.2 Geometry

The simulated domain is defined in Figure 5.2 with two main geometries: one without confinement - the combustion chamber is not considered - and one with confinement. The reference plane, defining the altitude  $x = 0$ , for the different simulations is chosen to be the exit of the injector. The first configuration considered is used for validation purposes only: the optical access is simplified when the circular quartz tube is absent and laser diagnostics like Laser Doppler Velocimetry (LDV) are easier to implement. Moreover, to validate the liquid phase models with accurate data such as droplet diameters, it is more convenient to do experiments without a quartz wall that may be severely wetted by the liquid droplets thus affecting the quality of Phase Doppler Anemometry (PDA) measurements. As a consequence, the unconfined configuration is used for non-reactive flow and liquid injection validation. The confined geometry (Figure 5.2, bottom) is used for reactive simulations. In both geometries, the plenum is much shorter than the one used in the experimental bench. This numerical choice has several explanations:

- In the experiment, the gaseous injection system is placed at a relatively large distance from the exit of the burner as can be observed in Figure 5.1. The convection time of any applied flow perturbation would require a larger amount of time that cannot be afforded numerically.
- Simulations with the entire plenum have run but feature meshing issues at some delicate geometrical points (like corners or rapid area changes, ...). The mesh quality had to be increased in regions where no interesting information would have been gathered. This would have, once again, increased the cost of the calculation.
- In the experiment, as discussed in Chapter 4, the reference point for the measurement of the velocity perturbation is the hot wire, placed 100 mm before the

exit of the swirler.

Note that the rest of the simulated domain is the exact representation of the experiment. In conclusion, it has been decided to cut the plenum at the altitude  $x = -100$  mm. As a consequence, this section is the gaseous inlet for the geometry. This choice is then much more convenient when it will come to force the flame by modulating the incoming air flow. A secondary volume is added around the chamber (not shown in Figure 5.2) to represent the atmosphere. This allows to place the output boundary condition far away from the region of interest, which is the combustion zone. Even if this choice adds a certain number of elements to the mesh, it requires a relatively small addition of grid points but allows an improved description of the physics in the combustion chamber. Figure 5.3 presents cuts of the numerical domain including the volume representing the atmosphere. To model the natural entrainment of the air surrounding the experiment induced by the mixture escaping from the chamber and by the room exhaust vent, it is convenient to add a slow co-flow of  $0.3 \text{ m s}^{-1}$ .

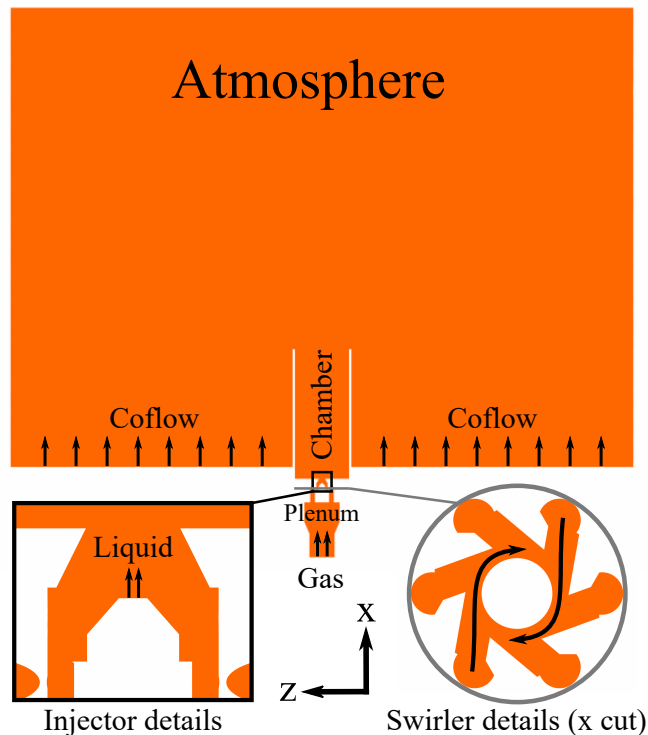


**Figure 5.3.** Cuts of the geometry depicting the atmosphere size with close-up views on the injector internal geometry (bottom left) and on the swirler (bottom right). Gas, liquid, and co-flow inlets are indicated.

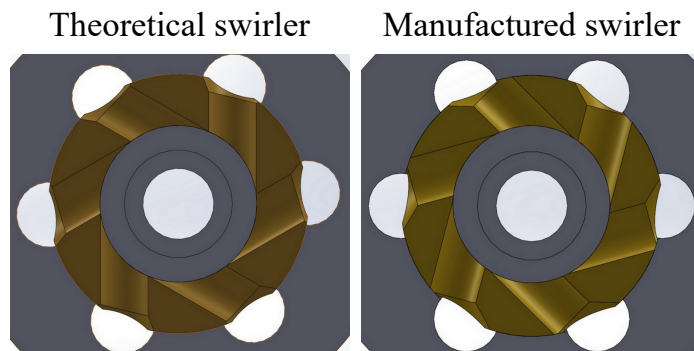


**Figure 5.4.** Cuts of the assembly of the main air ducts leading to the swirler. Left: Theoretical assembly. Right: Manufactured assembly. The swirler has been reconstructed via a 3D-scanner.

### 5.2.2.1 Swirler manufacturing problems

As mentioned earlier, the main difference between this new geometry and the one calculated by [Lancien et al. \(2017\)](#) stands in the swirler design. It has been shown in the different chapters of this document that the swirler with 4.5 mm holes exhibits relatively strong self-excited instabilities. In spite of this interesting behavior, when controlling the manufacturing quality of the produced brass piece, many differences between the theoretical swirler and the manufactured one were noticed. A 3D-scanner has been used to measure the many dimensions of this component. Results show a notable difference between the theoretical design and the one that has been manufactured as one can be seen in [Figure 5.4](#). Two main defects can be detected: a first one lies in the alignment of the horizontal tubes with the vertical ducts and a second one in the shape of the cone on the outer part of the swirler. These differences have a sizable impact on the swirling flow that is being generated. After the discovery of this problem, it was decided to continue the analysis with this swirler geometry because of its rich flame dynamics leading to the partial blow-off of the MICCA-Spray chamber. Note that the simulated geometry corresponds to the manufactured assembly measured by the 3D-scanner.

### 5.2.3 Boundary conditions

The numerical domain is bounded by the gas input and the atmosphere outflow (see [Figure 5.3](#)). This geometry defines several boundary conditions that are presented in [Table 5.2](#). Parameters such as the gas and liquid injection temperatures and the species

	Air	n-Heptane
$\dot{m}$ (g s <sup>-1</sup> )	2.59	0.144

**Table 5.1.** Air and n-heptane mass flow rates used through this chapter.

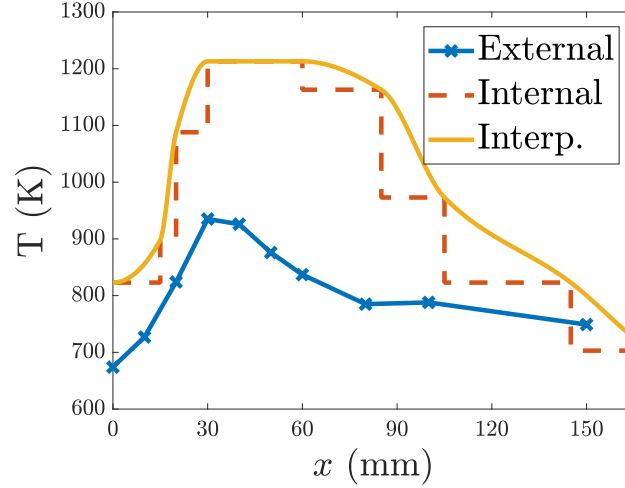


**Figure 5.5.** Wall temperature measurements on the external (blue) and internal (orange and yellow) parts of a 200 mm quartz tube when the burner is operated at nominal conditions.

mass fractions are specified. Table 5.1 indicates the nominal injection conditions used throughout this chapter to match the experimental conditions  $\phi = 0.85$ ,  $\mathcal{P} = 6.5 \text{ kW}$  and  $U_b = 43 \text{ m s}^{-1}$ . A relaxation coefficient  $K$  of the different boundaries needs to be adapted to the geometry. It can be estimated via the following equation proposed by Rudy and Strikwerda (1980):

$$K = \sigma (1 - \mathcal{M}^2) c/L \quad (5.1)$$

with  $\mathcal{M}$  the maximum Mach number in the system,  $L$  a characteristic size,  $c$  the speed of sound and  $\sigma$  a constant. One may estimate that  $\mathcal{M} = U_b/c \sim 0.15$ ,  $c \sim 700 \text{ m s}^{-1}$  in the chamber ( $T \sim 1200 \text{ K}$ ) and  $L = 570 \text{ mm}$  the size of the atmospheric volume. Selle et al. (2004) proposed to choose  $0.1 < \sigma < \pi$  to suppress reflected acoustic waves that perturb the flow at the inlet and outlet and to ensure that the mean pressure stays constant. Chosen relaxation coefficients are included in Table 5.2.

Wall temperature is an important parameter if one wishes to retrieve the proper flame behavior. In a first approximation, one may consider that the temperature is a constant along the chamber axis an assumption that is usually adopted in the acoustical analysis of the system. This assumption is too simple when dealing with fluid mechanics treated by LES. As it has been seen in previous chapters, the flow establishes outer recirculation zones (ORZ) which, when the flame is stabilized, induce a recirculation of hot burnt gases next the walls, changing their temperature. A 1D axial temperature gradient was measured on the experimental bench and is included in the numerical simulation. Figure 5.5, shows the measured internal and external temperatures of the

Patch	Boundary conditions	Relaxation coefficient	Physical parameters	Species mass fractions
Gas inlet	Flat velocity profile (RHO UVW)	$1000 \text{ s}^{-1}$	$\dot{m}_{air} = 2.59 \text{ g s}^{-1}$ $T = 298 \text{ K}$	$Y_{O_2} = 0.233$ $Y_{N_2} = 0.767$
Co-flow inlet	Target velocity (UVW)	$500 \text{ s}^{-1}$	$U = 0.3 \text{ m s}^{-1}$ $T = 298 \text{ K}$	$Y_{O_2} = 0.233$ $Y_{N_2} = 0.767$
Liquid inlet	Velocity profile (alpha UVW)	×	$\dot{m}_{fuel} = 0.144 \text{ g s}^{-1}$ $T = 298 \text{ K}$	$Y_{C_7H_{16}} = 1.0$
Walls	No slip	×	×	×
Chamber backplane	Wall law	×	$T = 450 \text{ K}$	×
Chamber walls	Isothermal	×	$T(x)$	×
Outlet	Outlet P 3D	$100 \text{ s}^{-1}$	$p_0 = 101,325 \text{ Pa}$	×

**Table 5.2.** NSCBC conditions for the different boundary conditions.

quartz wall. The external temperature was estimated with a K-thermocouple. The measurement is done every 10 mm along the quartz height when the flame has been running for 10 min in order to reach stable thermal conditions. The inner temperature is deduced by using a thermochromic paint with 14 levels of color changes between 433 and 1513 K. Note that these levels are not equally distributed in this temperature range. Each color change indicates the minimum local temperature which the paint has been exposed to. A thin layer of paint is deposited on the quartz inner part and exposed to the flame for 5 min. The time of exposure has to be limited because the paint color drifts as it is exposed to high temperatures. It is then possible to interpolate the temperature using “pchip” algorithms as shown in the figure. These results are used to impose the temperature of the chamber wall  $T(x)$  as described in Table 5.2.

#### 5.2.4 Mesh

The geometry shown in Figure 5.3 is meshed using an unstructured grid of tetrahedra with varying sizes. A number of rules need to be used in order to have a sufficient number of cells in important regions like those corresponding to the swirler channels, the flame zone, the liquid injection patch and the internal components of the injector. These parameters are summarized in Table 5.4.

For the confined geometry, the calculated domain is discretized with 16.7 millions cells, corresponding to 2.9 millions nodes (see Figure 5.6). The mesh quality is assured with a minimum tetrahedron volume of  $1.4 \times 10^{-4} \text{ mm}^3$ , a skewness of 1 and a

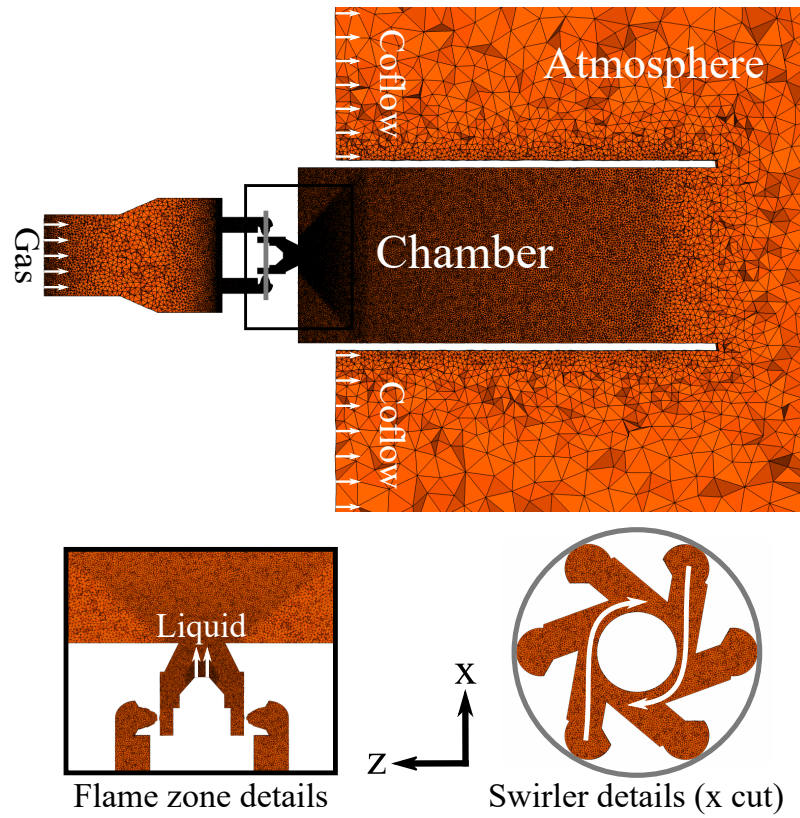


**Figure 5.6.** Meshed numerical model with flame tube and atmosphere.

sliver of 348. The grid is optimized in order to have the largest minimum tetrahedron volume which defines the physical time step of the simulation  $\Delta t = \text{CFL} \Delta x / (u + c)$  with  $\text{CFL} = 0.7$  the fixed CFL number. In the unconfined geometry case, these quantities remain nearly the same.

Part	Characteristic size	Number of elements
Swirler tubes	4.5 mm	20
Liquid injection patch	2 mm	15
Injector exit	8 mm	40
Flame zone (thickened)	1 mm	5

**Table 5.4.** Number of element for important parts of the geometry.

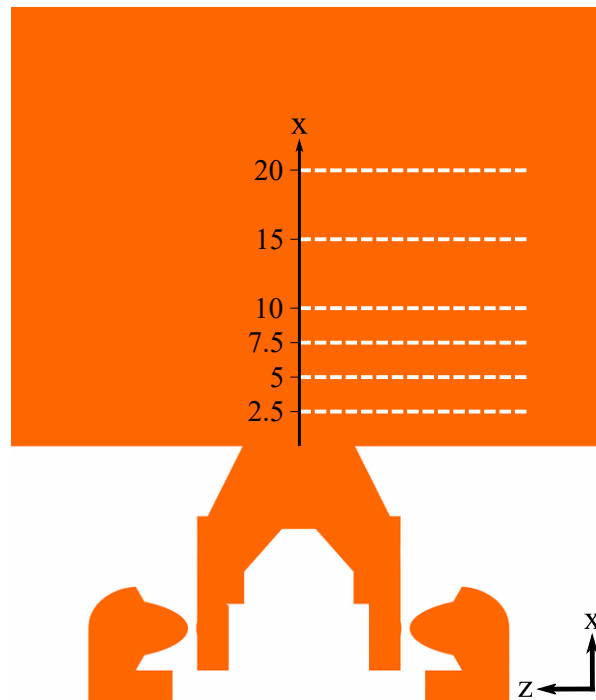


**Figure 5.7.** Measurement planes for comparison of numerical results with experimental data. Distances are in millimeters.

### 5.3 Steady-state flame

The numerical set-up presented in the last section is now used to establish a steady turbulent flame in the combustion chamber. This work can be decomposed into three stages. The first is to establish and validate the cold flow by just injecting pure air in the system. This is done in section 5.3.1 with quantitative experimental comparisons. The second step described in section 5.3.2 is to choose the parameters for the liquid phase and validate calculations of the spray with experimental measurements. The last step, detailed in section 5.3.3, is to ignite the mixture with a hot kernel and stabilize an “M” shaped flame as observed experimentally in the confined geometry.

#### 5.3.1 Cold flow simulations

In this first step the cold flow is established for an air mass flow rate  $\dot{m}_{air} = 2.59 \text{ g s}^{-1}$  without and with confinement, without and with liquid fuel injection. The different comparisons between experimental and numerical results, are carried out in the transverse planes shown in Figure 5.7. In this section, the time step is set to  $\Delta t = 7 \times 10^{-8} \text{ sec /ite}$  and remains fixed in the two cases with or without confinement.

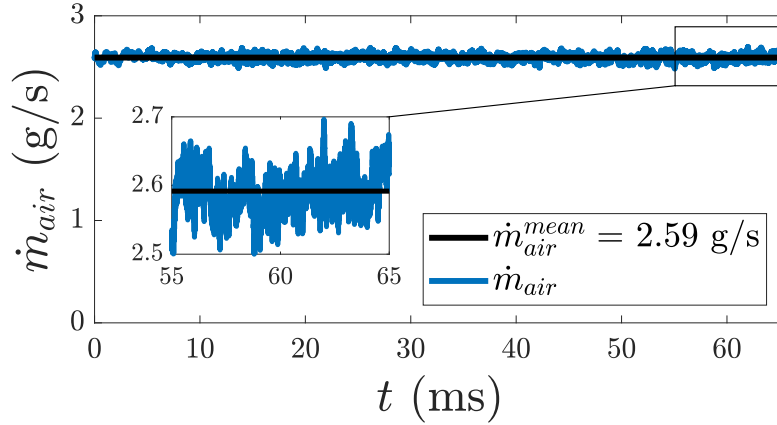


**Figure 5.8.** Air mass flow rate  $\dot{m}$  at the numerical domain inlet with a zoom on the last 10 ms.

### 5.3.1.1 Without confinement

The simulated geometry is that shown in Figure 5.4. Pure air is injected at 298 K through the inlet boundary of the numerical domain with a target flow rate of  $2.59 \text{ g s}^{-1}$ . The air mass flow rate fluctuations are plotted in Figure 5.8. One can see that the average value, in black, is the desired flow rate of  $2.59 \text{ g s}^{-1}$  and that its RMS fluctuations are less than 2% as seen on the close-up view. The simulation is run for 60 ms to reach steady state and then averaged for another 40 ms which corresponds to a total physical time of 100 ms.

Numerical results are now validated with LDV measurements in different transverse planes. The local velocity vector  $\{U_r, U_\theta, U\}$  is measured and the three components,  $U_r$  the radial velocity,  $U_\theta$  the azimuthal velocity and  $U$  the axial velocity can be used for detailed comparisons. Figure 5.9 present the results for six axial positions in the chamber and for the three velocity components. Experiments are plotted as orange symbols and numerical results are shown as black solid lines. Each numerical curve is the result of an azimuthal averaging of each component: the velocity is extracted and then averaged on cuts every  $\theta = \pi/90$  from 0 to  $2\pi$ . The first plots show the radial velocity. Note that this quantity is usually difficult to determine experimentally. Velocities are relatively small. The agreement between experimental data and numerical results is not perfect. But it is important to keep in mind that the radial velocity component is of lesser importance in the characterization of a swirling flow and the physics of such flows can be well captured by the simulation even if  $U_r$  does not perfectly match the experimental data. Examining the tangential velocity  $U_\theta$ , the fit between the numerical and the experimental results is more acceptable. The global trend is captured with a relatively large maximum rotating velocity of  $\sim 50 \text{ m s}^{-1}$  in both cases at  $x = 2.5 \text{ mm}$ . The major problem is the position of the maximum which is not well estimated in the simulation. This reduces the jet expansion rate in the LES.

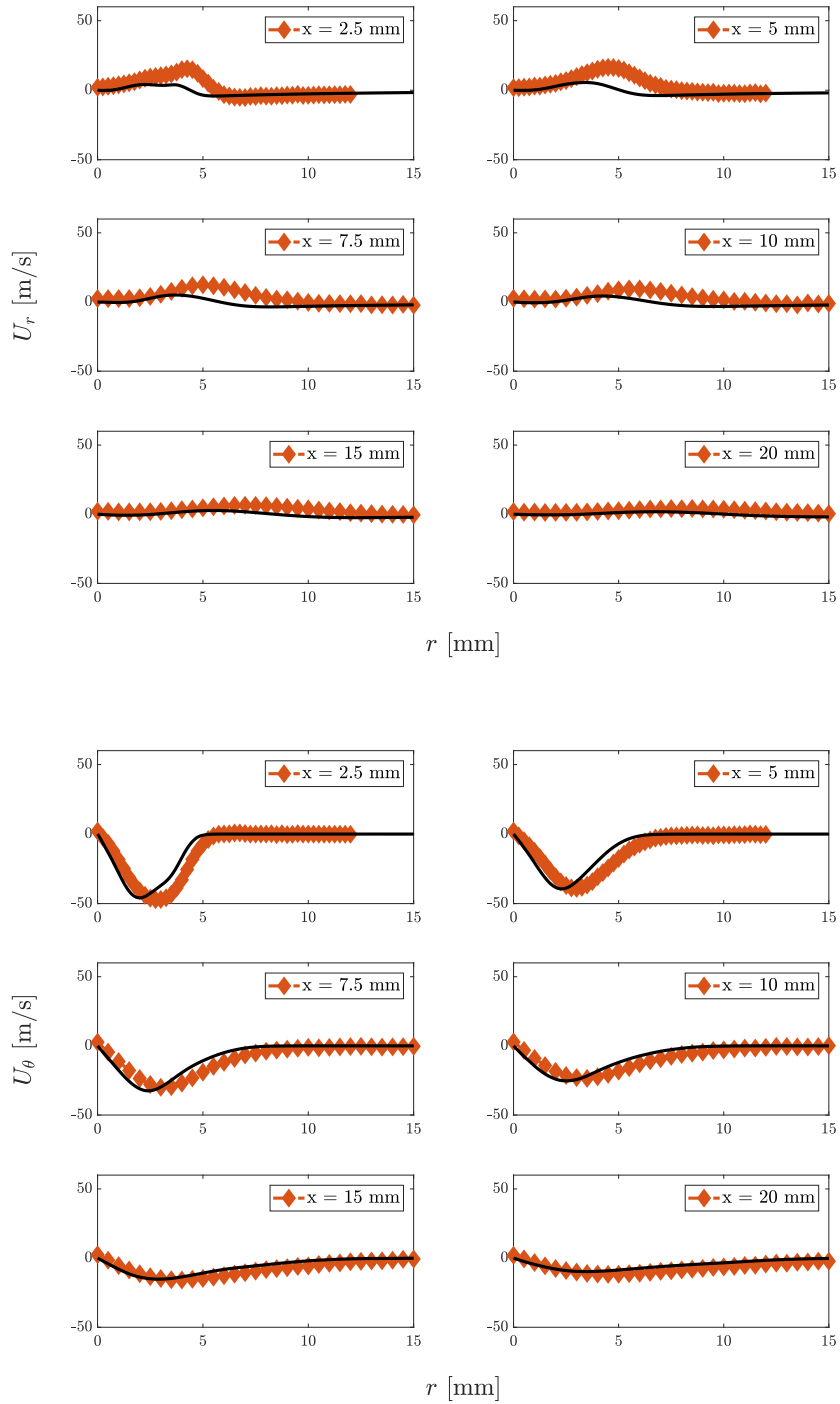


**Figure 5.9.** Experimental (orange) and numerical (black) radial  $U_r$  (top), azimuthal  $U_\theta$  (bottom) velocities without confinement for pure air injection.

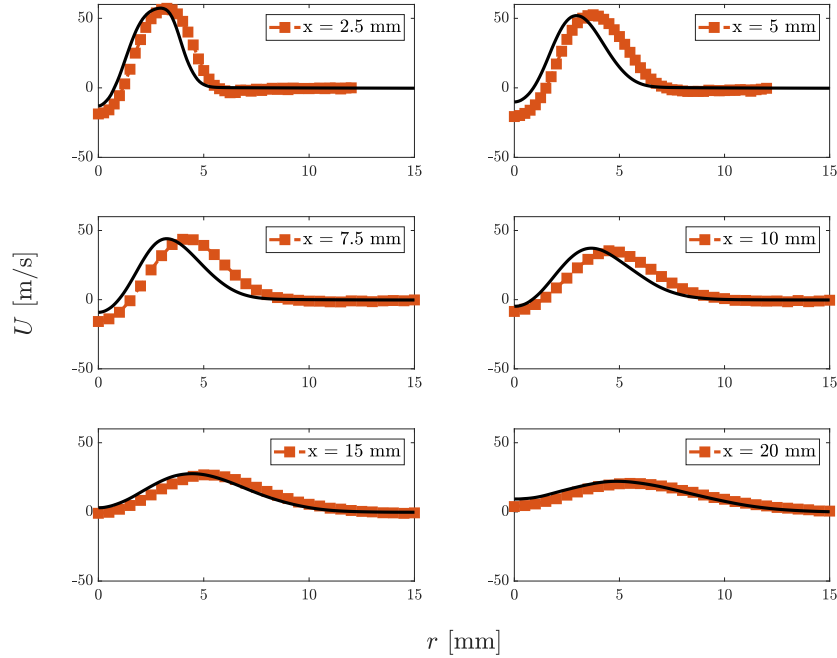


**Figure 5.9.** Experimental (orange) and numerical (black) axial  $U$  velocities without confinement for pure air injection.

Various elements have been tried to correct this problem. A wall law has first been applied on the convergent end-piece to better catch the physics of the flow. A finer mesh, with a scale reduction of 0.75 of the original mesh, has been used to verify the convergence of the calculation. This confirmed that the first mesh was adequate. The major problem that was identified is the precise definition of the geometry as explained in section 5.2.2.1. More than ten different geometries have been tested and have revealed a strong sensitivity of the flow to the alignment of the air ducts of the injector with the swirler tubes (see Figure 5.4). The last plots in Figure 5.9 show the axial velocity  $U$ . Once again, the peak velocity is well captured in all sections. The agreement between experimental data and numerical results is adequate. As for the azimuthal velocity, the jet expansion is not well predicted with, at  $x = 5$  mm, a maximum velocity at  $r = 3$  mm in the numerical results and at  $r = 4$  mm in the experimental data. The intensity of the recirculation zone is also under-predicted with minimum values of  $-12 \text{ m s}^{-1}$  where the experimental results indicate  $-18 \text{ m s}^{-1}$  at  $x = 2.5$  mm. Whatever the effort, it was not possible to perfectly match the experimental velocity profiles.

It is also important to verify characteristic numbers of the flow such as the swirl number and the head loss of the system. The swirl number  $S$  can be defined by the ex-

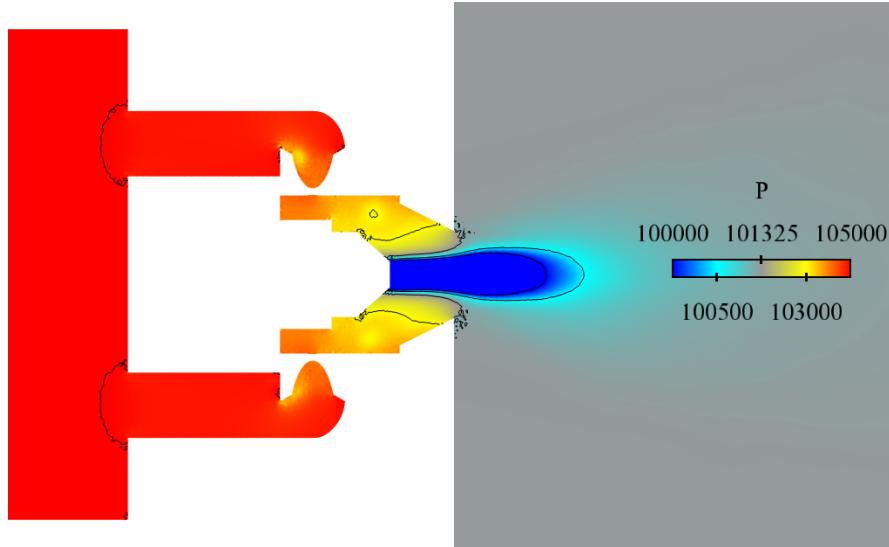


**Figure 5.10.** Static pressure distribution in the plenum and in the chamber. The scale is adapted to plot the maximum pressure in red (105,000 Pa).

pression proposed in Table 5.5 with  $R$ , a reference radius. In this case, the radius is fixed to  $R = 4$  mm and corresponds to the exit radius of the injector. This equation is the result of several assumptions to simplify terms that could not be experimentally estimated such as the pressure difference in the injector. The head loss  $\Delta p$  defined by the difference between the maximum static pressure in the plenum and in the chamber is also an important design parameter. In the case of the SICCA-Spray burner, the chamber is at atmospheric pressure, so the reference pressure is  $p_0$ . The head loss was measured between the plenum and the atmosphere with a Kimo MP111 pressure-gauge. The distribution of static pressure in the injector geometry can be seen in Figure 5.10. These two quantities are synthesized in Table 5.5. It is worth noting that the predicted head loss is in good agreement with experiments and that the relative difference of 5% is quite small. The results are less satisfactory for the swirl number. One finds a difference of 18% between experimental and numerical results. As explained in the last paragraph, this difference is linked to the slight errors in the jet expansion rate. To calculate the swirl number, one has to integrate  $U(r)$  over the radius  $R$  of the jet. As  $U(r)$  is not suitably predicted, this leads to an underestimation of the swirl number as observed in Table 5.5.

Quantity	Equation	Experiment	Simulation
Swirler number	$S = \frac{\int_0^R 2\pi\rho U U_\theta r^2 dr}{R \int_0^R 2\pi\rho U^2 r dr}$	0.55	0.45 (−18%)
Head loss	$\Delta p = p - p_0$	3900 Pa	3700 Pa (−5%)

**Table 5.5.** Experimental and numerical estimations of the swirl number and head loss.

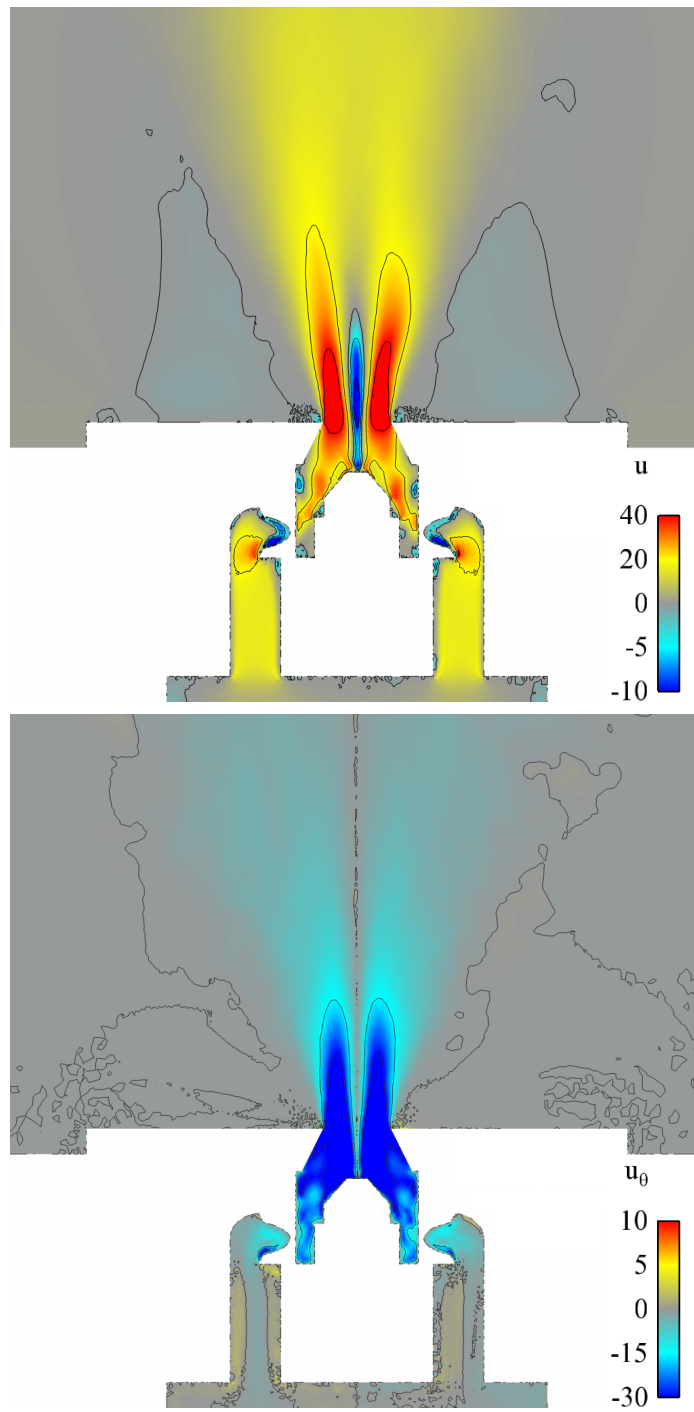


**Figure 5.11.** Distributions of axial  $U$  (top) and tangential  $U_\theta$  (bottom) velocities in the injector and in the chamber colored by their magnitudes.

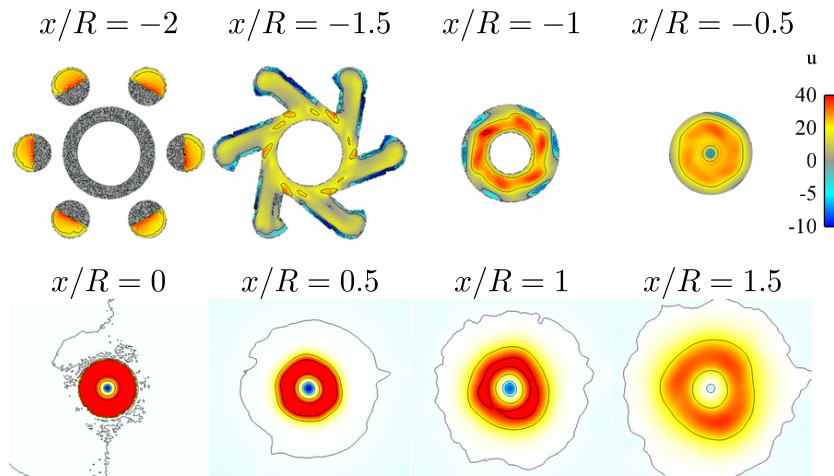


**Figure 5.12.** Axial velocity  $U$  distribution with iso-contours in various axial sections ( $x$  constant), before and after the injector exit, to underline the flow inhomogeneities developing in the chamber. Flow is averaged over 60 ms.

The jet expands as soon as it exits the injector as can be seen in Figure 5.11 which shows distributions of  $U$  and  $U_\theta$ . One can see that a large Central Recirculation Zone (CRZ) is established by the swirled jet. As observed on the velocity plots, the jet exhibits very high axial and tangential velocities. It is worth noting that the jet has a slight asymmetry even if the simulation is converged. Several horizontal cuts ( $x$  constant) are shown in Figure 5.12 from  $x/R = -2$  to  $x/R = 1.5$ . The distributions of axial velocity indicate that the flow is first well balanced between the different injection ducts. The air then enters the swirler that induce the flow rotation (not shown here as the axial velocity is plotted). The flow then progresses towards the exit of the injector, accelerating through the convergent end-piece. Relatively small inhomogeneities seem to appear near  $x/R = 0$  but, as soon as the jet expands in the chamber, much larger inhomogeneities appear and are made more apparent near  $x/R = 1.5$ . These are typical of the asymmetry every  $2\pi/6$  that can be observed in the geometry. One may also observe that the geometry is simulated without any confinement. This produces a swirled flow with a strong CRZ but with very weak Outer Recirculation Zones (ORZ) that are characteristic of unconfined swirled flows.

### 5.3.1.2 With confinement

The parameters of the simulation are kept identical to those used without confinement but the geometry is now calculated with a flame tube of 165 mm length as in Figure 5.4, bottom. Pure air is injected at 298 K through the inlet boundary with a target flow rate of  $2.59 \text{ g s}^{-1}$ . The simulation is run for 100 ms in total and the results are averaged over the last 40 ms. The swirl number and the head loss remain of the order of those calculated without confinement. The velocity profiles in different axial sections in the chamber are plotted in Figure 5.13. As for the simulation without

confinement, the global structure of the flow is well captured. The CRZ, as for the previous case, is under-predicted with a numerical minimum velocity of  $-13 \text{ m s}^{-1}$  while the experimental value is  $-21 \text{ m s}^{-1}$  at  $x = 2.5 \text{ mm}$  from the exit of the injector. The RMS values of the different velocity components are calculated and compared to those measured with the LDV system in Figure 5.14. One can see an acceptable agreement between the experimental and numerical data except, for the jet expansion which shifts the RMS peaks with an underestimation of peak values. This means that the numerical flow features a lesser degree of turbulence than the experimental flow.

### 5.3.2 Liquid injection

The complexity of the liquid phase dynamics forces current simulations to model part of it. First of all, the physics of the generation of small droplets from a liquid sheet, known as primary atomization, cannot be rendered in such simulations because of computational costs and this has to be modelled. It is usually decided to directly inject a certain distribution of liquid droplets in the airflow, avoiding the calculation of the separation of the liquid phase into a spray, creating large droplets that then interact and generate smaller droplets.

The second issue is the representation of the droplet spray. There are two major approaches, the first of which exemplified by Sanjosé et al. (2011) and Senoner et al. (2009) relies on an Eulerian-Eulerian description of the two-phase flow system. The principle is to transport moments of the number density function (NDF). The second approach adopted for example by Luo et al. (2011) relies on an Eulerian-Lagrangian model where a set of individual particles are being tracked to simulate the spray. These two methods have their strengths and weaknesses. As indicated in the last chapters, the n-heptane spray in the single injector system mainly comprises small droplets with a narrow dispersion in diameter, with a relatively limited poly-dispersion. This simulation is based on the numerical framework developed by Lancien et al. (2017) which have chosen a mono-disperse spray of droplets and have adopted an Eulerian-Eulerian framework for the simulation of the transient ignition of the MICCA-Spray burner. At the time of the study, the validation of the Lagrangian tools in the AVBP solver was not fully performed. Moreover, the Eulerian-Lagrangian approach would have demanded the use of a computational load balancing that is complex to handle on parallel machines as shown by Garcia (2009).

In conclusion the liquid phase is described with an Eulerian-Eulerian mono-disperse approach validated by Lancien et al. (2017) in the studied configuration. This approach yields results that are in good agreement with the experimental data in cold and hot flow validations. Flames obtained in this way have also been compared to the experimental flames and had very similar shapes. In the study presented in the present document, the liquid is injected through a 2 mm circular patch located at the atomizer tip. This diameter is larger than the size of the atomizer orifice in order to correctly reproduce the behavior of the liquid spray with enough elements to represent the in-

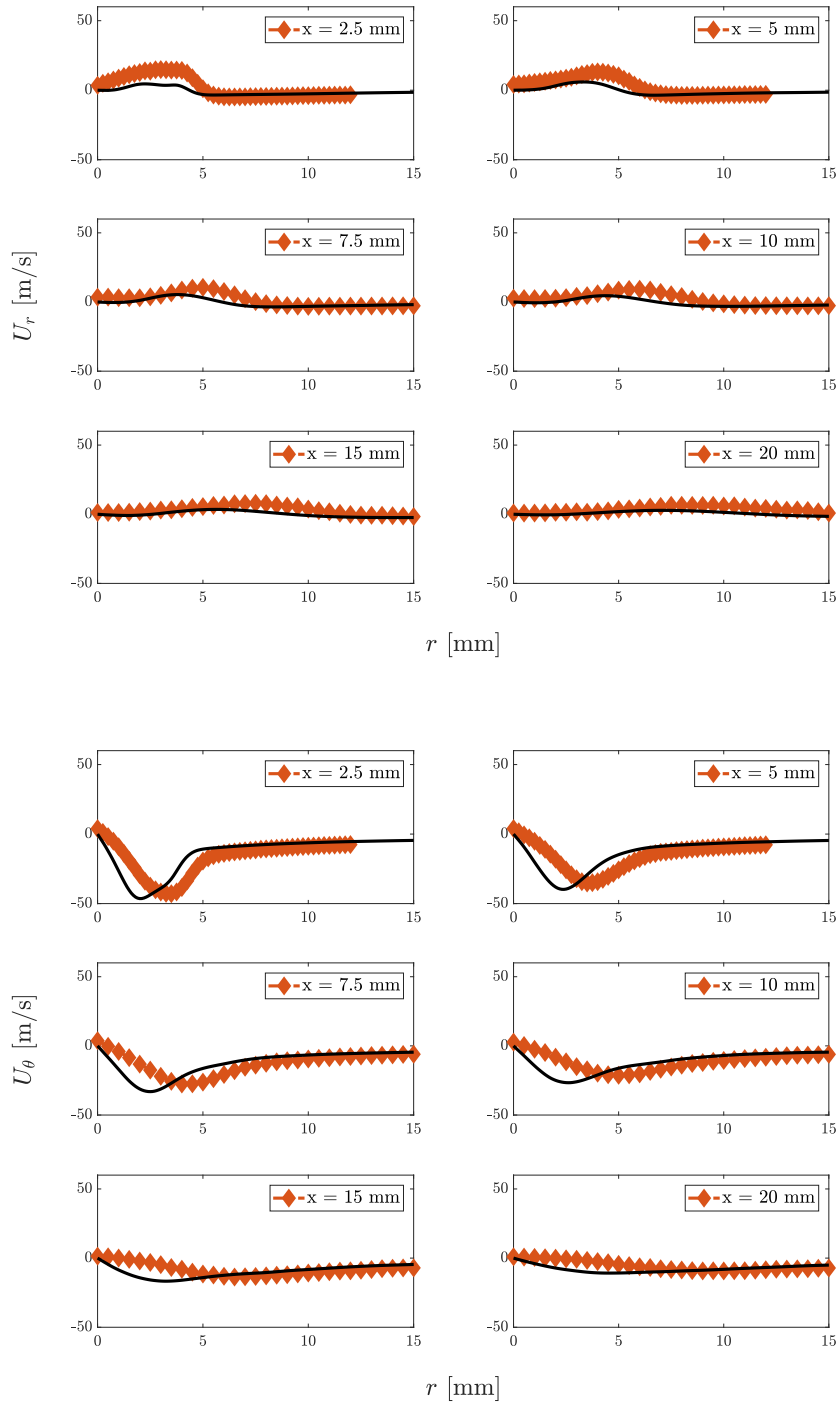


**Figure 5.13.** Experimental (orange) and numerical (black) radial  $U_r$  (top) and azimuthal  $U_\theta$  (bottom) velocities with confinement and pure air injection.

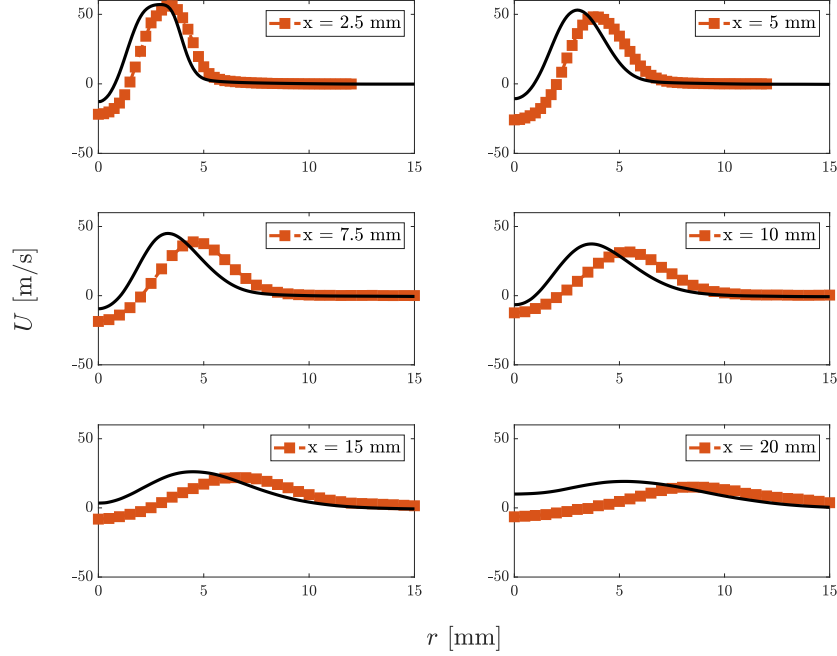


**Figure 5.13.** Experimental (orange) and numerical (black) axial  $U$  velocities with confinement and pure air injection.

jection patch and, at the same time limit its size. This defines a minimal surface for the liquid patch, larger than the experimental surface but again this model does not aim at catching the primary atomization of the spray.

The spray is experimentally characterized, but, as the liquid injection is mono-disperse in the simulation, one has to use an optimization of the injected diameter to represent the poly-disperse nature of the droplet mist. This optimization has been carried out by [Lancien et al. \(2017\)](#) by making use of several injected diameters  $d_l^{inj}$  in combination of Polynomial Chaos Expansions to reduce the number of tests. The objective was to select the most representative diameter by making use of the two-phase laminar burning velocity  $S_l^{t-p}$  proposed by [Ballal and Lefebvre \(1981\)](#):

$$S_l^{t-p} = \alpha_g \left[ \frac{C_3^3 \rho_l D_{32}^2}{8C_1 \rho_g \ln(1+B)} + \frac{\alpha_g^2}{S_L^2} \right]^{-0.5} \quad (5.2)$$

with  $\alpha_g$  the gas thermal diffusivity,  $\rho_l$  and  $\rho_g$  the liquid and gaseous densities,  $B$  the Spalding transfer number and  $S_L$  the gaseous laminar burning velocity. This expression accounts for poly-dispersion through the coefficients  $C_1 = D_{20}/D_{32}$  and  $C_3 = D_{30}/D_{32}$ , which are both equal to unity in the case of a mono-disperse spray. When optimized, one finds that  $d_l^{inj} = 15.3 \mu\text{m}$  in order to correctly reproduce the

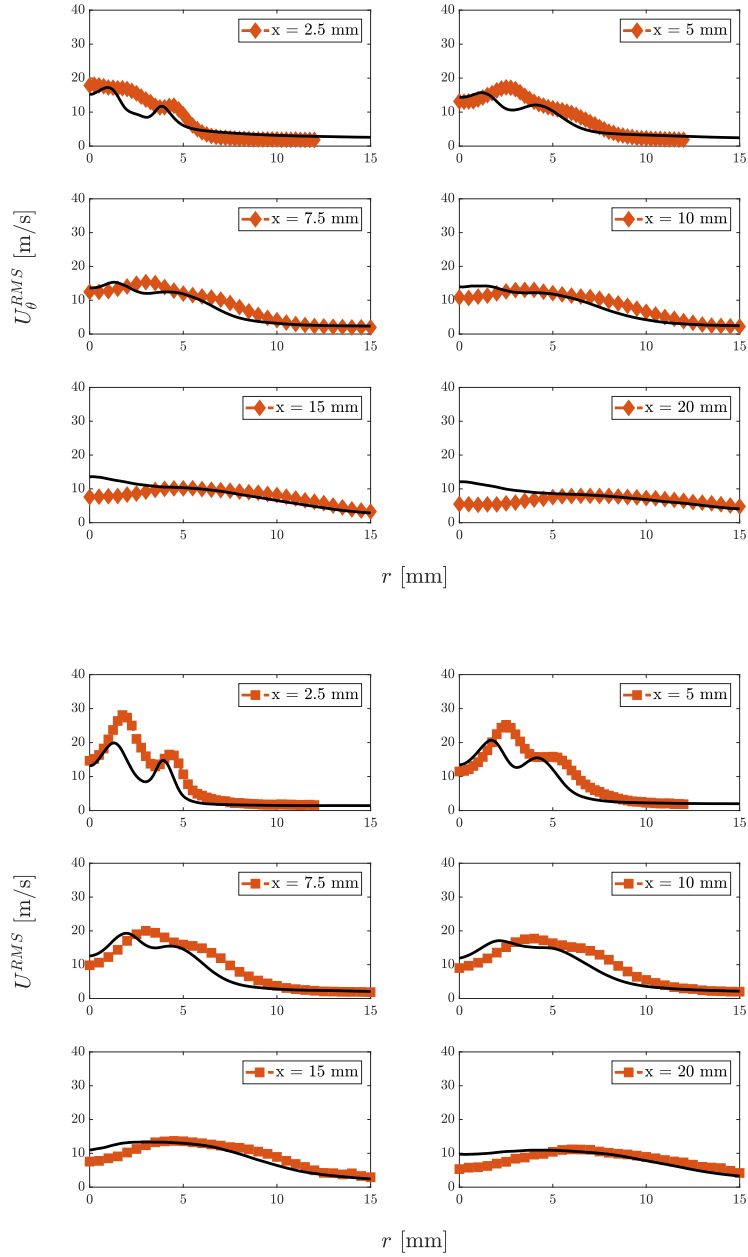


**Figure 5.14.** Experimental (orange) and numerical (black) RMS values for the azimuthal  $U_{\theta}$  (top) and axial  $U$  (bottom) velocities with confinement and pure air injection.

burning velocity of n-heptane in air. One may look the cited article for the full explanation of the method and a comparison between experimental and numerical results. Nevertheless, it is interesting to study the impact of the liquid fuel on the air velocity

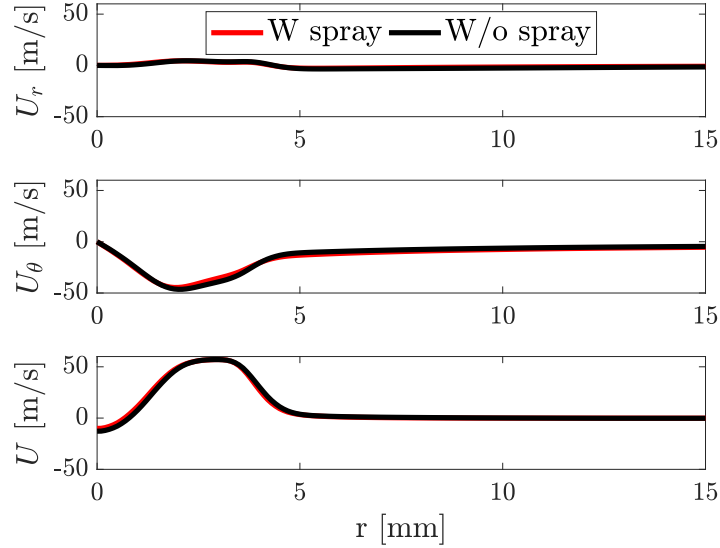


**Figure 5.15.** Gas velocity components without liquid injection (black lines) and with liquid injection  $\dot{m}_{fuel} = 0.144 \text{ g s}^{-1}$  (red lines) at  $x = 2.5 \text{ mm}$ .

profile. The numerical model used for the two-phase flow includes a two-way coupling between gaseous and liquid phases, meaning that the droplet spray can have an influence on the air flow. One may now compare the air flow in the case where no fuel is injected to the case where a nominal fuel flow rate is injected (Figure 5.15). One can see that the two lines are nearly collapsing, indicating that differences are quite small. As a consequence, one can deduce that the liquid droplets have a small influence on the air flow. This is easily argued as the fuel load of the air is rather low in the experiment and that the droplets have only a weak influence on it.

### 5.3.3 Flame stabilization

Once the liquid phase is well stabilized in the chamber after 100 ms of simulation, the system is ignited by a spherical gas kernel of hot gases with a diameter  $d = 10 \text{ mm}$  corresponding to the energy deposited by a spark igniter in the experimental test bench.

The Thickened Flame model for Large Eddy Simulation (TFLES), developed by [Colin et al. \(2000\)](#), artificially thickens the flame front by a factor  $F$ . Increasing the thickness of the flame front can result in a lesser sensitivity of the flame layer to the local turbulence of the flow. This phenomenon is taken into account with an efficiency function  $\mathcal{E}$  that accounts for the subgrid scale flame wrinkling. In the present study, this factor is set to  $F = 5$ .

After a few milliseconds, the flame stabilizes in the combustion chamber and adopts an “M” shape, slightly lifted from the lips of the injector, as can be seen in Figure 5.16.

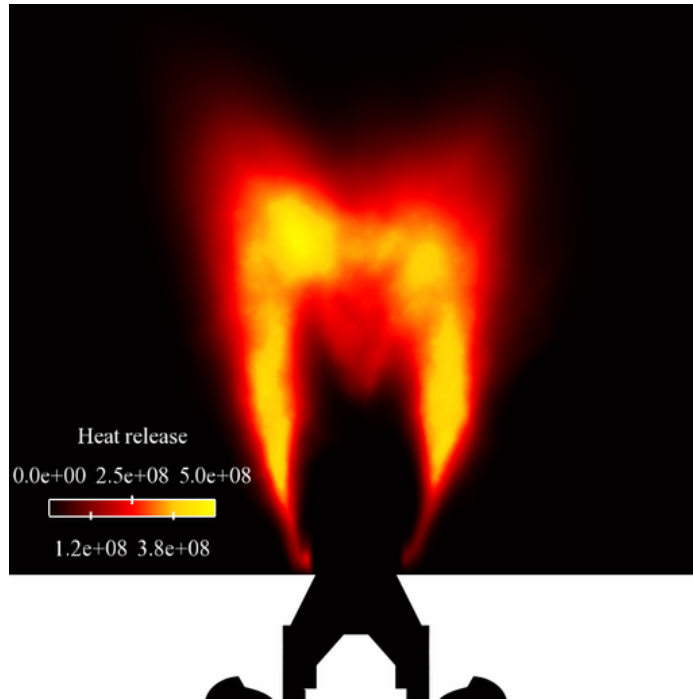


**Figure 5.16.** Heat release rate distribution ( $\text{W/m}^3$ ) exhibiting the “M” shape of the flame.

The global power  $\mathcal{P}$  of the flame can be estimated by integrating the heat release rate over the volume of the combustion chamber. One then finds that  $\mathcal{P} = 7.4 \text{ kW}$ , which

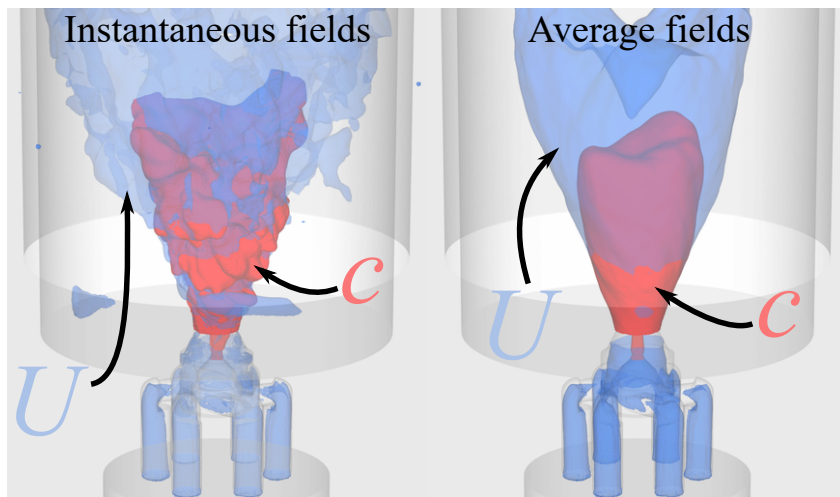


**Figure 5.17.** Iso-surfaces of the axial velocity  $U = 10 \text{ m s}^{-1}$  (in blue) and progress variable  $c = 0.9$  (in red). Left: Instantaneous fields. Right: Average fields over 25 ms.

is to be compared to the experimental value of 6.4 kW. A 15% relative difference can be found in the estimation of the power. A quick calculation showed that, in order to fill the entire chamber with a constant equivalence ratio, one has to simulate more than 1 s of physical time. This difference in the estimated power is then probably due to the fact that the flow is not fully established and that some n-heptane has accumulated in the system and is being chemically converted with an additional heat release rate.

The progress variable  $c$  may be used in practice to locate the flame front once the flame is stabilized. This variable is defined by:

$$c = \frac{Y_{CO_2} + Y_{CO}}{Y_{CO_2}^{eq} + Y_{CO}^{eq}} \quad (5.3)$$

An iso-surface of  $c = 0.9$  is shown in Figure 5.17 along with the iso-surface of the axial velocity  $U = 10 \text{ m s}^{-1}$ . These surfaces are plotted for an instantaneous solution and one average solution. One can clearly see the wrinkling of the flame linked to the turbulence of the flow on the left figure. It is also interesting to note that the flame is not quite symmetric in both solutions, instantaneous and averaged. The flame is slightly longer on its right hand side.

A Pi-Max 4 camera is equipped with a  $\text{CH}^*$  filter to record the chemiluminescence of the flame. In order to take into account the asymmetry of the flame and to better compare the flame to the experimental snapshots, the heat release rate  $\dot{Q}$  is integrated over the equivalent of the line of sight of the camera. The image obtained in this way

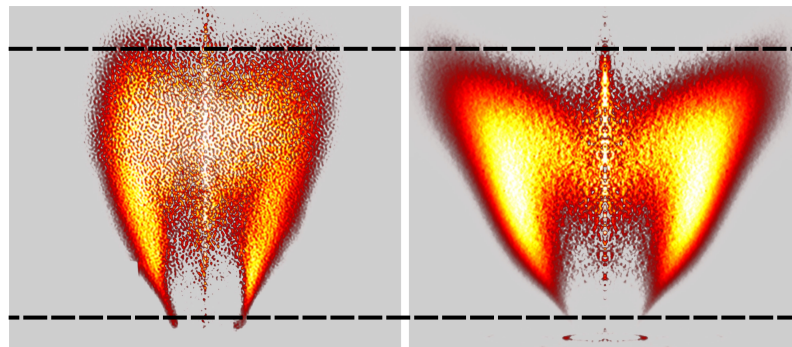


**Figure 5.18.** Comparison of the numerical (left) and experimental (right) flame shape. The top images present the line of sight integration of the heat release rate. Numerical results are integrated over 25 ms and experimental data are averaged over 2.4 s. The white dashed lines symbolize the foot and tip of the flame. The bottom images present the Abel transform of the top snapshots to retrieve an axial slice through the flame. Images are displayed in false color with yellow and dark red respectively corresponding to high and low light emission levels.

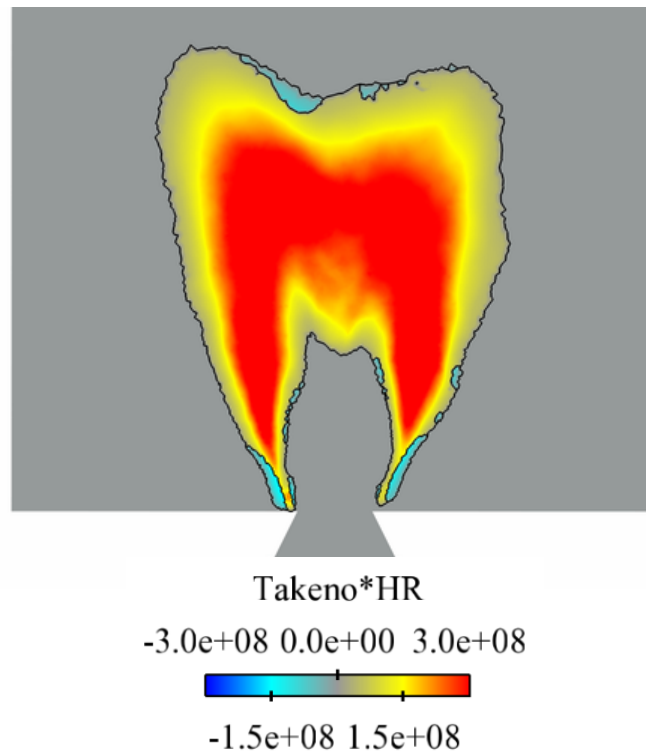


**Figure 5.19.** Distribution of Flame Index multiplied by the heat release rate  $F.I. \times HR$  to determine the regime of combustion in the different parts of the flame.

is compared to the experimental chemiluminescence image. The Abel transformed emission images are also plotted in Figure 5.18. The flame anchoring is apparently well estimated. This is confirmed by the Abel transforms, even if the numerical flame seems to be attached to the lips of the burner. This later effect is mainly due to the better sensitivity of the numerical simulation compared to that of the camera where the absence of light does not mean that there is no emission at all. The white dashed lines are positioned at the foot and tip of the numerical flame. One can see that there is a fairly good agreement between the experiment and the numerical prediction. This confirms what was observed under cold flow conditions where the predictions of the peak velocities were correct (see Figure 5.9 and 5.13). However, the flame expansion is not perfect as can be seen in the Abel transforms. The flame angle with its pseudo-axis of symmetry is noted  $\theta$ . In the numerical case  $\theta = 24^\circ$  is lower compared to the experimental value  $\theta = 29^\circ$ . It is also worth noting the asymmetry of the flame shape observed in the experimental results. This phenomenon is less pronounced in the numerical simulation, but as one can see in Figure 5.17, it can be retrieved, at least qualitatively.

To evaluate the combustion regime, Yamashita et al. (1996) proposed a Flame Index  $F.I. = \nabla Y_{C_7H_{16}} \cdot \nabla Y_{O_2}$ , with  $Y_{C_7H_{16}}$  and  $Y_{O_2}$  involving the fuel and oxidizer mass

fractions. This index may be used to determine the type of combustion, premixed ( $F.I. > 0$ ) or diffusion ( $F.I. < 0$ ), depending on the sign of the index. The Flame Index is represented multiplied by the heat release HR in Figure 5.19 to indicate the combustion intensity in the different regions. It is then easy to see that the chemical conversion takes place in the premixed mode through gaseous n-heptane and air flame elements. Only small portions of the combustion process is operating in a diffusion flame mode. This means that the spray is first evaporated by the high temperatures of the recirculating burnt gases. Note that the n-heptane boiling point is low  $T_b = 371$  K. The high turbulence of the swirling jet then premixes the evaporated fuel with the incoming air before combustion occur in regions of reduced velocities.

Distributions of average heat release rate, liquid volume and axial velocity are presented in Figure 5.20. One can see that the flame is clearly stabilizing in the vicinity of the air jet

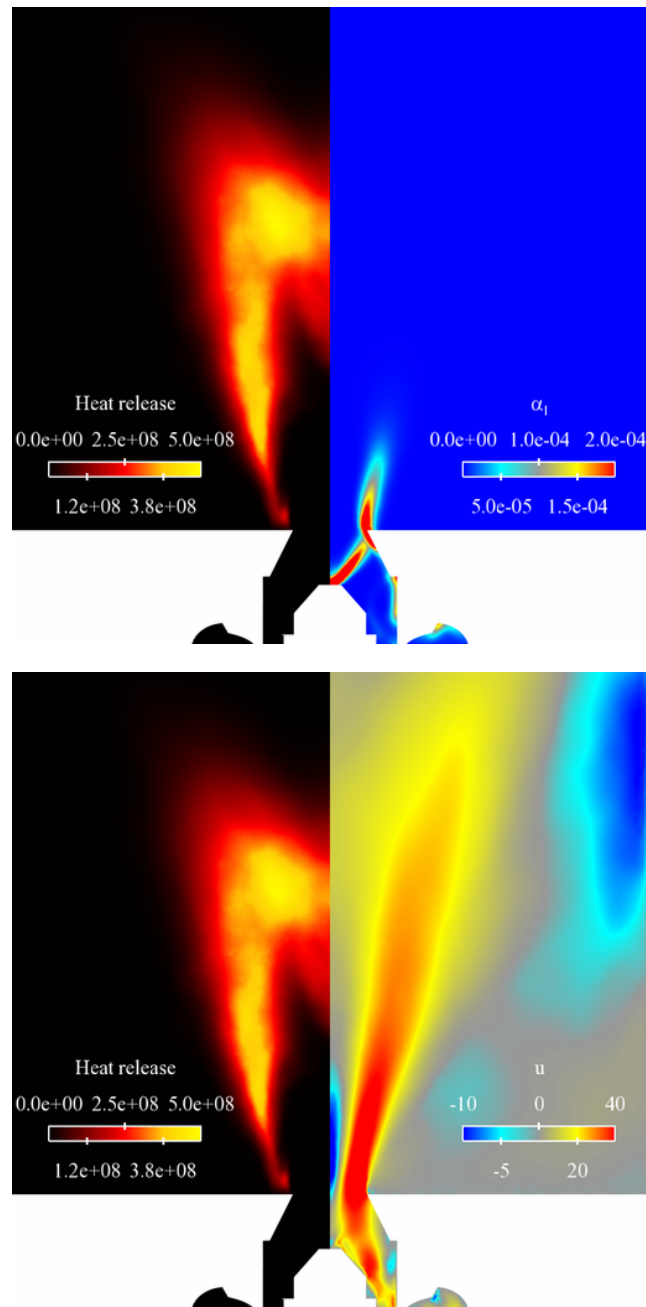


**Figure 5.20.** Distributions of average heat release rate  $\dot{Q}$  ( $\text{W}/\text{m}^3$ ) and liquid volume fraction  $\alpha_l$  (top) and heat release rate  $\dot{Q}$  ( $\text{W}/\text{m}^3$ ) and axial velocity  $U$  (m/s) (bottom).

## 5.4 Self-excited flame

It is experimentally demonstrated that the flame can couple to a strong longitudinal acoustic mode to naturally sustain a combustion instability (Chapter 4). To replicate

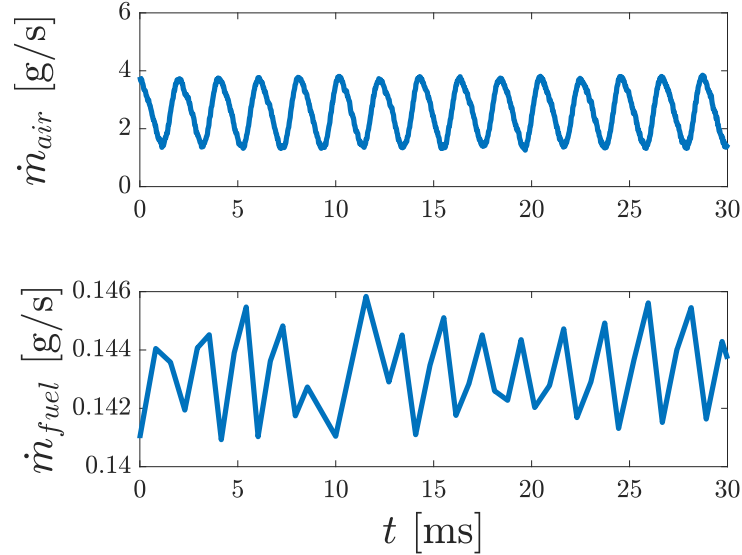


**Figure 5.21.** Air mass flow rate  $\dot{m}_{air}$  and fuel mass flow rate  $\dot{m}_{fuel}$  during 30 ms of simulation once the unstable mode has reached a limit cycle.

this phenomenon, the wall length  $l_c$  of the combustion chamber is increased from 165 to 280 mm. The rest of the geometry and the boundary conditions described previously remain the same. The simulation is first run in order to get to the limit cycle and average the phenomenon over several periods of oscillation. The results are then compared to the experimental results presented in section 4.4 of Chapter 4.

#### 5.4.1 Limit cycle oscillations

After a transient regime of 10 ms where the instability grows, the system reaches a stable limit cycle and the calculation is run for 20 cycles. The perturbation can be clearly observed in the air and liquid mass flow rates as seen in Figure 5.21. The amplitudes of fluctuation are 40% for the air and less than 1% for the fuel when compared to their mean values. Note that, in the experiment, the fuel flow rate cannot oscillate at the frequency  $f$  of the instability as the fuel is injected under high pressure ( $> 9$  bar). The acoustic pressure during a longitudinal mode in SICCA-Spray does not exceed 5000 Pa, preventing it from perturbing the pressurized incoming liquid fuel. Nevertheless, the perturbation amplitude for the liquid injection in the simulation is quite low and does not influence the comparison with experiments. These oscillations are due to non-characteristic treatment in the AVBP solver of the system of Euler equations for the liquid phase.

The heat release rate  $\dot{Q}$  is plotted in Figure 5.22, along with the axial velocity  $U$  at the air inlet, corresponding to the position of the hot wire in SICCA-Spray. The frequency  $f = 490$  Hz of the instability is determined using a Power Spectral Density

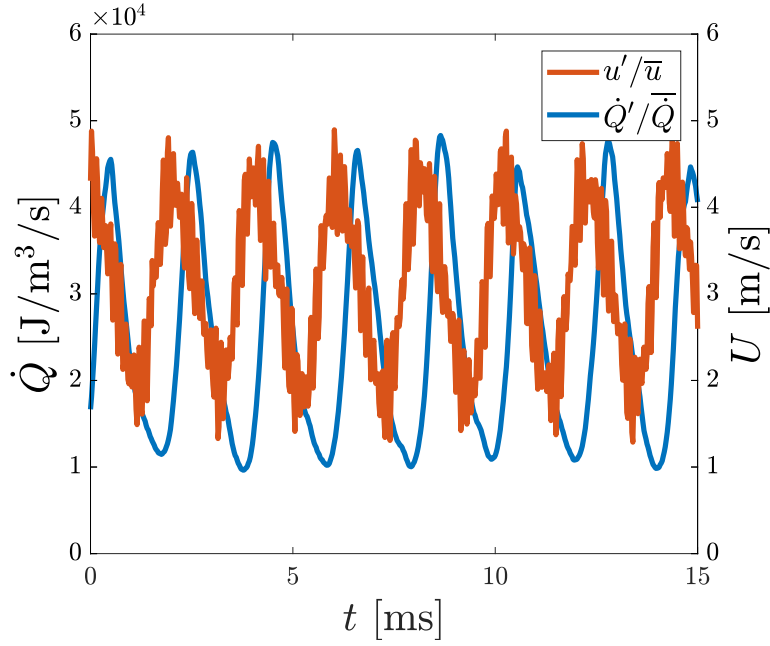


**Figure 5.22.** Heat release rate  $\dot{Q}$  (in blue) and axial velocity  $U$  at the inlet (in orange) during several cycles of oscillations at  $f = 490$  Hz in the case of the self-excited flame.

(PSD) analysis. Axial velocity and heat release rate  $\dot{Q}$  oscillate at the same frequency  $f$  and with a phase difference of  $\varphi_{U/\dot{Q}} = \pi/2$ . The PSD also gives access to the RMS values of  $U'/\bar{U} = 0.31$  and  $\dot{Q}'/\bar{\dot{Q}} = 0.45$ , indicating the presence of a strong oscillation in the heat release rate with a limited fluctuation of the axial velocity at the inlet. These values compare with the one observed experimentally in Figure 4.5 in Chapter 4. Note that the heat release rate fluctuations are slightly overestimated in the numerical simulation. It is worth noting that the frequency  $f = 490$  Hz is slightly lower than the experimental value  $f_{exp} = 530$  Hz. This shift is perhaps due to the fact that the calculated geometry, as shown in Figure 5.2, does not quite correspond to the real geometry and it may also be linked to the relaxation coefficient of the numerical domain inlet boundary condition.

Full solutions are stored every  $T/12$  seconds, with  $T = 1/f = 2.04$  ms the period of the oscillation. It is then possible to phase average the different calculated quantities over 20 cycles. Selected averaged fields are plotted in Figure 5.23. The phase  $\theta = 0$  corresponds to the instant when the axial velocity fluctuation  $U$  is maximum at the inlet. It is possible to follow the flame front motion by tracking the heat release rate  $\dot{Q}$  distribution in the simulation. One can see that the flame is affected along the oscillation cycle. The roll up of the tip of the flame is clearly observed. The heat release rate fluctuates with a large amplitude over the cycle as observed previously. It is minimum

around  $\theta = 3\pi/6$  and maximum at  $\theta = 5\pi/5$ . The flame shape changes over one period of oscillation, with the “M” shape severely perturbed when the flame is pushed toward the chamber backplane by the acoustic field.

The axial velocity sternly influences the motion of the flame as confirmed by the second row of images. One can see that the air jet is not constant and is pulsed at the frequency of the combustion instability. At one instant, nearly no air flows from the injector and the injection velocity is less than  $20 \text{ m s}^{-1}$ , compensated by a much higher velocity at the opposite side of the cycle, with velocities around  $70 \text{ m s}^{-1}$ . The Outer (ORZ) and Central (CRZ) Recirculation Zones are strongly affected by the instability. At  $\theta = 0$ , the CRZ is intense, with recirculating velocities of  $-20 \text{ ms}$ . This amplitude decreases along with the flame length until it totally vanishes at  $\theta = 3\pi/6$ , when the axial velocity of the incoming fresh air is maximum and blows away the entire structures at the exit of the injector. This phenomenon also couples with the entrainment of fresh air coming from the atmosphere as one can imagine by examining axial velocities around  $\theta = 4\pi/6$ . This results in a decrease of the local equivalence ratio, adding more perturbation to the combustion. The ORZ are also influenced by the instability cycle as can be seen in the axial velocity  $U$ . They strengthen when the incoming fresh air jet is strong, at  $\theta = 4\pi/6$ , forcing more burned gases to recirculate toward the flame foot, thus reheating the fresh gases and vaporizing liquid n-heptane.

Finally, the liquid jet is observed using the liquid volume fraction  $\alpha_l$  in the bottom images in Figure 5.23. As for the other quantities,  $\alpha_l$  is also affected by the instability. It is interesting to note that, at  $\theta = \pi/6$  during the cycle, nearly no liquid is injected in the chamber. This explains why the flame heat release rate dramatically decreases a few instants after and nearly switches-off the combustion process. As soon as the axial velocity becomes high enough, n-heptane droplets are re-injected in the combustion chamber, augmenting the local equivalence ratio, with an additional quantity of fuel accumulated during the previous blockage, causing the extra heat release rate observed at the peak of the cycle. This phenomenon can be correlated to the local equivalence ratio variations observed in the last row of images. It is worth noting that, at  $\theta = 3\pi/6$ , a lot of fuel has been accumulated in the injector and blocked during the previous part of the cycle. At this moment, a lot of n-heptane is released in the chamber and notably increases the local equivalence ratio, producing a rich pocket of fuel. The equivalence ratio then decreases as the cycle goes on and the blockage of the fuel is repeated. All these phenomena are synchronized, resulting in the large modulation of the flame motion, luminosity and heat release rate.



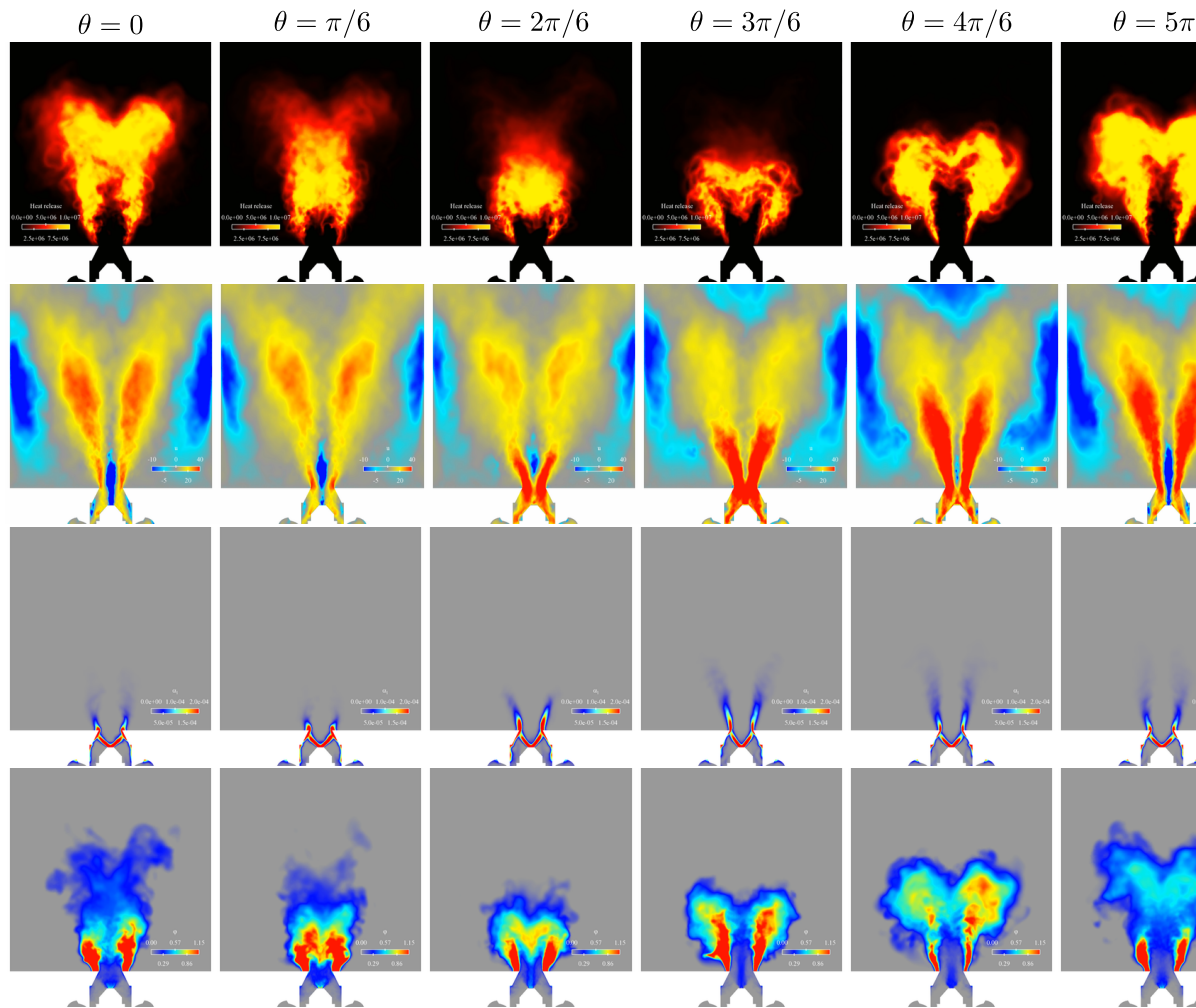


**Figure 5.23.** Phased average heat release rate  $\dot{Q}$  (top), axial velocity  $U$  (2nd line), liquid volume fraction  $\alpha_l$  ratio  $\phi$  (bottom) during a cycle of oscillation. Each snapshot is averaged over 20 cycles of the combustion instabilities to the instant where the velocity fluctuation is maximum at the injector inlet.

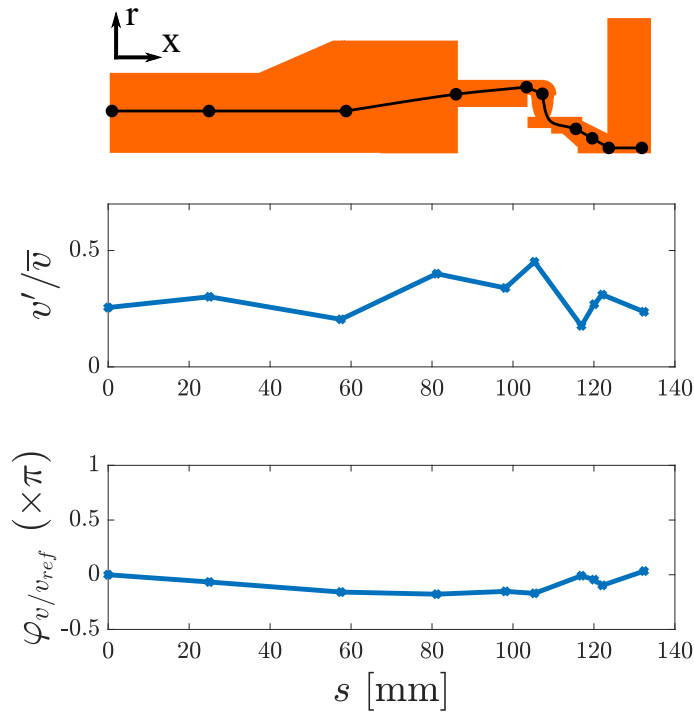


**Figure 5.24.** Top: Positions of the probes where the velocity  $\vec{v} = \vec{u}_x + \vec{u}_y + \vec{u}_z$  magnitude and phase are compared. Bottom: Velocity fluctuation ratio  $v'/\bar{v}$  and phase variations  $\varphi$  of the velocity fluctuations versus the curvilinear abscissa  $s$ . The reference signal is the first probe, on the air inlet.

One important feature that is retrieved with the simulation is the phase shift between the liquid volume fraction  $\alpha_l$  and the heat release rate  $\dot{Q}$ . One can see that  $\dot{Q}$  is maximum when nearly no fuel is injected in the combustion chamber. Half a cycle later,  $\dot{Q}$  is minimum, corresponding to a moment where the largest volume of fuel is injected. These two quantities are in phase opposition. By this observation, one can imagine that this cycle could be altered if the fuel were replaced by another fuel, of lesser volatility, that would take more time to evaporate. In the case of n-heptane, the boiling point is quickly reached at  $T_b = 371$  K, whereas for heavier fuels, such as Jet-A, the boiling point is much higher at  $T_b > 500$  K. Another important parameter is the droplet size. The present atomizer has been designed to produce a spray of small droplets ( $d < 25 \mu\text{m}$ ), with a low size dispersion. Industrial atomizers usually provide a spray composed of larger droplets with greater thermal inertia and aerodynamic drag. In conclusion, the fuel type and the spray composition are two parameters that need to be taken into account when struggling with combustion instabilities.

It is interesting to follow the velocity perturbation across the geometry, from the plenum to the chamber (see Figure 5.24). Several probes have been introduced in the

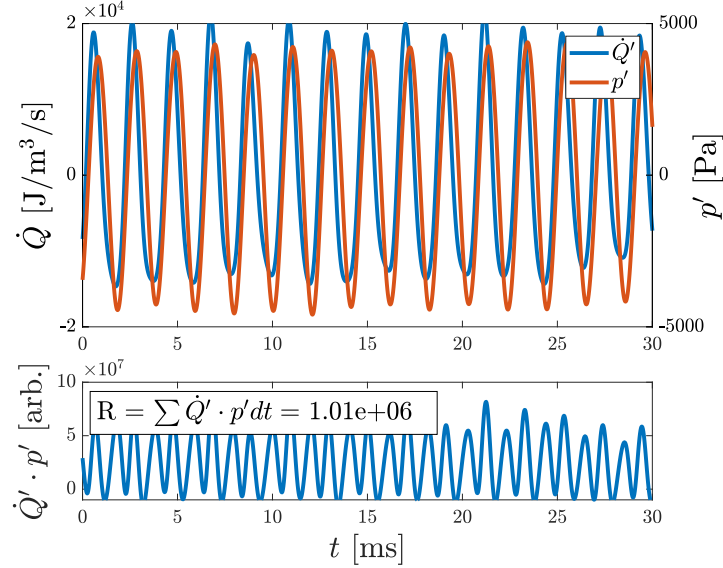


**Figure 5.25.** Top: Heat release rate fluctuation  $\dot{Q}'$  and acoustic pressure  $p'$  over 30 ms. Bottom: Product between  $\dot{Q}'$  and  $p'$  and calculated Rayleigh source term  $R = \int_V \dot{Q}' p' dt$ .

numerical domain and are used to measure the velocity fluctuation at several points. As these points are distributed in the plenum, the injector and the chamber, it is convenient to consider the magnitude of the total velocity  $|v|$  with  $\mathbf{v} = \mathbf{u}_x + \mathbf{u}_y + \mathbf{u}_z$ . One can see that, from the air inlet to the foot of flame, the amplitude of fluctuation is relatively constant, with a mean value around 0.3. Note that the calculated quantities are RMS values at the frequency  $f = 490$  Hz of the naturally triggered instability. The phase between the local and the reference velocities  $\varphi$  is also calculated. It is worth noting that this phase barely changes when one probes different parts of the injector cavity. This behavior is natural as the instability is coupled to a longitudinal acoustic mode of the system which is a stationary wave. The only phase changes occur at the nodes of the mode. This is confirmed by calculating the acoustic response of the system with a Helmholtz solver (Figure 4.4 of Chapter 4).

In the combustion dynamics field, one interesting criterion often cited has been expressed by [Rayleigh \(1878\)](#). According to this criterion oscillations are amplified if pressure  $p'$  and heat release rate  $\dot{Q}'$  fluctuations are in phase or equivalently if :

$$R = \int_V p' \dot{Q}' dt > 0 \quad (5.4)$$

is positive. This is a necessary condition for instability. The Rayleigh source term is calculated in Figure 5.25, where  $\dot{Q}'$  and  $p'$  are plotted. One can see that the product  $\dot{Q}' p'$  is nearly always positive with only minor negative excursions. This implies that

$R$  is essentially positive, indicating that the heat release rate fluctuations feed the acoustic mode and compensate losses in the system.

#### 5.4.2 Comparison of the naturally excited flame with experiments

It is important to first notice the difference in frequency between the experiment  $f_{exp} = 490$  Hz and the numerical simulation  $f_{num} = 530$  Hz. This difference may be linked to, as proposed before, the choice made to consider a geometry that only partially represents the plenum. It may also be related to the value of the relaxation coefficient  $K$  of the air inlet. The Navier-Stokes Characteristic Boundary Conditions (NSCBC) used at the inlet define a reflection coefficient  $R$  that may be cast in the form:

$$R = \frac{1}{1 + (2\omega/K)^2} \quad (5.5)$$

where  $\omega = 2\pi f$  designates the angular frequency. The cut-off frequency  $f_c$  can then be estimated from this relation, so  $f_c = K/4\pi$ . In the present case,  $f_c = 1000/4\pi \sim 80$  Hz, which is much lower than the frequency of oscillation of the system. This means that the incoming acoustic pressure waves will be damped by the boundary. This value has been chosen to stabilize the air mass flow rate to obtain the steady state flame and to not reflect too much low frequencies. This means that frequencies above the cut-off frequency  $f_c \sim 80$  Hz will not be reflected ( $R \sim 0$ ) which is the case for the frequency of the longitudinal excited mode, 490 Hz in the simulation.

To compare numerical to experimental results, it is first important to look at the heat release rate and at the chemiluminescence of the flame. One may consider that the  $\text{CH}^*$  chemiluminescence is a good marker of the heat release rate. This is a correct assumption in the case of a lean premixed flame. It has been demonstrated with the numerical study that combustion mainly takes place in the premixed mode. Figure 5.26 compares experimental (left) and numerical (right) snapshots at six different times during the instability cycle. Even if the flame expansion is not perfect, the numerical results are in good agreement with the experiment. The motion of the flame is correctly reproduced with the correct length and shape. For example, the very compact ‘‘M’’ shape flame at  $\theta = 3\pi/6$  is correctly predicted. This is also the case at  $\theta = \pi/6$  with a roll-up of the flame tip. Note that experimental images are averaged over 30 times more cycles than the numerical ones. As a consequence, one can say that, in a first approximation, the simulation is able to correctly predict the natural dynamical behavior of the confined flame. A particular attention has to be given to the excited frequency as it will be done in future investigations.

The SICCA-Spray experiment is equipped with several fine diagnostics such as microphones, hot wire and photomultipliers (PM), making quantitative comparisons possible. Heat release rate, velocity fluctuations and the acoustic pressure in the chamber

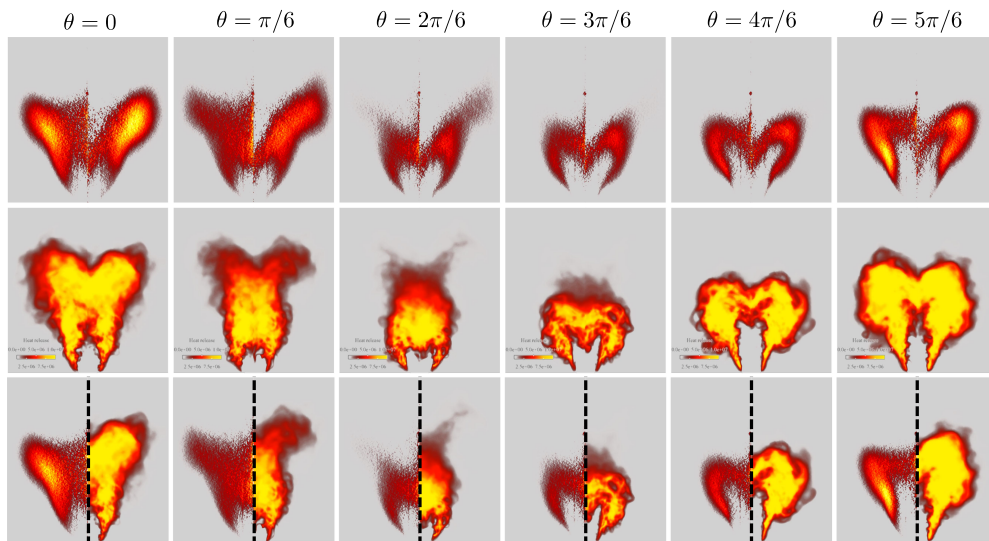


**Figure 5.26.** Comparison of the experimental  $\text{CH}^*$  chemiluminescence (top) and numerical heat release rate (middle) during one cycle of oscillation. Experimental and numerical images are averaged over 600 and 20 cycles respectively. Experimental images are displayed on a scale of false colors to ease comparison. The bottom of these images corresponds to the chamber backplane. On the last line, experimental (left) and numerical (right) images are compared side by side.

and in the plenum are compared in the self-excited oscillation case in Figure 5.27. Signals are plotted with respect to a dimensionless time obtained by dividing by the period of oscillation  $T$ . Signals are synchronized at  $t/T = 0$  when the hot wire features a maximum level.

The top left plot in Figure 5.27 indicates a very good agreement between experimental data and numerical results. The calculated amplitude is close to that recorded in the experiment. The heat release rate on the top right plot also shows a fairly good agreement. Signals have been normalized in order to be compared. In the experiment, the PM measurement is quoted in arbitrary units whereas, in the simulation, the value is proportional to  $\text{Jm}^{-3}\text{s}^{-1}$ . The phase between the experiment and the numerical simulation is close to zero, even if a discrepancy can be observed in the 5th oscillation. The main differences lie in the calculated pressure. In the plenum, the amplitude of the two signals are quite close. One can only find, on average, a 10% relative difference between the two amplitudes. The largest difference stands in the phase between the two signals which are nearly in quadrature. This shows that the self-sustained mode in the numerical simulation differs from the one in the experiment. The coupling between the plenum and the chamber might not be perfectly reproduced because the plenum response is not fully described in the simulation. Finally, one can analyse the acoustic pressure in the chamber in the bottom right subfigure. This time, the phase differs from that found experimentally and the amplitude is over-predicted by a factor of 2.

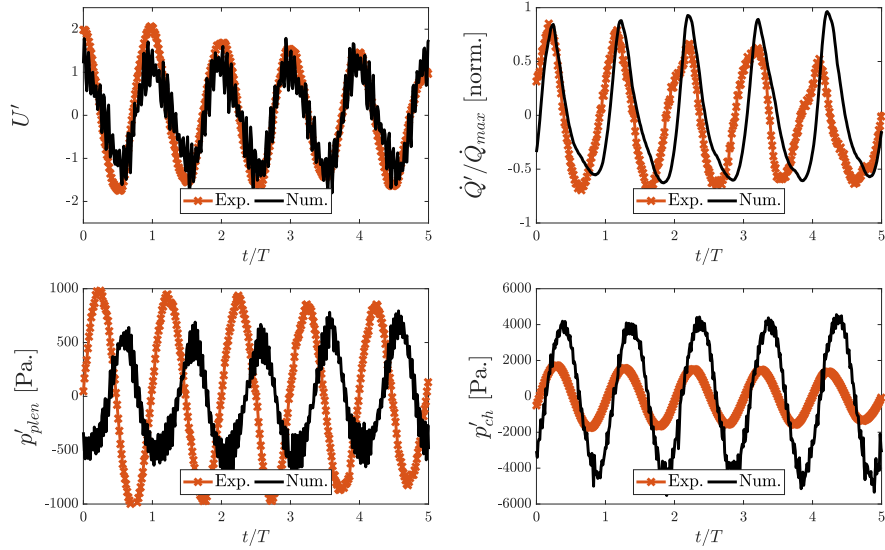


**Figure 5.27.** Comparison of experimental and numerical results for the self-excited flame. In each plot, numerical results are represented by a black solid line and experimental data by an orange crossed line. To eliminate the frequency differences, time is divided by the oscillation period  $T$ . Top left: Axial velocity fluctuation  $u'$  at the inlet (hot wire location in the experiment). Top right: relative heat release rate fluctuation  $\dot{Q}'$  normalized by the maximum value  $\dot{Q}_{max}$ . Bottom left: Acoustic pressure in the plenum, downstream the hot wire. Bottom right: Acoustic pressure in the chamber near the backplane.

This later result is probably linked to the fact that damping mechanisms are not well accounted for in the simulation. Acoustic energy is mainly brought by the flame during its oscillations. In the experiment, acoustic energy is lost, damped by the air flow, but also radiated at the chamber exit into the surrounding atmosphere and these processes are not well represented in the calculations. Lastly, the experiment is equipped with two driver units that, when not used, consist of a free moving membrane that can absorb acoustic energy. As a consequence, the level of acoustic pressure in the entire chamber is overestimated.

## 5.5 Externally modulated flame

The previous sections demonstrated that the numerical simulation was able to faithfully reproduce the self-excited oscillation observed in the single injector experiment. As indicated in Chapter 4, this test bench has also been used to measure the Flame Describing Function of the flame. Because the FDF gives access to the prediction of combustion dynamics, it is worth trying to determine it numerically. To do so, the length  $l_c$  of the combustion chamber is set to 165 mm to establish a steady flame. The air inlet boundary condition is changed to represent the modulation applied in

Frequency (Hz)	$u'_a/\bar{U}$ (RMS)	Available experiments
490	0.34	No data
530	0.60	Chemiluminescence, acoustic pressure, heat release rate
640	0.14	Idem
640	0.38	Idem
640	0.45	Idem

**Table 5.6.** Simulated frequencies and amplitude of forcing.

the experiment where driver units create a longitudinal acoustic perturbation. The modulation is measured by a hot wire in the experiment. In the simulation, one fixes the target mean air mass flow rate, the excitation amplitude and frequency at the inlet to match that recorded at the position of the hot wire in the experiment. To obtain a stable excitation signal, the simulation is first run for a few cycles before data are acquired. The objective of this section is to correctly reproduce the forcing mechanism used in the experiment, to force the flame at the same amplitude and frequency that are used in the experiment and to compare the effects on the flame to what was observed experimentally. The final objective is to see if the FDF can be determined by numerical simulation. Several simulations have been run with different amplitudes and frequencies of forcing, each time for 20 periods. These levels are summed-up in Table 5.6.

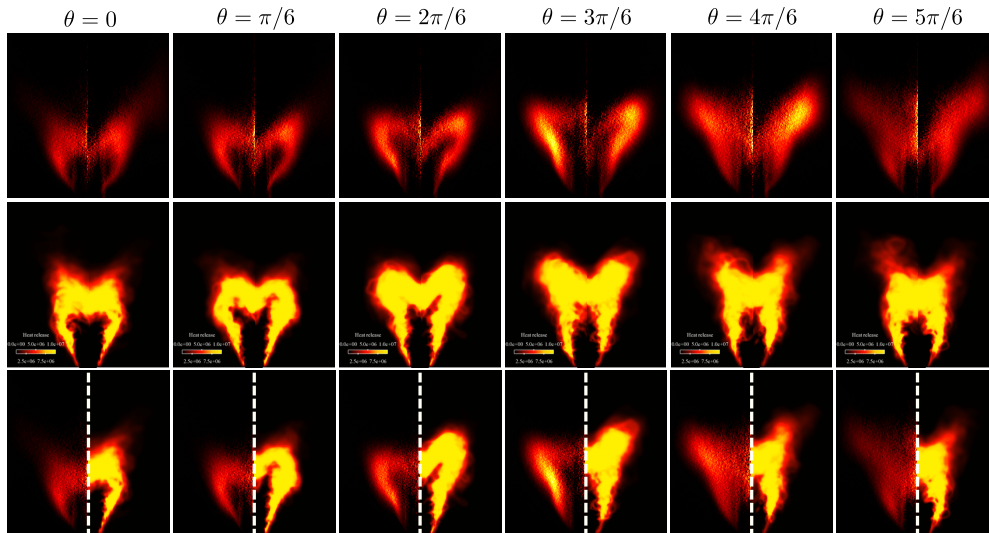


**Figure 5.28.** Comparison of the experimental  $\text{CH}^*$  chemiluminescence (top) and numerical heat release rate (middle) during one cycle of oscillation. Experimental and numerical images are averaged over 600 and 20 cycles respectively. Experimental images are displayed on a scale of false colors to ease comparison. The bottom of these images corresponds to the chamber backplane. On the last line, experimental (left) and numerical (right) images are compared side by side.

### 5.5.1 Validation of the numerical method with experimental comparison at 530 Hz

As indicated in Table 5.6, experimental data are available for the forced flame at  $f = 530$  Hz and  $u'_a/\bar{U} = 0.45$ . CH\* Chemiluminescence images and heat release rate distributions are compared in Figure 5.28 where one can see a fairly good agreement between the experiment (left half flames) and the numerical simulation (right half flames). Qualitatively, some differences are found in the flame motion and in the flame length.

As for the self-excited case, Figure 5.29 shows the comparison of velocity, heat release rate and acoustic pressure fluctuations. Signals are synchronized with respect to  $u'_a$  at the numerical domain inlet. One can see that the agreement is quite good for both phase and amplitude between numerical and experimental data for the heat release rate fluctuation  $\dot{Q}'$  and the acoustic pressure in the plenum  $p'_{plen}$  when the same forcing amplitude is applied. Small discrepancies can be identified in the  $\dot{Q}'$  signal that are mainly due to the variability of the impinging velocity perturbation. The acoustic pressure in the chamber  $p'_{ch}$ , near the backplane, is less easy to compare. Levels of fluctuations, frequency and phase do not comply. This is the consequence of the

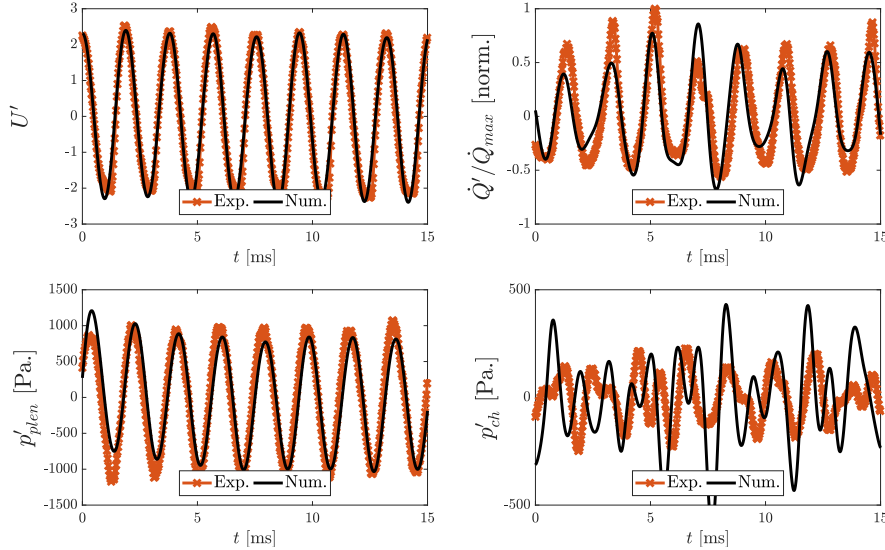


**Figure 5.29.** Comparison of experimental and numerical results for a forcing frequency of  $f = 530$  Hz and an amplitude  $u'_a/\bar{U} = 0.45$ . In each plot, numerical results are represented by a black solid line and experimental results by an orange crossed line. Top left: Axial fluctuation  $u'_a$  at the inlet (hot wire location for the experiment). Top right: Normalized heat release rate fluctuation  $\dot{Q}'$ . Bottom left: acoustic pressure in the plenum. Bottom right: Acoustic pressure in the chamber near the backplane with filtered numerical results.

low level of amplification of the acoustic waves since the system is not excited at a resonant frequency. In conclusion, the numerical simulation is able to correctly retrieve the forcing mechanism and the response of the flame.

### 5.5.2 Numerical Flame Describing Function

The Flame Describing Function, already introduced and measured experimentally in Chapter 4, is defined by:

$$\mathcal{F}(\omega, u') = \frac{\dot{Q}'/\overline{\dot{Q}'}}{u'/\overline{u}} = G(\omega, u') e^{i\varphi(\omega, u')} \quad (5.6)$$

As the system is forced at a frequency  $f$  and an amplitude  $u'_a/\overline{U}$ , it is possible to retrieve the FDF for several amplitudes. The gain and phase of the experimental interpolated FDF are plotted in Figure 5.30 along with the five numerical simulations presented in Table 5.6. One can see that the phase  $\varphi$  is correctly predicted for the five calculations. If one would plot the potential bands of instability by only using the numerical results, it would be possible to deduce from these calculations if the system is potentially unstable or not.

The gain is more critical to estimate. Raw values are not really comparable as the experiment evaluates the heat release rate  $\dot{Q}$  by measuring the OH\* chemiluminescence, which we consider as proportional to the heat release rate. It is worth noting that, despite this hypothesis, values are not totally different between experiments and numerical simulations. For example, at 490 Hz and 530 Hz,  $G_{exp} \sim 0.4$  and  $G_{num} \sim$

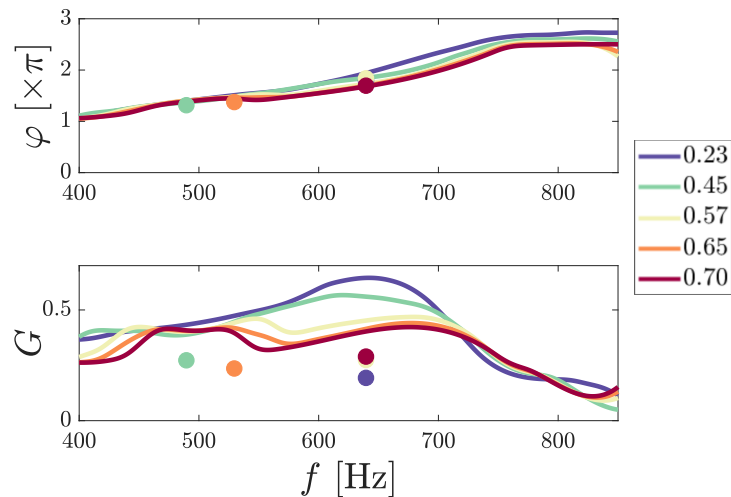


**Figure 5.30.** Experimental interpolated Flame Describing Function (FDF) in solid lines and numerical FDF in dots. Top: FDF phase  $\varphi$ . Bottom: FDF gain  $G$ .

0.3. The biggest issue is the evolution of the gain with the amplitude of forcing. As observed the experimental gain  $G$  decreases when  $u'_a/\bar{U}$  increases. The numerical simulation is not able to catch this feature. At 640 Hz, the simulated gain  $G$  increases from 0.19 to 0.28 when the amplitude of forcing increases from 0.23 to 0.70. This shows the exact opposite trend. Note that, due to the lack of computational resources, effects of the forcing amplitude has only been simulated at one frequency. It would be interesting to calculate another frequency, close to 600 Hz where the amplitude still has an effect on the gain FDF  $G$ . It is now interesting to use the numerical simulation which gives access to physical parameters in the entire geometry to evaluate the robustness of the forcing method.

### 5.5.3 Comparison of naturally excited and forced flame at 490 Hz

The FDF is built to represent the full dynamics of the flame over a wide range of frequencies. This section presents results for a forced case similar to the conditions of the naturally triggered flame. In this study, the flame is forced at 490 Hz with an amplitude of excitation of  $u'_a/\bar{U} = 0.34$ , very close to the value of the self-excited case,  $u'_a/\bar{U} = 0.31$ . Figure 5.31 shows the applied amplitude of velocity fluctuation at the numerical domain inlet and the heat release rate fluctuation, representative of the flame response. One can clearly see that the heat release rate  $\dot{Q}'$  oscillations are lower than those obtained in the self-excited case, which is confirmed in the central figure. The velocity signals are synchronized to only compare the flame response. Two major differences are observed: the amplitude of the flame response does not correspond in the two cases and the excited and forced flame are not in phase. When the flame is naturally excited,  $\dot{Q}'$  is in phase quadrature with the velocity at the inlet. For the forced flame, the heat release rate is out of phase by a value of  $\pi$ , meaning that  $\phi = 3\pi/4$ . Note that this was also clearly observed in the experiment in Figures 4.5 and 4.7 of Chapter 4. In conclusion, the numerical models are capable of correctly retrieving the forcing mechanisms, similar to those observed in the experiment, even if the response of the flame submitted to external forcing does not match to the self-triggered mode.

Different cuts of the geometry for the heat release rate  $\dot{Q}'$ , the axial velocity  $U$  and the liquid volume fraction  $\alpha_l$  are plotted in Figure 5.32. These images confirm the conclusions made previously that the flame response is very low, with almost no perturbation of the flame shape as one can see on the top images. The flame stretches out a bit during the cycle and the tips of the “M” formed by the flame are more pronounced, but the motion does not quite match that observed in Figure 5.23. For the axial velocity  $U$ , the velocity of the jet at the exit of the injector fluctuates but in a very different fashion. The jet accelerates and the CRZ is suppressed to some extent, but the amplitude of these velocity fluctuations is way lower than for the naturally excited flame. As a consequence, the liquid volume fraction does not fluctuate at all, limiting its influence on the variation of the local equivalence ratio.

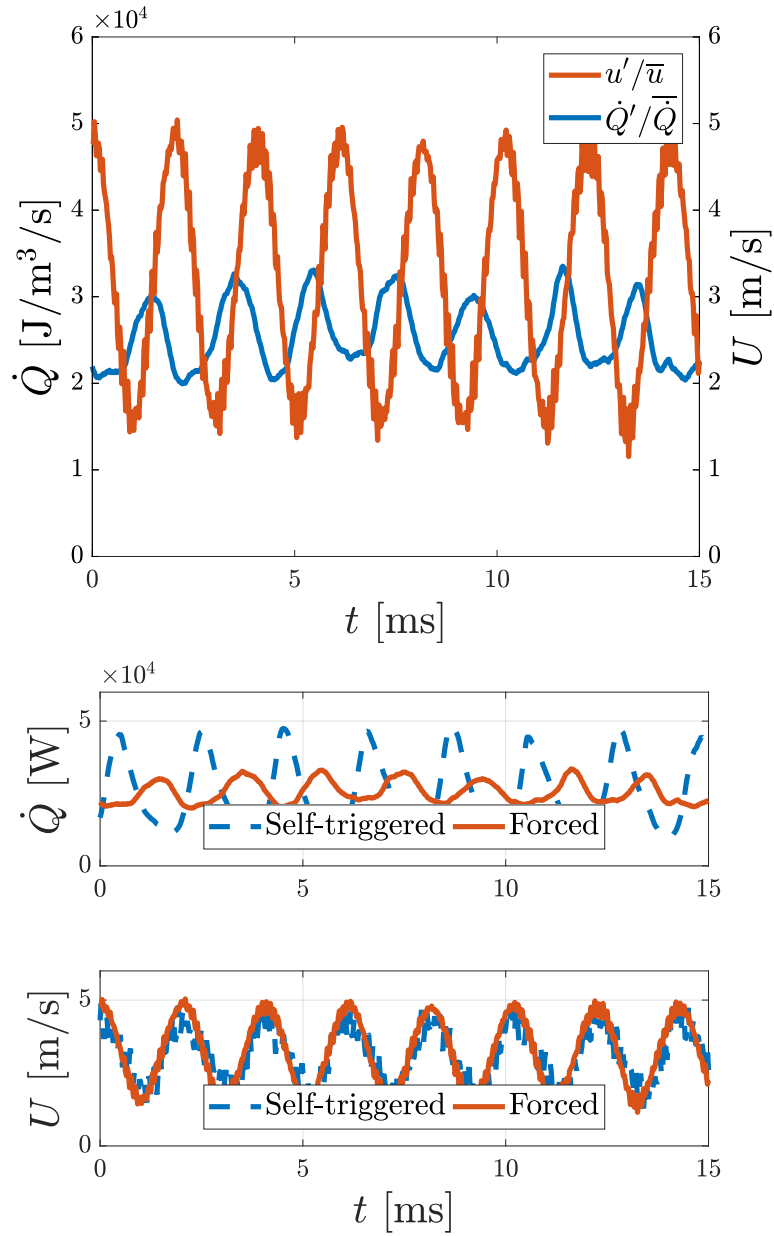


**Figure 5.31.** Top: Heat release rate fluctuations  $\dot{Q}'$  (in blue) and axial velocity  $u'_a$  at the inlet (in orange) during several cycles of oscillations at  $f = 490$  Hz when the flame is forced. Bottom: Comparison of  $\dot{Q}'$  (top) and  $u'_a$  for the self-excited case (in blue) and for the forced case (in orange).



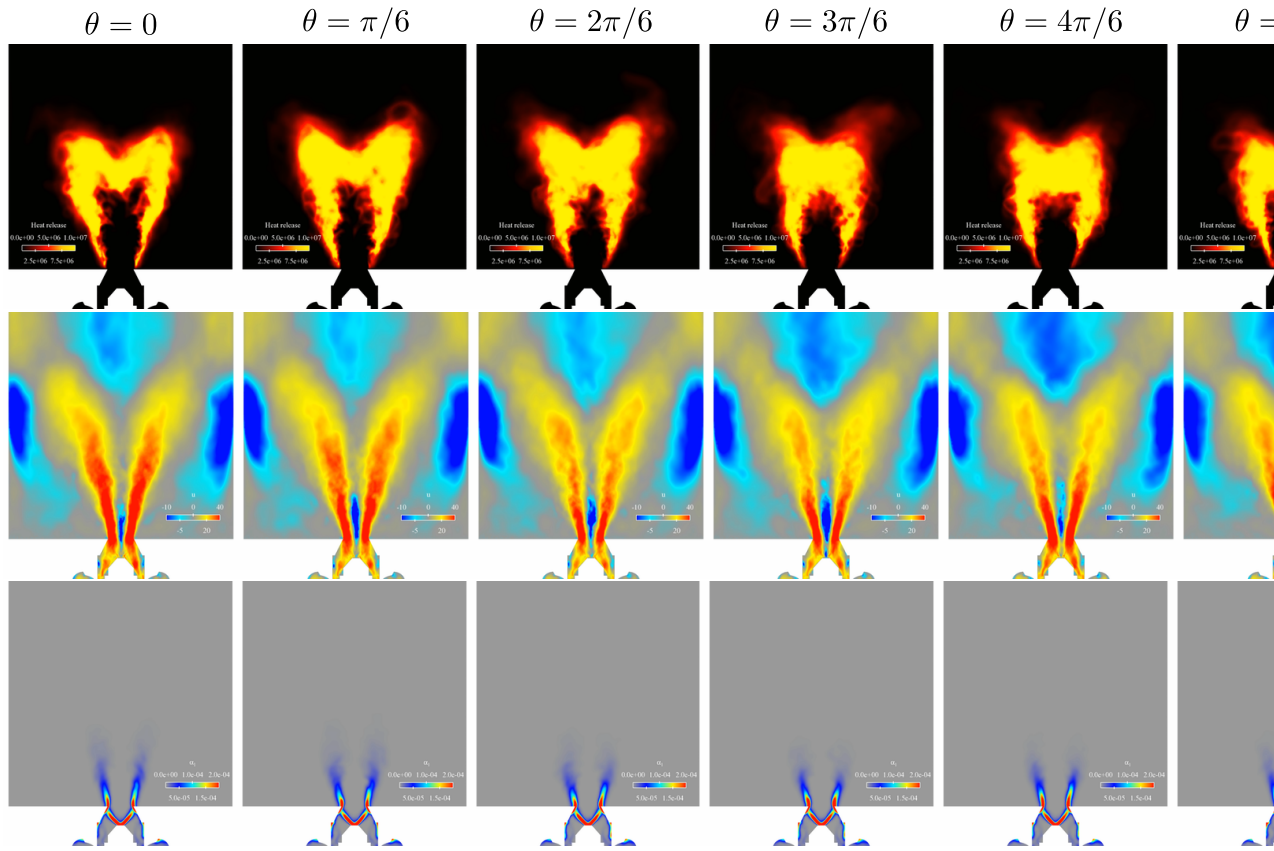


**Figure 5.32.** Phase average heat release rate  $\dot{Q}'$  (top), axial velocity  $u'_a$  (middle) and liquid volume fraction  $\alpha$  (bottom) at different phase angles of the combustion instability oscillation. Each snapshot is averaged over 20 cycles of the combustion instability.  $\theta = 0^\circ$  corresponds to the phase where the liquid volume fraction fluctuation is maximum at the inlet.

Numerical simulations give access to 3D fields of the different variables. It is then interesting to follow the velocity perturbation across the geometry for each computation presented in Table 5.6. Probes locations are indicated in Figure 5.33, top. For each probe, the amplitude of the velocity fluctuation and its phase compared to a phase reference are calculated and plotted in the figure. If needed, details are given in Section 5.4. One can see in the top plot that  $v'/\bar{v}$  is fixed at the inlet but rapidly drops when propagating in the plenum. On arriving in the injector channels and swirler, the amplitude of the fluctuation is severely damped. The remaining level of excitation at the last points, when  $s > 120$  mm, corresponds to what really forces the flame. In the case of the forcing at 640 Hz (green curve), the amplitude drops from 0.55 to 0.066 at the foot of the flame. As a consequence, the perturbation that impacts the flame is only 1/10th of what is imposed at the inlet. It is the direct result of the damping of the acoustic waves during their travelling in the different ducts. As the forcing does not correspond to a resonant frequency of the system, only travelling waves are established in the system and there is no amplification by a resonance. When looking at the phase  $\varphi$ , its behavior is totally different from that found in the self-excited case

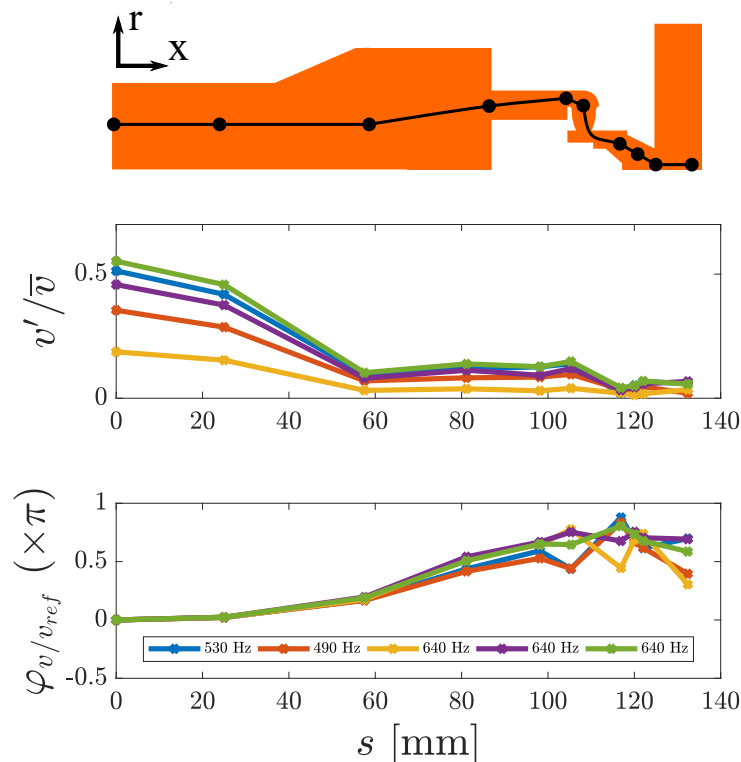


**Figure 5.33.** Top: Positions of the probes where the velocity  $\mathbf{v} = \mathbf{u}_x + \mathbf{u}_y + \mathbf{u}_z$  magnitude and phase are compared. Bottom: Velocity fluctuation ratio  $v'/\bar{v}$  and phase  $\varphi$  of the velocity fluctuation versus the curvilinear abscissa  $s$ . The phase reference is the first probe, on the air inlet.

where the phase barely changes with the arc length coordinate  $s$ . The phase of the forced case first changes in a nearly linear fashion due to the acoustic propagation of the perturbation. Its value is less well defined in the vicinity of the swirler. The small dimensions of this element and the conversion of acoustic energy into convective energy is probably responsible for this behavior.

These observations raise the problem of the measurement of the forcing applied to the flame when measuring Flame Describing Functions. If one wishes to reproduce the dynamics of the naturally excited flame by forcing it, one should impose an inlet velocity fluctuation high enough in order to obtain the correct level of perturbation at the flame ( $s = 135$  mm) (see Figure 5.24 and 5.33). Two problems are then encountered. First, the maximum possible forcing amplitude at the inlet is  $u'_a/\bar{U} = 1$ . At higher amplitudes the flow reverses and the inlet becomes an outlet inducing numerical difficulties. Secondly, even if the magnitude is increased, the damping of the modulation when propagating in the injection system is such that only a small part of it reaches the flame. This questions the method of forcing by modulating the flow in the plenum. In this kind of burner, with high speed, high swirled and turbulent flows and with parts of small dimensions, the head loss is large and the perturbation imposed in the plenum is attenuated to a large extent when it reaches the flame. One possible solution would be to modulate the downstream flow by placing actuators near the chamber outlet but this could not be done in the present project and might be worth investigating.

## 5.6 Conclusion

This chapter is concerned with the large eddy simulation of combustion dynamics in a single swirl spray injector configuration. The general idea is to obtain further information on the mechanisms leading to combustion oscillations, complement experimental data and possibly improve the understanding of the phenomena observed experimentally. To carry the dynamical simulations it is first necessary to establish a steady turbulent flame and verify that the flow and flame are in agreement with what is observed experimentally. It is shown that the simulation retrieves many of the features observed experimentally but that the match is not perfect. There are differences between the experimental velocity profiles and the numerical results. This in turn leads to differences in the expansion rate of the jet issuing from the injector and has an impact on the flame shape. It is however considered that the differences are acceptable and that the study of the dynamics of the flame and system can be envisaged. The next item is to see if the simulation is able to retrieve the self-excited oscillations observed in the experiment when the combustor length is augmented. This is shown to be feasible. The simulation exhibits a self-sustained oscillation at a frequency which is close to that observed experimentally. Here again, the match is not perfect but the flame dynamics is close to that found experimentally and some of the signals match those recorded in the experiment. The third item is to see if one can modulate the flame by external means and determine the flame motion resulting from this forcing. Another objective is to see if the flame describing function can be retrieved numerically.

These various aspects are treated by making use of a shorter combustor. The flame features then a steady turbulent motion. It can be modulated externally and the flame motion can be compared to that observed experimentally. Once again the match is not perfect but one retrieves many of the experimental features. The calculations also help in the interpretation of experimental findings. In its present state, the simulation yields an FDF that is in agreement with the experiment when looking at the phase, but which differs when the gain is considered, especially its response to different perturbation amplitude. Finally, the numerical simulation provides clues on the possible improvements of simulation and experimentation.





## **Part II**

# **A premixed annular combustor called MICCA**



## Chapter 6

# Flame pattern alternation

*Experiments in cold and reactive conditions carried out in linear arrays of injectors indicate that the flows established by neighbouring injectors exhibit alternating patterns if the distance between two injectors is too small. This issue is investigated in this chapter on the MICCA chamber equipped with multiple swirling premixed injectors. Its side walls are made of quartz providing full optical access to the flame region thus allowing detailed studies of the combustion region structure and dynamics. Experiments reported in this chapter rely on direct observations of the flame region through light emission imaging using two standard cameras and an intensified high speed CMOS camera. The data gathered indicate that interactions between successive injectors give rise to patterns of flames which exhibit an alternate geometry where one flame has a relatively low expansion angle while the next spreads sideways. This pattern is then repeated with a period which corresponds to twice the injector spacing. Such arrangements arise when the angle of the cup used as the end-piece of each injector exceeds a critical value. Effects of mass flow rate, equivalence ratio, and injector offset are also investigated. It is shown that the angle which defines the cup opening is the main control parameter. It is also found that when this angle exceeds a certain value and when the laminar burning velocity is fast enough, the flame pattern switches in an unsteady manner between two possible configurations. It is shown that these alternating flame patterns lead to alternating heat release rate distributions and inhomogeneous heat transfer to the chamber walls featuring a helicoidal pattern. Conditions leading to alternating flame patterns are finally discussed by making use of a recent flow regime diagram.*

### 6.1 Introduction

Design of annular combustion chambers needs to meet conflicting criteria. They must be compact and achieve an homogeneous thermal load with reduced pollutant emission levels and stable combustion over the largest possible operability domain. For several decades, manufacturers have used swirling injectors capable of delivering

compact flames with reduced emissions as shown by [Lefebvre \(2010\)](#). Annular combustors with premixed swirling injectors are however more prone to combustion instabilities as the following studies show ([Krebs et al. \(2002\)](#); [Candel \(2002\)](#); [Lieuwen and V. \(2005\)](#)). Compact chambers may also lead to flow interactions between adjacent burners and therefore to thermal load heterogeneities on their boundaries (see [Worth and Dawson \(2012\)](#) and [Kao et al. \(2015\)](#)). These last two issues are examined in the present study. The aim is to observe the behavior and interactions of closely packed swirling flames in the MICCA chamber under hot fire conditions and identify the resulting flame patterns.

[Kao et al. \(2013\)](#) investigated the effects of injectors spacing on the structure of flows and flames by using a linear injector arrangement. The swirling injectors are geometrically similar to industrial units and comprise counter-rotating, radial-radial swirlers and a flared cup-shaped outlet with a diverging angle of  $108^\circ$  (the angle of the conical outlet piece). These injectors were placed in a rectangular cavity open to the atmosphere and a detailed analysis of the flow patterns was carried out for the jets formed by a single, three and five injectors regularly distributed in a linear row. Configurations with three and five injectors exhibit strong interactions when these units are close enough. The air stream from the middle injector is in this case widely flared with low velocities in a large central recirculation zone, while the gaseous streams originating from adjacent injectors feature higher recirculation velocities with a more compact recirculation bubble. In the five injector case, the outer streams take a shape that is close to that of the central stream and an alternating pattern is observed between adjacent injectors. It was also found that a slight offset of the central injector exhaust relative to the chamber backplane could change the alternating pattern. [Kao et al. \(2014\)](#) indicate that alternating patterns are more pronounced when the injectors are tightly packed with a spacing factor  $s/D = 1.75$ , where  $s$  is the distance between the axes of neighbouring injectors and  $D$  is the diameter of the injector cup outlet. The alternation is still well marked when the injectors are set further away from each other ( $s/D = 2.75$ ), but a change in the flow pattern is observed between  $s/D = 2$  and  $s/D = 2.5$ .

Calculations based on RANS and comparisons with experiments by [Rojatkar et al. \(2014\)](#) indicate that a small injector offset may change the flow distribution, but the mechanisms leading to the observed flow patterns need to be documented (see for example [Kao et al. \(2013\)](#), [Kao et al. \(2014\)](#) and [Rojatkar et al. \(2014\)](#)). A recent article by [Kao et al. \(2015\)](#) discusses the behavior of the system under hot fire conditions. Alternating flow structures are observed for small spacing values but under conditions differing from those found in cold flow experiments. For  $s/D = 2.5$ , the pattern is uniform in contrast with what was found under cold flow conditions. Alternating configurations are attributed to hydrodynamic interactions and flow bifurcations between neighbouring injectors.

Recent studies carried out with multiple swirling injectors with straight channel out-

lets or slightly convergent nozzles, which were carried out on linear arrays placed in a rectangular chamber (Cordier et al. (2013)) or in annular combustors (Worth and Dawson (2013b); Worth and Dawson (2013a); Bourgouin et al. (2013)) do not exhibit these alternating flow patterns even for small spacing ratios  $s/D$  like those considered by Kao et al. (2014). This indicates that the injector cup geometry plays a significant role in the development of the alternating phenomenon. It is also well known that the cup angle at the injector outlet plays a considerable role in the jet opening angle. A small cup angle variation may cause large changes of the jet expansion angle (see for example Wang et al. (1995)). One may thus suspect strong neighbouring jet interactions when the cup angle is large and injectors are closely packed.

An additional geometrical parameter to consider is the dump ratio between the injector outlet and combustion chamber section. Impact of confinement on a single injector flow and on injectors set in an annular chamber was studied by Fanaca et al. (2010). It is found that a swirling injector operating in a “wall jet” regime in the single injector test rig may switch to a “free jet” regime when the stream is injected in an annular chamber configuration. The spreading angle is much smaller in this last case due to a change in the angular momentum distribution. These considerations lead to a correlation for a critical value of  $A_{cc}/A_{bu}$  as a function of an effective swirl number yielding the same flame topology in the single burner and annular chamber equipped with multiple burners. However, these authors did not identify alternating patterns between flames stabilized in their annular chamber experiment.

Flame alternations are usually undesirable, but might perhaps be used to hinder combustion instabilities in annular combustion chambers provided that the resulting thermal inhomogeneities remain within sustainable limits. One infers from previous work that thermo-acoustic instabilities could be reduced by modifying the sensitivity of flames to flow perturbations. It is known that flame dynamics strongly depends on their shape (see for example Durox et al. (2009), Fanaca et al. (2010), Kim et al. (2010) or Hermeth et al. (2014)) and that consequently a change in the flame configuration can suppress combustion instabilities at a given level of thermal power as shown by Durox et al. (2013) and Bauerheim et al. (2015). On the basis of theoretical and numerical investigations carried out in annular geometries, Moeck et al. (2010) and Noiray et al. (2011) have suggested that injector arrangements with different flame dynamical properties could be used to counteract instabilities, but this has not been substantiated by a practical application. Following this line of thought, it appears possible to modify the injector arrangement to create interactions between the fluid streams generated by each unit and change the dynamics of the system.

This review of the state of the art indicates that it is worth pursuing further studies of these issues in a laboratory scale annular combustor and investigate conditions giving rise to alternating flame patterns, investigate effects of the injector cup angle and consider the consequences in terms of heat load to the chamber backplane and to the combustor walls. The MICCA setup used to this purpose is described in Section 6.2.

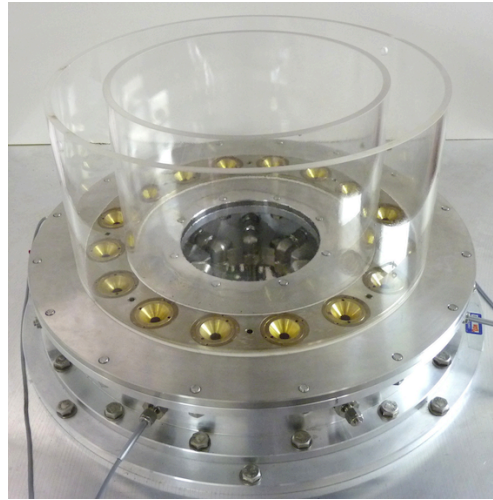


**Figure 6.1.** View of the annular combustion chamber. The mean diameter of the ring is 350 mm. The walls are 200 mm in length. The injectors are equipped with cups with an angle of  $90^\circ$  in this case.

Effects of injector cup angle, air flow rate and equivalence ratio are examined in Section 6.3. A special regime of operation featuring a low frequency irregular oscillation of the alternating flame pattern is analysed in Section 6.4. Effects of alternating flames on light intensity emission and on heat load to the walls are considered in Sections 6.5 and 6.6. Results are then used in Section 6.7 to check the correlation derived by [Fanaca et al. \(2010\)](#) and see it can be used to predict the flow regime.

## 6.2 Experimental Setup

The MICCA test rig, sketched in Fig. 6.1, is very close to MICCA-Spray with a horizontal upstream plenum closed at the top by an annular plate with sixteen swirling pre-mixed injectors and a combustion chamber made of two cylindrical concentric quartz tubes mounted on the horizontal annular plate which serves as a chamber backplane. The diameters of the inner and outer quartz tubes are 300 mm and 400 mm respectively. The chamber axial dimension is 200 mm.

A propane/air premixed flow is delivered by a premixing unit. The mixture is then conveyed to an annular plenum through eight channels which are plugged on the internal sides of the annulus. Gases in the plenum are exhausted through the sixteen swirling injectors mounted on the flange which separates the plenum from the chamber and constitutes the chamber backplane. Each injector comprises six tangential tubes to set the flow in rotation. A detailed view of the swirler is given in Fig. 6.2. When viewed from above the flow in the swirlers rotates in the clockwise direction. The streams formed in the six tangential tubes are injected in a  $d = 10$  mm diameter cylindrical channel that can be terminated by a cup with different flaring angles of

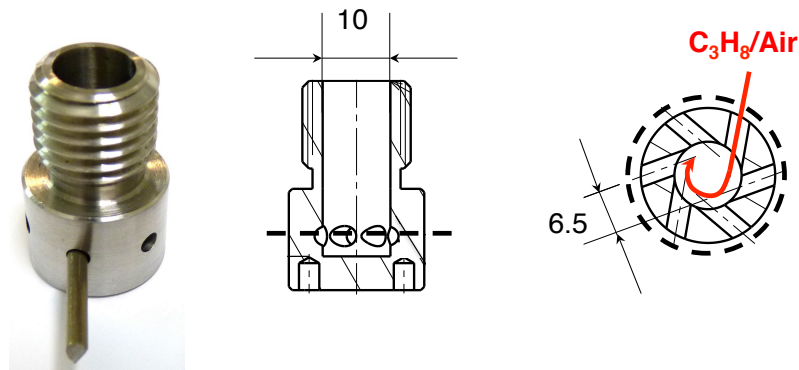


**Figure 6.2.** View of the swirler. The six holes are 3 mm in diameter.

70°, 90° or 105° sketched in Fig. 6.3. The cup is 10 mm long and its outlet is flush mounted to the chamber backplane or protrudes in the chamber with an positive offset of 1.5 or 3 mm with respect to the backplane. The injectors can be also mounted without cups providing a cylindrical outlet of 10 mm diameter. Velocity profiles measured at the outlet of the cylindrical tube are shown in Fig. 6.4. Measurements were carried out with a laser Doppler velocimeter, at 1.7 mm downstream of the outlet. To reproduce the effects of confinement, a cylindrical tube, 50 mm in diameter and 200 mm in length, confines the jet. The axial velocity profile reveals a weak recirculation region established in the center. The azimuthal velocity profile  $U_\theta$  shows a nearly linear increase between  $R = 1$  and 4 mm. Beyond  $R = 6$  mm, the slope of the azimuthal velocity profile changes, with a constant velocity gradient. Integration of the velocity profiles in the region corresponding to the swirling jet up to  $R = 6$ mm

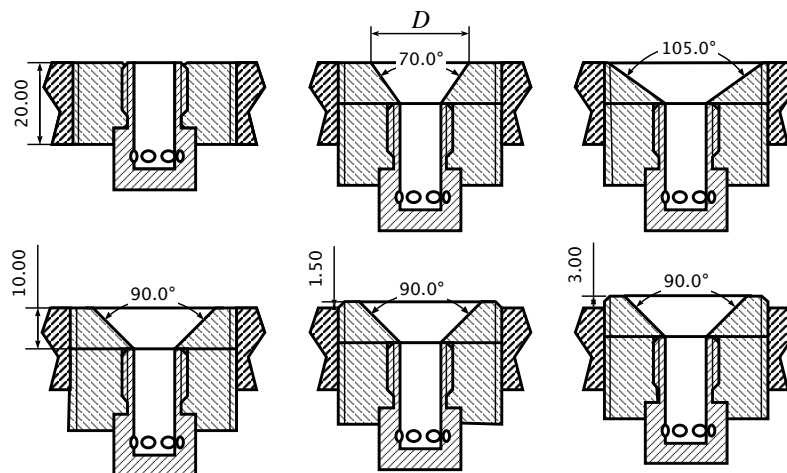


**Figure 6.3.** The different injectors with and without cups. The offset is measured with respect to the combustion chamber backplane.  $D$  corresponds to the outlet diameter of the cups.

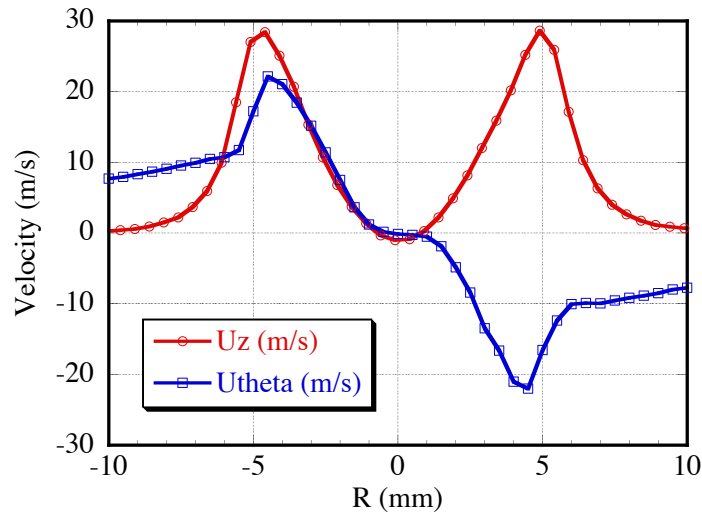


**Figure 6.4.** Axial and azimuthal velocities profiles,  $U_z$  and  $U_\theta$ . These profiles are measured by Laser Doppler Velocimetry, at 1.7 mm downstream of the outlet of a single injector. There is no cup, like in Fig. 3, at the top left. For this test, the mean flow rate is  $U_b = 17.1 \text{ m}\cdot\text{s}^{-1}$ . The flow is confined by a cylindrical tube, 50 mm in diameter, 200 mm in length.

gives a swirl number of  $S = 0.71$ . A theoretical estimate developed in [Durox et al. \(2013\)](#) and [Candel et al. \(2014\)](#) may be obtained from  $S_0 = (\pi DR_0)/(4A_t)$  where  $D$  is the outlet diameter,  $R_0$  denotes the distance between the axis of one inlet pipe and the axis of the injector and  $A_t$  is the total surface area of the inlet pipes: here  $D = 10 \text{ mm}$ ,  $R_0 = 3.25 \text{ mm}$  and  $A_t = 42.4 \text{ mm}^2$  and one finds  $S_0 = 0.60$ . The measured swirl number is slightly larger than the estimated value, but the measurements are made slightly downstream of the injector outlet, and velocity profiles do not quite correspond to those existing at the injector outlet. In addition, the theoretical formulation assumes a solid body rotation for the azimuthal component, which is not completely reflected in the velocity profile in Fig. 6.4. The swirl number has a value which is typical of those observed in industrial annular combustors.

Head loss measurements through the injectors have also been carried out for the injectors equipped with the  $90^\circ$  cups (see Fig. 3 bottom left). The measured pressure loss increases with the injection velocity square, and its relative value with respect to atmospheric pressure, is 3.3 % when the bulk velocity in the cylindrical part of the injector is  $U_b = 20 \text{ m}\cdot\text{s}^{-1}$ . This value is similar to those typically found in gas turbine injectors.

The injectors are fixed in the chamber backplane made of stainless steel and cooled by a water circulation. The temperature in the plenum never exceeds  $35^\circ\text{C}$ , even after operation of the combustion chamber over a long duration. The spacing factor for the different injectors equipped with cups is given in Tab. 6.1. For the largest cup angles,

Cup angle ( $^{\circ}$ )	w/o	70	90	105
$s/D$	6.87	2.86	2.29	1.70

**Table 6.1.** Spacing factors of the different injectors.  $s$  is the arc length between the axes of neighbouring injectors and  $D$  is the outlet diameter of the cup.

values of  $s/D$  are of the same order as those used in [Kao et al. \(2014\)](#), meaning that interactions between adjacent injectors are studied under cold flow conditions in that reference.

The side walls confining the flame are made of quartz allowing optical visualization of the flame and transmitting its radiation in the near ultraviolet and visible ranges. They provide a direct access to the flame pattern. Flame snapshots were taken with two cameras, positioned at  $90^{\circ}$  from each other. One camera provides images of the full annular combustor. The second camera yields closer views of the flames. The two systems use a full aperture with an exposure time of 0.6 s. These parameters are kept constant during the experiments, so that the picture brightness is roughly proportional to the light intensity. The fast motion of the flame was also observed in one of the test conditions with a high speed intensified CMOS camera APX-i2 ( $512 \times 256 \text{ px}^2$ ) providing an 8-bit grey level resolution. This camera was set to record images of all the flames at a sampling rate of 500 frames per second, with a shutter duration of 1.2 ms. For each test with this high speed camera, 6,000 images were acquired.

Six flow rates and equivalence ratio conditions were investigated and are indicated in [Tab. 6.2](#). The first three conditions correspond to operation at a constant equivalence ratio  $\phi = 0.74$ . The bulk velocity in the cylindrical part of the injector varies from  $U_b = 12.2 \text{ m.s}^{-1}$  to  $22 \text{ m.s}^{-1}$ . For the second series, the equivalence ratio is varied between  $\phi = 0.64$  and  $0.94$ , and the flow velocity is roughly constant and equal to  $U_b = 17.1 \text{ m.s}^{-1}$ . In these latter experiments, the air flow is kept constant and only the propane flow rate is changed. Since the propane flow rate is small compared to the air flow rate, a change in the propane flow rate only slightly changes the bulk flow velocity  $U_b$  in the injector. All measurements presented in this study are carried out after operating the combustion chamber for several minutes to reach a steady thermal state.

$U_b$ ( $\text{m.s}^{-1}$ )	12.2	17.1	22.0	17.1	17.1	17.2	17.3
$\phi$	0.74	0.74	0.74	0.64	0.74	0.84	0.94

**Table 6.2.** Flow conditions. The bulk velocity  $U_b$  is determined in the cylindrical injection channel.  $\phi$  designates the equivalence ratio.

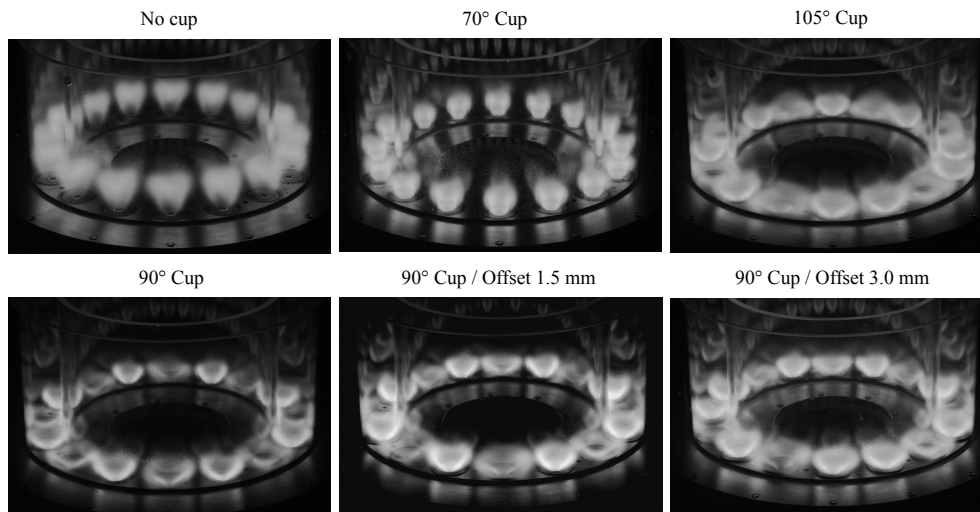


**Figure 6.5.** Typical flame shapes obtained for the different injector geometries.  $U_b = 17.1 \text{ m.s}^{-1}$ ,  $\phi = 0.74$ .

### 6.3 Analysis of flame patterns

Effects of cup angle, injection velocity and equivalence ratio are now considered successively.

#### 6.3.1 Influence of injector cup angle

Flame patterns are first examined in Fig. 6.5 for a fixed flow velocity  $U_b = 17.1 \text{ m.s}^{-1}$  and equivalence ratio  $\phi = 0.74$ , but with different injector geometries. Without cup and with the  $70^\circ$  cup, flames are all similar to each other within the annular chamber. Without cup, the flame luminosity appears well above the injectors. The center of the flame is hollow, due to the recirculation of the burnt gases induced by the swirl at the outlet of each injector. The  $70^\circ$  cups yield flames which are slightly shorter but they are well separated from each other. Each flame cone matches the shape of the cup and slightly protrudes in the injector. For a  $90^\circ$  cup, one distinguishes an alternating pattern of the flame shapes. Flames can be elongated and take a V-shape. In Fig. 6.5, V-flames are surrounded by neighbouring flames expanding in the lateral direction and taking an M-shape. This is clearly visible in the three cases:  $90^\circ$  cup,  $90^\circ$  cup/ Offset 1.5 mm and  $90^\circ$  cup/ Offset 3 mm. This alternating configuration remains in place over a long period of time. The fact that the number of injectors is even (16) probably favors a stable situation. For the  $90^\circ$  cups, there is no significant difference in the flame geometry with or without offset. This is at variance with results obtained under cold flow conditions and presented by [Kao et al. \(2013\)](#) and [Rojatkar et al. \(2014\)](#). With cups of  $105^\circ$ , the alternating pattern is stronger but it becomes unstable and switching begins to appear when the equivalence ratio approaches stoichiometry. This situation will be discussed in section 3.3.

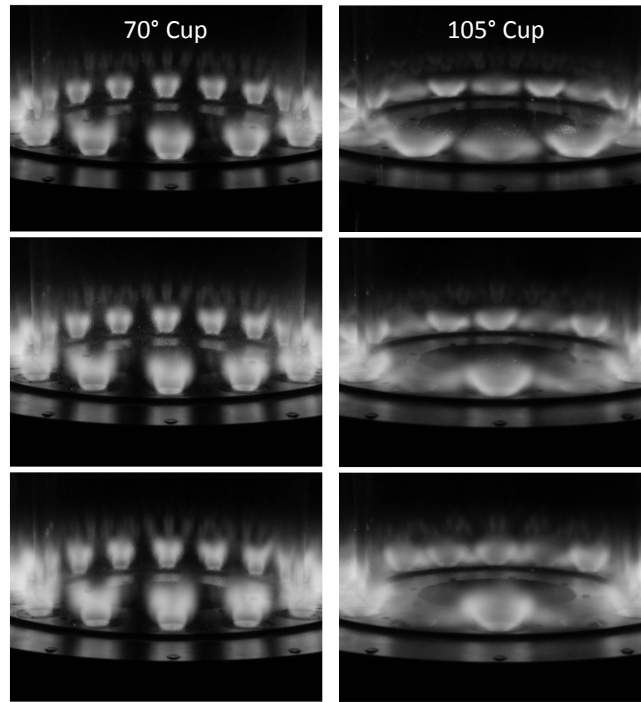


**Figure 6.6.** Influence of the bulk velocity on the flame topology. The left column corresponds to a 70° cup, the right column pertains to a 105° cup.  $\phi = 0.74$ . From the top to the bottom rows  $U_b = 12.2, 17.1$  and  $22 \text{ m.s}^{-1}$  respectively.

### 6.3.2 Influence of bulk velocity

Effects of the bulk velocity are now investigated by considering the 70° and 105° cups shown in Fig. 6.6. For the low flaring angle, the flames expand axially but there is no other effect. If the flames develop uniformly at low flow velocity (Fig. 6.6, left), they also develop in a similar fashion at full power. For the high flaring angle the situation changes. The alternating pattern appears at low injection velocity (Fig. 6.6, right), and persists when the flow rate increases. As the flow rate is increased, flame interactions are stronger and the alternating pattern is more visible. The blooming M-flames extend sideways to find a place under the V-shaped flames. The light from the V-flames is more intense than that radiated by the M-flames. There are at least four possible reasons for this:

1. The mass flow rate of the successive injectors may be modulated due to the change in the downstream flow. The result could be that the two types of flames will have a different level of heat release and subsequently will differ in their light radiation,
2. The light intensity is reduced because the M-flame entrains more burnt gases and the fresh stream is diluted by combustion products reducing the flame chemiluminescence,

3. The M-flame is closer to the chamber backplane which is kept at a low temperature by the water cooling system and the flame temperature is reduced diminishing the light radiated by excited radicals,
4. The M-flame occupies a larger volume and the heat release rate per unit volume is lower than that corresponding to the V-flame and this is reflected in a lower level of radiation in the M-flame with respect to the V-flame.

These different possibilities are evaluated in section 6.5.

### 6.3.3 Influence of equivalence ratio

The flame geometries are more sensitive to changes of the equivalence ratio.

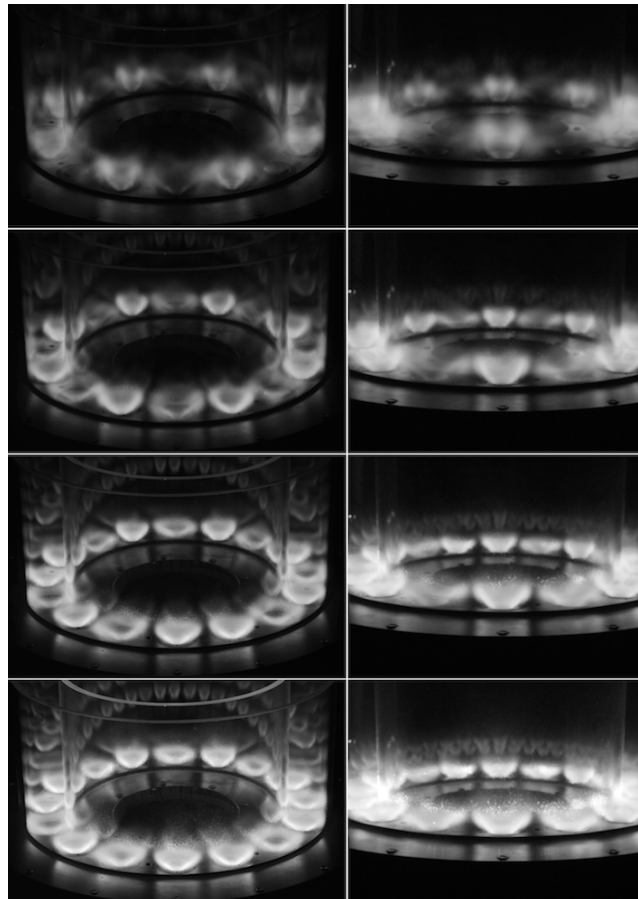


**Figure 6.7.** Influence of the equivalence ratio on the flame topology. 90° cup.  $U_b \simeq 17.1 \text{ m.s}^{-1}$ . Two cameras are positioned near the combustion chamber, with two different viewing angles. From the top to the bottom rows  $\phi = 0.64, 0.74, 0.84$  and  $0.94$ .

An example is shown in Fig. 6.7 for the 90° cup which exhibits alternating flame configurations. The equivalence ratio varies from  $\phi = 0.64$  to 0.94. At  $\phi = 0.64$ , the periodic flame arrangement is quite visible because the blooming M-flames, which are shorter, are not very bright. The tip of these flames lies underneath the neighbouring V-flames. Increasing the equivalence ratio, the flared flames become brighter. The angle of the V-flames widens compared to the case at  $\phi = 0.64$ . This phenomenon is accentuated when the equivalence ratio increases towards stoichiometric conditions. The V- and M-flames are more difficult to distinguish. The angles of neighbouring flames are substantially the same at  $\phi = 0.94$ . There still remains a small difference and the tip of each M-flame is tucked below the tip of the adjacent V-flame.

It is worth noting that the cylindrical injection systems (without cup) could not be tested beyond  $\phi = 0.89$  because the flame entered the injector and reached the bottom of this unit. It was not possible to operate the combustor for a long time in this configuration, without risking flashback. In contrast, when the injector is equipped with a cup, and for the cup angles considered in this study, the flames are always stabilized at the outlet and no combustion reaction takes place in the cylindrical injection channel.

#### 6.4 Alternating pattern switching

At low equivalence ratio,  $\phi = 0.64$  and 0.74, and for the largest cup angles of 90° and 105° one observes alternating patterns with similar features. At  $\phi = 0.84$ , a chaotic oscillation phenomenon appears between adjacent flames. The flames, which were elongated in the axial direction to form V-shapes, become crushed while the flames which were blooming sideways are lengthened in the axial direction. The process is then reversed at low frequency of the order of one Hertz, but the phenomenon is not cyclic and the flame pattern flips between two positions. Increasing the equivalence ratio to  $\phi = 0.94$ , switching occurs more frequently, with a nearly regular period. This process was characterized by taking a high-speed film with the intensified CCD camera. Four images in a sequence are shown in Fig. 6.8. The time interval between each frame is 62 ms. The two flames that are closest to the camera are designated "A" and "B". It can be seen that the flame "A", which is elongated at  $t = 0$ , becomes

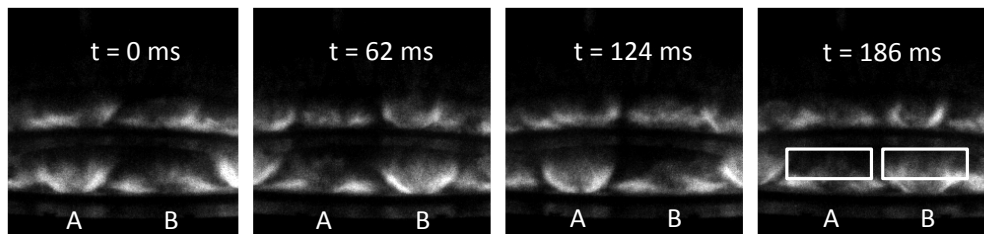


**Figure 6.8.** 105° cup.  $U_b \simeq 17.3 \text{ m.s}^{-1}$ .  $\phi = 0.94$ . Instability at low frequency of the flame patterns.

flared at  $t = 62$  ms, and then elongated again at  $t = 124$  ms and so on. Its neighbor, the flame "B" features the opposite geometry. The switching motion is synchronous and all flames move simultaneously. This is highlighted in Fig. 6.8 for flames which are diametrically opposed to flames A and B in the combustor ring. It is likely that a small difference between the flames exists in the time of the flip-flop, because the switching must be initiated at a specific location of the annulus, but the visualizations are not sufficiently well resolved to refine this observation.

The switching frequency is explored by examining the light intensity level at the tips of flames "A" and "B". The mean light intensity, measured in the rectangles drawn in the right image in Fig. 6.8, is plotted versus time in Fig. 6.9. It can be seen that the two signals are nearly out of phase, indicating that the neighbouring flames have strictly opposite shapes. The frequency is low and almost regular. It is of about 7.8 Hz for the conditions investigated in this study. The mechanism is reminiscent of fluidic oscillations. It has not yet been possible to determine if the source of this instability lies in the burnt gas recirculation zone, or if it is generated in the jets, under the action of instabilities in the pressure drops induced by the injectors. A numerical computation, carried out in parallel to this study, with the same conditions and geometry of the combustion chamber, might help clarify the origin of this mechanism. In particular, it is important to know, if the origin is linked solely to the jets interaction, or if the presence of flames, which strongly interact, plays a role in this phenomenon. A measure of the pressure drop of each injector is difficult to achieve in the current experimental configuration but measurements of the velocity field in the combustion chamber, with and without flames, will help analyze this low frequency oscillation.

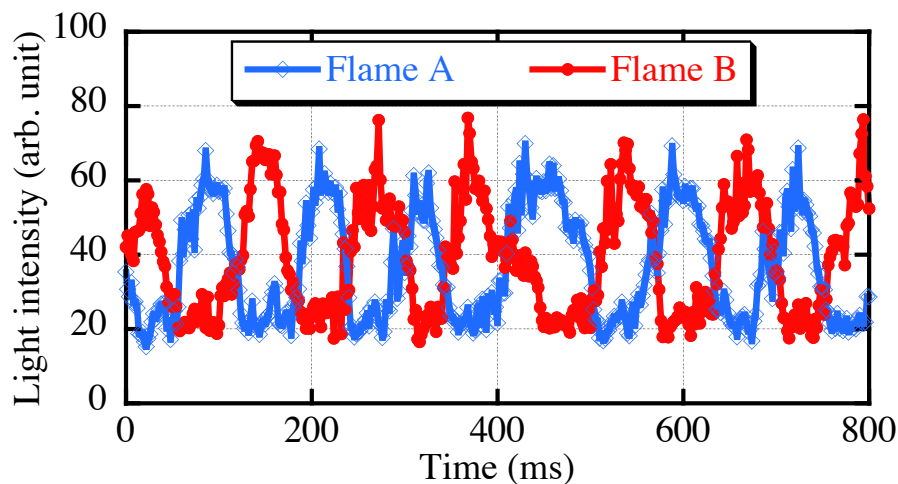


**Figure 6.9.** Time evolution of the light intensity for flames A and B defined in Fig. 8.

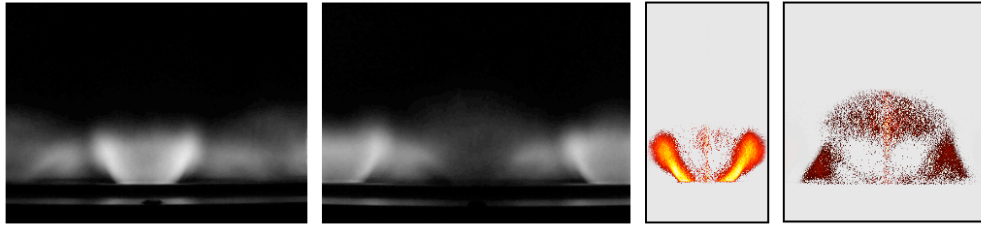


**Figure 6.10.**  $90^\circ$  cup.  $U_b \simeq 14.7 \text{ m.s}^{-1}$ .  $\phi = 0.74$ . The first two images show light emission from the two types of flames : the V-type flame and the M-type flared flame. The result of an Abel inversion of the two flames is shown in the last two images.

## 6.5 Influence of the flame shape on the light intensity distribution

It has already been pointed out that when the alternating flame pattern arises, the flared M-type flames appear to radiate less light than the elongated V-type flames. Since flames of propane/air are operating under lean conditions in this study, the light emission, in the visible domain, is mainly due to  $\text{CH}^*$  radicals and to a lesser extent to  $\text{C}_2^*$  radicals. It is known that the light intensity from these radicals is roughly proportional to the heat release rate, as shown by [Hurle et al. \(1968\)](#) and [Price et al. \(1969\)](#). To verify that this observation of a difference in light emission corresponds to a difference in the heat release rate per unit volume, it is necessary to take the Abel transform of the flame images and examine the levels of intensity corresponding to the M- and V- flames. Images of these two types of flames are recorded with a long exposure time, by setting the camera lens axis at right angles to the flame axis. A first image was acquired of an elongated V-flame and the camera was then moved by  $1/16$  of a turn around the combustion chamber, to obtain an average image of a flared flame as shown in Fig. 6.10. On average, these two flames are approximately axially symmetric, and it is therefore possible to perform an Abel inversion. Results of this processing presented on the right hand side in Fig. 6.10 indicate that the elongated V-flame exhibits an intensity distribution with values higher than those found in the flared M-flame. As the two flames correspond to the same equivalence ratio, one may deduce from this observation that the reaction rate per unit volume takes larger values in the V-flame.

It is however important to consider the other possible reasons of the observed difference in brightness. Four such reasons were listed above. The first possibility is that when the alternating flame configuration occurs, the flow rates in two adjacent injectors differ from each other and correspondingly the heat release of two adjacent injectors also leads to an unbalanced distribution. For this to be so, the flow rate in the injector corresponding the flared flame would have to be lower than that passing through the injector producing the V-flame. It is however worth noting that calculations of cold flow alternating patterns done by [Rojatkar et al. \(2014\)](#) indicate that

there are no variation in the flow rate delivered by adjacent injectors. The second possibility put forward is that the recirculation of burnt gases modifies the mixture at the outlet of each injector and in particular changes the composition in the flame region. It is known from [Garcia-Armingol et al. \(2014\)](#) that dilution reduces the level of radiation from excited radicals. It is however necessary to show that gases giving rise to M-flames are more diluted than those inducing the V-flame. A third hypothesis considers the temperature in the flame region. The flared flame extends sideways and is quite close to the backplane of the combustion chamber, much more than the elongated V-flame. The M-flame is cooled by the wall and its temperature is lower which in turn reduces the light radiated by the  $C_2^*$  and  $CH^*$  radicals reducing the light intensity. To confirm this assumption, temperature measurements were made in the heart of the two flames, using a type *R* thermocouple (Platinum/Platinum-13%Rhodium). The thermocouple was placed at a distance of 12 mm above the backplane, and at two different positions for each flame: on the axis, and then in vertical alignment with the outlet of the cup. The experiment was done with the  $90^\circ$  cup, at an equivalence ratio of  $\phi = 0.74$  and a flow velocity of  $U_b = 17.1 \text{ m.s}^{-1}$ . It was found that the flared M-flame had a combustion temperature  $140^\circ\text{C}$  lower than the elongated V-flame. The important heat losses to the chamber backplane largely explain the difference in brightness between the two flames. The fourth possibility is that the flame volumes of the two flames differ and this will have a direct effect on the heat release rate per unit volume reflected in the light radiation. This may well also be the reason for the reduced luminosity observed in the experiment. Numerical simulations, taking into account the conditions in the annular combustor, should also help to better explain the mechanisms leading to the alternating flame pattern.

## 6.6 Influence of the flame shapes on heat load on the inner wall

Given the two different shapes of alternating flames and the difference in combustion temperatures, it is evident that the heat transfer to the walls near the injector outlets will not be identical for the two flames. Figure 6.11 shows a view of the combustion chamber, when it is equipped with an inner wall of refractory steel. The combustion chamber is in operation for several minutes and the thermal equilibrium state is reached. The temperature of the inner wall is high enough to see a strong light radiation of this wall. The elongated V-flames which are the most luminous and which have the highest combustion temperatures, give the maximum temperature on the wall. Yet they have the lowest opening angle, but the heat transfer to the walls is much stronger than for the flared flames. Although the tip of the flared flames reach the metal wall, the heat flux is not sufficient to bring the wall to bright red. The wall in the near vicinity of these flames is brown red indicating that its temperature does not exceed  $700^\circ\text{C}$ . For the elongated V-flames, the color is red, pink down to the backplane, indicating that the temperature is much higher, of the order of  $850^\circ\text{C}$ .



**Figure 6.11.** Visualization of the thermal effects. 90° cup.  $U_b \approx 17.1 \text{ m.s}^{-1}$ .

The fact that the flames which are flared, heat the walls to a lesser extent than the elongated V-flames, while their outer diameter is greater, confirms that the volumetric heat release rate is much lower for the flared flames and that the combustion temperature is smaller. The colored spiral stripes, visible on the inner wall, are due to the tangential motion of the burnt gases generated by the swirling motion induced by the set of injectors, which induce a mean rotation in the clockwise direction (see Fig. 6.2). The induced rotating component is significant, since the angular rotation level is of about 1/16 of a turn for an elevation of 0.2 m in the combustion chamber. It is possible to deduce the induced azimuthal velocity  $v_\theta$ . One finds that  $v_\theta \simeq 0.29v_x$ , where  $v_x$  is the mean axial velocity of the burnt gases in the combustion chamber. This rough approximation gives an estimate of the rate of rotation induced by the swirling jets emerging from the injectors.

## 6.7 Influence of the jet confinement on flame shape

It is shown in the previous sections that strong interactions take place between adjacent flames when the cup angle takes large values (90° and 105°). One may wonder if this feature can be predicted with the correlation proposed by [Fanaca et al. \(2010\)](#). Their analysis relies on work by [Fu et al. \(2005\)](#) dealing with the behavior of a swirling jet confined between lateral walls. A model is derived for swirling jets that are close to each other and that are confined between side walls, as in annular combustion chambers. This correlation exploits a balance of angular momentum fluxes between adjacent swirling flows, to determine whether the confined swirling jet flows behave as “free jets” or as “wall jets”. The model uses an effective swirl number and the ratio between the cross-sections of the injector outlet and the chamber backplane  $A_{cc}/A_{bu}$ .

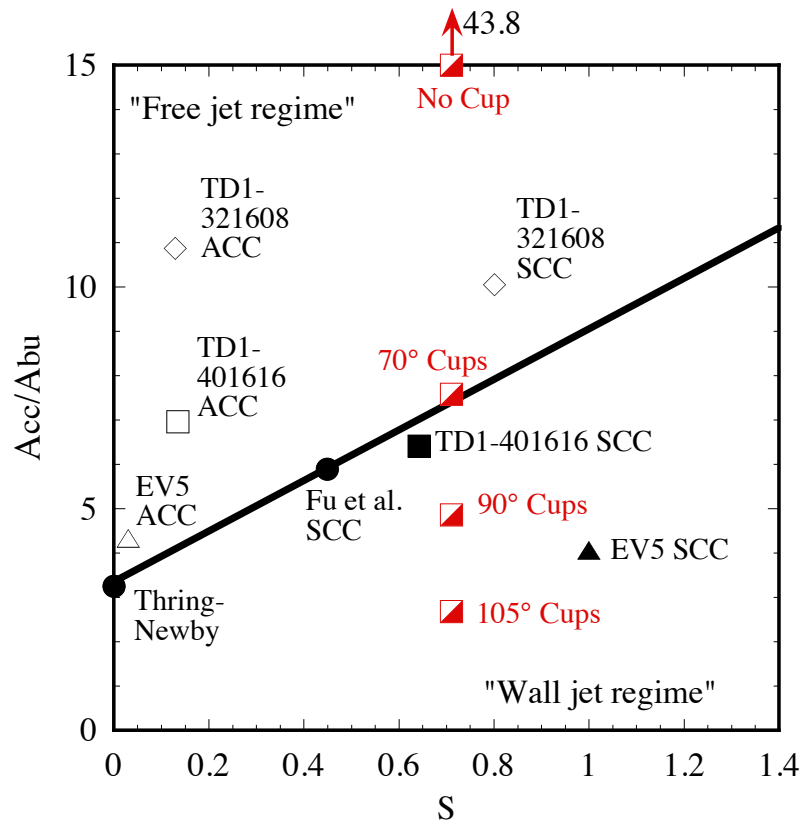


**Figure 6.12.** Operating map introduced by Fanaca et al. (2010). The present data are plotted on this map in red squares located at a swirl number  $S = 0.71$ . For the injectors without cup, the ratio  $A_{cc}/A_{bu}$  is equal to 43.8 and lies outside this graph.

Conditions explored in the present study are superposed to the regime diagram proposed by Fanaca et al. (2010). Points corresponding to the four injector geometries tested (no cup, 70°, 90° and 105°) are plotted in Fig. 6.12. The section area  $A_{cc}$  corresponds to 1/16 of the annular backplane area of the combustion chamber and  $A_{bu}$  corresponds to the section area at the cup outlet of one injector. The swirl number  $S = 0.71$  was measured on the single burner test rig with an injector without cup and this value serves as a reference. For a single combustion chamber (SCC), Fig. 6.12 shows that the 90° and 105° cups lead to flame interactions with the walls. The 70° cup lies close to the transition limit between the two regimes. The burner with a cylindrical outlet (no cup) operates in the free jet regime.

Fanaca et al. (2010) also examined changes induced by the presence of neighbouring flames in the case of an annular combustion chamber (ACC). For an arrangement of co-rotating swirlers, the swirling flow above each injector is rotating in the same direction leading to azimuthal counter-flows at the periphery between neighbouring injectors. This leads to a reduction in the intensity of the swirling flow of each injector.

From velocity measurements made on a SCC injector and one of the ACC injectors, these authors deduced an effective swirl number for the ACC case. This effective swirl number is much smaller than the swirl number deduced from the SCC case (see Fig. 6.12). Their results show that flames which are in the domain of “wall jet regime” shift to the left on the diagram and may transit to the domain of “free jet regime”. In the present study, the velocity fields were not determined on the different injectors and results are interpreted for the measured swirl number  $S = 0.71$ . Following [Fanaca et al. \(2010\)](#), one may guess that the results plotted in Fig. 6.12 will be moved to the left for the injectors set in the annular combustion chamber. However, cases  $90^\circ$  and  $105^\circ$  lying far away from the transition regime boundary will probably remain in the “wall jet regime” domain. These results help interpreting the strong interactions of neighbouring flames observed at large cup angles, leading to well defined large alternations of the flame shapes. Assuming a slight shift to the left, flames stabilized with the  $70^\circ$  injector cups will probably transit in the “free jet regime” in the ACC condition and this is well verified in the annular combustor. Due to the fixed separation distance between neighbouring injectors in the annular chamber, flames in the “wall jet regime” can only fully develop above one injector over two in the annular combustor leading to an alternating flame pattern.

## 6.8 Conclusion

This chapter describes experiments carried out on the MICCA annular combustion chamber equipped with swirling premixed injectors comprising a cup at their outlet. Under certain operating conditions in premixed combustion an alternating flame pattern arises. In this pattern, the flames periodically take a V-shape elongated in the axial direction and an M-shape extending in the azimuthal direction. There are an even number of injectors in the annulus, allowing the formation of a regular alternating pattern of flame shapes. To observe this configuration, the injectors need to end with a cup. If the cup angle is less than  $70^\circ$ , the phenomenon does not occur. For  $90^\circ$  and above the alternating pattern is quite visible. Tests carried out with swirling injectors, but without cup, indicate that the flame pattern does not feature such a periodic structure. Results indicate that the flow rate has a moderate influence. An increase in flow rate only lengthens the V-type flames. The influence of the equivalence ratio is much greater. At low equivalence ratio, the difference is the largest between the elongated V-flames and the flared M-flames. For injectors the larger cup angles (equal or greater than  $105^\circ$ ) and an equivalence ratio close to the stoichiometry, the alternating arrangement of flames becomes unstable and unsteady switching takes place. The V-flames which were elongated in the axial direction take a flared M-shape, and the process is reversed at a later time. This happens at a relatively low frequency of a few Hz and is reminiscent of flip-flop fluidic dynamics.

It is found from thermocouple measurements that the flared flames have a combustion temperature which is less than that of the elongated V-flames. The observed cooling is probably related to the fact that the flared flames are closer to the backplane augment-

ing the level of heat losses under these conditions. The alternation of flame shapes in an annular combustion chamber may have important consequences for steady state operation and it may also influence thermo-acoustic dynamics of the system. If the flames have different shapes, they necessarily have different dynamics, and one can imagine that if some of the flames contribute to the instability, the other group of flames can be used to reduce the perturbation.

While this chapter provides data on the pattern formation process, it does not fully explain the origin of the mechanism. This requires further exploration, probably with numerical simulations because measurements in the injector cups are difficult. Nevertheless, a scenario based on transitions of the swirling flames between “free jet” and “wall jet” regimes is confirmed by the present annular combustor experiments.







## Chapter 7

# Flame dynamics during an hysteresis in an annular combustor

*Thermo-acoustic instabilities in annular combustors with swirling turbulent injectors are most often coupled by azimuthal modes with a spinning or a standing structure. Experiments, and recent large eddy simulations, indicate that switching takes place between these two types of modes while in other cases a single mode type prevails. Why and how one type arises is a subject of ongoing discussions in recent theoretical and numerical investigations. The present chapter considers this intriguing issue by making use of well controlled experiments carried out in an annular combustion system comprising 16 identical matrix injectors operating in a laminar premixed mode and allowing full optical access to the flame region. This setup is used in a first stage to determine regions of instability as a function of equivalence ratio and injection velocity. It is shown that regions corresponding to spinning and standing azimuthal modes are well separated in this diagram, but with some overlap giving rise to a "dual mode" domain. For the same operating conditions, this annular system thus exhibits self-sustained instabilities with stable limit cycles coupled by a spinning or a standing mode. It is next shown that the mode which appears in that region depends on the path followed to reach the operating point. Starting from a lean operating condition, the system first develops a chugging instability with a broad frequency spectrum, which then gives rise to a well established spinning oscillation with a narrow peak frequency in the dual mode region. When operation begins under rich conditions one first observes another chugging mode that finally yields a standing mode when the equivalence ratio is diminished. Away from these regimes, well defined slanted modes and longitudinal modes can also be triggered. In the dual mode region, the type of instability is controlled by an hysteresis phenomenon and the respective chugging modes act as precursors to these established azimuthal modes. It is found that the trajectories in a Poincaré map contain indications on the kind of azimuthal oscillation that will be observed when the target operating point is reached. Beyond the various theoretical explanations of the prevalence of one type of mode on the other, the present observations indicate that spinning or standing modes may also appear in annular combustors as a result of the path used to enter the region of azimuthal instability.*

## 7.1 Introduction

It has been seen in the previous chapters that aircraft engines and gas turbines use annular shaped combustor (Krüger et al. (1999); Schuermans et al. (1999); Krebs et al. (2002); Moeck et al. (2010); Worth and Dawson (2013b); Worth and Dawson (2013a); Bourgouin et al. (2013b)). As circular dimensions of these devices are of the same order of magnitude or greater than the longitudinal dimensions, azimuthal modes involve lower resonant frequencies located in bands where combustion is more sensitive to incoming perturbations. It is therefore important to have a good knowledge of the mechanisms leading to resonant motions coupled by such modes. During the last period a large research effort was undertaken to understand the origin of these instabilities and to offer solutions for their reduction and control. One important question concerns the nature of the coupling modes and the factors which determine the spinning or standing type of these modes. The objective of the present study is to provide experimental data on these issues. It specifically considers a hysteresis phenomenon where an annular combustor exhibits spinning and standing modes for the same operating conditions. Issues of this kind, such as switching are discussed in technical articles, but the case studied here does not seem to be reported in previous studies. It is shown that the two azimuthal modes, spinning or standing, are possible for the same exact conditions of flow rate and equivalence ratio. The mode type only depends on the path followed to get to the target operating point. It is also shown that forerunner signals announce the nature of the mode that will appear eventually allowing to predict the mode type.

This chapter begins with a synthesis of the current state of knowledge on combustion instabilities coupled by azimuthal modes in Section 7.2. The experimental setup is briefly described in Section 7.3. The stability map is introduced in Section 7.4 together with a description of the chugging modes which naturally arise in the system. It is then shown in Section 7.5 that a hysteresis phenomenon may give rise to a spinning or a standing mode for the same operating conditions.

## 7.2 Combustion instabilities coupled by azimuthal acoustic modes

It is at this point interesting to review the literature and begin with Large Eddy Simulations (LES) which are quite promising, but only provide partial answers due to the computational time required and to the cost of calculations (see Staffelbach et al. (2009), Wolf et al. (2012) and Wolf et al. (2012)). Among these articles, it is worth noting that Wolf et al. (2012) find that the azimuthal instability arising in a helicopter engine combustor with a choked nozzle preferentially involves a standing mode with some switching into a spinning mode. Alternative numerical strategies have been developed that are less demanding in terms of computational resources and therefore better suited to engineering needs. Helmholtz solvers, which take into account the

full geometry of the annular combustion chambers offer an interesting framework for linear and nonlinear stability analysis of real systems (Nicoud et al. (2007) and Camporeale et al. (2011)) but they require accurate data on the flame dynamics in the form of Flame Describing Functions, the nonlinear extension of the Flame Transfer Functions. These data are often missing for a successful prediction of combustion instabilities. Recent improvements by Campa and Camporeale (2014) allow detailed investigations of the effect of the time delay introduced by the Flame Transfer Functions on the combustor stability, but with a lack of experimental comparisons. Despite recent progress, these works have not been able to determine the nature, spinning or standing, of the azimuthal modes involved in the coupling.

Mode type selection is a difficult problem. Due to the rotational symmetry of the system, it admits a two-dimensional eigenspace for azimuthal modes, hosting standing and spinning solutions and every combinations thereof. This problem has essentially been investigated with low order models because they provide a physical representation of the system dynamics and are easy to implement (see for examples Krüger et al. (2001), Stow and Dowling (2001), Evesque and Polifke (2002), Schuermans et al. (2003), Dowling and Stow (2003) and Morgans and Stow (2007)). Their results obviously depend on measured acoustic boundary conditions and adequate representations of the flame dynamics of each burner. These models rely on different approximations about the system geometry, acoustic propagation, interaction with the mean flow and flame responses to flow perturbations. The major results concerning azimuthal mode selection are synthesized in Tab. 7.1 and are briefly described below. Note that the work presented bellow may not be only analytical but this table summarizes the theoretical part of each paper.

Ref.	Geometrical model	Acoustic model	Flame model	Conclusions
Pankiewitz and Sattelmayer (2003)	Generic annular chamber connected to a plenum by 12 injection tubes	Time domain wave equation simulations	Nonlinear time lag model $\dot{Q} = \eta(t - \tau)$ with static gain saturation	Mode type selection seems to be related to the presence of a mean flow.

Evesque and Polifke (2002) and (2003)	Generic annular chamber connected to a plenum by 12 injection tubes	Frequency domain acoustic network	Linear burner transfer matrix determined in a single burner numerical or experimental setup	No impact of the mean flow is found on mode type selection. A spin-ratio indicates if the mode is preferably spinning or standing.
Schuermans et al. (2006)	Annular geometry with plenum and chamber	Time domain state-space network	Nonlinear time lag model $\dot{Q} = \eta(t - \tau)$ with static gain saturation (Pankiewicz and Sattelmayer (2003)), values are fitted from burner transfer matrix measurements	For symmetric configuration with identical burners, a standing mode may develop but rapidly changes for a spinning type, which is the only stable limit cycle.
Noiray et al. (2011) and Noiray and Schuermans (2013)	Annular chamber with a continuous distribution of heat release, no plenum	Analytical model	Nonlinear model $\dot{Q} = \beta p - \kappa p^3$ , with parameters fitted to measurements close to the resonant frequency	Spinning type if all the flames have the same response, standing type either in most cases. Mixed mode can sustain can however be predicted.

Bothien et al. (2015)	Annular geometry with plenum and chamber	Frequency domain acoustic network	Nonlinear model $\dot{Q} = \beta p - \kappa p^3$	Models are adjusted and compared to experiments in a real gas turbines.
Ghirardo et al. (2015) and (2016)	Annular chamber with $N_b$ discrete burners, no plenum	Analytical model	Nonlinear model $\dot{Q} = F(p)$ , where $F$ is a nonlinear time-invariant operator	Stability conditions for spinning and standing modes are given as a function of the number of burners and Flame Describing Function.
Bauerheim et al. (2014) and Bauerheim et al. (2014)	Annular chamber connected to a plenum by $N$ discrete burners	Analytical matrix model	Linear time lag model $\dot{Q} = \eta(t - \tau)$	Mode type selection may differ in the plenum and chamber. Symmetry breaking leads to a preferred standing type.

**Table 7.1.** Synthesis of the main investigations dealing with mode type selection.

In an early investigation, Schuermans et al. (2006) concluded that the instability is coupled by an azimuthal acoustic mode of spinning type if all burner responses are identical and that spinning prevails because of the nonlinearity in the flame response to incoming perturbations. Noiray et al. (2011) take into account the flame response nonlinearity by expressing the heat release rate as a third order polynomial of the pressure fluctuation :  $\dot{Q} = \beta p - \kappa p^3$ , where  $\beta$  and  $\kappa$  are positive real constants. When all burners have the same response, they give rise, according to this analysis, to a spinning mode while changes in the dynamics of some flames, associated for example with the staging of some burners, lead to a standing mode. By adding a stochastic term representing turbulence effects always observed in real systems, the modes are found to randomly switch between standing and spinning (Noiray and Schuermans (2013)). This generally corresponds to what is observed in combustion chambers equipped

with swirling turbulent burners (Krebs et al. (2002), Worth and Dawson (2013b), Worth and Dawson (2013a), Bourgoïn et al. (2013a)). However, in these experimental studies, the standing type is more probable than the spinning type (see Worth and Dawson (2013b), Worth and Dawson (2013a), and Bourgoïn et al. (2013a)). There is also a dependence on the burner spacing and operating conditions as shown by Worth and Dawson (2013a).

In recent articles Ghirardo et al. (2015) and Ghirardo et al. (2016) use a general nonlinear formulation  $\dot{Q} = F(p)$  of heat release rate in terms of local pressure and express the pressure field in the system as the sum of two orthogonal standing modes. They show that the thermoacoustic instability can be standing or spinning according to the number of burners and the nonlinear flame response  $F$ . They also identified necessary conditions leading to stable standing and spinning limit cycles based on an indicator  $N_{2n}$  derived from their model. If  $N_{2n} < 0$ , only spinning solutions are stable. If  $N_{2n} > 0$ , standing solutions may exist and if they exist, they are stable. In this latter case, stable spinning solutions may exist as well allowing the possibility of co-existence of both modes for the same operating conditions. These features were however not observed yet in real systems.

Investigations (see Schuermans et al. (2006), Noiray and Schuermans (2013), Ghirardo et al. (2015) and Ghirardo et al. (2016)) do not include a plenum in their model. There is only one combustion chamber and a few burners uniformly distributed around the ring. However, Bauerheim et al. (2014) and Bauerheim et al. (2014) develop an analytical model that is complete, including a combustion chamber, a plenum and  $N$  burners equally distributed around the circumference. Depending on the level of the acoustic coupling between the two cavities (Schuller et al. (2012)), and following the amplitude and the time delay of the transfer function of the burners, they show that the two types of modes, standing or spinning, can occur. The analysis is however limited to the linear regime for vanishingly small perturbations and cannot be used to predict the final state of the system.

This review of the literature indicates that low-order models provide interesting clues on the physics of acoustic-combustion interactions, although the geometric modelling remains simple, but there are very few predictions validated by measurements. One difficulty is that most experiments are conducted with turbulent flames leading to limit cycles, which are never fixed on a purely spinning or standing mode (Krebs et al. (2002), Worth and Dawson (2013b), Worth and Dawson (2013a) and Bourgoïn et al. (2013a)).

There are only a few instrumented configurations where self-sustained oscillations coupled by azimuthal modes remain stable over time for fixed flow operating conditions. This is achieved by Moeck et al. (2010), but the burners are replaced by electrically heated Rijke tubes and the annular chamber has no plenum. Noiray and Schuermans (2013) also provide experiments on real gas turbines where limit cycle

seems to be reached for a certain amount of time. Other experimental investigations, which feature stable limit cycles coupled by azimuthal modes, were carried out in the MICCA facility at EM2C laboratory (see [Durox et al. \(2013\)](#), [Bourgouin et al. \(2015\)](#) and [Bourgouin et al. \(2015\)](#)). These studies make use of an arrangement of sixteen matrix burners in the annular chamber and operate in a premixed laminar flame regime. [Bourgouin et al. \(2015\)](#) and [Durox et al. \(2013\)](#) showed that, depending on the bulk injection velocity and equivalence ratio, pure spinning modes or pure standing modes are observed providing insight into the dynamics of thermo-acoustic phenomena in annular combustion chambers and a database for theoretical and numerical validations.

To reduce combustion instabilities, it is also important to detect their possible early manifestations, to implement control strategies or define operating point trajectories avoiding large amplitude oscillations. The possible detection of instability precursors has recently been explored by Sujith and his team ([Nair et al. \(2013\)](#); [Nair et al. \(2014\)](#); [Nair and Sujith \(2015\)](#); [Pawar et al. \(2015\)](#)). Within simplified systems, they identified the first characteristic signs preceding fully developed instabilities, by combining information on the frequency of intermittent bursts and their spectral content, using phase diagrams (Poincaré plots) and recurrence maps, based on temporal plots of the occurrence of intermittent cyclic phenomena aimed at identifying precursors.

### 7.3 Experimental setup

The MICCA burner, described previously and seen in [Fig. 7.1](#), comprises an upstream plenum, a combustion chamber made of two cylindrical concentric quartz tubes and sixteen matrix injectors. The inner and outer quartz tubes diameters are 300 and 400 mm respectively and share the same length  $l_t = 200$  mm as shown in [Fig. 7.2](#). The propane/air mixture delivered by a premixing unit is conveyed to the annular plenum. Gases are then exhausted through the sixteen matrix injectors and react in the combustion chamber. Each injector consists of a 6 mm-thick perforated plate made of brass, pierced with 89 holes of diameter  $d_p = 2$  mm shown in the close-up photo in [Fig. 7.1](#). When running, the chamber features 16 flame regions, each made of 89 small laminar premixed conical flames.

The gaseous mixture is ignited in the chamber by a single electrode introduced from the top of the chamber and is removed when the chamber is fully ignited to ensure that the system is symmetric at steady state.

[Figure 7.3](#) indicates the positions of the eight Brüel & Kjær microphones used in the setup. For each experiment, the sampling rate is  $f_s = 32,768$  Hz and the data are recorded over a period of 4 s. Four microphones are located in the plenum (MP“x”) and four are located in the chamber (MC“x”), each spaced by  $90^\circ$ . Microphones are flush-mounted in each cavity. For the unsteady pressure measurements in the combustion chamber, waveguide microphones are used to avoid sensor exposure to excessive temperatures. The microphone is located close to the injector compared to the length

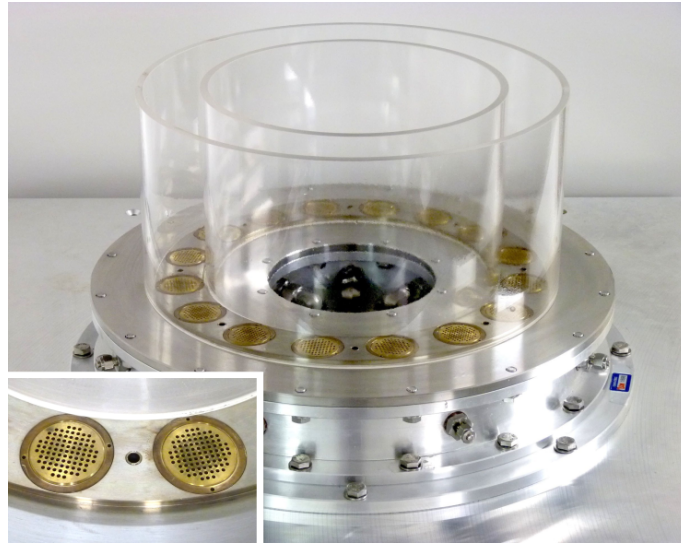


**Figure 7.1.** Photograph of the MICCA chamber equipped with matrix injectors. The injectors comprise 89 holes of 2 mm diameter spaced by 3 mm. The injector plate thickness is fixed to 6 mm. The chamber formed by two cylindrical quartz tubes provides full optical access to the flame region.

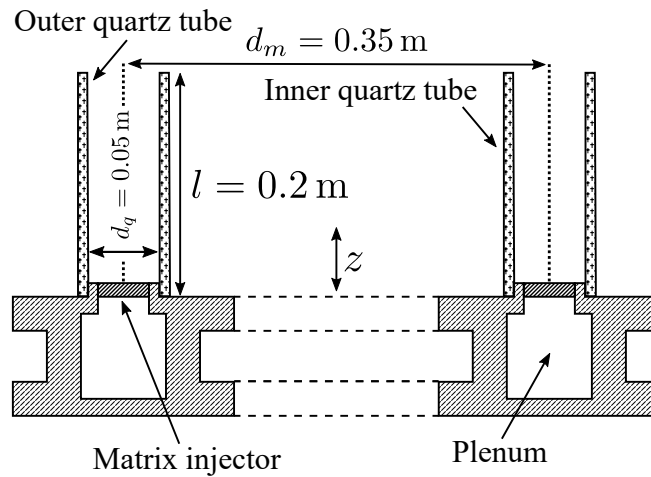


**Figure 7.2.** Lateral view of the MICCA chamber equipped with matrix injectors. The length of the inner and outer quartz tubes is equal to  $l = 0.2$  m,  $d_q$  is the gap between the two quartz tubes and  $d_m$  is the mean diameter of the chamber. The diameter of the inner and outer quartz tubes are respectively 0.3 and 0.4 m. The plenum is an annular cavity with a 0.07 m square cross section.

of the whole system, and the amplitude recorded by this sensor is a good approximation of the pressure in the chamber near the waveguide outlet, but with a delay

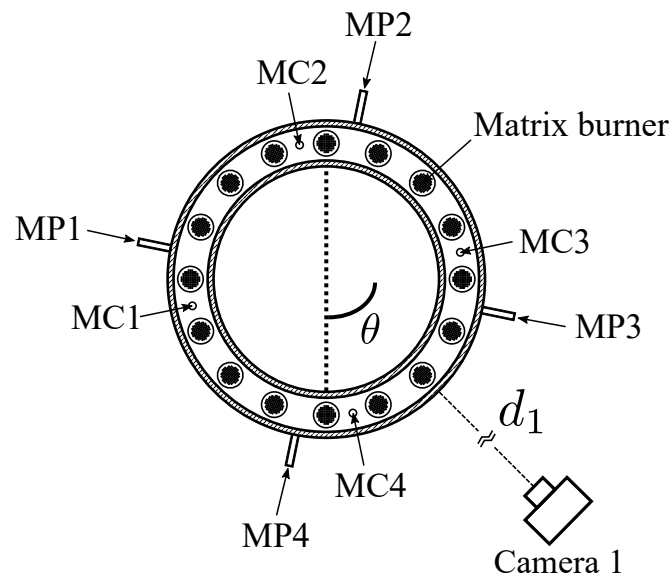


**Figure 7.3.** The system is equipped with eight quarter inch Brüel & Kjær microphones (four positioned in the plenum, four positioned in the chamber) and an ICMOS camera. Waveguide microphones are mounted on the chamber to avoid overheating. Two camera positions give either full images of the annular chamber or close-up views of the flame motion at one matrix injector.

corresponding to a time lag of 0.5 ms. This delay has to be taken into account in the signal processing when one compares pressure signals from the chamber to pressure signals from the plenum as done by [Bourgouin et al. \(2015\)](#).

Combustion instabilities are analysed as a function of the injection velocity  $U_b$  in the perforations of the matrix burners and equivalence ratio  $\phi$  of the combustible mixture. Records of the pressure signals that are presented in this study are all made once the fuel and oxidizer mass flow controllers have reached stable states corresponding to the desired values of the fuel and air mass flow rates injected into the mixing chamber feeding the annular combustor plenum. This transient state lasts typically less than 5 seconds. Several additional seconds are waited further to let time to reach fully premixed conditions in the annular chamber at the desired flow operating conditions before acquisition of the pressure signals is started. For about the same flow injection velocities as those explored in this study, but away from unstable regimes where the flames are steady and conical, it was checked that these durations before acquisition is initiated are long enough to get a stable and constant signal of the light intensity emission originating from one matrix burner of the annular chamber. This signal was recorded by a photomultiplier equipped with an  $\text{OH}^*$  filter. This signal was also found to be independent of the location of the matrix burner in the annular chamber. These precautions have been taken to allow that the 16 burners are operating under fully premixed conditions at the same fixed equivalence ratio and injection velocity in all

experiments carried out in this work.

Figure 7.3 also depicts the position where the dynamics of the annular chamber can be captured. Camera 1 is positioned at  $d_1 = 2.3$  m and 1 m above the chamber exhaust plane. This camera is used to take full annular images of the combustion chamber. An intensified CMOS camera APX-i2 with an 8-bit resolution in gray level providing square  $512 \times 512$  pixels images. To get a complete picture of the annular chamber, the camera is equipped with a Nikon 35-200 mm zoom lens used at 70 mm. The frame rate and shutter duration are respectively set at 6000 Hz and 166 ms. The UV radiation coming from the flame is filtered by the glass lenses of the camera. The light intensity recorded by the camera is then dominated by the emission of excited species in the visible domain, mainly originating from  $\text{CH}^*$  and  $\text{C}_2^*$  radicals. Images recorded by this device can therefore be interpreted as representative of the instantaneous heat release rate for the lean operating conditions in the study by Price et al. (1969). Another CCD camera is also used to get averaged images of the chamber.

## 7.4 Instability regimes

### 7.4.1 Stability map

The MICCA chamber features different regimes of combustion instabilities involving longitudinal, spinning, standing and slanted modes. A chugging mode is present when the chamber is not locked on one of the other thermo-acoustic modes. Let  $U_b$  designate the bulk velocity in each hole of the perforated plates. By fixing  $U_b$  and scanning a range of equivalence ratios  $\phi$ , the chamber exhibits the different regimes of oscillation shown in Fig. 7.4 which are discussed in the following subsections.

### 7.4.2 Longitudinal mode

Strong longitudinal instabilities with stable limit cycles are observed for a wide range of flow conditions  $(U_b, \phi)$  when  $\phi$  is roughly ranged between 0.8 and 0.9. Figure 7.5 shows the acoustic pressure in the plenum and the associated spectrum for  $\phi = 0.84$  and  $U_b = 2.03 \text{ m s}^{-1}$ . All microphone signals in the plenum are in phase and the response is sinusoidal. The pressure signals have the same amplitude  $A = 125$  Pa and have a frequency  $f = 320$  Hz. The amplitude and frequency at limit cycle remain roughly constant for the different flow conditions  $(U_b, \phi)$  where this mode appears. Note that the results in the chamber are similar to the ones found in the plenum, but they feature a more complex harmonic structure. Pressure data in the chamber are not shown here and are currently under investigation to determine the origin of this more complex behavior.

### 7.4.3 Azimuthal modes

The MICCA chamber also features combustion instabilities coupled by azimuthal acoustic modes that belong to three different classes. Pressure signals in the plenum

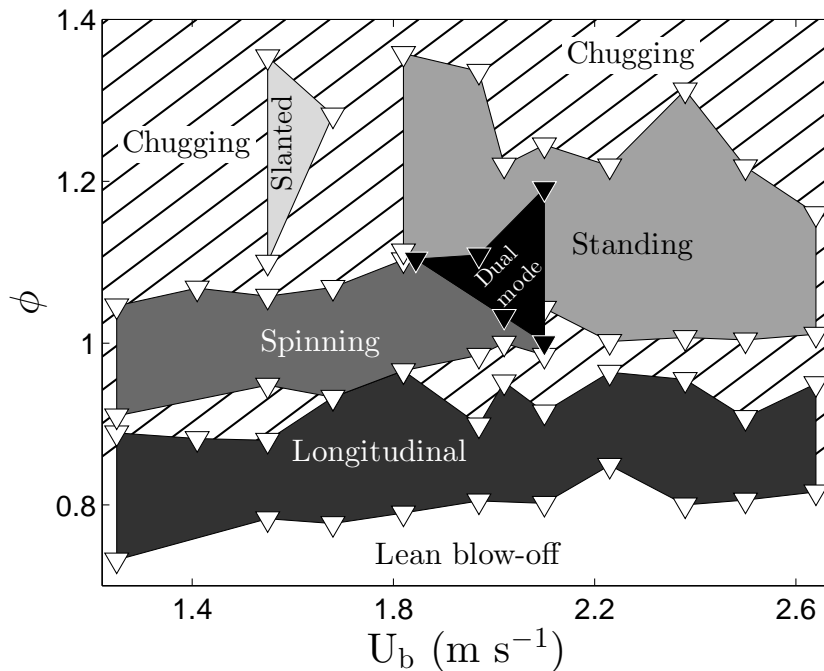


**Figure 7.4.** Stability map of the MICCA combustor delineating the different thermo-acoustic modes of the system. The “Dual mode” region is where the spinning and standing regions overlap. The hatched area is where the chugging mode is manifested. The blank area corresponds to the lean extinction limits of the chamber.

and the associated spectrum are shown in Figs. 7.6 and 7.7.

Except in the small region designated in Fig. 7.4 by “dual mode”, a spinning mode is observed for  $U_b < 2 \text{ m s}^{-1}$  and  $0.9 < \phi < 1.1$ . This oscillation is characterized by pressure signals in phase quadrature, corresponding to their relative positions, and with the same amplitude as illustrated in the top plot in Fig. 7.6. The pressure fluctuation reaches in this case an amplitude  $A = 300 \text{ Pa}$  in the plenum and the spectrum in Fig. 7.7 reveals a sharp peak at the fundamental frequency of 485 Hz. The rotation direction of the azimuthal mode depends on the initial conditions, but, when a mode is rotating in one direction, this persists as long as the operating conditions are kept constant. The rotation direction, clockwise (CW) or counter-clockwise (CCW), is visible on high-speed camera records as shown in Fig. 7.8. In the present case, the mode is rotating in the counter-clockwise direction. To obtain a CW rotating mode, flow conditions have to be changed so that the mode is made to vanish and then brought back to the initial values. Successive images indicate that the amplitudes of the excited flames are the same.

Except in the dual mode region, a standing mode is observed for  $U_b > 1.8 \text{ m s}^{-1}$  and  $1.0 < \phi < 1.3$  in Fig. 7.4. When  $\phi = 1.05$  and  $U_b = 2.09 \text{ m s}^{-1}$ , Fig. 7.6 (middle)

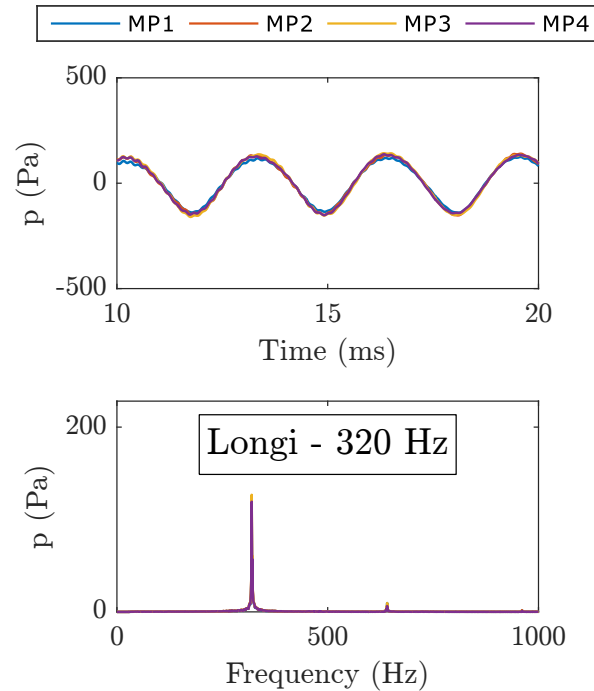


**Figure 7.5.** Longitudinal mode for  $\phi = 0.84$  and  $U_b = 2.03 \text{ m s}^{-1}$ : acoustic signature in the plenum (top) and spectral content of the acoustic pressure (bottom). The bottom plot shows the pressure amplitude in constant frequency bands  $\Delta f = 0.5 \text{ Hz}$ .

shows that signals measured by microphones MP2 and MP4 lying on opposite sides of the annular plenum feature a large harmonic oscillation sharing the same amplitude  $A_1 = 320 \text{ Pa}$ , but are in phase opposition. Microphones MP1 and MP3, which are also on opposite sides of the plenum but are shifted by  $90^\circ$  in the counter-clockwise direction with respect to microphones MP2 and MP4 measure also both a harmonic oscillation but at much lower amplitude  $A_2 = 40 \text{ Pa}$ . The MP1 and MP3 microphone signals are however in this case roughly in phase. This means that the flames are exposed to different levels of velocity fluctuations. Note that MP1 and MP3 are on a fixed pressure nodal line since the amplitude of pressure oscillation is quite low. The frequency of this mode  $493 \text{ Hz}$  is close to the one found for the spinning mode at  $485 \text{ Hz}$  (Fig. 7.7). As already observed for the longitudinal mode, the standing mode features more harmonic content in the chamber than the spinning mode. Images recorded by the high-speed camera corresponding to a full cycle are shown in Fig. 7.9. In these images, the nodal line is almost horizontal and fixed between two injectors during the experiment. One can see that the flames next to the nodal line are less elongated than the flames at  $90^\circ$ , which lie around the anti-nodal line.

[Bourgoin et al. \(2015\)](#) showed that a slanted mode may also be detected for a small set of operating conditions. An example of pressure signals are shown in Fig. 7.6

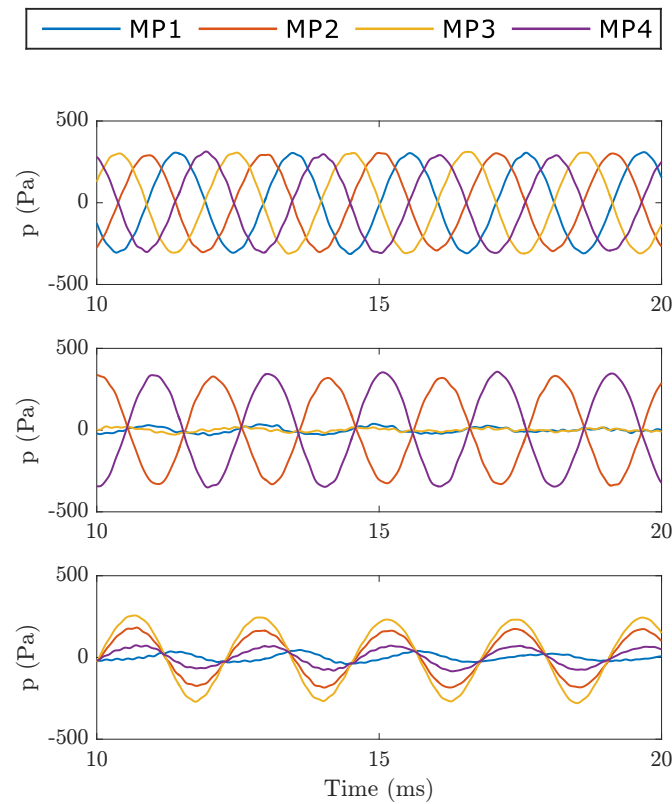


**Figure 7.6.** Azimuthal modes. Top: 485 Hz spinning mode at  $\phi = 1.07$  and  $U_b = 2.04 \text{ m s}^{-1}$ . Middle: 493 Hz standing mode at  $\phi = 1.05$  and  $U_b = 2.09 \text{ m s}^{-1}$  with a pressure nodal line fixed between two injectors. Bottom: 443 Hz slanted mode at  $\phi = 1.18$  and  $U_b = 1.44 \text{ m s}^{-1}$

(bottom plot). This mode is a phase-coupled superposition of a longitudinal mode and an azimuthal mode with a symmetry line around which the flames execute a slanted oscillation at 443 Hz (Fig. 7.7). Pressure plots reveal large fluctuations with different amplitudes of oscillation. MP1 and MP4 have the lowest amplitudes, indicating they are close to the symmetry line. MP2 and MP3 feature a higher fluctuation level. In this region, the flames are detached from the grid periphery of the matrix burners. Further details on this mode may be found in the study by [Bourgouin et al. \(2015\)](#).

#### 7.4.4 Chugging mode

When the chamber is not locked on one of the longitudinal or azimuthal modes, the system operates in a “chugging” mode manifested in the hatched region on the stability map in Fig. 7.4. The oscillation amplitude is modulated and somewhat intermittent. Figures 7.10 and 7.11 show the pressure signals and their spectrum for two of these chugging modes at different flow operating conditions. Time domain records exhibit

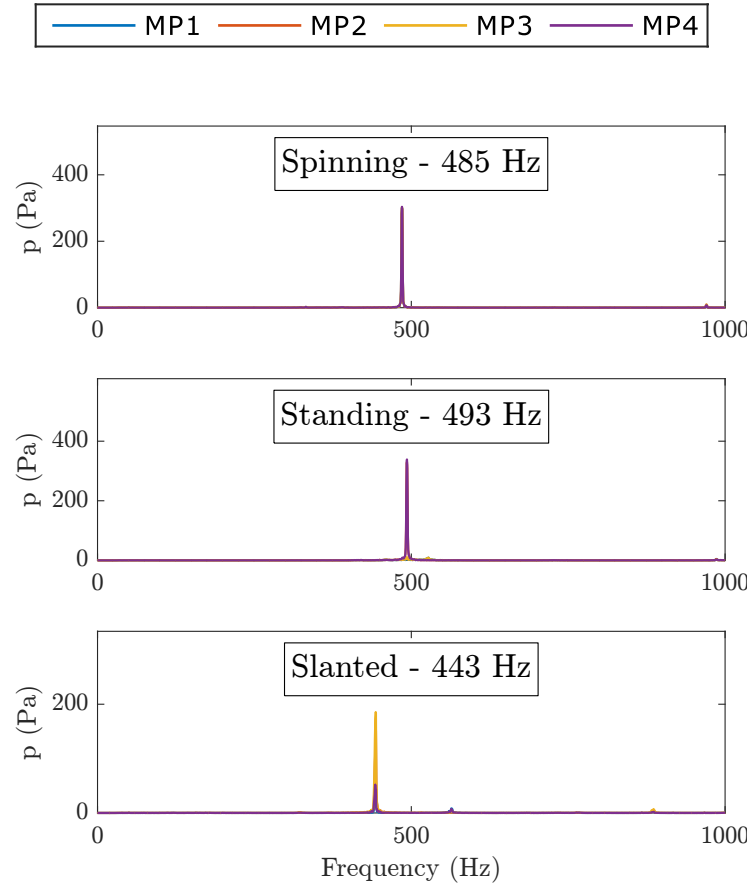


**Figure 7.7.** Spectral content for the azimuthal modes shown in Fig. 7.6. The plots show the pressure amplitude in constant frequency bands  $\Delta f = 0.5$  Hz.

powerful bursts at about 50 Hz, modulating a higher frequency signal between 70 and 350 Pa. The spectral signature of the two chugging modes do not exactly coincide, but the modulation at about 50 Hz is present in both cases. If we take the “Chugging 1” as example, its spectral signature looks like the superposition of two Dirac combs. These peaks are typical of the nonlinear mixing of the characteristic modes of oscillation taking place in the system. The first one is centered on 370 Hz and spans from 270 to 470 Hz. This comb can be interpreted as the modulation of the longitudinal mode of the annular chamber at 320 Hz, shifted by the equivalence ratio increase, with the bursts at 50 Hz. The second Dirac comb is centered on 480 Hz and spans from 430 to 530 Hz. It is here interesting to note that the spectral signature of these intermittent oscillations features a peak close to the frequencies of the spinning mode ( $\sim 485$  Hz) in the case of the “Chugging 1”. In the case of the “Chugging 3”, the second comb is centered on 498 Hz, very close the frequency of the standing mode ( $\sim 495$  Hz) of the annular chamber.

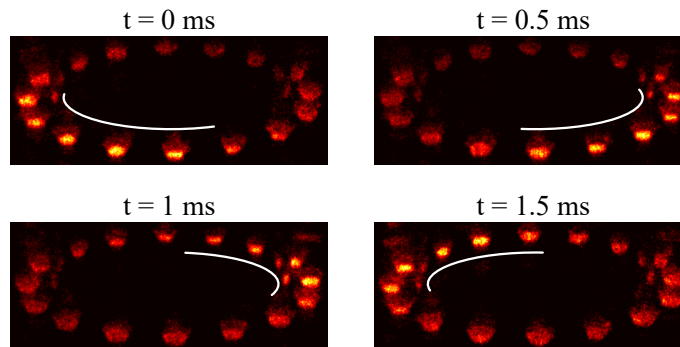


**Figure 7.8.** High-speed snapshots of the full annular combustion chamber during a spinning mode cycle ( $T = 2$  ms). The mode is rotating in a counter-clockwise direction and the maximum luminosity reached by each flame during the cycle is the same for all burners.

#### 7.4.5 Dual mode region

The different regions of instabilities with stable limit cycles are well separated in Fig. 7.4 except in a domain named “Dual mode”, where spinning and standing regions overlap. In this region, the mode that develops in the system depends on the path followed to reach the targeted operating condition. For example, if ignition is achieved under lean conditions ( $\phi < 1$ ) in the chugging region and the equivalence ratio is then increased up to  $\phi = 1.1$ , with air mass flow rate kept constant, to reach the “Dual mode” region, a spinning mode with a stable limit cycle arises. If the system is ignited in the chugging mode under rich conditions ( $\phi > 1.2$ ) and the equivalence ratio is brought down to  $\phi = 1.1$  to enter in the “Dual mode” region, the system gives rise to a standing azimuthal mode with a stable limit cycle. This demonstrates that

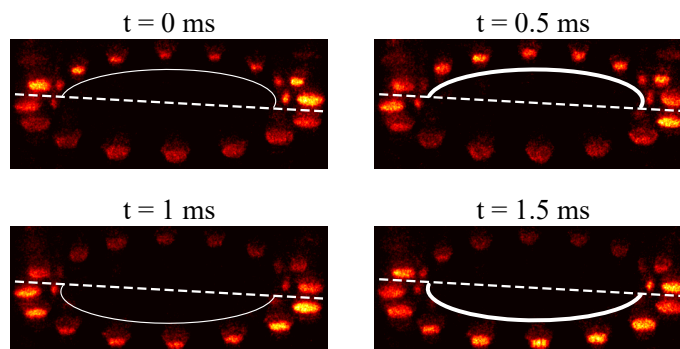


**Figure 7.9.** High-speed images of the full annular combustion chamber during a standing mode cycle ( $T = 2$  ms). The nodal line (dashed line) is fixed between two burners. The thickness of the curved line gives an indication on the oscillation level. The flames next to the nodal line have a lower amplitude of oscillation than those situated near the anti-nodal region.

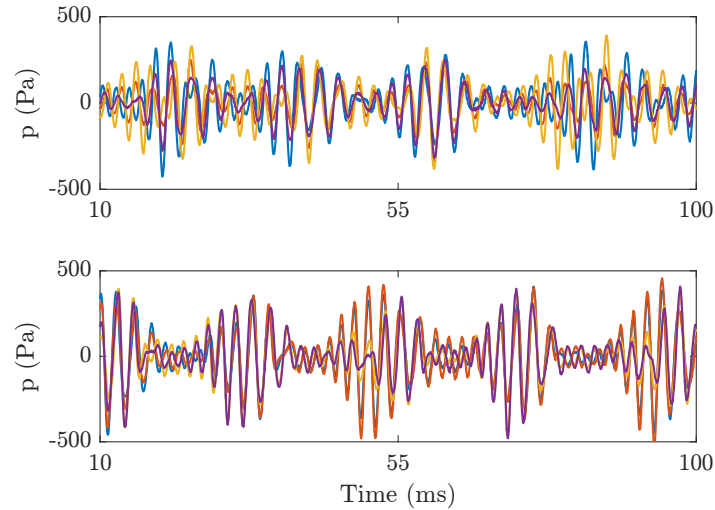


**Figure 7.10.** Chugging modes with a low modulation frequency of about 50 Hz (puffs). Top: “Chugging 1”:  $\phi = 0.92$  and  $U_b = 2.03 \text{ m s}^{-1}$ . “Chugging 3”:  $\phi = 1.21$  and  $U_b = 2.05 \text{ m s}^{-1}$ .

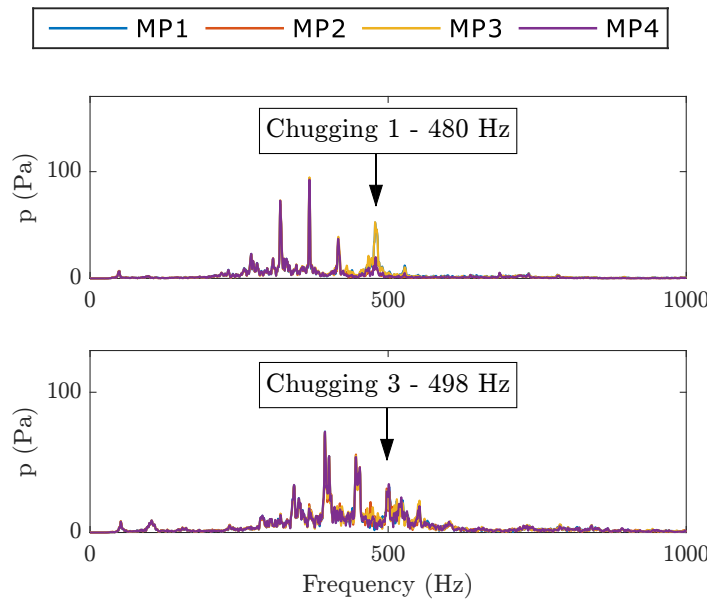


**Figure 7.11.** Spectral content of modes shown in Fig. 7.10. “Chugging 1”:  $\phi = 0.92$  and  $U_b = 2.03 \text{ m s}^{-1}$ . “Chugging 3”:  $\phi = 1.21$  and  $U_b = 2.05 \text{ m s}^{-1}$ . The plots show the pressure amplitude in constant frequency bands  $\Delta f = 0.5 \text{ Hz}$ .

the dynamical state is controlled by hysteresis and that history defines the spinning or standing mode type.

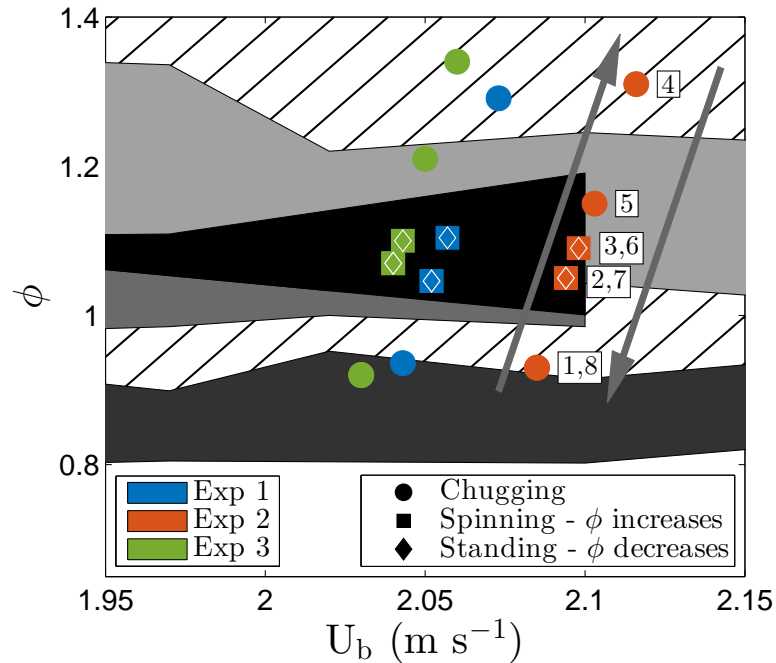


**Figure 7.12.** Detailed view of the stability map shown in Fig. 7.4 around the "Dual mode" region. Exp 1, 2 and 3 are conducted for three different air flow rates. For each air flow rate, only the fuel flow rate is modified. Symbols indicate the nature of the observed instability that eventually arises when the equivalence ratio increases or decreases for the same operating conditions ( $U_b, \phi$ ).

Point	1	2	3
$\phi$	0.93	1.05	1.09
$U_b$ ( $\text{m s}^{-1}$ )	2.08	2.09	2.10
Mode	Chugging 1	Spinning 1	Spinning 2
Point	4	5	6
$\phi$	1.31	1.15	1.09
$U_b$ ( $\text{m s}^{-1}$ )	2.12	2.10	2.10
Mode	Chugging 2	Chugging 3	Standing 2
Point	7	8	
$\phi$	1.05	0.93	
$U_b$ ( $\text{m s}^{-1}$ )	2.09	2.08	
Mode	Standing 1	Chugging 1	

**Table 7.2.** Path followed to explore hysteresis during "Exp 2". During this experiment, the air mass flow rate is kept constant.

Such observations can be made during the same experiment by modifying the operating condition path as exemplified in Tab. 7.2. In this experiment, designated in the following as “Exp 2”, the air flow rate is kept constant and combustion is initiated under lean conditions in a chugging mode (point 1). The fuel mass flowrate is then slightly increased and the system develops a well established spinning mode (points 2 and 3). By further increasing the fuel flow rate, the spinning mode disappears and the system develops a new chugging mode (point 4). At this stage, the fuel mass flowrate is now progressively reduced. The system then evolves from a chugging mode (point 5), to a well established standing mode (point 6 and 7), which disappears again when the fuel flow rate is further reduced to its initial value (point 8). Points 1, 4, 5 and 8 are outside the “Dual mode” region. For these operating conditions, chugging is the only instability state observed. The pair of points 2 and 7 and the pair 3 and 6 correspond to the same flow operating conditions situated in the “Dual mode” domain with a stable limit cycle featuring a spinning or a standing structure depending on the history to reach this operating condition.

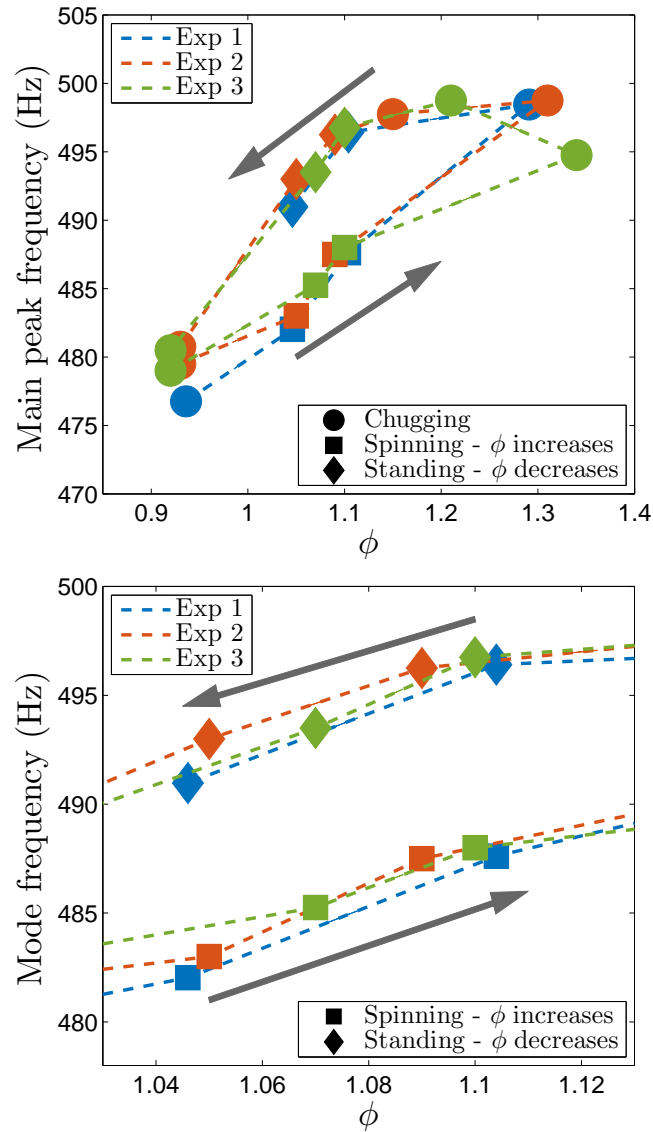
Three sets of experiments of this type were carried out following the operating paths indicated in Fig. 7.12. For each experiment, initial and final operating conditions ( $U_b, \phi$ ) are chosen outside the “Dual mode” region and the operating path crosses this region. Acoustic signals and light emission records are then used to identify unambiguously the nature of the excited azimuthal mode. Results are analysed in the next section.

## 7.5 Hysteresis phenomenon

The main peak frequency detected in the power spectra from the microphone signals is analysed first. In the chugging mode spectral signature, one only considers the peak that is closest to the azimuthal mode frequency ( $\simeq 490$  Hz). Figure 7.13 represents the evolution of the main peak frequency along the operating paths described in Fig. 7.12.

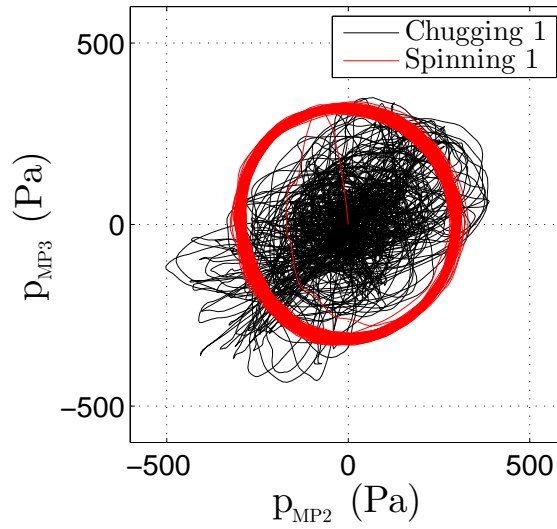
For the three air flow rates explored, the peak instability frequency always describes a closed loop when equivalence ratio is varied with extremities corresponding to the chugging modes. Increasing the equivalence ratio leads to the appearance of stable spinning modes with a peak frequency evolving from 483 to 488 Hz. Decreasing it, leads to stable standing modes with a peak frequency decreasing from 497 to 491 Hz. At fixed operating conditions, the frequency difference between the two modes is always about 10 Hz. It is next logical to examine the chugging mode just before a spinning mode occurs, designated in what follows as “chugging 1”, and the chugging mode that yields a standing mode to occur, designated as “chugging 2” (see Tab. 7.2).

Figure 7.14 shows the state space maps of the pressure signals delivered by the plenum microphones MP2 and MP3 for four operating conditions synthesized in Tab. 7.2. These two sensors are at  $90^\circ$  from each other (see Fig. 7.3). In the first plot, one examines the “chugging 1”, which precedes the “spinning 1”, and the resulting “spinning

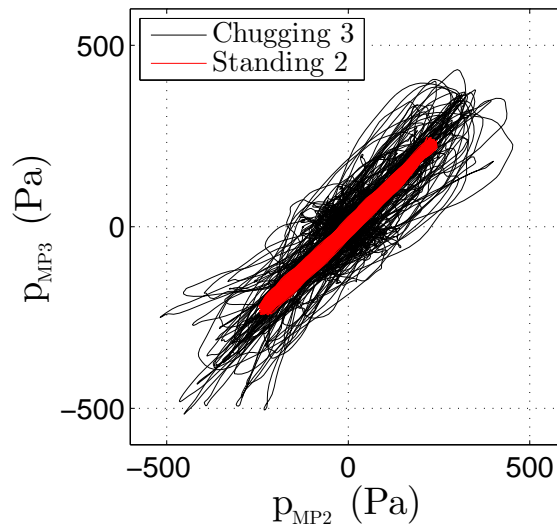


**Figure 7.13.** Top: hysteresis cycles for operating conditions indicated in Fig. 7.12. Arrows indicate the path followed during the experiment. When  $\phi$  increases from 0.9 to 1.1 a spinning mode arises. When  $\phi$  is diminished from 1.2 to 1.1 a standing mode prevails. Bottom: zoom on the loop for  $\phi$  ranging between 1.03 and 1.13.

1” oscillation. A purely spinning mode corresponds to a circle in state space because microphone signals are in this case in quadrature. One can see that the “chugging 1” path draws a complex trajectory in this map, but the region covered by this trajectory approaches that of a disk with about the same limits as the spinning oscillation. In the second case, one examines the “chugging 3” mode, which precedes the “standing 2”, leading to the “standing 2” mode. A purely standing mode corresponds to a straight



(a) "spinning 1" (red) and "chugging 1" (black) trajectories.



(b) "standing 2" (red) and "chugging 3" (black) trajectories.

**Figure 7.14.** State space maps of the pressure signals ( $t_{max} = 0.4$  s) recorded by microphones MP2 and MP3 in the plenum separated by a  $90^\circ$  angular shift for operating conditions indicated in Tab. 7.2.

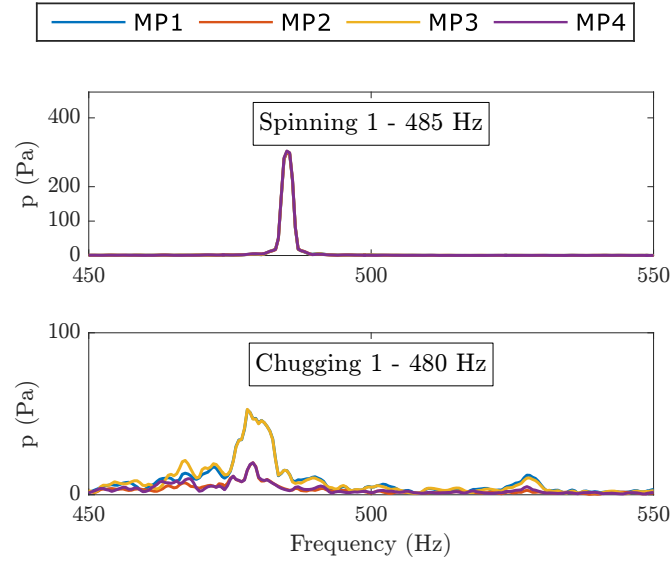


**Figure 7.15.** Power spectral content of pressure signals recorded under “spinning 1” and “chugging 1” modes. The plots show the pressure amplitude in constant frequency bands  $\Delta f = 0.5$  Hz.

line at  $45^\circ$  in the state space map because microphone signals oscillate in this case in phase. Once again, the “chugging 3” mode describes a complex trajectory, but the global shape follows the diagonal and encloses the linear signature of the pure “standing 2” mode. It appears that information on the thermo-acoustic mode type (spinning or standing) that will appear in the chamber may be deduced from the chugging mode dynamical trajectory in state space map.

From these experiments, recurrence plots are investigated. This technique may be used to characterize the system dynamics and allows one to identify periodicity in the signal. In order to apply this method, one has to calculate the recurrence matrix  $R_{ij}$  defined by Eq. (7.1) and detailed in [Nair et al. \(2014\)](#) and [Marwan et al. \(2007\)](#):

$$R_{ij} = \begin{cases} 1, & \text{if } \|p_i - p_j\| < \epsilon \\ 0, & \text{if } \|p_i - p_j\| > \epsilon \end{cases} \quad (7.1)$$

with  $\epsilon$  the maximum accepted distance between pressure fluctuations  $p_i$  and  $p_j$ . This value is deduced from the Poincaré figures by measuring the maximum size  $\lambda$  of the attractor in phase space. Here, we choose  $\epsilon = \lambda/5$  ([Nair et al. \(2014\)](#)) which sets, in our cases,  $\epsilon \sim 150$  Pa. The recurrence plot is the representation of the  $R_{ij}$  matrix which is symmetric and composed of zeros (white points) and ones (colored points). Thus, colored points correspond to instants where the distance between the pair  $\{p_i, p_j\}$  is less than  $\epsilon$ .

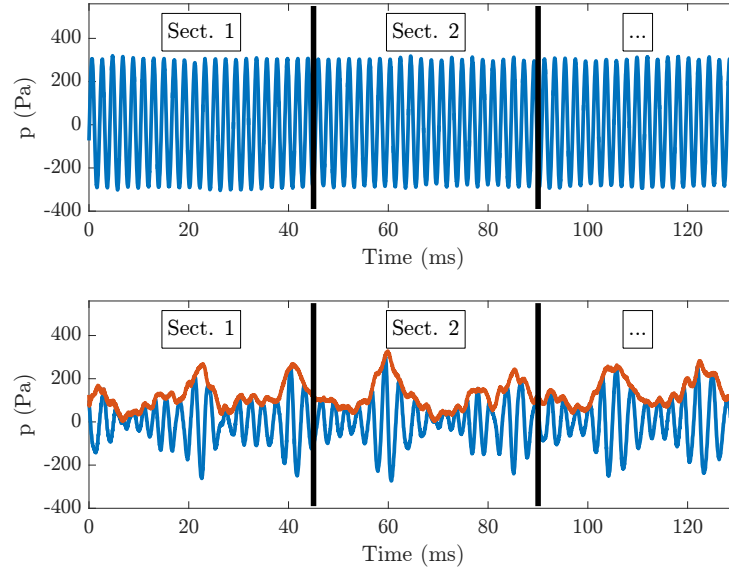


**Figure 7.16.** Acoustic pressure recorded by MP2. Top : “spinning 1” mode. Bottom: “chugging 1” mode. The envelop of the chugging mode is extracted with an Hilbert transform and is plotted in orange. Vertical lines indicate the different time intervals used to calculate the recurrence matrices  $R_{ij}^k$  and  $\bar{R}_{ij}$ .

This method is now used to analyse the chugging modes close to the hysteresis region, “chugging 1” and “chugging 3”, and the stable limit cycles coupled by azimuthal modes corresponding to “spinning 1” and “standing 2” in Tab. 7.2. Pressure signals are divided into  $N$  time intervals of  $\sim 45$  ms each as described in Fig. 7.16 to reveal the periodicity of the different pressure signals. The envelope of the chugging modes is extracted with a Hilbert transform. A recurrence matrix  $R_{ij}^k$  is calculated for each time interval  $k$ . An average recurrence matrix  $\bar{R}_{ij}$  is computed as:  $\bar{R}_{ij} = \frac{1}{N} \sum_{k=1}^N R_{ij}^k$ . Figure 7.17 shows the averaged recurrence plots calculated for the different modes. The periodicity of the phenomenon is represented by the diagonal patterns arising in these plots. Figures 7.16(a) and 7.16(b) show results for the pure ‘spinning 1’ and ‘standing 2’ modes. The instability frequency can be directly deduced from these plots. The perfect lines drawn in the plots indicate a very good stability of the limit cycle during the 2 s-recording of the thermo-acoustic modes.

For the “chugging 1” and “chugging 3” modes, recurrence matrices of the entire signal and of its envelope shown in Fig. 7.16 are calculated and plotted in Fig. 7.17 from (c) to (f). Recurrence plots of the envelope reveals a main oscillation frequency of these modes at 50 Hz. Recurrence plots of the full signal show both the envelope pattern which is superimposed to the pattern corresponding to the spinning or standing modes. This shows that the chugging modes feature both a quasi-periodic low

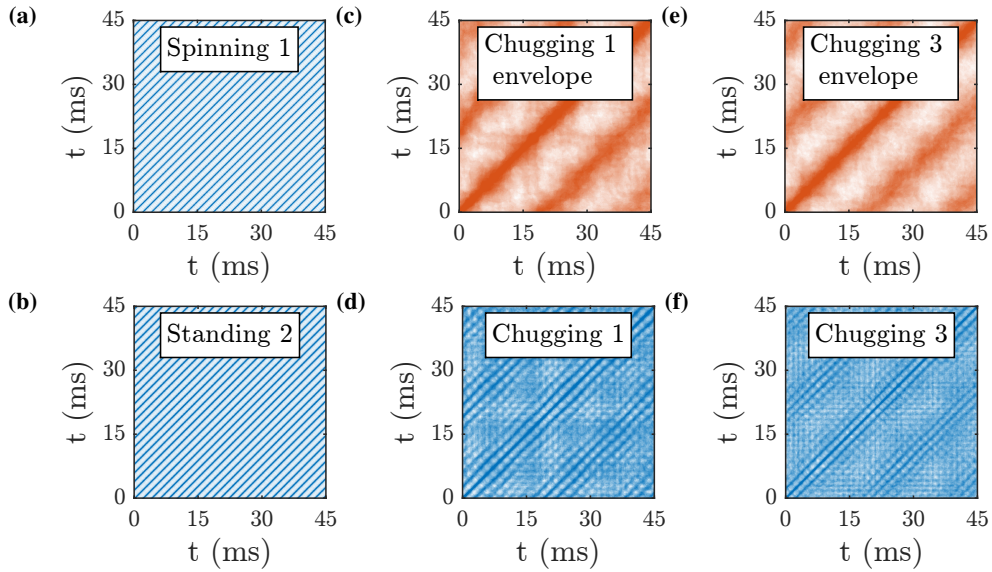


**Figure 7.17.** Averaged recurrence plots for “spinning 1”, “standing 2”, “chugging 1” and “chugging 3” modes. Recurrence plots of the envelope signal of “chugging 1” and “chugging 3” are also displayed. The diagonal pattern found in the figures exhibits the periodic nature of the different modes.

frequency modulation at 50 Hz, but also a strong periodic azimuthal component, of spinning or standing nature, an information that complements that of the Poincaré maps and of the power spectral densities showed before.

Nair et al. (2014) propose to quantify the periodicity of the instability by counting the number of colored points in the recurrence plots and use the density  $RR$  defined by:

$$RR = \frac{1}{N^2} \sum_{i,j=1}^N \bar{R}_{ij} \quad (7.2)$$

with  $N$  the number of segments used to calculate the recurrence matrix  $\bar{R}_{ij}^{av}$ . The more the signal is periodic, the more  $RR$  will tend toward zero. Results are shown in Tab. 7.3.

Spinning 1	Standing 2	Chugging 1	Chugging 3
$0.8 \times 10^{-2}$	$1 \times 10^{-2}$	$1.7 \times 10^{-2}$	$1.7 \times 10^{-2}$

**Table 7.3.** Density  $RR$  of colored points for the different investigated modes.

This is also confirmed by a close examination of the power spectra of the pressure signals. One sees in Fig. 7.15 that the peak in the “chugging 1” case is close to the peak of the “spinning 1” oscillation and similarly that the peak corresponding to “chugging

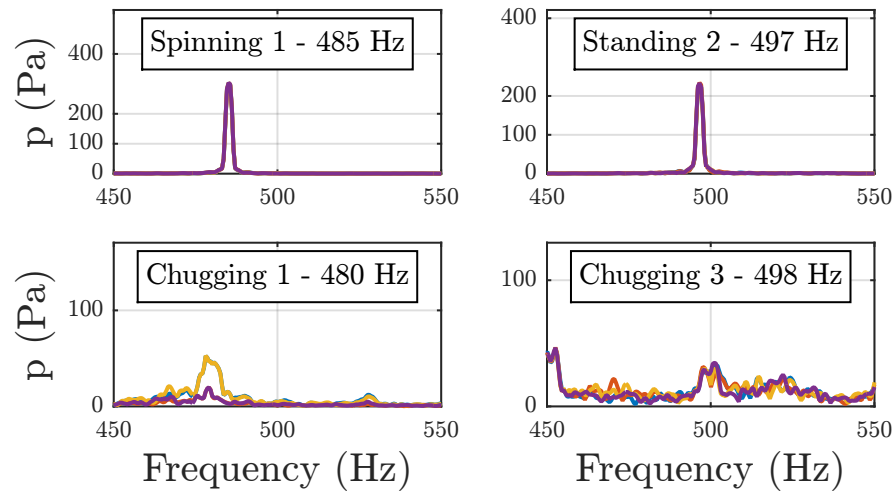


**Figure 7.18.** Power spectral of pressure signals recorded under “spinning 1”, “standing 2” and “chugging 1” and “chugging 3” modes.

3” matches that of the “standing 2” mode in Fig. 7.19. One finds that the amplitude of the chugging peaks is much lower because the azimuthal mode is not locked and is only manifested during short periods of time. It is probable that the small shift between the chugging and the pure modes is mainly due to thermal effects due to changes of the equivalence ratio that increase/decrease the speed of sound  $c$  in burnt

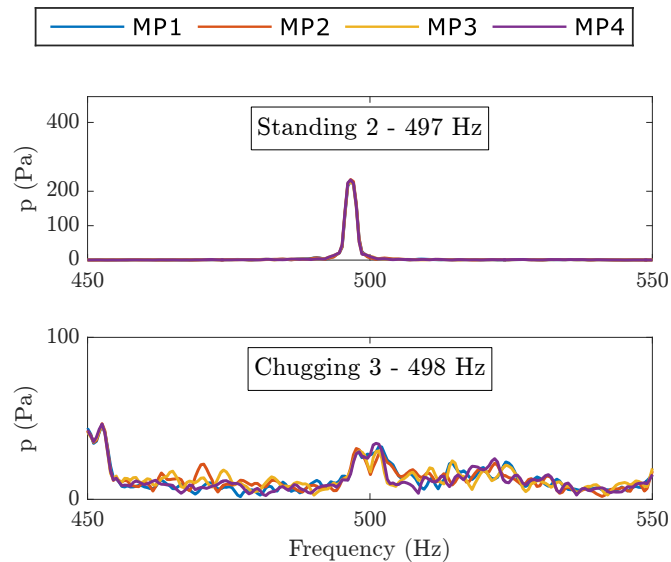


**Figure 7.19.** Power spectral content of pressure signals recorded under “standing 2” and “chugging 3” modes. The plots show the pressure amplitude in constant frequency bands  $\Delta f = 0.5$  Hz.

gases leading to increased/decreased oscillation frequencies.

These observations indicate that the chugging mode may be seen as a precursor of combustion instabilities. Note that these considerations pertain to the chugging modes appearing in the near vicinity of the region where azimuthal coupling takes place.

## 7.6 Conclusions

This chapter focuses on the mode types appearing in an axisymmetric annular chamber equipped with multiple identical matrix injectors operating in a laminar regime. This allows well controlled experiments of combustion dynamics in this kind of geometry. The azimuthal mode types arising in the system are characterized and a hysteresis phenomenon is uncovered and shown to lead to different modal structures for the same flow conditions. The findings of this study may be listed as follows:

- Multiple longitudinal and azimuthal modes are observed in the annular configuration in regions which in general do not overlap.
- Spinning and standing modes with stable limit cycles are observed for the same flow operating conditions in a limited “Dual mode” domain.
- The oscillation arising in this “Dual mode” region depends on the path taken to reach the operating point  $(U_b, \phi)$ . If  $\phi$  is increased, with the same air mass flow rate, from lean conditions to the target value, a spinning mode is obtained. If  $\phi$  is decreased from rich conditions, a standing mode is manifested at the target conditions.
- The spinning and standing modes do not switch from one to the other but instead when a mode arises, it is locked on.
- The chugging oscillation observed just outside the region of azimuthal instability contains information that can be used to predict the azimuthal mode structure that will be established in the “Dual mode” domain. Recurrence plots are also used to characterize this phenomenon.

It would be interesting to see if these observations can be explained by recent theoretical analysis like those developed by [Ghirardo et al. \(2015\)](#) and [Ghirardo et al. \(2016\)](#) which allow the coexistence of both spinning and standing modes for the same operating conditions. This is however not straightforward since the theory relies on a nonlinear time invariant relationship between heat release rate and pressure fluctuation in the chamber.





# Conclusion

This manuscript is essentially concerned with the analysis of combustion dynamics in annular systems. The first group of investigations rely on a series of novel experiments focused on the combustion dynamics of an annular system fed with multiple swirled spray injectors called MICCA-Spray. These experiments are the result of a continuous effort spent at the EM2C, CNRS to develop a laboratory scale device representative of what is found in the industry of gas turbines and more specifically in combustion systems like those found in aircraft engines. In these fields, there is a lack of experimental data that can be accessed in the open scientific literature. Industrial manufacturers perform tests on their own devices but rarely communicate on the results. In addition, experiments carried out on industrial configurations do not allow an optical access to the combustion region and the measurements are often limited to a few measurement points. The present work contributes to fill this gap and aims at collecting information on the problem of combustion dynamics in a situation where the fuel is injected in liquid form as a spray. The work of J-F. Bourgouin carried out on a similar set-up dealt with premixed combustion. A rich variety of combustion instabilities was found and led to the development of models as well as to a detailed characterization of the light-round process. The present study extends this previous work to the case of liquid fuel spray injection. With this in mind, a specific injector has been designed at EM2C, CNRS to fulfill different requirements such as the ease of maintenance, the flexibility in changing components to allow for different applications and the need for a simple design that could be easily modeled and simulated. The present work considers two fundamental issues, of fundamental as well as practical interest. The first pertains to the ignition process in annular combustors, designated as the light-round while the second concerns combustion instabilities coupled to azimuthal modes of in the annular geometry. A particular attention is given to combustion instabilities which are first encountered in the annular combustor MICCA-Spray. This is complemented by further investigations of the combustion dynamics of a single swirl spray injector in a tubular burner SICCA-Spray. The single injector system is also simulated using Large-Eddy Simulations to complement experimental data and explore the possibility to use calculations to obtain further information on the process and determine flame describing functions.

### **Ignition dynamics of annular combustors**

Thanks to a design admitting both premixed and spray combustion, it has been possible to obtain experimental observations of the dynamics of the light-round process in an annular chamber equipped with multiple swirling injectors. Gaseous propane, liquid n-heptane and liquid dodecane are considered as fuels. The behavior of the light-round depending on the type of fuel is studied using high-speed diagnostics including high-speed imaging. This gives access to the flame propagation in the entire annular chamber, a process designated as the light-round. This dynamical phenomenon is characterized in terms of structure and of time of propagation. It is found that the three fuels give rise to similar spreading processes in the annular chamber. The major difference is found in the time delay of the light-round, corresponding to the time between the ignition of the first injector and the ignition of the entire chamber. This delay is characterized as a function of equivalence ratio, power level and injection velocity. In general, premixed gaseous injection of propane yields the shortest time delay. For liquid fuel spray injection, the delay is shorter when the fuel is easy to vaporize (n-heptane) and it is the longest for dodecane spray injection because this fuel is less volatile. It has been shown that experiments can be interpreted in terms of a burning velocity which mainly depends on the thermal expansion, turbulent flame wrinkling and on laminar burning velocity in the spray reactive mixture. The detailed propagation of the flame in the annulus is then investigated. A particular attention is given to the evolution of the flame structure established by each injector after it is swept by the traveling flame branch. This branch propagates in the azimuthal direction from one injector to the next. The flame features a pure horizontal displacement, and the front moves in the vicinity of the chamber backplane. A second type of motion is induced by the volumetric expansion and gives rise to a motion towards the combustor exhaust section. The propagation of the flame is also seen to have a strong influence on the flow well before it reaches the point of observation. This is due to the piston effect associated with the volumetric expansion induced by the flame. As a consequence, this induces a concentration of n-heptane droplets in certain regions of the combustor. A second observation indicates that the ignition of an injector by the traveling combustion wave first initiates a flame that is anchored inside the body of the injector before being expelled from this region after a certain delay. Finally, a simplified model is derived by making use of flow rate considerations. This provides estimates of the delay and a qualitative understanding of the flame behavior during the first instants after the passage of the flame branch. This later phenomenon is of particular importance for practical devices because the flame is seen to be first stabilized inside the injector body, and this may induce additional heat loads and accelerate the degradation of these injection units.

### **Combustion dynamics of the MICCA-Spray burner in spray mode**

The MICCA-Spray system is equipped with a new design of the swirling system in order to exhibit strong combustion instabilities coupled to the first azimuthal mode of the chamber when it is fed with liquid n-heptane. The instability takes the form of

long bursts at a repetition rate of 2 Hz. The peak pressure oscillations reach values of the order of 5000 Pa (about 5% of the chamber pressure). During these very large oscillations, the coupling mode is essentially standing with a fixed nodal line. This allows a precise characterization of the phenomenon at different angular positions around the annulus:

- Near the pressure anti-node, the flames exhibit an axial motion induced by the large axial velocity excursions with a strong positive heat release rate fluctuation. Chemiluminescence data show the link in terms of amplitude and phase lag between pressure and the heat release.
- The flames located near the pressure nodal line exhibit a large sweeping motion around their axis as they are submitted to large transverse velocity fluctuation levels. Image processing is used to determine the evolution of the lateral flame sweeping motion as a function of the amplitude of the pressure fluctuations.
- It is found that the Rayleigh source term always brings energy to the system during the instability bursts and cannot cause the decay in amplitude that is observed experimentally.
- Saturation and decay that take place might perhaps be due to an additional dissipation in the system, or to a sudden detuning of the resonance due to a frequency shift or to an alternate flame dynamics saturation mechanisms taking place at the other injector locations.
- When the pressure oscillation amplitude exceeds a certain threshold, the flames located near the pressure nodal line are extinguished, a mechanism that has the immediate effect of reducing the pressure amplitude and allowing re-ignition of the extinguished flames. This phenomenon can be modeled by considering the flame displacement induced by the transverse velocity oscillations. This defines a critical value linking the pressure amplitude to the partial blow-off of the system.

To obtain additional information of the mechanism involved in these instabilities, it is useful to examine the dynamics of a single swirl spray injector placed in a tubular system called SICCA-Spray, equivalent to one sector of the annular system. This device is first used to trigger naturally excited longitudinal instabilities around 500 Hz. This yields data pertaining to combustion instabilities in this configuration. It is found that the oscillation arises when the size of the combustion chamber wall exceeds a certain threshold. By using a tube that is shorter than this critical value it is possible to stabilize the flame and obtain a steady regime. It is then possible to use excite the driver units and create an axial velocity fluctuation at a given frequency and amplitude. The Flame Describing Function can then be determined for a wide range of frequencies and amplitudes of modulation by taking the ratio between the relative heat release rate and the relative velocity fluctuation. Another FDF is also measured by considering the ration between the relative heat release rate and the relative pressure fluctuation at the chamber backplane. It is shown however that this is not a meaningful quantity because the acoustic pressure detected at the backplane is essentially the result of the

rate of change of the heat release in the flame. Thus the pressure is not a proper input for the FDF and the quantity defined by taking the ratio of the relative heat release to the relative pressure fluctuation does not provide a suitable portrayal of the dynamics of the combustion region. In effect the measured pressure is more like an output of the unsteady flame and cannot be used as an input. This illustrates the difficulty of experimental determinations of relations linking the heat release rate fluctuations to the pressure signal. The velocity perturbation constitutes a physical input to the FDF. The single injector tubular device is then used to compare the flame behavior under forced operation and under self-excited oscillations. It is found that the flame dynamics under forced modulation or under self-sustained oscillations are quite similar and that the signals corresponding to the heat release rate fluctuations are quite similar. The FDF framework is then applied to determine potential bands of instability of the measured FDF phase response measured in this single injector configuration. This allows to explain the naturally excited instabilities observed in SICCA-Spray depending on the combustor wall length. Finally, an extension to the MICCA-Spray azimuthal instabilities observed around 750 Hz is also proposed using the FDF framework.

### **Numerical simulations of the SICCA-Spray device**

Large Eddy Simulations (LES) of the SICCA-Spray burner are performed to calculate the combustion dynamics measured on the experimental bench. The study aims at obtaining information on the mechanisms leading to self-sustained combustion oscillations, complement experimental data and possibly improve the understanding of the phenomena observed experimentally. A steady flame is first stabilized in the combustion chamber and compared to available experimental data with a fairly good agreement. Much of the differences are found in the expansion rate of the jet issuing from the injector that has an impact on the flame shape. As the wall length is increased, the flame exhibits naturally excited oscillations at a frequency close to 500 Hz. This can be used to compare results of calculations to the naturally excited oscillations observed in the experiment at nearly the same frequency. The motion of the experimental and numerical flames are compared using phase average chemiluminescence signals and heat release rate fluctuations determined numerically. These signals are found to be quite similar. Finally, the incoming air flow is modulated to reproduce the external excitation of the flame as in the experiment. The flame motion is simulated for several frequencies and amplitudes in order to estimate a numerical Flame Describing Function that can be compared to the experimental one acquired on the SICCA-Spray bench. Once again the match is not perfect but one retrieves many of the experimental features. The calculations also help in the interpretation of experimental findings. In its present state, the simulation correctly predicts the FDF phase but the gain behavior is not well retrieved. Finally, LES provides further information on the various processes and guidelines for possible improvements of the experimental bench to better measure the flame dynamics.

### Combustion dynamics of the MICCA burner in premixed mode

The MICCA annular chamber developed during the doctoral thesis of J-F. Bourgoïn was operating under premixed conditions. This device is used to study two experimental phenomena, the first is observed with swirl injector units while the second is obtained with the matrix injectors producing a large number of small laminar flames.

The chamber is first equipped with swirled premixed injectors equipped with cups. The cup angles may be varied. It is shown that, under certain operating conditions, an alternating flame pattern arises and that this is evenly distributed around the annulus. If the cup angle is less than  $70^\circ$ , the phenomenon does not occur, but for  $90^\circ$  and above the alternating pattern is quite visible. In this pattern, the flames periodically take a V-shape elongated in the axial direction and an M-shape extending in the azimuthal direction. An increase of the flow rate barely changes the shape of the pattern whereas a decrease of the equivalence ratio strengthens the alternation with greater differences between the two flame shapes. When the cups with the angle of  $105^\circ$  are mounted, an unstable and unsteady switching between “V” and “M” flames takes place. Whatever the angle of the cups mounted, when the alternating pattern is observed, strong variations of the thermal load at the walls have been observed. As a consequence, the alternation of flame shapes in an annular combustion chamber may have important consequences for the steady state operation of the system.

A second study is carried out on the MICCA chamber equipped with laminar matrix burners that exhibit well established combustion instabilities at a limit cycle. The combustion dynamics of these flames is well known and the azimuthal mode excited in this configuration can be easily chosen by changing the operating conditions as the different mode types do not overlap in general. The different known mode types arising in the system (standing, spinning, slanted and longitudinal) as well as a new type of instability, the chugging mode, are characterized. For specific operating conditions, a hysteresis phenomenon is uncovered and shown to lead to different modal structures for the same flow conditions, depending on the history of, essentially, the equivalence ratio. This defines the so called “Dual mode” region. If  $\phi$  is increased to enter this region from lean conditions to the target value, a spinning mode is obtained and the chamber is locked on this mode until the equivalence ratio is modified to exit the dual mode region. On the other hand, if  $\phi$  is decreased from rich conditions, a standing mode arises at the target operating conditions. Finally, it is shown that the chugging oscillations observed just outside the region of azimuthal instability contains information that can be used to predict the azimuthal mode structure that will be established.

### Perspectives

Combustion dynamics in annular combustors still raises many fundamental and more practical issues. The well controlled experiments in tubular or annular configurations examined in the present document have provided a large amount of information

that has improved the understanding of the processes involved in the light-round and in the occurrence of azimuthally coupled thermo-acoustic oscillations and provide a large and valid dataset for modeling and simulations. The two main topics of interest in this manuscript then feature interesting perspectives.

In view of the many questions tackled in the present document, it appears that ignition and relight still raise fundamental issues and technical questions.

- One important item is to develop prediction methods that will provide a precise description of the ignition probability and of the light-round process in annular geometries. This will help design combustors with the specified ignition and relight capabilities. The predictive methods could be used to select geometrical parameters and operating conditions allowing a reliable initiation of the combustion process. The modeling effort should be supported by further experimentations and detailed investigations of the dynamics of the traveling flame and its effects on the flow.
- It is shown in the present document that the transient behavior of the flame after initiation of a particular injector raises interesting questions on the physics of this process. It would be useful to examine this particular aspect in further detail and see if this can be reproduced using large eddy simulation. This might also require to instrument a particular injector with additional sensors that will allow a more detailed description of the flow and flame during this transient process.
- The air conditions in terms of pressure, temperature and humidity on the relight of an engine in case of accidental shut down also need to be considered in practice and their effect might be evaluated with simulations if these simulations are sufficiently well validated. It is also important to consider the thermal conditions prevailing at the combustor walls and document their effects with systematic experiments and numerical simulations.
- Experiments indicate that the volatility of the fuel influences the light-round delay. This characteristic can be varied by making use of different fuels. It might be worth extending the present study by considering other fuels and eventually bio-fuels.
- The injector used in the MICCA-Spray experiments has been designed to be flexible, easy to model and easy to simulate. It might be interesting to examine swirling injectors that are closer to those found in industrial applications.

As indicated across this document, combustion instabilities constitute an important issue for gas turbines. Progress has been achieved and this manuscript proposes a set contributions that are mainly focused on the combustion dynamics of spray flames. The case of annular geometries is specifically examined because in these configurations the azimuthal modes are poorly damped and correspond to resonant frequencies that fall in the range of sensitivity of swirling flames. It is possible to design dampers that may be used to suppress some of the coupling modes but this solution may not be practical in aircraft combustors where space and weight are limited. It is then impor-

tant to design combustors that are dynamically stable and this can only be achieved on the basis of a physical understanding of the mechanisms leading to instability. It is then clear that the research effort should be pursued and that further progress will require additional experimentation and a parallel development of theory and simulation. Here is a list of items that may be considered or that need to be addressed.

- It was found that the liquid spray had its own dynamics during an instability cycle. Changing the fuel type, for example by using heavier less volatile fuels, might have a strong impact on the flame dynamics. The atomization process also participates to the formation of the liquid phase and thus has an influence on the combustion dynamics. It might be interesting to change the size distribution of the droplets injected in the chamber, for example by modifying the size of the convergent end-piece of the injector.
- It is shown that azimuthal instabilities arising in the MICCA-Spray chamber appear in the form of long bursts at a low repetition rate. This phenomenon indicates that a well established limit cycle is never reached. A damping or a saturation phenomenon, not yet identified, may be the reason for this behavior. The control of this feature would be of interest to appropriately characterize the limit cycles of standing and spinning modes in the chamber. Understanding this issue could also be a good path to control the limit cycle growth, making the design of damping systems possible. On the scientific level, this would also ease the study of the oscillation growth and decay in this kind of geometry.
- The current work identified the head loss of the injector as an influential parameter controlling the instabilities in the annular bench. It was observed that a swirler with a large head loss ( $> 6\%$  of the nominal pressure) would not trigger instabilities whereas a swirler with a lower head loss ( $\sim 4\%$ ) leads to large amplitude oscillations in the combustor. One should note that the two tested swirlers were not designed to produce the exact same flame. As the flame shape controls many of the dynamical characteristics of the combustion process, one has to design swirlers that stabilize the same flame shape but do not have the same head loss. This work is now being investigated in doctoral thesis of Guillaume Vignat.
- A significant effort has been made to experimentally determine the Flame Describing Function with satisfactory results. There are however limitations in the forcing level that can be reached that are mainly due to the presence of the swirler in the fluid stream. The strong impact of the swirler channels and other small parts of the injector is also highlighted in the numerical simulations. It might be interesting to consider another way of externally exciting the flame, for example with driver units placed downstream the injection system, after the combustion region.
- The numerical work performed on the single injector tubular burner needs to be pushed forward and used in an efficient manner to complement experimental results. Many calculations have been done but the lack of time inhibited further analysis and limited the information extracted from the simulations. It would be

natural and logical to pursue this effort in the framework of the next and future doctoral investigations.





## Appendix A

# Flame shape during the MICCA ignition sequence

### Appendix A: Flame shape in MICCA

It is interesting to see whether the evolution of flame shapes observed in a swirl spray configurations can also be observed in the case of fully premixed gaseous injection. The spray injectors of MICCA-Spray are replaced by premixed injectors with a different swirling system as in [Bourgouin et al. \(2013\)](#). Figure A.1 shows at the top the ignition of the annular combustor with these injectors for a propane/air mixture at  $\phi = 0.76$  and  $P = 60$  kW. One can see that flames at 120 ms and 160 ms are very different. The same injection system is mounted on the SICCA burner to examine the ignition steps. As for the spray injector, the flame is first quite compact and moves into the injection system before stabilizing and being lifted at about 40 ms. This confirms that the phenomenon observed previously is not specific to spray swirl injection configurations.

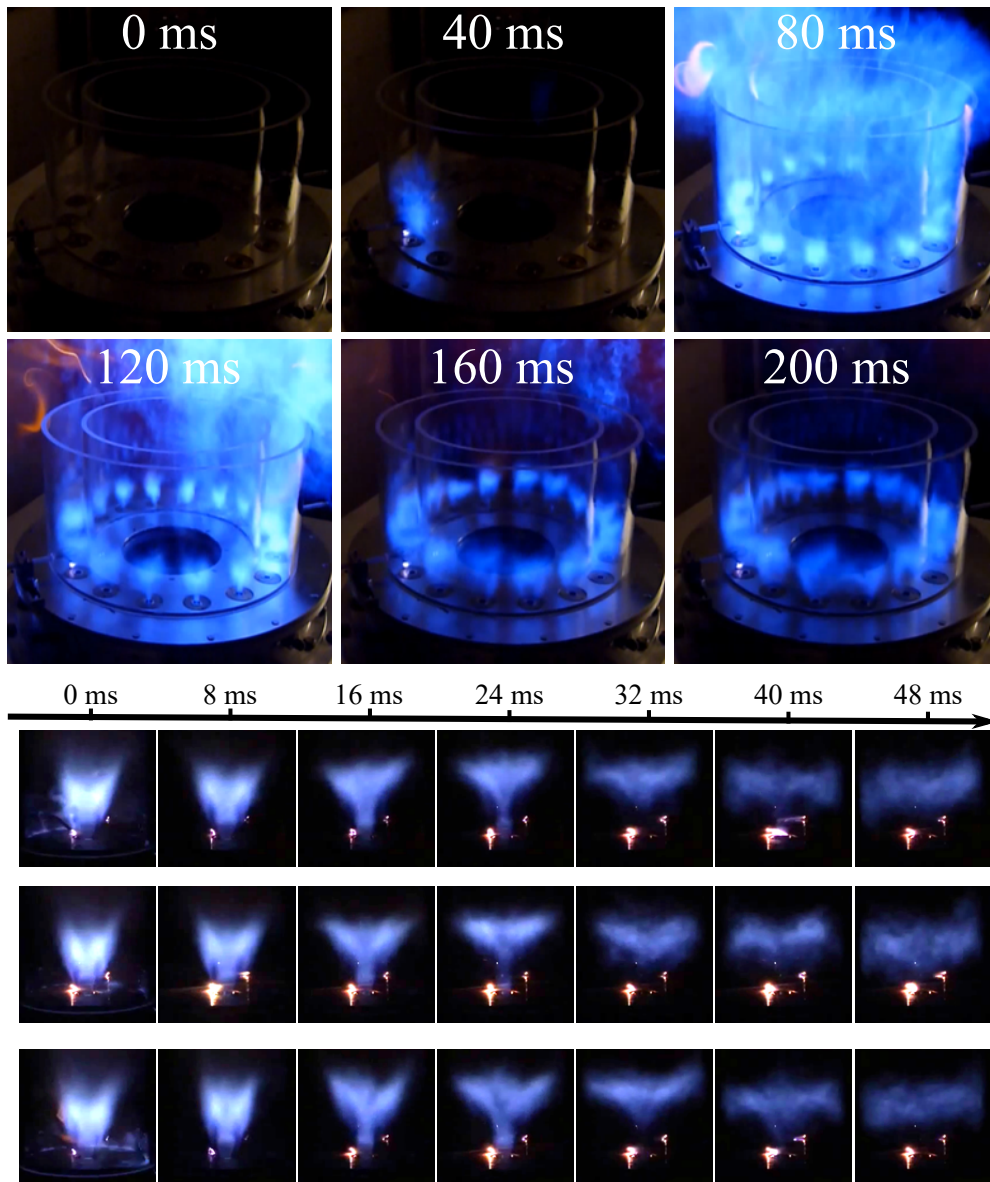


**Figure A.1.** Top: True-color low-speed images of the light-round in the MICCA combustion chamber under premixed conditions. Bottom: Ignition of the SICCA burner equipped with the MICCA premixed injector with  $\phi = 0.76$  and  $P = 60$  kW.





## Appendix B

# Decomposition of spinning and standing modes

An acoustic mode in an annular chamber can be decomposed into  $a$  and  $b$  waves going in the clockwise and anti-clockwise directions as eq. B.1 shows:

$$p = |a|e^{i(\theta+\varphi)-i\omega t} + |b|e^{-i\theta-i\omega t} \quad (\text{B.1})$$

For a spinning mode rotating in the clockwise direction, only one wave subsist,  $|a| = |a|$  and  $|b| = 0$ , eq. B.1 can then be written as:

$$p = |a| \cos(\theta + \varphi - \omega t) + i|a| \sin(\theta + \varphi - \omega t) \quad (\text{B.2})$$

Which real part corresponds to the following statement:

$$\text{real}(p) = a \cos(\theta + \varphi - \omega t)$$

For a spinning mode rotating in the anti-clockwise direction,  $a = 0$  and  $b = |b|$

$$p = b \cos(\theta - \omega t) + i|b| \sin(\theta - \omega t) \quad (\text{B.3})$$

Which real part corresponds to the following statement:

$$\text{real}(p) = b \cos(\theta - \omega t) = b \cos(\theta + \omega t)$$

For a standing mode,  $a$  and  $b$  waves have the same amplitude  $|a| = |b|$  meaning that:

$$p = |a| \cos((\omega + \varphi) - \omega t) + |b| \cos(-\theta - \omega t) + i(|a| \sin(\theta + \varphi - \omega t) + |b| \sin(\theta - \omega t))$$

(B.4)

Which real part corresponds to the following statement:

$$\text{real}(p) = |a| \cos(\theta + \varphi - \omega t) + |b| \cos(\theta + \omega t)$$

Two cases are then studied: Case A,  $|a| = |b|$  and  $\varphi = 0$

$$\begin{aligned} \text{real}(p) &= |a| (\cos(\theta - \omega t) + \cos(\theta + \omega t)) \\ &= |a| 2 \cos\left(\frac{\theta - \omega t + \theta + \omega t}{2}\right) \cos\left(\frac{\theta - \omega t - \theta - \omega t}{2}\right) \\ &= 2|a| \cos(\theta) \cos(-\omega t) \end{aligned} \quad (\text{B.5})$$

Case B,  $|a| = |b|$  and  $\varphi \neq 0$

$$\begin{aligned} \text{real}(p) &= |a| (\cos(\theta + \varphi - \omega t) + \cos(\theta + \omega t)) \\ &= 2|a| \cos\left(\frac{\theta + \varphi - \omega t + \theta + \omega t}{2}\right) \cos\left(\frac{\theta + \varphi - \omega t - \theta - \omega t}{2}\right) \\ &= 2|a| \cos\left(\theta + \frac{\varphi}{2}\right) \cos\left(\frac{\varphi}{2} - \omega t\right) \end{aligned} \quad (\text{B.6})$$

Two special cases can be highlighted.

If  $\varphi = \frac{\pi}{2}$

$$\text{real}(p) = 2|a| \cos\left(\theta + \frac{\pi}{4}\right) \cos\left(\frac{\pi}{4} - \omega t\right) \quad (\text{B.7})$$

If  $\varphi = \pi$

$$\text{real}(p) = 2|a| \cos\left(\theta + \frac{\pi}{2}\right) \cos\left(\frac{\pi}{2} - \omega t\right) \quad (\text{B.8})$$

$$= 2|a| \sin \theta \sin(-\omega t) \quad (\text{B.9})$$





# Bibliography

- Abramzon, B. and W. Sirignano (1989). Droplet vaporization model for spray combustion calculations. *International Journal of Heat and Mass Transfer* 32(9), 1605 – 1618. (p. 115)
- Ahmed, S. F., R. Balachandran, T. Marchione, and E. Mastorakos (2007). Spark ignition of turbulent nonpremixed bluff-body flames. *Combust. Flame* 151, 366–385. (p. 33)
- Armitage, C., R. Balachandran, E. Mastorakos, and R. Cant (2006). Investigation of the nonlinear response of turbulent premixed flames to imposed inlet velocity oscillations. *Combustion and Flame* 146(3), 419–436. (p. 112)
- Bach, E., J. Kariuki, J. R. Dawson, E. Mastorakos, and H.-J. Bauer (2013). Spark ignition of single bluff-body premixed flames and annular combustors. In *AIAA Aerospace Sciences Meeting 2013*, Number 51, Grapevine, Texas, USA. (p. 2, 33, 47)
- Baillet, F. and F. Lespinasse (2014). Response of a laminar premixed v-flame to a high-frequency transverse acoustic field. *Combustion and Flame* 161(5), 1247 – 1267. (p. 67)
- Ballal, D. and A. Lefebvre (1974). The influence of flow parameters on minimum ignition energy and quenching distance. *Proc. Combust. Inst.* 15, 1473–1481. (p. 33)
- Ballal, D. R. and A. H. Lefebvre (1977). Ignition and flame quenching in flowing gaseous mixtures. *Proceedings of the Royal Society of London. Series A* 357, 163–181. (p. 33)
- Ballal, D. R. and A. H. Lefebvre (1978). Ignition and flame quenching of quiescent fuel mists. *Proceedings of the Royal Society of London. Series A* 364, 277–294. (p. 33)
- Ballal, D. R. and A. H. Lefebvre (1981). Flame propagation in heterogeneous mixtures of fuel droplets, fuel vapor and air. *Proc. Combust. Inst.* (8), 321–328. (p. 33, 45, 131)
- Barre, D., L. Esclapez, M. Cordier, E. Riber, B. Cuenot, G. Staffelbach, B. Renou, A. Vandiel, L. Y. M. Gicquel, and G. Cabot (2014). Flame propagation in aeronautical swirled multi-burners: Experimental and numerical investigation. *Combust. Flame* 161, 2387–2405. (p. 33)
- Bauerheim, M., J. Parmentier, P. Salas, F. Nicoud, and T. Poinsot (2014, may). An analytical model for azimuthal thermoacoustic modes in an annular chamber fed by an annular plenum. *Combustion and Flame* 161(5), 1374–1389. (p. 2, 66,

- 188, 189)
- Bauerheim, M., P. Salas, F. Nicoud, and T. Poinsot (2014). Symmetry breaking of azimuthal thermo-acoustic modes in annular cavities: a theoretical study. *Journal of Fluid Mechanics* 760, 431–465. (p. 66, 188, 189)
- Bauerheim, M., G. Staffelbach, N. A. Worth, J. R. Dawson, L. Y. M. Gicquel, and T. Poinsot (2015). Sensitivity of LES-based harmonic flame response model for turbulent swirled flames and impact on the stability of azimuthal modes. *Proc. Combust. Inst.* 35(3), 3355–3363. (p. 2, 165)
- Birouk, M. and I. Gökalp (2006). Current status of droplet evaporation in turbulent flows. *Prog. Energy Combust. Sci.* 32, 408–423. (p. 20, 37)
- Boileau, M., G. Staffelbach, B. Cuenot, T. Poinsot, and C. Berat (2008). Les of an ignition sequence in a gas turbine engine. *Combust. Flame* 154, 2–22. (p. 2, 33, 115)
- Borghesi, G., F. Biagioli, and B. Schuermans (2009). Dynamic response of turbulent swirling flames to acoustic perturbations. *Combustion Theory and Modeling* 13(3), 487–512. (p. 92)
- Bothien, M. R., N. Noiray, and B. Schuermans (2015). Analysis of azimuthal thermo-acoustic modes in annular gas turbine combustion chambers. *Journal of Engineering for Gas Turbines and Power* 137(6), 061505. (p. 2, 188)
- Boudy, F., D. Durox, T. Schuller, G. Jomaas, and S. Candel (2011). Describing function analysis of limit cycles in a multiple flame combustor. *Journal of Engineering for Gas Turbines and Power* 133. (p. 3)
- Bourgouin, J. F., D. Durox, J. P. Moeck, T. Schuller, and S. Candel (2013a). Self-sustained instabilities in an annular combustor coupled by azimuthal acoustic modes. In *ASME Conference Proceedings*, Number GT2013-95010, San Antonio, Texas, USA, pp. 1–13. (p. 2, 17, 19, 66, 67, 68, 76, 189)
- Bourgouin, J. F., D. Durox, J. P. Moeck, T. Schuller, and S. Candel (2013b). Self-sustained instabilities in an annular combustor coupled by azimuthal acoustic modes. In *Proceedings of ASME Turbo Expo 2013*, Number GT2013-95010, San Antonio, Texas, USA. (p. 185)
- Bourgouin, J.-F., D. Durox, J. P. Moeck, T. Schuller, and S. Candel (2015). A new pattern of instability observed in an annular combustor: The slanted mode. *Proceedings of the Combustion Institute* 35, 3237–3244. (p. 2, 3, 67, 68, 190, 195, 196)
- Bourgouin, J.-F., D. Durox, J. P. Moeck, T. Schuller, and C. S. (2015). Characterization and modelling of a spinning thermoacoustic instability in an annular combustor equipped with multiple matrix injectors. *J Eng Gas Turb Power* 137, 021503. (p. 67, 68, 190, 192)
- Bourgouin, J.-F., D. Durox, T. Schuller, J. Beaunier, and S. Candel (2013). Ignition dynamics of an annular combustor equipped with multiple swirling injectors. *Combustion and Flame* 160(8), 1398–1413. (p. 3, 17, 33, 43, 44, 47, 51, 52, 165, 221)
- Bradley, D. and F. K.-K. Lung (1987). Spark ignition and the early stages of turbulent flame propagation. *Combust. Flame* 69, 71–93. (p. 33)

- Campa, G. and S. M. Camporeale (2014). Prediction of the thermoacoustic combustion instabilities in practical annular combustors. *J Eng Gas Turb Power* 136(091504 (10 pages)). (p. 66, 186)
- Camporeale, S. M., B. Fortunato, and G. Campa (2011). A finite element method for three-dimensional analysis of thermo-acoustic combustion instability. *J Eng Gas Turb Power* 133(011506 (13 pages)). (p. 66, 186)
- Candel, S. (2002). Combustion dynamics and control : progress and challenges. *Proceedings of the Combustion Institute* 29, 1–28. (p. 5, 92, 164)
- Candel, S., D. Durox, T. Schuller, J. Bourgoïn, and J. Moeck (2014). Dynamics of swirling flames. *Annu. Rev. Fluid Mech.* 46, 147–173. (p. 168)
- Champion, M., B. Deshaies, G. Joulin, and K. Kinoshita (1986). Spherical flame initiation: Theory versus experiments for lean propane-air mixtures. *Combust. Flame* 65(3), 319–337. (p. 33)
- Charlette, F., C. Meneveau, and D. Veynante (2002). A power-law flame wrinkling model for LES of premixed turbulent combustion part I: non-dynamic formulation and initial tests. *Combustion and Flame* 131(1–2), 159 – 180. (p. 115)
- Colin, O., F. Ducros, D. Veynante, and T. Poinso (2000). A thickened flame model for large eddy simulations of turbulent premixed combustion. *Physics of Fluids* 12(7), 1843–1863. (p. 115, 133)
- Colin, O. and M. Rudgyard (2000). Development of high-order taylor–galerkin schemes for LES. *Journal of Computational Physics* 162(2), 338 – 371. (p. 114)
- Cordier, M., A. Vandel, G. Cabot, B. Renou, and A. M. Boukhalfa (2013). Laser-induced spark ignition of premixed laser-induced spark ignition of premixed confined swirled flames. *Combust. Sci. Technol.* 185, 379–407. (p. 33, 165)
- Cordier, M., A. Vandel, B. Renou, G. Cabot, M. A. Boukhalfa, L. Esclapez, D. Barre, E. Riber, B. Cuenot, and L. Gicquel (2013, June 3-7, 2013,). Experimental and numerical analysis of an ignition sequence in a multiple-injectors burner. In *Proceedings of ASME Turbo Expo 2013*, Number GT2013-94681, San Antonio, Texas, USA. (p. 33)
- Culick, F. and P. Kuentzmann (2006). Unsteady motions in combustion chambers for propulsion systems. Technical report, NATO RESEARCH AND TECHNOLOGY ORGANIZATION NEUILLY-SUR-SEINE (FRANCE). (p. 5)
- Davis, S. G. and C. K. Law (1998). Laminar flame speeds and oxydation kinetics of iso-octane-air and n-heptane-air flames. *Proc. Combust. Inst.* 27, 521–527. (p. 44)
- Dawson, J. R. and N. A. Worth (2014). Flame dynamics and unsteady heat release rate of self-excited azimuthal modes in an annular combustor. *Combustion and Flame* 161(10), 2565 – 2578. (p. 67)
- Dowling, A. (1999). A kinematic model of a ducted flame. *Journal of Fluid Mechanics* 394, 51–72. (p. 92)
- Dowling, A. P. (1997). Nonlinear self-excited oscillations of a ducted flame. *Journal of Fluid Mechanics* 346, 271–290. (p. 92)
- Dowling, A. P. and S. R. Stow (2003, Sep-Oct). Acoustic analysis of gas turbine combustors. *Journal of Propulsion and Power* 19(5), 751–764. (p. 186)

- Ducruix, S., D. Durox, and S. Candel (2000). Theoretical and experimental determination of the transfer function of a laminar premixed flame. *Proceedings of the Combustion Institute* 28(1), 765–773. (p. 92)
- Durox, D., J. F. Bourgouin, M. Philip, T. Schuller, S. Candel, J. P. Moeck, M. Philip, T. Schuller, and S. Candel (2013). Nonlinear interactions in combustion instabilities coupled by azimuthal acoustic modes. In *Proceedings of International Workshop on Non-normal and Nonlinear effects in aero- and thermo-acoustics. Munich, June 18-21. (14 pages)*, pp. 1–14. (p. 190)
- Durox, D., J. P. Moeck, J. F. Bourgouin, P. Morenton, M. Viallon, T. Schuller, and S. Candel (2013). Flame dynamics of a variable swirl number system and instability control. *Combustion and Flame* 160(9), 1729–1742. (p. 104, 165, 168)
- Durox, D., T. Schuller, N. Noiray, A. L. Birbaud, and S. Candel (2009). Rayleigh criterion and acoustic energy balance in unconfined self-sustained oscillating flames. *Combustion and Flame* 156(1), 106–119. (p. 104)
- Durox, D., T. Schuller, N. Noiray, and S. Candel (2009). Experimental analysis of nonlinear flame transfer functions for different flame geometries. *Proceedings of the Combustion Institute* 32(1), 1391–1398. (p. 92, 165)
- Eckstein, J., E. Freitag, C. Hirsch, and T. Sattelmayer (2006). Experimental Study on the Role of Entropy Waves in Low-Frequency Oscillations in a RQL Combustor. *Journal of Engineering for Gas Turbines and Power* 128(April 2006), 264. (p. 92)
- Evesque, S. and W. Polifke (2002). Low-order acoustic modelling for annular combustors: Validation and inclusion of modal coupling. In *ASME Conference Proceedings, Paper GT 2002-30064*. (p. 186, 187)
- Evesque, S., W. Polifke, and C. Pankiewicz (2003). Spinning and azimuthally standing acoustic modes in annular combustors. In *AIAA Conference Proceedings Paper 2003-3182*. (p. 66, 76, 187)
- Fanaca, D., P. R. Alemela, C. Hirsch, and T. Sattelmayer (2010). Comparison of the Flow Field of a Swirl Stabilized Premixed Burner in a Annular and a Single Burner Combustion Chamber. *J Eng Gas Turb Power* 132(7). (p. 165, 166, 177, 178, 179)
- Fanaca, D., P. R. Alemela, C. Hirsch, T. Sattelmayer, and B. Schuermans (2009). Comparison of the flow field of a swirl stabilised premixed burner in an annular and a single burner combustion chamber. *ASME Conference Proceedings*, 679–688. (p. 25)
- Franzelli, B., E. Riber, M. Sanjosé, and T. Poinso (2010). A two-step chemical scheme for kerosene–air premixed flames. *Combustion and Flame* 157(7), 1364–1373. (p. 115)
- Fu, Y., J. Cai, S.-M. Jeng, and H. Mongia (2005, June 6-9,). Confinement effects on the swirlings flowof a counter-rotating swirl cup. In *ASME Paper, Number GT2005-68622, Reno, Nevada, USA*. (p. 177)
- Gajan, P., A. Strzelecki, B. Platet, R. Lecourt, and F. Giuliani (2007). Investigation of Spray Behavior Downstream of an Aeroengine Injector with Acoustic Excitation. *Journal of Propulsion and Power* 23(2), 390–397. (p. 92, 93)

- Garcia, M. (2009). *Development and validation of the Euler-Lagrange formulation on a parallel and unstructured solver for large-eddy simulation*. Ph. D. thesis, Institut National Polytechnique de Toulouse. (p. 129)
- Garcia-Armingol, T., Y. Hardalupas, A. Taylor, and J. Ballester (2014). Effect of local flame properties on chemiluminescence-based stoichiometry measurement. *Exp. Thermal Fluid Sci.* 53(0), 93–103. (p. 176)
- Ghirardo, G., M. Juniper, and J. P. Moeck (2016, October). Weakly nonlinear analysis of thermoacoustic instabilities in annular combustors. *Journal of Fluid Mechanics* 805, 52–87. (p. 66, 92, 188, 189, 208)
- Ghirardo, G. and M. P. Juniper (2013). Azimuthal instabilities in annular combustors: standing and spinning modes. *Proceedings of the Royal Society A: Mathematical, Physical and Engineering Science* 469(2159). (p. 2, 66, 78)
- Ghirardo, G., M. P. Juniper, and J. P. Moeck (2015). Stability criteria for standing and spinning waves in annular combustors. In *ASME Conference Proceedings*, Number GT2015-43127, Montreal, Canada, pp. 1–14. (p. 66, 188, 189, 208)
- Gicquel, L., G. Staffelbach, and T. Poinsot (2012). Large eddy simulations of gaseous flames in gas turbine combustion chambers. *Progress in Energy and Combustion Science* 38(6), 782–817. (p. 111)
- Giuliani, F., P. Gajan, O. Diers, and M. Ledoux (2002). Influence of pulsed entries on a spray generated by an air-blast injection device: An experimental analysis on combustion instability processes in aeroengines. *Proceedings of the Combustion Institute* 29, 91–98. (p. 92, 93)
- Haile, E., O. Delabroy, F. Lacas, D. Veynante, and S. Candel (1996). Structure of an acoustically forced turbulent spray flame. *Symposium (International) on Combustion* 26(1), 1663–1670. (p. 92)
- Han, X., J. Li, and A. S. Morgans (2015). Prediction of combustion instability limit cycle oscillations by combining flame describing function simulations with a thermoacoustic network model. *Combustion and Flame* 162(10), 3632–3647. (p. 112)
- Hauser, M., M. Lorenz, and T. Sattelmayer (2011, April). Influence of transversal acoustic excitation of the burner approach flow on the flame structure. *J Eng Gas Turb Power* 133, 041501. (p. 67)
- Hermeth, S., G. Staffelbach, L. Gicquel, and T. Poinsot (2013). Les evaluation of non-linear effects on the dynamic flame response in a real gas turbine combustion chamber. In *ASME Turbo Expo 2013: Turbine Technical Conference and Exposition*, pp. V01BT04A052–V01BT04A052. American Society of Mechanical Engineers. (p. 112)
- Hermeth, S., G. Staffelbach, L. Y. M. Gicquel, V. Anisimov, C. Cirigliano, and T. Poinsot (2014). Bistable swirled flames and influence on flame transfer functions. *Combust. Flame* 161(1), 184–196. (p. 165)
- Huang, Y. and V. Yang (2009). Dynamics and stability of lean-premixed swirl-stabilized combustion. *Progress in Energy and Combustion Science* 35(4), 293–384. (p. 5)
- Hurle, I. R., R. B. Price, T. M. Sugden, and A. Thomas (1968). Sound emission from

- open turbulent premixed flames. *Proceedings of the Royal Society of London Series a-Mathematical and Physical Sciences* 303(1475), 409–427. (p. 21, 107, 175)
- Kao, Y.-H., M. Denton, X. Wang, J. S.-M., and M.-C. Lai (2015, June 15-19,). Experimental spray structure and combustion of a linearly-arranged 5-swirler array. In *ASME Paper*, Number GT2015-42509, Montreal, Canada. (p. 164)
- Kao, Y.-H., S. Tambe, and S.-M. Jeng (2013, June 3-7,). Aerodynamics of linearly arranged rad-rad swirlers, effect of numbers of swirlers and alignment. In *ASME Paper*, Number GT2013-94280, San Antonio, Texas, USA. (p. 164, 170)
- Kao, Y.-H., S. Tambe, and J. S.-M. (2014, June 16-20,). Aerodynamics study of a linearly-arranged 5-swirler array. In *ASME Paper*, Number GT2014-25094, Düsseldorf, Germany. (p. 164, 165, 169)
- Kim, K. and S. Hochgreb (2011). The nonlinear heat release response of stratified lean-premixed flames to acoustic velocity oscillations. *Combustion and Flame* 158, 2482–2499. (p. 93)
- Kim, K., J. Lee, B. Quay, and D. Santavicca (2010). Response of partially premixed flames to acoustic velocity and equivalence ratio perturbations. *Combustion and Flame* 157, 1731–1744. (p. 165)
- Kim, K.T. and Lee, J.G. and Quay, B.D. and Santavicca, D.A. (2010). Spatially distributed flame transfer functions for predicting combustion dynamics in lean premixed gas turbine combustors. *Combustion and Flame* 157(9), 1718 – 1730. (p. 92)
- Kopitz, J., A. Huber, T. Sattelmayer, and W. Polifke (2005). Thermoacoustic stability analysis of an annular combustion chamber with acoustic low order modeling and validation against experiment. *ASME Paper No. GT2005-68797*. (p. 2)
- Krebs, W., P. Flohr, B. Prade, and S. Hoffmann (2002). Thermoacoustic stability chart for high-intensity gas turbine combustion systems. *Combustion Science and Technology* 174, 99–128. (p. 2, 164, 185, 189)
- Krüger, U., J. Hüren, S. Hoffmann, W. , and D. Bohn (1999). Prediction of thermoacoustic instabilities with focus on the dynamic flame behavior for the 3A-series gas turbine of Siemens KWU. In *Proceedings of ASME Turbo Expo 1999, Paper 99-GT-111*. (p. 185)
- Krüger, U., J. Hüren, S. Hoffmann, W. Krebs, P. Flohr, and D. Bohn (2001). Prediction and measurement of thermoacoustic improvements in gas turbines with annular combustion systems. *J Eng Gas Turb Power* 123(3), 557–566. (p. 186)
- Kumar, K. and C. J. Sung (2007). Laminar flame speeds and extinction limits of preheated n-decane/o<sub>2</sub>/n<sub>2</sub> and n-dodecane/o<sub>2</sub>/n<sub>2</sub> mixtures. *Combust. Flame* 151, 209–224. (p. 45)
- Laera, D., K. Prieur, D. Durox, T. Schuller, S. M. Camporeale, and S. Candel (2016a). Flame describing function analysis of spinning and standing modes in an annular combustor and comparison with experiments. *Combustion and Flame, under revision*. (p. 77)
- Laera, D., K. Prieur, D. Durox, T. Schuller, S. M. Camporeale, and S. Candel (2016b, June 13-17). Impact of heat release distribution on the spinning modes of an

- annular combustor with multiple matrix burners. In *Proceedings of ASME Turbo Expo 2016*, Number GT2016-56309, Seoul, South Korea. (p. 66)
- Laera, D., T. Schuller, K. Prieur, D. Durox, S. M. Camporeale, and S. Candel (2017). Flame describing function analysis of spinning and standing modes in an annular combustor and comparison with experiments. *Combustion and Flame* 184, 136–152. (p. 2)
- Lancien, T., K. Prieur, D. Durox, S. Candel, and R. Vicquelin (2017). Large-eddy simulation of light-round in an annular combustor with liquid spray injection and comparison with experiments. (p. 47, 61, 113, 115, 118, 129, 131)
- Lefebvre, A. (1989). *Atomization and Sprays*. London: Taylor and Francis. (p. 115)
- Lefebvre, A. (2010). *Gas turbine combustion : alternative fuels and emissions* (3rd ed.). Hoboken, NJ : CRC Press. (p. 164)
- Lefebvre, A. H. (1983). *Gas Turbines Combustion*. New York: McGraw Hill. (p. 33)
- Legier, J. P., T. Poinsot, and D. Veynante (2000). Dynamically thickened flame les model for premixed and non-premixed combustion. In *Proc. Summer Program, Center for Turbulence Research, NASA Ames/Stanford Univ.* (p. 115)
- Lespinasse, F., F. Baillot, and T. Boushaki (2013). Responses of v-flames placed in an hf transverse acoustic field from a velocity to pressure antinode. *Comptes Rendus Mécanique* 341(1), 110 – 120. (p. 67, 85)
- Lewis, B. and G. V. Elbe (1987). *Combustion, Flames and Explosions of Gases* (third ed.). New York: Academic Press. (p. 33)
- Lieuwen, T. and Y. V. (2005). Combustion instabilities in gas turbine engines : operational experience, fundamental mechanisms and modeling. *Progress in astronautics and aeronautics* 210, 657. (p. 164)
- Luo, K., H. Pitsch, M. G. Pai, and O. Desjardins (2011). Direct numerical simulations and analysis of three-dimensional n-heptane spray flames in a model swirl combustor. *Proceedings of the Combustion Institute* 33(2), 2143–2152. (p. 129)
- Machover, E. and E. Mastorakos (2015). Spark ignition of annular non-premixed combustors. *Experimental Thermal and Fluid Science* 73, 64–70. (p. 33)
- Marchione, T., S. F. Ahmed, and E. Mastorakos (2009). Ignition of turbulent swirling n-heptane spray flames using single and multiple sparks. *Combust. Flame* 156, 166–180. (p. 33)
- Marwan, N., M. C. Romano, M. Thiel, and J. Kurths (2007). Recurrence plots for the analysis of complex systems. *Physics Reports* 438(5-6), 237–329. (p. 204)
- Mastorakos, E. (2009). Ignition of turbulent non-premixed flames. *Prog. En. Combust. Sci.* 35, 57–97. (p. 33)
- Mejia, D., M. Miguel-Brebion, A. Ghani, T. Kaiser, F. Duchaine, L. Selle, and T. Poinsot (2018). Influence of flame-holder temperature on the acoustic flame transfer functions of a laminar flame. *Combustion and Flame* 188(Supplement C), 5 – 12. (p. 113)
- Mirat, C., D. Durox, and T. Schuller (2015). Stability analysis of a swirl spray combustor based on flame describing function. *Proceedings of the Combustion Institute* 35(3), 3291–3298. (p. 21, 92, 93, 96)
- Moeck, J. P., M. Paul, and C. O. Paschereit (2010). Thermoacoustic Instabilities in an

- Annular Rijke Tube. In *ASME Conference Proceedings, Paper GT 2010-23577*. (p. 165, 185, 189)
- Morgans, A. S. and S. R. Stow (2007). Model-based control of combustion instabilities in annular combustors. *Combustion and Flame* 150(4), 380–399. (p. 186)
- Myers, G. D. and A. H. Lefebvre (1986). Flame propagation in heterogeneous mixtures of fuel drops and air. *Combust. Flame* 66, 193–210. (p. 45)
- Nair, V. and R. Sujith (2015). A reduced-order model for the onset of combustion instability: Physical mechanisms for intermittency and precursors. *Proceedings of the Combustion Institute* 35, 3193–3200. (p. 190)
- Nair, V., G. Thampi, and R. Sujith (2013). Intermittent bursts presage the onset of instability in turbulent combustors. In *Proceedings of International Workshop on Non-normal and Nonlinear effects in aero- and thermo-acoustics. Munich, June 18-21. (14 pages)*. (p. 190)
- Nair, V., G. Thampi, and R. Sujith (2014). Intermittency route to thermoacoustic instability in turbulent combustors. *Journal of Fluid Mechanics* 756, 470–487. (p. 190, 204, 206)
- Neophytou, A. and E. Mastorakos (2009). Simulations of laminar flame propagation in droplet mists. *Combust. Flame* 156, 1627–1640. (p. 44, 45)
- Nicoud, F., L. Benoit, C. Sensiau, and T. Poinot (2007). Acoustic modes in combustors with complex impedances and multidimensional active flames. *AIAA Journal* 45, 426–441. (p. 186)
- Nicoud, F. and F. Ducros (1999). Subgrid-scale stress modelling based on the square of the velocity gradient tensor. *Flow, Turbulence and Combustion* 62(3), 183–200. (p. 114)
- Noiray, N., M. Bothien, and B. Schuermans (2011). Investigation of azimuthal staging concepts in annular gas turbines. *Combustion Theory and Modelling* 15(5), 585–606. (p. 66, 78, 80, 165, 187, 188)
- Noiray, N., D. Durox, T. Schuller, and S. Candel (2008a, nov). A unified framework for nonlinear combustion instability analysis based on the flame describing function. *Journal of Fluid Mechanics* 615, 139–167. (p. 92)
- Noiray, N., D. Durox, T. Schuller, and S. Candel (2008b). A unified framework for nonlinear combustion instability analysis based on the flame describing function. *Journal of Fluid Mechanics* 615, 139–167. (p. 3, 78)
- Noiray, N. and B. Schuermans (2013). On the dynamic nature of azimuthal thermoacoustic modes in annular gas turbine combustion chambers. In *Proc. R. Soc. A*, Volume 469, pp. 20120535. The Royal Society. (p. 2, 66, 92, 187, 188, 189)
- O'Connor, J., V. Acharya, and T. Lieuwen (2015). Transverse combustion instabilities: Acoustic, fluid mechanic, and flame processes. *Progress in Energy and Combustion Science* 49, 1–39. (p. 67)
- O'Connor, J. and T. Lieuwen (2011). Disturbance field characteristics of a transversely excited burner. *Combustion Science and Technology* 183(Issue 5), 427–443. (p. 67)
- O'Connor, J. and T. Lieuwen (2012). Further characterization of the disturbance field in a transversely excited swirl-stabilized flame. *Journal of Engineering for Gas*

- Turbines and Power* 134, 011501. (p. 67)
- Palies, P., D. Durox, T. Schuller, and S. Candel (2010). The combined dynamics of swirler and turbulent premixed swirling flames. *Combustion and Flame* 157, 1698–1717. (p. 112)
- Palies, P., D. Durox, T. Schuller, and S. Candel (2011). Nonlinear combustion instability analysis based on the flame describing function applied to turbulent premixed swirling flames. *Combustion and Flame* 158(10), 1980–1991. (p. 3, 92, 99)
- Palies, P., T. Schuller, D. Durox, L. Gicquel, and S. Candel (2011). Acoustically perturbed turbulent premixed swirling flames. *Physics of Fluids* 23, 037101 (15 pages). (p. 112)
- Pankiewitz, C. and T. Sattelmayer (2003). Time domain simulation of combustion instabilities in annular combustors. *Journal of Engineering for Gas Turbines and Power* 125(3), 677–685. (p. 186, 187)
- Paulhiac, D. (2015). *Modélisation de la Combustion d'un spray dans un Bruleur Aéronautique*. Ph. D. thesis, INP Toulouse. (p. 115)
- Pawar, S., R. Vishnu, M. Vadivukkarasan, M. Panchagnula, and S. Raman (2015, June 15-19,). Intermittency route to combustion instability in a laboratory spray combustor. In *Proceedings of ASME Turbo Expo 2015*, Number GT2015-42919, Montréal, Canada. (p. 190)
- Philip, M., M. Boileau, R. Vicquelin, E. Riber, T. Schmitt, B. Cuenot, D. Durox, and S. Candel (2015). Large eddy simulation of the ignition sequence of an annular multiple injector combustor. *Proc. Combust. Inst.* 35(3), 3159–3166. (p. 3, 33)
- Philip, M., M. Boileau, R. Vicquelin, T. Schmitt, D. Durox, J. F. Bourgoïn, and S. Candel (2014a). Ignition sequence in a multi-injector combustor. *Physics of Fluids* 26(9). (p. 33, 84)
- Philip, M., M. Boileau, R. Vicquelin, T. Schmitt, D. Durox, J. F. Bourgoïn, and S. Candel (2014b). Simulation of the ignition process in an annular multiple-injector combustor and comparison with experiments. *J. Eng. Gas Turbines Power (ASME)* 137(3), 031501 (9 pages). (p. 33)
- Poinsot, T. (2016). Prediction and control of combustion instabilities in real engines. In *Proceedings of the Combustion Institute*, Volume in press. (p. 5, 66)
- Poinsot, T. and S. Lele (1992). Boundary conditions for direct simulations of compressible viscous flows. *Journal of Computational Physics* 101(1), 104 – 129. (p. 115)
- Price, R. B., I. R. Hurle, and T. M. Sugden (1969). Optical studies of the generation of noise in turbulent flames. *Proceedings of the Combustion Institute* 12(1), 1093–1102. (p. 21, 175, 193)
- Providakis, T., L. Zimmer, P. Scoufflaire, and S. Ducruix (2012). Characterization of the Acoustic Interactions in a Two-Stage Multi-Injection Combustor Fed With Liquid Fuel. *Journal of Engineering for Gas Turbines and Power* 134(11), 111503. (p. 92)
- Ranz, W. E. and W. R. Marshall (1952). Evaporation from Drops. *Chem. Eng. Prog* 48, 141–146. (p. 73)
- Rayleigh, J. W. S. (1878). The explanation of certain acoustical phenomena. *Na-*

- ture 18(455), 319–321. (p. 145)
- Rojatkar, P., Y.-H. Kao, S. Jog, M.A., and S.-M. Jeng (2014, June 16-20,). Effect of swirler offset on aerodynamics of multiswirler arrays. In *ASME Paper*, Number GT2014-26236, Düsseldorf, Germany. (p. 164, 170, 175)
- Rudy, D. H. and J. C. Strikwerda (1980). A nonreflecting outflow boundary condition for subsonic navier-stokes calculations. *Journal of Computational Physics* 36(1), 55–70. (p. 119)
- Sanjosé, M., J. M. Senoner, F. Jaegle, B. Cuenot, S. Moreau, and T. Poinso (2011, 6). Fuel injection model for Euler–Euler and Euler–Lagrange large-eddy simulations of an evaporating spray inside an aeronautical combustor. *Int. Journal of Multiphase Flow* 37(5), 514–529. (p. 129)
- Saurabh, A., J. P. Moeck, and C. O. Paschereit (2017). Swirl flame response to simultaneous axial and transverse velocity fluctuations. *Journal of Engineering for Gas Turbines and Power* 139(6), 061502. (p. 66)
- Saurabh, A. and C. O. Paschereit (2017). Dynamics of premixed swirl flames under the influence of transverse acoustic fluctuations. *Combustion and Flame* 182, 298–312. (p. 66)
- Schmid, P. J. (2010). Dynamic mode decomposition of numerical and experimental data. *Journal of Fluid Mechanics* 656, 5–28. (p. 82)
- Schönfeld, T. and M. Rudgyard (1999). Steady and unsteady flow simulations using the hybrid flow solver avbp. *AIAA Journal* 37(11), 1378–1385. (p. 114)
- Schuermans, B., V. Bellucci, and C. O. Paschereit (2003). Thermoacoustic modeling and control of multiburner combustion systems. In *ASME Conference Proceedings, Paper GT 2003-38688*. (p. 186)
- Schuermans, B., C. O. Paschereit, and P. Monkewitz (2006, January). Non-linear combustion instabilities in annular gas-turbine combustors. In *44th AIAA Aerospace Sciences Meeting and Exhibit*, Number AIAA paper 2006-0549. (p. 66, 92, 187, 188, 189)
- Schuermans, B., W. Polifke, and C. O. Paschereit (1999). Modeling transfer matrices of premixed flames and comparison with experimental results. In *ASME Conference Proceedings Paper 99-GT-132*. (p. 185)
- Schuller, T., D. Durox, and S. Candel (2002). Dynamics of and noise radiated by a perturbed impinging premixed jet flame. *Combustion and Flame* 128(1-2), 88–110. (p. 107)
- Schuller, T., D. Durox, and S. Candel (2003). A unified model for the prediction of laminar flame transfer functions: comparisons between conical and v-flames dynamics. *Combustion and Flame* 134, 21–34. (p. 3, 92, 104)
- Schuller, T., D. Durox, P. Palies, and S. Candel (2012). Acoustic decoupling of longitudinal modes in generic combustion systems. *Combustion and Flame* 159(5), 1921 – 1931. (p. 189)
- Selle, L., F. Nicoud, and T. Poinso (2004). Actual impedance of nonreflecting boundary conditions: Implications for computation of resonators. *AIAA journal* 42(5), 958–964. (p. 119)
- Senoner, J. M., M. Sanjosé, T. Lederlin, F. Jaegle, M. García, E. Riber, B. Cuenot,

- L. Gicquel, H. Pitsch, and T. Poinsot (2009). Eulerian and Lagrangian Large-Eddy Simulations of an evaporating two-phase flow. *Comptes Rendus Mécanique* 337(6–7), 458–468. (p. 129)
- Shum-Kivan, F., J. M. Santiago, A. Verdier, E. Riber, B. Renou, G. Cabot, and B. Cuenot (2016). Experimental and numerical analysis of a turbulent spray flame structure. *Proceedings of the Combustion Institute* 36(2), 2567–2575. (p. 115)
- Staffelbach, G., L. Y. M. Gicquel, G. Boudier, and T. Poinsot (2009). Large Eddy Simulation of self excited azimuthal modes in annular combustors. *Proceedings of the Combustion Institute* 32, 2909–2916. (p. 2, 66, 185)
- Stow, S. R. and A. P. Dowling (2001). Thermoacoustic oscillations in an annular combustor. In *ASME Conference Proceedings, Paper GT 2001-0037*. (p. 186)
- Tay-Wo-Chong, L., T. Komarek, R. Kaess, S. Foller, and W. Polifke (2010). Identification of flame transfer functions from LES of a premixed swirl burner. *ASME Turbo Expo 2010: Power for Land, Sea, and Air*, 623–635. (p. 112)
- Tay-Wo-Chong, L., A. Scarpato, and W. Polifke (2017). LES combustion model with stretch and heat loss effects for prediction of premix flame characteristics and dynamics. In *ASME Turbo Expo 2017: Turbomachinery Technical Conference and Exposition*, pp. V04AT04A029–V04AT04A029. American Society of Mechanical Engineers. (p. 112)
- Vagelopoulos, C. M., F. N. Egolfopoulos, and C. K. Law (1994). Further considerations on the determination of laminar flame speeds with the counterflow twin-flame technique. *Proc. Combust. Inst.* 25, 1341–1347. (p. 44)
- Wagner, P. and G. Dugger (1955). Flame propagation. v. structural influences on burning velocity. comparison of measured and calculated velocity. *J. Am. Chem. Soc.* 77, 227–231. (p. 45)
- Wang, H., V. McDonnell, and S. S. (1995). Influence of hardware design on the flow field structures and the pattern of droplet dispersion, part 1: mean quantities. *ASME J. Eng. Gas Turbines Power* 117, 282–289. (p. 165)
- Wolf, P., R. Balakrishnan, G. Staffelbach, L. M. Gicquel, and T. Poinsot (2012). Using LES to Study Reacting Flows and Instabilities in Annular Combustion Chambers. *Flow, Turbulence and Combustion* 88(1-2, SI), 191–206. (p. 2, 66, 185)
- Wolf, P., G. Staffelbach, L. Gicquel, J.-D. Müller, and T. Poinsot (2012). Acoustic and large eddy simulation studies of azimuthal modes in annular combustion chambers. *Combustion and Flame* 159, 3398–3413. (p. 2, 66, 80, 185)
- Worth, N. A. and J. R. Dawson (2012). Cinematographic OH-PLIF measurements of two interacting turbulent premixed flames with and without acoustic forcing. *Combust. Flame* 159(3), 1109–1126. (p. 164)
- Worth, N. A. and J. R. Dawson (2013a). Modal dynamics of self-excited azimuthal instabilities in an annular combustion chamber. *Combustion and Flame* 160(11), 2476–2489. (p. 67, 68, 165, 185, 189)
- Worth, N. A. and J. R. Dawson (2013b). Self-excited circumferential instabilities in a model annular gas turbine combustor: Global flame dynamics. *Proceedings of the Combustion Institute* 34(2), 3127–3134. (p. 2, 19, 67, 68, 165, 185, 189)

- Worth, N. A., J. R. Dawson, J. A. Sidey, and E. Mastorakos (2017). Azimuthally forced flames in an annular combustor. *Proceedings of the Combustion Institute* 36(3), 3783–3790. (p. 2)
- Worth, N. A., J. R. Dawson, J. A. M. Sidey, and E. Mastorakos (2016). Azimuthally forced flames in an annular combustor. *Proceedings of the Combustion Institute in press*. (p. 67)
- Wu, J., Y. Liu, and H. Sheen (2001). Effects of ambient turbulence and fuel properties on the evaporation rate of single droplets. *Int. J. Heat Mass Transf* 44(24), 4593–4603. (p. 20, 36, 37)
- Yamashita, H., M. Shimada, and T. Takeno (1996). A numerical study on flame stability at the transition point of jet diffusion flames. In *Symposium (International) on Combustion*, Volume 26, pp. 27–34. Elsevier. (p. 136)
- Yi, T. and D. Santavica (2009). Forced flame response of turbulent liquid-fueled lean-direct-injection combustion to fuel modulations. *Journal of Propulsion and Power* 25(6), 1259–1271. (p. 92)
- Yi, T. and D. A. Santavicca (2012). Combustion instability and flame structure of turbulent swirl-stabilized liquid-fueled combustion. *Journal of Propulsion and Power* 28(5), 1000–1014. (p. 92)



---

**Titre:** Dynamique de la combustion dans un foyer annulaire multi-injecteurs diphasique

**Résumé :** Ces dernières décennies ont vu apparaître de nombreuses innovations dans le domaine de la combustion afin de réduire la consommation et les émissions polluantes. De nouveaux types d'injecteur, de type LPP - Lean Premixed Prevaporized, ont été mis au point permettant de diminuer le rapport combustible/air et visent à pré-vaporiser le carburant en amont de la combustion afin de mieux le mélanger à l'air issu du compresseur. Cette architecture permet une amélioration de la consommation et des émissions polluantes, mais rend les foyers annulaires plus sensibles à des phénomènes instationnaires qui perturbent le fonctionnement du système, accroissent les flux de chaleur vers les parois de la chambre, induisent des vibrations de structures, entraînent une fatigue cyclique des pièces mécaniques et dans des cas extrêmes conduisent à des dommages irréversibles.

L'objectif est de poursuivre l'effort engagé au laboratoire EM2C sur ce thème et plus particulièrement sur celui de la dynamique de la combustion dans les chambres annulaires. La thèse concerne plus spécialement le cas où l'injection du combustible s'effectue sous forme liquide. La configuration reproduit sous forme idéalisée celle que l'on trouve en pratique dans les moteurs aéronautiques. La chambre, désignée sous le nom de MICCA-Spray, est équipée de 16 injecteurs swirlés pouvant être alimentés par un combustible liquide ou gazeux, permettant ainsi une combustion diphasique ou prémélangée. Le système possède des parois en quartz donnant un accès optique à la zone de flamme. Il est aussi équipé d'un ensemble de diagnostics tels des microphones, des photomultiplicateurs ainsi que des systèmes d'imagerie à haute cadence.

---

**Title:** Combustion dynamics of an annular combustion chamber equipped with multiple spray injectors

**Abstract:** These last decades have seen many innovations in the field of combustion to reduce fuel consumption and pollutant emissions. New types of injector, for example LPP - Lean Premixed Prevaporized, have then been developed to reduce the fuel / air ratio and aim to pre-vaporize the fuel upstream of the combustion in order to mix it better with the air coming from the compressor. Unfortunately this architecture makes annular chambers more sensitive to unsteady phenomena which disturb the functioning of the system, increase the heat flows towards the walls of the chamber, induce vibrations of structures, cause cyclic fatigue of mechanical parts and in extreme cases lead to irreversible damage. The objective of this thesis is to continue the effort undertaken at the EM2C lab-

oratory on this topic and more particularly on the dynamics of combustion in annular chambers comprising a set of injectors. The thesis concerns more particularly the case where the injection of the fuel takes place in liquid form. This configuration reproduces, in idealized form, what can be found in practice in aeronautical engines. It is also a configuration studied at the fundamental level. The chamber, known as MICCA-Spray, is equipped with 16 swirled injectors that can be powered by liquid or gaseous fuel, thus enabling two-phase or fully premixed combustion. The system has quartz walls giving optical access to the flame zone. It is also equipped with a set of diagnostics such as microphones, photomultipliers and high-speed imaging systems.

**Titre :** Dynamique de la combustion dans un foyer annulaire multi-injecteurs diphasique

**Mots clés :** dynamique de la combustion – instabilités de combustion – chambre annulaire - allumage

**Résumé :** Ces dernières décennies ont vu apparaître de nombreuses innovations dans le domaine de la combustion afin de réduire la consommation et les émissions polluantes. De nouveaux types d'injecteur, de type LPP - Lean Premixed Prevaporized, ont été mis au point permettant de diminuer le rapport combustible/air et visent à pré-vaporiser le carburant en amont de la combustion afin de mieux le mélanger à l'air issu du compresseur. Cette architecture permet une amélioration de la consommation et des émissions polluantes, mais rend les foyers annulaires plus sensibles à des phénomènes instationnaires qui perturbent le fonctionnement du système, accroissent les flux de chaleur vers les parois de la chambre, induisent des vibrations de structures, entraînent une fatigue cyclique des pièces mécaniques et dans des cas extrêmes conduisent à des

dommages irréversibles. L'objectif est de poursuivre l'effort engagé au laboratoire EM2C sur ce thème et plus particulièrement sur celui de la dynamique de la combustion dans les chambres annulaires. La thèse concerne plus spécialement le cas où l'injection du combustible s'effectue sous forme liquide. La configuration reproduit sous forme idéalisée celle que l'on trouve en pratique dans les moteurs aéronautiques. La chambre, désignée sous le nom de MICCA-Spray, est équipée de 16 injecteurs swirlés pouvant être alimentés par un combustible liquide ou gazeux, permettant ainsi une combustion diphasique ou prémélangée. Le système possède des parois en quartz donnant un accès optique à la zone de flamme. Il est aussi équipé d'un ensemble de diagnostics tels des microphones, des photomultiplicateurs ainsi que des systèmes d'imagerie à haute cadence.

**Title:** Combustion dynamics of an annular combustor with multiple spray injectors

**Keywords:** combustion dynamics – combustion instabilities – annular chamber – light-round

**Abstract:** These last decades have seen many innovations in the field of combustion to reduce fuel consumption and pollutant emissions. New types of injector, for example LPP - Lean Premixed Prevaporized, have then been developed to reduce the fuel / air ratio and aim to pre-vaporize the fuel upstream of the combustion in order to mix it better with the air coming from the compressor. Unfortunately this architecture makes annular chambers more sensitive to unsteady phenomena which disturb the functioning of the system, increase the heat flows towards the walls of the chamber, induce vibrations of structures, cause cyclic fatigue of mechanical parts and in extreme cases lead to irreversible damage. The objective of this thesis is to continue the effort undertaken at the EM2C

laboratory on this topic and more particularly on the dynamics of combustion in annular chambers comprising a set of injectors. The thesis concerns more particularly the case where the injection of the fuel takes place in liquid form. This configuration reproduces, in idealized form, what can be found in practice in aeronautical engines. It is also a configuration studied at the fundamental level. The chamber, known as MICCA-Spray, is equipped with 16 swirled injectors that can be powered by liquid or gaseous fuel, thus enabling two-phase or fully premixed combustion. The system has quartz walls giving optical access to the flame zone. It is also equipped with a set of diagnostics such as microphones, photomultipliers and high-speed imaging systems.

